Universidade do Minho
U.PORTO
Universidade de Aveiro
2020
Departamento de Eletrónica,
Telecomunicações e Informática

PEDRO MIRASSOL
TOMÉ

CARACTERIZAÇÃO, MODELAÇÃO E COMPENSAÇÃO DE EFEITOS DE MEMÓRIA LENTA EM AMPLIFICADORES DE POTÊNCIA BASEADOS EM GAN HEMTS

CHARACTERIZATION, MODELING AND COMPENSATION OF LONG-TERM MEMORY EFFECTS IN GAN HEMT-BASED RADIO-FREQUENCY POWER AMPLIFIERS

U. PORTO

Universidade de Aveiro Departamento de Eletrónica, Telecomunicações e Informática
2020

PEDRO MIRASSOL TOMÉ

CARACTERIZAÇÃO, MODELAÇÃO E COMPENSAÇÃO DE EFEITOS DE MEMÓRIA LENTA EM AMPLIFICADORES DE POTÊNCIA BASEADOS EM GAN HEMTS

CHARACTERIZATION, MODELING AND COMPENSATION OF LONG-TERM MEMORY EFFECTS IN GAN HEMT-BASED RADIO-FREQUENCY POWER AMPLIFIERS

Tese apresentada à Universidade do Minho, Universidade de Aveiro, e Universidade do Porto para cumprimento dos requisitos necessários à obtenção do grau de Doutor em Telecomunicações no âmbito do programa doutoral MAP-tele, realizada sob a orientação científica do Doutor Telmo Reis Cunha, professor auxiliar do Departamento de Eletrónica, Telecomunicações e Informática da Universidade de Aveiro, e sob a coorientação científica do Doutor Filipe Miguel Esturrenho Barradas, investigador do Instituto de Telecomunicações de Aveiro.

Apoio financeiro da FCT e do FSE no âmbito do III Quadro Comunitário de Apoio. Bolsa FCT ref. PD/BD/128198/2016.

o júri

presidente

Prof. Dr. Paulo Jorge de Melo Matias Faria de Vila Real
Professor Catedrático, Universidade de Aveiro

vogais

Prof. Dr. Henrique Manuel de Castro Faria Salgado
Professor Associado, Universidade do Porto

Prof. Dr. José Manuel Neto Vieira
Professor Auxiliar, Universidade de Aveiro

Prof. Dr. Telmo Reis Cunha
Professor Auxiliar, Universidade de Aveiro (orientador)

Dr. John Wood
Owner, Obsidian Microwave, LLC

Dr. Sérgio Carlos da Conceição Pires
Senior Director—Innovation and Advanced Concepts, Ampleon Semiconductors BV

agradecimentos

Aos meus orientadores, Prof. Dr. Telmo R. Cunha e Dr. Filipe M. Barradas, agradeço pela dedicação e disponibilidade demonstradas ao longo do meu doutoramento, pela autonomia que me conferiram para direcionar e realizar o meu trabalho de investigação, e pela constante exigência pelo máximo rigor técnico e científico; o vosso apoio foi instrumental no meu crescimento como investigador, cientista e engenheiro. Ao Prof. Dr. José C. Pedro, ao Dr. Luís C. Nunes, e aos restantes membros do grupo *Wireless Circuits* do Instituto de Telecomunicações de Aveiro, agradeço pelas muitas discussões técnicas relacionadas com o meu trabalho de investigação; em particular, ao Prof. Dr. José C. Pedro agradeço também pelas discussões não-técnicas sobre a minha carreira, a atividade de investigação científica, e outros assuntos relevantes para o meu crescimento pessoal e profissional. Ao Prof. Dr. Pedro M. Cabral e ao Dr. Luís C. Nunes agradeço pelo fornecimento dos circuitos amplificadores de radiofrequência e outro *hardware* necessário para o teste das hipóteses propostas nesta tese.

Ao pessoal técnico, administrativo e de suporte do Instituto de Telecomunicações de Aveiro, incluindo Hugo Mostardinha, Paulo Gonçalves, Nuno Silva, Yannick Sucá, Suzana Condesso, e Dª Elisabete, agradeço pelo seu suporte contínuo e confiável. Ao Instituto de Telecomunicações agradeço pela facultação de instalações, ferramentas e equipamento de reconhecida excelência para a realização do meu trabalho de investigação científica. Ao Departamento de Eletrónica, Telecomunicações e Informática da Universidade de Aveiro agradeço pela facultação de um ambiente único para o crescimento pessoal, a aprendizagem, e o desenvolvimento do pensamento crítico. Ao Programa Doutoral em Telecomunicações MAP-tele e à Fundação para a Ciência e a Tecnologia agradeço pelo apoio financeiro concedido sob a forma de uma bolsa de doutoramento.

Aos meus gatos, o Tesla e a Lunastra, agradeço pela sua companhia e pelo carinho demonstrado de forma espontânea (em troca de petiscos); em particular, ao Tesla agradeço também pela coautoria (não atribuída) da minha tese e dos artigos escritos. Aos meus pais, à Sara e Ricardo, e ao Diogo e William, agradeço pelo apoio incondicional e incansável, pela compreensão e encorajamento, e pela amizade sempre presente. Finalmente, à Jéssica, minha noiva, agradeço pelo amor demonstrado diariamente, pela companhia e conforto, pela alegria e partilha das nossas conquistas, e pelas muitas discussões técnicas e outras contribuições para o meu trabalho.

palavras-chave

Captura eletrónica, efeitos de memória lenta, linearização analógica, linearização de amplificadores de potência, predistorção digital, processamento analógico de signal, processamento digital de signal, transístor de alta mobilidade eletrónica.

resumo

Os transístores de alta mobilidade eletrónica de nitreto de gálio (GaN HEMTs) são considerados a tecnologia mais atrativa para a transmissão de sinais de radiofrequência de alta potência para comunicações móveis celulares e aplicações de radar. No entanto, apesar das suas notáveis capacidades de transmissão de potência, a utilização de amplificadores de potência (PAs) baseados em GaN HEMTs é frequentemente desconsiderada em favor de tecnologias alternativas baseadas em transístores de silício. Uma das principais razões disto acontecer é a existência pervasiva na tecnologia GaN HEMT de efeitos de memória lenta causados por fenómenos térmicos e de captura eletrónica. Apesar destes efeitos poderem ser compensados através de algoritmos sofisticados de predistorção digital, estes algoritmos não são adequados para transmissores modernos de células pequenas e interfaces massivas de múltipla entrada e múltipla saída devido à sua complexidade de implementação e extração de modelo, assim como a elevada potência necessária para a sua execução em tempo real. De forma a promover a utilização de PAs de alta densidade de potência e elevada eficiência baseados em GaN HEMTs em aplicações de comunicação e radar de nova geração, nesta tese propomos novos métodos de caracterização, modelação, e compensação de efeitos de memória lenta em PAs baseados em GaN HEMTs. Mais especificamente, nesta tese propomos um método de caracterização do comportamento dinâmico de autopolarização de PAs baseados em GaN HEMTs; vários modelos comportamentais de fenómenos de captura eletrónica e a sua implementação como circuitos eletrónicos analógicos para a previsão em tempo real da variação dinâmica da tensão de limiar de condução de GaN HEMTs; um método de compensação da instabilidade entre pulsos de PAs baseados em GaN HEMTs para aplicações de radar; e um esquema híbrido analógico/digital de linearização de PAs baseados em GaN HEMTs para comunicações de nova geração.

keywords

Analog linearization, analog signal processing, charge trapping, digital predistortion, digital signal processing, electron trapping, GaN high-electron-mobility transistor, long-term memory effects, power amplifier linearization.

abstract

Gallium nitride (GaN) high-electron-mobility transistors (HEMTs) have emerged as the most compelling technology for the transmission of high-power radio-frequency (RF) signals for cellular mobile communications and radar applications. However, despite their remarkable power capabilities, the deployment of GaN HEMT-based RF power amplifiers (PAs) in the mobile communications infrastructure is often ruled out in favor of alternative silicon-based technologies. One of the main reasons for this is the pervasiveness of nonlinear long-term memory effects in GaN HEMT technology caused by thermal and charge-trapping phenomena. While these effects can be compensated for using sophisticated digital predistortion algorithms, their implementation and model-extraction complexity—as well as the power necessary for their real-time execution—make them unsuitable for modern small cells and large-scale multiple-input multiple-output transceivers, where the power necessary for the linearization of each amplification element is of great concern. In order to address these issues and further the deployment of high-power-density high-efficiency GaN HEMT-based RF PAs in next-generation communications and radar applications, in this thesis we propose novel methods for the characterization, modeling, and compensation of long-term memory effects in GaN HEMT-based RF PAs. More specifically, we propose a method for the characterization of the dynamic self-biasing behavior of GaN HEMT-based RF PAs; multiple behavioral models of charge trapping and their implementation as analog electronic circuits for the accurate real-time prediction of the dynamic variation of the threshold voltage of GaN HEMTs; a method for the compensation of the pulse-to-pulse instability of GaN HEMT-based RF PAs for radar applications; and a hybrid analog/digital scheme for the linearization of GaN HEMT-based RF PAs for next-generation communications applications.

Contents

List of Figures xvii

List of Tables xxiii

List of Abbreviations xxv

1 Introduction 1

1.1 Background Information 1

1.2 Problem Statement and Objectives 3

1.3 Main Contributions 5

1.3.1 List of Contributions 6

1.4 Outline of the Thesis 8

2 Literature Review 9

2.1 Gallium Nitride High-Electron-Mobility Transistors 9

2.1.1 Heterostructure 10

2.2 Origin of Charge-Trapping Phenomena 14

2.2.1 Surface Trapping 15

2.2.2 Buffer Trapping 15

2.2.3 Gate Lag and Drain Lag 15

2.3 Characterization of Charge-Trapping Phenomena 16

2.3.1 Drain-Current Deep-Level Transient Spectroscopy 17

2.3.2 Low-Frequency Admittance Measurements 18

2.3.3 Pulse-Modulated RF Measurements 18

2.3.4 Two-Tone-Modulated RF Measurements 19

2.4 Modeling of Charge-Trapping Phenomena 20

2.4.1 Single-Time-Constant Jardel Model 20

2.4.2 Multiple-Time-Constant Jardel Model 21

2.4.3 Shockley–Read–Hall Statistics-Based Model 22

2.5 Prevention of Charge-Trapping Phenomena 23
2.5.1 Passivation 23
2.5.2 Field Plates 24
2.6 Analog Predistortion 24
2.6.1 Series-Diode Predistorters 24
2.6.2 Cubic Predistorters 25
2.6.3 Generalized IMD Generators 25
2.6.4 Polynomial Predistorters 26
2.6.5 Artificial Neural Networks 27
2.7 Digital Predistortion 27
2.7.1 Memory Polynomial 28
2.7.2 Generalized Memory Polynomial 28
2.7.3 Parametric Generalized Memory Polynomial 29

3 Hybrid Analog/Digital Linearization of GaN HEMT-Based PAs 31
3.1 Introduction 31
3.2 Compensation Strategy 32
3.3 Charge-Trapping Model 34
3.4 Analog Compensation Circuit 35
3.5 Practical Validation 36
3.5.1 Validation Procedure 36
3.5.2 Laboratory Setup 38
3.5.3 Setup Calibration 39
3.6 Results 40
3.7 Conclusion 44

4 Charge Emission as a Multiple-Time-Scale Phenomenon 45
4.1 Introduction 45
4.2 Compensation Model 46
4.2.1 Qualitative Operation 46
4.2.2 Comparison With Other Models 48
4.2.3 Mathematical Formulation 50
4.2.4 Temperature Considerations 51
4.3 Analog Compensation Circuit 52
4.4 Measurement Setup 54
4.5 Pulse Response Compensation 56
4.5.1 Setup Calibration 56
4.5.2 Measurement Procedure 57
4.5.3 Circuit Parameter Extraction 57
4.5.4 Compensation Results 58

4.6 Two-Tone Response Compensation 60
4.6.1 Setup Calibration 61
4.6.2 Measurement Procedure 61
4.6.3 Circuit Parameter Extraction 61
4.6.4 Compensation Results 63
4.7 Self-Biasing Compensation 64
4.8 5G NR Linearization 65
4.8.1 Measurement Procedure 66
4.8.2 Compensation Results 66
4.9 Conclusion 68

5 Pulse-to-Pulse Instability of GaN HEMT-Based PAs 71
5.1 Introduction 71
5.2 Pulse-to-Pulse Stability 72
5.3 Compensation Method 73
5.4 Implementation Details 75
5.5 Results 77
5.6 Conclusion 79

6 Dynamic Self-Biasing Behavior of GaN HEMT-Based PAs 81
6.1 Introduction 81
6.2 Theoretical Background 82
6.3 Characterization 83
6.3.1 Transient Two-Tone RF Characterization Method 84
6.3.2 Experimental Results 87
6.4 Modeling 90
6.4.1 Model Extraction 91
6.4.2 Model Definition 92
6.4.3 Experimental Results 92
6.5 Analog Compensation 94
6.5.1 Analog Compensation Circuit 94
6.5.2 Experimental Results 98
6.6 Conclusion 99

7 Conclusion 101
7.1 Summary of Main Contributions 101
7.2 Future Research 102

Appendix A Schematic of the Jardel ACC 105

Appendix B Schematic of the Variable-Time-Constant Emission ACC 107

Appendix C Schematic of the Piecewise-SRH ACC 109

Appendix D Extended Variable-Time-Constant Charge-Trapping Model 111

Appendix E Paper J2: Hybrid Analog/Digital Linearization of GaN HEMT-Based Power Amplifiers 113

Appendix F Paper J4: A Multiple-Time-Scale Analog Circuit for the Compensation of Long-Term Memory Effects in GaN HEMT-Based Power Amplifiers 121

Appendix G Paper J5: Characterization, Modeling, and Compensation of the Dynamic Self-Biasing Behavior of GaN HEMT-Based Power Amplifiers 137

Appendix H Paper C3: Compensation of the Pulse-to-Pulse Instability of GaN HEMT-Based Power Amplifiers 151

Appendix I Paper C4: A Transient Two-Tone RF Method for the Characterization of Electron Trapping Capture and Emission Dynamics in GaN HEMTs 157

References 163

List of Figures

1.1 Requirements for the different use cases of 5G [2]. 2

1.2 (a) Expected and (b) actual (typical) response of a GaN HEMT-based PA to a burst of square pulses, a waveform commonly used in radar applications. 4

2.1 Example of a typical GaN HEMT heterostructure (not to scale). 10

2.2 Example of a commercially available 15 W 28 V GaN HEMT. 10

2.3 Conduction band profile (solid line) and 2DEG distribution (dashed line) in AlGaN/GaN heterostructures [46]. z denotes the distance from the surface to the inside of the heterostructure. 12

2.4 Gate lag observed in the response of the drain current to a step variation in the gate voltage [63]. 16

2.5 Drain lag observed in the response of the drain current to a step variation in the drain voltage. 16

2.6 (a) Pulsed I-DLTS. (b) Isothermal double-pulsed I-DLTS. 17

2.7 Typical low-frequency admittance measurement results. 18

2.8 Typical (a) pulse-modulated and (b) two-tone-modulated RF measurements-based charge-trapping characterization results. 20

2.9 Equivalent circuit of the Jardel model. 21

2.10 Equivalent circuit of the SRH model. 23

2.11 Series-diode predistorter. 25

2.12 Cubic predistorter. 25

2.13 Fifth-order generalized IMD generator predistorter [115]. 26

2.14 Four-quadrant analog multiplier. 27

3.1 Nonlinear multiple-time-constant model of the self-biasing caused by charge trapping in GaN HEMTs. V_E is the amplitude of the input envelope; V_{BG} is the back gate voltage. The diode is assumed to be ideal ($V_f = 0$ V). 34

3.2 Diagram of the analog feedforward circuit for the compensation of long-term memory effects due to the self-biasing caused by charge trapping in GaN HEMTs. 35
3.3 Photograph of the analog compensation circuit. 36
3.4 Envelope amplitude of the 4-carrier GSM PA input signal. 37
3.5 Diagram of the laboratory setup. 38
3.6 Photograph of the laboratory setup. 39
3.7 Photograph of the GaN HEMT-based PA. 40
3.8 Output of the ACC—the compensated gate bias voltage of the GaN HEMT—and, in the background, a representation of the input envelope amplitude (for visual reference). 41
3.9 Long-term residual error signal of the predistorted PA output when the ACC is disabled and when the ACC is enabled. Also, in the background, a representation of the input envelope amplitude is shown for visual reference. 42
3.10 Spectra of the PA output without any compensation, with linearization using a GMP, and after being linearized using our hybrid analog/digital linearization scheme. 43
3.11 (a) AM–AM and (b) AM–PM profiles of the PA without any compensation, with compensation of trapping effects using the ACC, and after being linearized using the hybrid analog/digital linearization scheme. 43

4.1 Nonlinear multiple-time-scale variable-emission-time-constant model for the compensation of long-term memory effects in GaN HEMT-based PAs. All diodes are assumed to be ideal ($V_f = 0$ V). 47
4.2 Comparison between the output of our model with a variable two-branch emission time constant, a model with two independent emission time constants (1 ms and 10 ms), a model with one fixed emission time constant equal to 10 ms, and a model with one fixed emission time constant equal to 1 ms for (a) a pulsed excitation and (b) a two-tone excitation. 49
4.3 Trapping core of the variable-emission-time-constant compensation model. 50
4.4 Variability of the pulse response of our compensation model with a state-dependent variable emission time constant for a fixed set of resistors R_n and various sets of breakpoint voltages V_n. 51
4.5 Photograph of the variable-emission-time-constant ACC. 53
4.6 Simplified schematic of the trapping core of the ACC. Red arrows indicate potential sources of discrepancies between the model and its practical implementation. v_x is the input envelope amplitude. 54
4.7 Diagram of the measurement setup. 55
4.8 Photograph of the measurement setup. 55
4.9 Photograph of the GaN HEMT-based PA. 56

4.10 Pulse response of the GaN HEMT-based PA (a) without compensation and (b) with compensation using our ACC. A zoomed-in view of the same data can also be seen in (c) for the case without compensation and (d) for the case with compensation. 59
4.11 Compensation of the response to a 30 dBm pulse using an ACC with one fixed emission time constant. 60
4.12 Two-tone response of the GaN HEMT-based PA (a) without compensation and (b) with compensation using our ACC. 64
4.13 Dynamic gain profile of the GaN HEMT-based PA (a) without compensation and (b) with compensation using our ACC. 65
4.14 Envelope of the PA input signal. 67
4.15 Spectra of the PA input, the PA output without linearization, the PA output with linearization using a simple memory-polynomial DPD, the PA output with linearization using this same DPD and an ACC with a fixed emission time constant, and the PA output with linearization using the DPD and our proposed ACC with a state-dependent variable emission time constant. 68
4.16 Temporal evolution of the EVM of the PA output after (a) linearization using a simple memory-polynomial DPD unit, (b) linearization using this same DPD unit and an ACC with a fixed emission time constant, and (c) linearization using the DPD unit and our proposed ACC with a state-dependent variable emission time constant. In the background, a representation of the input envelope is shown for visual reference. 69

5.1 Measured response of a GaN HEMT-based PA to a burst of square pulses with equal amplitude. 72
5.2 Variation of (a) the small-signal power gain and (b) the large-signal gain of the GaN HEMT-based PA for various values of the gate–source voltage. Also, as plot inserts, the actual (a) G^{SS} and (b) G^{LS} gain profiles used for interpolation. 74
5.3 Diagram of the laboratory setup. 76
5.4 Photograph of the laboratory setup. 76
5.5 The first millisecond of the signal that compensates the pulse-to-pulse instability of the GaN HEMT-based PA. Also, in the background, a representation of the first four input pulses is shown for visual reference. 77
5.6 (a) Complete and (b) zoomed-in view of the compensated and uncompensated responses of the GaN HEMT-based PA to a pulsed waveform. 78
5.7 Pulse-to-pulse amplitude stability of the compensated and uncompensated responses of the GaN HEMT-based PA to a pulsed waveform. 79

6.1 Typical transient response of a GaN HEMT-based PA to a two-tone envelope excitation. Due to charge trapping, the PA gradually self-biases toward a deep class C and loses most of its small-signal gain. 82

6.2 Diagram of the proposed characterization method. First, the transient response of the PA to a series of large-signal two-tone excitations is measured. Then, specific small-signal points are selected at $t = t_{ss}(k)$. Finally, the equivalent gate–source voltage variation is estimated by mapping these points onto V_{GS} through the measured $P_{out}(V_{GS}, V_{ss})$ map. $y_a(t)$ is the PA output envelope, time-aligned with the corresponding two-tone input signal. 84

6.3 Comparison between the envelope alignment results obtained with different optimization cost functions. 86

6.4 Diagram of (a) the measurement setup for the characterization of the dynamic self-biasing behavior of a GaN HEMT-based PA, and (b) the calibration equipment. During calibration, the PA is disconnected from the measurement setup and the calibration equipment is connected in its stead at the α and β planes. 88

6.5 (a) Variation of the PA output power as a function of the gate–source voltage V_{GS} for a constant 0 dBm CW excitation. (b) Variation of the PA output power measured at the small-signal-input instants $t_{ss}(k)$ as a function of the two-tone frequency separation Δf. Also, in black markers, an example of the gradual self-biasing for $\Delta f = 100$ kHz. 90

6.6 Result of the extraction of (a) the Jardel model and (b) the SRH model. In the background, the estimated variation of the threshold voltage of the GaN HEMT is also shown. 93

6.7 Block diagram of the analog compensation circuit. 94

6.8 Equivalent circuit of the piecewise-SRH model. 95

6.9 Photograph of the Jardel ACC. 97

6.10 Photograph of the piecewise-SRH ACC. 97

6.11 Result of the extraction of the piecewise-SRH model and, in the background, the estimated variation of the threshold voltage of the GaN HEMT. 98

6.12 Diagram of the measurement setup for the compensation of the dynamic self-biasing behavior of a GaN HEMT-based PA. 99

6.13 Dynamic variation of the small-signal PA output power when compensated by (a) the Jardel ACC and (b) the piecewise-SRH ACC. 100

7.1 Multiple-time-scale charge-trapping behavioral model with state-variable capture and emission time constants. 103

7.2 Compensation signal during the emission phase for a pulsed excitation with a peak power of 30 dBm and 26 dBm. The signal corresponding to the 26 dBm pulse is time-shifted to demonstrate that the rate of discharge is not solely dependent on the instantaneous output state. 104

List of Tables

1.1 Key specifications of 4G LTE-Advanced and 5G NR. 3

3.1 Summary of the linearization results. 44

4.1 Pulse response compensation parameters. 58
4.2 Two-tone response compensation parameters. 63

List of Abbreviations

Abbreviation	Meaning	Pages
2DEG	Two-Dimensional Electron Gas	12, 13, 15, 16, 33
3GPP	3rd Generation Partnership Project	2, 66
4G	Fourth-Generation	2
5G	Fifth-Generation	2–4, 45, 46, 65–67, 69, 101
ACC	Analog Compensation Circuit	35–42, 45, 46, 52, 54, 56–69, 82, 94, 96, 98–102, 104
ACLR	Adjacent-Channel Leakage Ratio	26
AlGaN	Aluminum Gallium Nitride	11–15, 23, 33, 83
AlN	Aluminum Nitride	11, 13, 14, 23, 24
AM–AM	Amplitude-to-Amplitude Modulation	25, 42, 48
AM–PM	Amplitude-to-Phase Modulation	25, 42
ANN	Artificial Neural Network	27
AWG	Arbitrary Waveform Generator	75, 77, 87
CMA-ES	Covariance Matrix Adaptation Evolution Strategy	58, 62, 85, 91
CMOS	Complementary Metal–Oxide–Semiconductor	26, 27
CW	Continuous-Wave	57, 62, 84, 86, 87, 89
DPD	Digital Predistortion	4, 5, 8, 25, 27, 29, 31, 32, 34, 36, 37, 39, 41, 44–46, 65–69, 83, 100–102
EVM	Error-Vector Magnitude	67, 69
FIR	Finite-Impulse-Response	28, 61
GaN	Gallium Nitride	1, 3–6, 8–16, 18, 19, 21, 23, 29, 31–33, 35, 36, 38, 40–42, 44–48, 52, 54, 56–60, 63–69, 71–73, 75, 79–84, 87, 89–91, 94, 98–104
GMP	Generalized Memory Polynomial	28, 29, 32, 36, 37, 39, 41, 44
GSM	Global System for Mobile Communications	31, 32, 37, 38, 41, 44
HEMT	High-Electron-Mobility Transistor	1, 3–6, 8–24, 29, 31–36, 38, 40–42, 44–48, 52, 54, 56–60, 63–69, 71–73, 75, 77, 79–84, 87, 89–92, 94, 98–104
I-DLTS	Drain-Current Deep-Level Transient Spectroscopy	17, 81

IMD	Intermodulation Distortion	25, 26, 31, 32
IMR	Intermodulation Distortion Ratio	41, 44
LTE	Long-Term Evolution	2, 26
MBE	Molecular-Beam Epitaxy	10, 11
MgCaO	Magnesium Calcium Oxide	14, 23
MIMO	Multiple-Input Multiple-Output	2, 4, 5, 46, 65
MOCVD	Metalorganic Chemical Vapor Deposition	10, 11
MP	Memory Polynomial	28
MSE	Mean Squared Error	58, 62, 91
MTI	Moving Target Indication	71, 79
NR	New Radio	2, 4, 45, 46, 65–67, 69, 101
PA	Power Amplifier	3–6, 8, 19, 20, 22, 24–29, 31–42, 44–48, 50, 52, 54, 56–69, 71–75, 77, 79, 81–87, 89–95, 98–104, 111
PAE	Power-Added Efficiency	41, 42, 44, 67–69, 87
PAPR	Peak-to-Average Power Ratio	67, 68
PM	Power Meter	39, 40, 54, 56, 88
RF	Radio-Frequency	2–5, 10, 14, 18–20, 22, 24, 25, 27, 28, 31, 32, 45, 47, 56, 57, 60, 71, 81, 82, 84, 85, 87, 92–94, 99, 101
RMS	Root Mean Square	67
SiC	Silicon Carbide	10
SiN	Silicon Nitride	14, 23, 24
SRH	Shockley–Read–Hall	22, 81, 82, 92–96, 98–100
TDD	Time-Division Duplexing	4, 45, 65, 66
VNA	Vector Network Analyzer	40, 87
VSA	Vector Signal Analyzer	19, 39, 54, 56, 61, 75, 81, 85, 87, 88
VSG	Vector Signal Generator	19, 39, 54, 56, 57, 61, 75, 77, 81, 85, 87
WCDMA	Wideband Code-Division Multiple Access	26

CHAPTER 1

Introduction

Synopsis — In this chapter we establish the background information, motivation, and objectives of the work reported in this thesis. Moreover, we also summarize the main contributions of our work to the state of the art in the characterization, modeling, and compensation of long-term memory effects in GaN HEMT-based radio-frequency power amplifiers.

1.1 Background Information

Cellular mobile communications has become one of the most significant and transformative technologies in history. From voice calls and text messaging to mobile broadband Internet access, mobile communications has contributed to the staggering economic and social development that has taken place in the past three decades and continues to accelerate toward the future. The evolution of mobile communications has largely been shaped by the continuously increasing traffic volume and the growing number of connected devices and services, as well as consumer demands for greater affordability and enhanced user experience. However, the achievement of all seventeen sustainable development goals set by the United Nations General Assembly in 2015 [1], from affordable and clean energy to responsible consumption and production, as well as greater social awareness on the contribution of carbon emissions to climate change, call for more than a simple incremental step in the evolution of mobile communications—rather, they call for a generational leap in the way mobile communications are facilitated and how energy is consumed in the process.

With the objective of meeting the growing demand for enhanced mobile broadband (hugely increased data rates, user density and mobility for access to multimedia content, services and data), ultra-reliable and low-latency communications (for safety-critical applications, wireless control of industrial processes, remote medical surgery, etc.), and massive machine-type communications (for the autonomous communication between large numbers of low-cost connected devices), the International Telecommunication Union has put

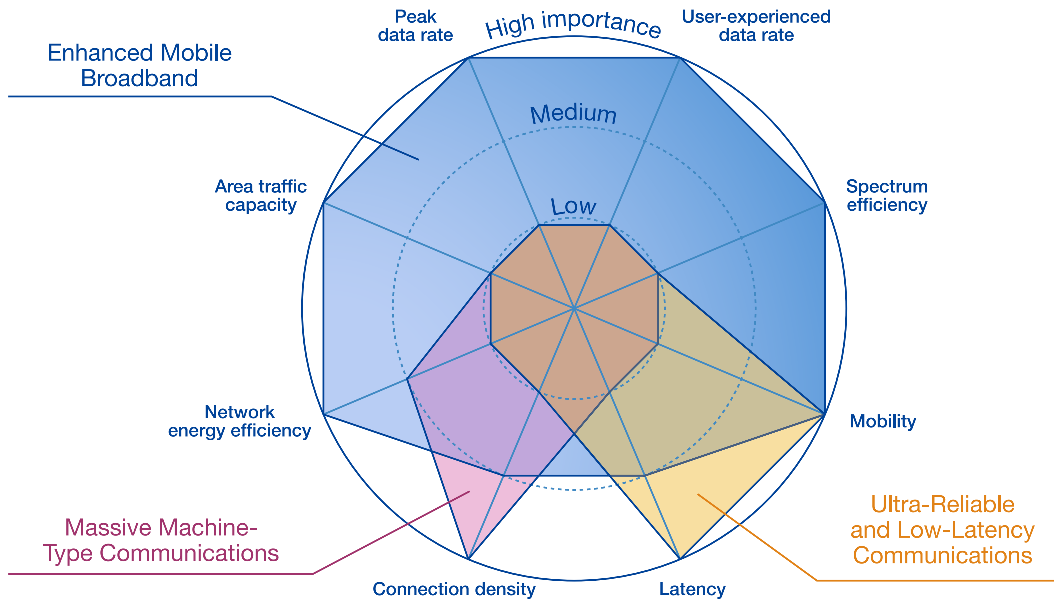

Figure 1.1 Requirements for the different use cases of 5G [2].

forth a set of requirements [2], illustrated in Figure 1.1, for the fifth generation of mobile communications (5G). In response to these requirements, the 3rd Generation Partnership Project (3GPP) has delivered the specifications for New Radio (NR), the fifth-generation radio access technology. Compared to the fourth-generation (4G) Long-Term Evolution (LTE)-Advanced radio access technology, NR features significantly improved operational performance and user experience [3]—see Table 1.1. Moreover, NR introduces foundational technologies such as massive multiple-input multiple-output (MIMO) and multi-beam operation (beamforming) for increased network capacity, throughput, and spectral efficiency. These technologies also contribute to better energy efficiencies, since they allow for the transmission of data in multiple highly directional radiation beams, rather than the nearly omnidirectional radiation patterns employed in earlier standards.

Besides introducing new multi-antenna technologies, 5G exploits new spectra well beyond that of previous generations—frequencies up to 114.25 GHz are being considered for upcoming releases of NR [4]. While radiation at such high frequencies will enable novel use cases and ultra-wideband cellular applications, it will also necessarily lead to structural changes in network architectures due to the crippling path loss incurred during the propagation of radio-frequency (RF) or millimeter-wave signals in dense urban environments. Thus, instead of network coverage being provided by central hugely encompassing high-power transmitters, it will preferably be done through the massive deployment of small cells consisting of low-power distributed transmitters [5], [6]. Naturally, this does not preclude the deployment of macro cells, as these are not only necessary for backward compatibility and the servicing of rural areas but may also enable the concurrent utilization of the various spectrum ranges available in 5G NR, especially in the earlier stages of its

Table 1.1 Key specifications of 4G LTE-Advanced and 5G NR.

	LTE-Advanced (Release 10)	NR (Release 15)
Frequency range	699–3800 MHz	FR1: 450–7125 MHz FR2: 24.25–52.60 GHz
Maximum bandwidth	Per CC: 20 MHz With CA: 100 MHz	Per CC: 100 MHz (FR1), 400 MHz (FR2) With CA: 1.6 GHz (FR1), 6.4 GHz (FR2)
Peak data rate (downlink)	Per CC: 600 Mbit/s With CA: 3 Gbit/s	Per CC: 4.9 Gbit/s (FR1), 10.7 Gbit/s (FR2) With CA: 78.2 Gbit/s (FR1), 171.2 Gbit/s (FR2)
Peak data rate (uplink)	Per CC: 300 Mbit/s With CA: 1.5 Gbit/s	Per CC: 2.4 Gbit/s (FR1), 4.0 Gbit/s (FR2) With CA: 38.2 Gbit/s (FR1), 64.6 Gbit/s (FR2)
Average spectral efficiency	Downlink: 3.2 (bit/s)/Hz Uplink: 2.5 (bit/s)/Hz	Downlink: 13.9 (bit/s)/Hz Uplink: 7.7 (bit/s)/Hz
Minimum latency	4.8 ms	0.48 ms
Maximum mobility	350 km/h	500 km/h

CC: component carrier; CA: carrier aggregation (5 CCs in LTE-Advanced, 16 CCs in NR).

deployment. For instance, control channels at microwave frequencies can be used to set up reliable connections on top of which blazing-fast data transmissions can be arranged over short-range millimeter-wave links [7].

The deployment of 5G technology will undoubtedly spur a breadth of new applications across every industry and accelerate economies across the globe. However, from the operation at millimeter-wave frequencies to the demand for greater power densities and efficiencies, 5G also introduces new challenges that call for a technological change at the semiconductor device level. For this reason, novel semiconductor technologies with the capability of taking on all of the challenges and requirements brought about by the introduction of 5G are expected to be an important enabler of the next generation of mobile communications.

1.2 Problem Statement and Objectives

Gallium nitride (GaN) high-electron-mobility transistors (HEMTs) have emerged as the most compelling technology for the transmission of high-power RF signals for cellular mobile communications and radar applications [8], [9]. However, despite their remarkable power capabilities, the deployment of GaN HEMT-based RF power amplifiers (PAs) in the mobile communications infrastructure is often ruled out in favor of alternative silicon-based technologies. One of the reasons for this is the pervasiveness of nonlinear long-term memory effects in GaN HEMT technology caused by thermal and charge-trapping phenomena: the capture and emission of charge carriers in deep-level traps. These effects, which include current collapse [10], knee walkout [11] and dc–RF dispersion [12], lead to a slow dynamic nonlinearity that manifests itself as a seemingly intractable post-linearization

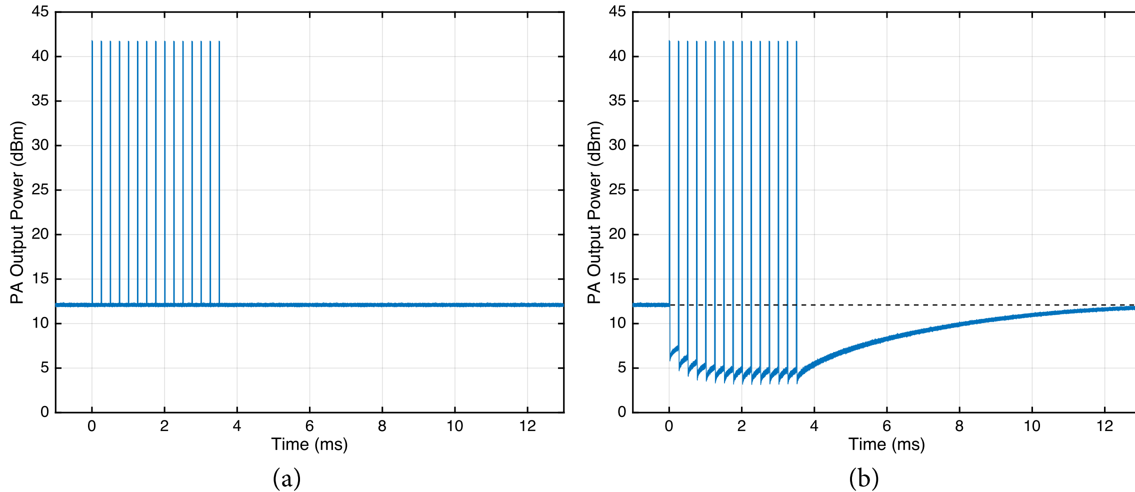

Figure 1.2 (a) Expected and (b) actual (typical) response of a GaN HEMT-based PA to a burst of square pulses, a waveform commonly used in radar applications.

residual distortion in communications applications [13] and a severe deterioration of the pulse-to-pulse stability in radar applications [14]. Figure 1.2 illustrates a clear example of the long-term variation of the transfer characteristics of a GaN HEMT-based PA due to charge-trapping phenomena. The first objective of the work reported in this thesis was, therefore, as follows:

Objective 1: Study and advance the state of the art in the characterization and modeling of the nonlinear long-term memory effects caused by thermal and charge-trapping phenomena in GaN HEMT-based RF PAs.

In addition to addressing the characterization and modeling of long-term memory effects, the compensation of these effects using analog electronic circuits was also investigated. This marks a clear difference between the work reported in this thesis and the rest of the state of the art—and, indeed, the latest and hugely predominant digital predistortion (DPD)-based research trends concerning the linearization of RF PAs. The reason for the atypical analog approach explored in this work is that, with emerging standards for mobile communications such as 5G NR, the deployment of small-cell and massive-MIMO technology to enhance network coverage and capacity is expected to place new restrictions on the hardware complexity and the related power resources available for the linearization of each individual PA in a transmitter array [15], [16]. Thus, existing DPD algorithms for the linearization of GaN HEMT-based PAs, which are very power-demanding and do not scale with antenna count due to their outstanding complexity, will necessarily be phased out in favor of simpler, more efficient linearization schemes [17]. Furthermore, the flexible frame structure specified in 5G NR for the efficient multiplexing of services with diverse requirements—e.g., low latency and high reliability (short subframes), or delay tolerance and high spectral efficiency (long subframes)—, as well as the dynamic time-division du-

plexing (TDD) scheme for access to the air interface [18], will excite long-term memory in transmitting PAs with an even greater variety of time scales than previous generations of mobile communications architectures and waveforms. The second objective of the work reported in this thesis was, therefore, as follows:

Objective 2: Design, implement and test novel analog electronic circuits for the compensation of the nonlinear long-term memory effects caused by thermal and charge-trapping phenomena in GaN HEMT-based RF PAs.

With these two objectives, we envision a high-power-density high-efficiency GaN HEMT-based PA with an integrated and co-designed low-power analog signal-processing unit responsible for the compensation of the long-term memory effects caused by thermal and charge-trapping phenomena. For the linearization of this augmented PA with no apparent long-term memory effects, only a low-complexity low-power DPD unit should be required.

1.3 Main Contributions

From November 2016 to October 2020, this Ph.D. work produced the following contributions to the state of the art in GaN HEMT-based PA long-term memory characterization, modeling, and compensation.

In [J2], we proposed a hybrid analog/digital linearization scheme for GaN HEMT-based PAs that consisted of an analog electronic circuit for the compensation of the long-term memory effects caused by thermal and charge-trapping phenomena and a conventional DPD for the compensation of the short-term memory and static nonlinearity of the PA. The analog compensation circuit implemented a charge-trapping model with a fixed capture time constant and a fixed emission time constant. This work marked our first effort toward a more sustainable PA linearization scheme for modern small-cell and massive-MIMO transmitters. In reality, most of our posterior work focused on improving the accuracy of the charge-trapping model and compensation circuit—not just to advance the state of the art in the behavioral modeling of charge-trapping phenomena and their effects on the nonlinear behavior of GaN HEMT-based PAs, but also to further reduce the complexity of the complementary DPD model, whose real-time execution should draw as little electrical power as possible.

In [J4], we proposed a novel charge-trapping model with a state-dependent variable emission time constant (and its implementation as an analog compensation circuit) for the modeling and compensation of the nonlinear long-term memory effects experienced by GaN HEMT-based PAs with unprecedented accuracy. The variable-time-constant formulation of the proposed model allows for the online adaptation of the dynamics of the compensation circuit to varying operating conditions (e.g., process, supply voltage, and

ambient temperature variations) in order to meet even the most stringent field conditions that affect the trapping dynamics of the GaN HEMT. Moreover, in this paper we disproved the very common assumption that the phenomenon of charge emission can be accurately modeled using multiple emission time constants—instead, only one single variable emission time constant should be considered (as in the proposed model).

In [C3], we proposed a method for the compensation of the pulse-to-pulse instability of GaN HEMT-based PAs for radar applications caused by charge-trapping phenomena. To the best of our knowledge, this paper marks the first time a GaN HEMT-based PA (not biased in class A) produced a pulse response that was actually square in both the large-signal and small-signal regions, meaning that all thermal, charge-capture, and charge-emission effects had been perfectly compensated. This paper was extended in [J3].

Finally, in [C4] and [J5] we proposed an experimental method for the accurate characterization and extraction of the time constants associated with the charge capture and emission processes of charge-trapping phenomena in GaN HEMT-based PAs. With little requirements in terms of instrumentation and with applicability to fully assembled PAs, this simple method provides arguably the most complete characterization of the charge capture and emission dynamics close to the actual operating conditions of GaN HEMT-based PAs. The proposed characterization method was validated by completely eliminating any transient symptom of current collapse during the transient evolution of a GaN HEMT's internal trapping state using an analog compensation circuit that implemented an approximation of the Shockley–Read–Hall statistics-based physical model of charge trapping.

1.3.1 List of Contributions

Papers in Journals:

- [J1] F. M. Barradas, **P. M. Tomé**, J. M. Gomes, T. R. Cunha, P. M. Cabral, and J. C. Pedro, "Power, linearity, and efficiency prediction for MIMO arrays with antenna coupling," *IEEE Trans. Microw. Theory Techn.*, vol. 65, no. 12, pp. 5284–5297, Dec. 2017.
- [J2] **P. M. Tomé**, F. M. Barradas, T. R. Cunha, and J. C. Pedro, "Hybrid analog/digital linearization of GaN HEMT-based power amplifiers," *IEEE Trans. Microw. Theory Techn.*, vol. 67, no. 1, pp. 288–294, Jan. 2019.
- [J3] F. M. Barradas, **P. M. Tomé**, T. R. Cunha, and J. C. Pedro, "Compensation of power amplifier long-term memory behavior for pulsed radar applications," *IEEE Trans. Microw. Theory Techn.*, vol. 67, no. 12, pp. 5249–5256, Sep. 2019.
- [J4] **P. M. Tomé**, F. M. Barradas, T. R. Cunha, and J. C. Pedro, "A multiple-time-scale analog circuit for the compensation of long-term memory effects in GaN HEMT-based power amplifiers," *IEEE Trans. Microw. Theory Techn.*, vol. 68, no. 9, pp. 3709–3723, Jul. 2020.

- [J5] **P. M. Tomé**, F. M. Barradas, L. C. Nunes, J. L. Gomes, T. R. Cunha, and J. C. Pedro, "Characterization, modeling, and compensation of the dynamic self-biasing behavior of GaN HEMT-based power amplifiers," *IEEE Trans. Microw. Theory Techn.*, Jul. 2020, DOI: 10.1109/TMTT.2020.3006290.
- [J6] J. B. Sanson, **P. M. Tomé**, D. Castanheira, A. Gameiro, and P. P. Monteiro, "High-resolution delay-Doppler estimation using received communication signals for OFDM radar-communication system," *IEEE Trans. Veh. Technol.*, Sep. 2020, DOI: 10.1109/TVT.2020.3021338.

Papers in Conferences:

- [C1] J. B. Sanson, **P. M. Tomé**, and P. Georgieva, "Enabling MIMO beaforming through compressed CSI feedback based on principal component analysis," in *Proc. Portuguese Conf. Pattern Recognition*, Amadora, Portugal, Oct. 2017, pp. 13–14.
- [C2] T. R. Cunha, **P. M. Tomé**, and C. J. Castela, "Analysis of static analog linearizer architectures for power amplifiers," in *Proc. URSI Atlantic Radio Sci. Conf.*, Gran Canaria, May 2018, pp. 1–4.
- [C3] **P. M. Tomé**, F. M. Barradas, T. R. Cunha, and J. C. Pedro, "Compensation of the pulse-to-pulse instability of GaN HEMT-based power amplifiers," in *Proc. IEEE MTT-S Int. Microw. Symp.*, Boston, MA, USA, Jun. 2019, pp. 408–411.
- [C4] **P. M. Tomé**, F. M. Barradas, L. C. Nunes, J. L. Gomes, T. R. Cunha, and J. C. Pedro, "A transient two-tone RF method for the characterization of electron trapping capture and emission dynamics in GaN HEMTs," in *Proc. IEEE MTT-S Int. Microw. Symp.*, Los Angeles, CA, USA, Jun. 2020, pp. 428–431.

Workshops:

- [W1] F. M. Barradas, **P. M. Tomé**, L. C. Nunes, T. R. Cunha, P. M. Lavrador, P. M. Cabral, and J. C. Pedro, "Causes, identification and compensation of short-, medium- and long-term memory effects in power amplifiers," in *Proc. IEEE MTT-S Int. Microw. Symp. (Workshop)*, Philadelphia, PA, USA, Jun. 2018.
- [W2] L. C. Nunes, F. M. Barradas, C. Gonçalves, J. L. Gomes, **P. M. Tomé**, T. R. Cunha, P. M. Cabral, and J. C. Pedro, "Long-term memory effects in GaN devices: From modeling to compensation," in *Proc. Eur. Microw. Conf. (Workshop)*, Madrid, Spain, Sep. 2018.
- [W3] F. M. Barradas, T. R. Cunha, **P. M. Tomé**, P. M. Lavrador, P. M. Cabral, L. C. Nunes, and J. C. Pedro, "Prediction and compensation of PA linearity and efficiency in MIMO scenarios," in *Proc. Eur. Microw. Conf. (Workshop)*, Madrid, Spain, Sep. 2018.

1.4 Outline of the Thesis

In Chapter 2, we review the state of the art relevant to this thesis. In Chapter 3, we describe a novel hybrid analog/digital linearization scheme for GaN HEMT-based PAs for communications applications. In this linearization scheme, an analog electronic circuit compensates the long-term memory of the PA and a low-complexity DPD unit compensates the short-term memory and the static nonlinearity of the PA. In Chapter 4, we present a novel charge-trapping behavioral model that features a state-dependent variable emission time constant. The implementation of this model as an analog electronic circuit is demonstrated to be capable of eliminating any multiple-time-scale transient symptom of current collapse following a high-power excitation. In Chapter 5, we describe a method for the compensation of the pulse-to-pulse instability of GaN HEMT-based PAs for radar applications. In Chapter 6, we describe a novel method for the characterization of the dynamic self-biasing behavior of GaN HEMT-based PAs, as well as the capture and emission dynamics of charge trapping. In this chapter, we also present a novel charge-trapping behavioral model that features a state-dependent variable capture time constant. Finally, in Chapter 7, we summarize the main contributions of this work and propose relevant avenues for future research.

CHAPTER 2
Literature Review

Synopsis — In this chapter we summarize the epitaxial structure of GaN HEMTs and review the state of the art in the characterization, modeling, and prevention of long-term memory effects in GaN HEMTs caused by charge-trapping phenomena. Moreover, we also review the relevant state of the art in the compensation of short-term memory effects and static nonlinearities through analog and digital predistortion.

2.1 Gallium Nitride High-Electron-Mobility Transistors

GaN is a binary III/V semiconductor crystal that is most commonly used in optoelectronics thanks to the breakthrough invention of the blue light-emitting diode by Isamu Akasaki, Hiroshi Amano and Shuji Nakamura, who were awarded the Nobel Prize in Physics in 2014. GaN is also used in microwave and power electronics as the primary component in GaN HEMTs, which are an emerging technology of field-effect transistors based on lateral GaN heterostructures. From their first experimental demonstration in 1993 [19], GaN HEMTs have evolved to feature a unique combination of important characteristics that make them ideal for high-power, high-frequency and high-reliability applications such as cellular mobile communications, long-range space communications, weather monitoring, automotive radar, and power conversion [20]–[23]. A typical GaN HEMT heterostructure is shown in Figure 2.1 and an example of a commercially available 15 W 28 V GaN HEMT is illustrated in Figure 2.2.

GaN has a direct band gap of 3.4 eV, which is more than double that of gallium arsenide (1.42 eV) and more than triple that of silicon (1.12 eV), two of the main competing semiconductors. For this reason, GaN HEMTs can operate at higher temperatures and support higher breakdown voltages, since, ultimately, the breakdown field is the field required for band-to-band impact ionization [24], [25]. Higher breakdown voltages allow for larger

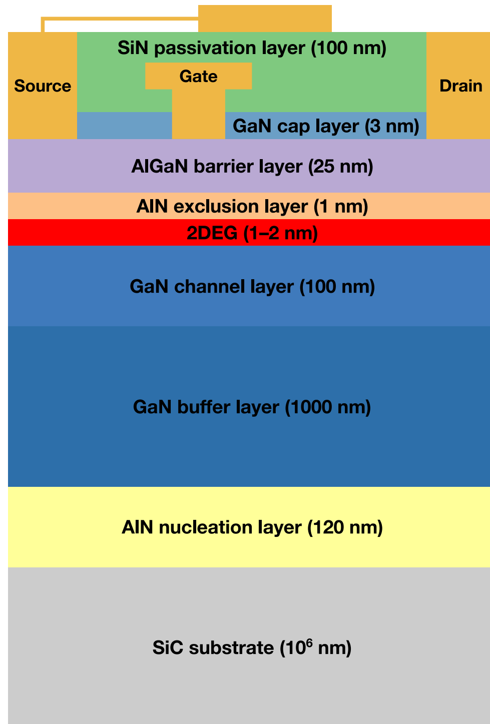

Figure 2.1 Example of a typical GaN HEMT heterostructure (not to scale).

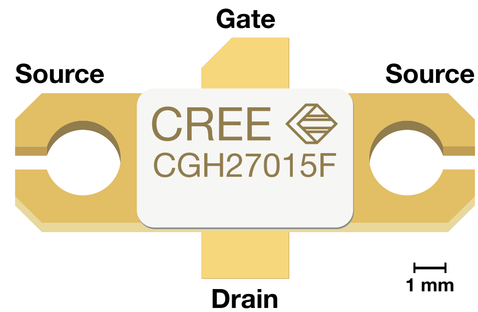

Figure 2.2 Example of a commercially available 15 W 28 V GaN HEMT.

drain voltages to be used, leading to higher output impedances and lower-loss matching networks [8]. Moreover, the high carrier concentration and carrier mobility of the channel in GaN HEMTs lead to very high current densities and a low channel resistance [8], [9], [24]. This allows for a smaller-size die to achieve a given current capability, and therefore results in lower input and output capacitances per watt of output power [8], [9]. In summary, GaN HEMTs provide high-frequency operation with higher power density and higher power efficiency than competing semiconductor technologies [26]. Notable technological achievements in GaN HEMT technology include a power density of 40 W/mm [27] and a current-gain/power-gain cuttof frequency ($f_T/f_{\max}$) exceeding 450/440 GHz [28], [29].

2.1.1 Heterostructure

Substrate: GaN HEMTs are layered stacks of ultra-thin semiconductor material that are typically grown at over 1000 °C by metalorganic chemical vapor deposition (MOCVD) [30] or molecular-beam epitaxy (MBE) [31] on a crystalline substrate such as sapphire (Al_2O_3), silicon, silicon carbide (SiC), or diamond [9]. Due to their very high thermal conductivity, SiC substrates are the most common type used in high-performance RF applications, as they allow the heat generated as a result of the high power densities of GaN HEMTs to be efficiently dissipated for realistic drain efficiencies [8].

Nucleation Layer: One of the historical challenges of growing GaN by MOCVD or MBE was the formation of large densities of dislocations and other surface defects due the large lattice mismatch and the large difference of thermal expansion coefficients between GaN and the substrate it was grown on [32]. To address this issue, a thin layer of aluminum nitride (AlN) is typically grown as a strain-relief buffer between the substrate and the subsequent GaN layers [33]. This layer promotes the nucleation of GaN, resulting in high-quality monocrystalline GaN films, and provides some degree of electrical isolation due to the wider band gap and resistive transport properties of AlN [34], [35].

Buffer Layer: High-quality semi-insulating GaN buffer layers are essential for achieving good device performance and sharp subthreshold current pinch-off. However, unintentionally doped GaN generally exhibits some degree of residual conductivity as a result of silicon or oxygen contamination through thermal etching or diffusion from the substrate [36], leading to significant leakage current and degraded power and efficiency performance [34], [36]. In order to compensate the excess charge at the GaN/substrate (or GaN/AlN) interface, the buffer layer is typically doped with carbon [37] or iron [36], [38], resulting in a highly resistive buffer at the cost of large densities of charge-trapping centers (buffer traps).

Moreover, the aggressive scaling of GaN HEMTs to achieve higher frequencies of operation leads to short-channel effects as a result of poor channel confinement [39]. These effects include, e.g., a high output conductance and the strong dependence of the pinch-off voltage on the drain voltage. To address this issue, the buffer can be intentionally doped to increase its resistivity, or, a thin film of aluminum gallium nitride (AlGaN) [40] or indium gallium nitride [41], [42] can be grown under the unintentionally doped GaN channel layer. As a result of the polarization charge at this secondary heterojunction, a potential barrier and an electric field are formed, confining the charge carriers in the channel and thus leading to a significant reduction of the output conductance and improvement of the pinch-off characteristics of the HEMT [40].

Channel Layer: To reduce the effect of buffer traps on the channel through which the drain–source current flows, an unintentionally doped GaN film is grown on top of the semi-insulating GaN buffer. It is found that thicker GaN channel layers lead to enhanced suppression of the depletion effect caused by buffer traps (not only because it reduces the capture probability, but also because it reduces the effect of captured charges) [43]. However, thicker channel layers contribute to increased short-channel effects [44] and lead to larger threshold voltages, which induce larger vertical electric fields across the gate and therefore result in much larger gate leakage currents [43]. The optimization of the channel layer thickness is therefore a balance between channel confinement and dispersion [44].

2DEG: The fundamental feature of GaN HEMTs is the two-dimensional electron gas (2DEG) that constitutes the channel between the drain and source terminals. The 2DEG is an extremely large concentration of highly mobile electrons located inside the unintentionally doped GaN channel layer, close to its interface with the barrier layer (or the exclusion layer, if there is one) [45], [46]—see Figure 2.3. In contrast to almost all known material systems, the 2DEG in an AlGaN/GaN structure is formed even in the absence of any doping in the barrier layer [47]. Thus, because of this native high-electron-mobility 2DEG channel, GaN HEMTs are inherently depletion-mode (normally-on) devices [9]; however, enhancement-mode (normally-off) GaN HEMTs are also available for power-switching applications [48]–[50].

Assuming an AlGaN barrier layer, the 2DEG is understood to be formed as a result of the spontaneous polarization of the GaN and AlGaN layers (due to intrinsically asymmetric atomic bondings in their wurtzite crystal structure) and the piezoelectric polarization of the AlGaN layer (due to the mechanical tensile strain caused by the lattice mismatch between AlGaN and GaN) [45], [51]. As a direct result of the net polarization, a very large positive sheet charge accumulates at the bottom of the AlGaN barrier layer and an equally large negative sheet charge accumulates at the top [31]. The polarization-induced positive charge is compensated by electrons that form the 2DEG at the AlGaN/GaN interface, and the negative polarization-induced charge is compensated by some positive surface charge [31]. While it might seem logical that the negative 2DEG charge accumulated inside the GaN channel layer at the AlGaN/GaN interface should come from either the GaN channel layer or the GaN buffer, this is not the case [52]. In fact, if these electrons had migrated from the channel or buffer layers, then positive charge would be left behind and the 2DEG would not be confined—which it demonstrably is [52]. Thus, the common consensus is that the origin

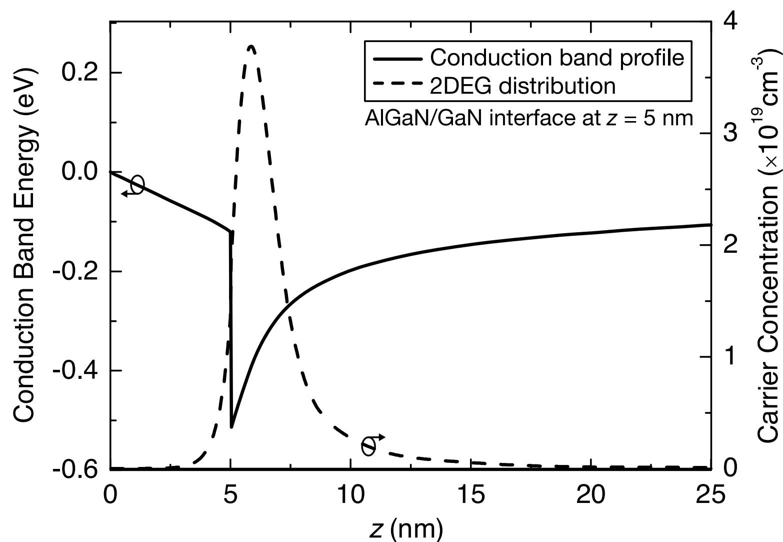

Figure 2.3 Conduction band profile (solid line) and 2DEG distribution (dashed line) in AlGaN/GaN heterostructures [46]. z denotes the distance from the surface to the inside of the heterostructure.

of the electrons in the 2DEG of a GaN HEMT is a large density of donor-like (neutral when occupied and positive when empty) electronic states at the surface of the AlGaN barrier layer [31], [47], [52]. Whether these donor-like surface states are intrinsic (e.g., due to dangling bonds) and/or impurity-related is still unknown [52].

Exclusion Layer: The room-temperature mobility of the electrons in the 2DEG of AlGaN/GaN structures is limited by alloy disorder scattering and interface roughness scattering [31], [53]. Since alloy disorder scattering only occurs in ternary or higher alloys (e.g., AlGaN) due to the random position of their constituent atoms in their crystal lattice [54], [55], an ultra-thin interfacial layer of AlN is typically grown between the GaN channel layer and the AlGaN barrier layer [54], [56]. The insertion of this thin AlN layer leads to the formation of a polarization-induced dipole in the AlN layer, which produces a larger conduction band offset between the AlGaN and GaN at both sides of the AlN layer [57]. The energy barrier introduced by the AlN exclusion layer therefore prevents the penetration of the 2DEG into the AlGaN barrier layer [58], reducing alloy disorder scattering and increasing the electron mobility.

Barrier Layer: The AlGaN barrier layer is the top part of the AlGaN/GaN heterojunction that results in a native 2DEG. It is found that an increase in the thickness of the AlGaN layer results in an increase in the 2DEG density and the surface barrier height (energy level), up to the point where the tensile strain in the AlGaN starts to relax [47], [59]. In light of the donor-like surface states hypothesis for the origin of the 2DEG, this can be explained by a lowering of the surface Fermi level (with respect to the conduction band) with an increase in the AlGaN thickness, resulting in an increased density of ionized donor-like surface states whose electrons collect at the 2DEG [47], [52]. In addition to the thickness of the barrier layer, the Al mole fraction x in the $\mathrm{Al}_x\mathrm{Ga}_{1-x}\mathrm{N}$ has been demonstrated to have a significant impact on both the surface barrier height and the 2DEG density [60].

Cap Layer: In order to suppress the current collapse induced by surface charge trapping, a GaN cap layer is sometimes grown over the AlGaN barrier layer. Even though the introduction of this layer does demonstrably achieve its desired outcome (to the point that no passivation layer may be necessary), it seems that the exact mechanism by which it works is still not fully understood. Some authors use thick GaN caps on the basis that they screen surface states and thus reduce their adverse effect on the channel (because they are literally farther away) [24], [61]; other authors use thin GaN caps on the basis that they compensate the negative polarization charge at the upper GaN/AlGaN interface [62], [63]. Some authors use n-doped GaN caps [62], [64]; other authors use p-doped GaN caps [65]; and other authors use entirely undoped GaN caps [61], [63]—all with reportedly successful results. In any case, the addition of a GaN cap layer generally results in a large increase in

the gate leakage current [63], [64]. Moreover, the effectiveness of the GaN cap to suppress surface trapping-related current collapse is diminished after high-electric-field stress. For these reasons, the use of a GaN cap should be complemented with other techniques such as surface passivation and the use of field plates [63].

Passivation Layer: In order to prevent the onset of surface charge-trapping effects, a thin layer of dielectric material such as silicon nitride (SiN) [66]–[69], magnesium calcium oxide (MgCaO) [70] or AlN [71] is typically deposited at the surface of the HEMT. The introduction of this passivation layer effectively reduces dc–RF dispersion and increases the output power. However, this layer also leads to a significant increase in the gate–drain capacitance (as well as the gate–source capacitance), limiting the high-frequency operation of the HEMT [42], [66].

Ohmic Contacts and Field Plates: The completion of the HEMT is performed by etching the superficial layers up to the AlGaN barrier layer and depositing the metalization for the gate, drain and source terminals. These are typically made using a titanium/aluminum/nickel/gold stack annealed at high temperature, resulting in a contact resistivity of 0.2–0.4 Ω mm [72].

At this point, gate-connected and source-connected field plates are also deposited to modify the electric field profile between the gate and the drain and to decrease its peak value [73], hence reducing trapping effects [68], [74] and increasing the breakdown voltage [24], [75]. Early field plates were either constructed as part of the gate [74]–[77] or connected to the gate externally [27], [68], [73]. However, in this configuration the capacitance between the field plate and the drain metalization is added to the gate–drain capacitance (and is multiplied due to the Miller effect), limiting the current-gain and power-gain cutoff frequencies (f_T and f_{max}) of the HEMT [24], [73], [75]. For this reason, gate-connected field plates were later complemented by source-connected field plates [11], [27], [78], [79]. Since the gate–source voltage swing in a typical GaN HEMT is only 4–8 V—much less than the dynamic output swing of up to 650 V [80] in modern devices—, connecting the field plate to the source instead of the gate also satisfies the electrostatics for it to be functional [24]. Thus, in this configuration the field plate delivers its benefits only at the cost of an increased drain–source capacitance, which can be absorbed in the output matching network [24].

2.2 Origin of Charge-Trapping Phenomena

There is not, as of yet, an established theory on the origin of the charge-trapping phenomena that result in the slow dynamic nonlinearity observed in GaN HEMTs. It is for this reason, actually, that in this thesis we use the more general term "charge trapping", and not "electron

trapping", even though the latter is more common. With that said, it is currently understood that there are two main regions where charge-trapping phenomena are most prevalent: the surface and the buffer of the HEMT. Other sources of charge-trapping phenomena may include the contamination of the AlGaN barrier layer with acceptor dopants introduced in the buffer [38], and the heterojunctions close to the 2DEG (namely the interface between the barrier and exclusion layers [81]), which may contain border traps whose ionization is not thermally assisted, but is instead realized through tunneling processes [11].

2.2.1 Surface Trapping

As reviewed in Section 2.1.1, the current understanding on the origin of the 2DEG is a large density of donor states at the surface of the HEMT that are ionized as a result of the polarization dipole in the AlGaN/GaN heterojunction [31], [52]. When the HEMT is biased at a large negative gate voltage, part of the electrons that are injected (leaked) from the gate metal into the semiconductor material flow laterally toward the drain (and, to a lesser extent, toward the source) due to the large lateral electric field resulting from the gate–drain (and gate–source) voltage [63], [74]. As a result, some of these electrons are captured by the ionized surface states [63], [69], [82] (which become neutral) at a rate that depends on the trap energy, the applied electric fields, and the surface mobility of the injected electrons [82]. Finally, the resulting accumulation of trapped electrons in the gate–drain (and gate–source) access region extends the depletion region, reducing the density of the 2DEG and degrading the current capabilities of the HEMT.

2.2.2 Buffer Trapping

Deep-level acceptor traps are essential to suppress buffer leakage, short-channel effects, and improve channel confinement. However, whether these arise due to intrinsic growth defects or are intentionally introduced by extrinsic dopants such as carbon or iron, their existence leaves the HEMT highly vulnerable to charge-trapping effects such as current collapse [83]. More specifically, when the HEMT is biased at a large drain voltage, electrons are injected from the 2DEG into the deep-level acceptor traps in the buffer, leading to the depletion of the 2DEG and the degradation of the current capabilities of the HEMT [83]. The exact electron injection mechanism is currently not established, and ranges from hot-electron injection (the large electric field induced by the drain voltage imparts a large kinetic energy onto the 2DEG electrons, which thus acquire the ability to escape the channel and become trapped in buffer traps) [83]–[85] to tunneling [86].

2.2.3 Gate Lag and Drain Lag

Surface trapping is commonly associated with gate lag, which is a delayed response of the drain current to a gate excitation, as illustrated in Figure 2.4. During a negative gate

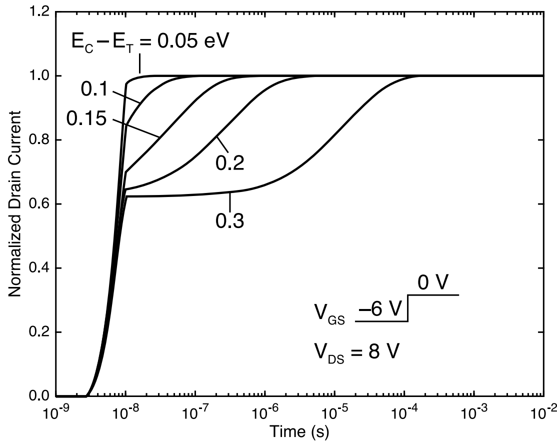

Figure 2.4 Gate lag observed in the response of the drain current to a step variation in the gate voltage [63].

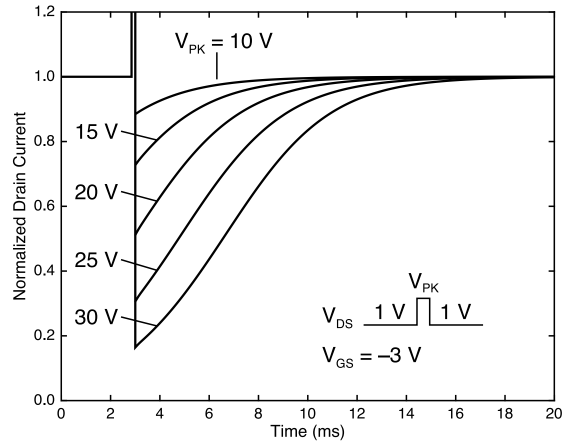

Figure 2.5 Drain lag observed in the response of the drain current to a step variation in the drain voltage.

bias, ionized donor-like surface traps capture electrons. Because of this, the response of the drain current to a step increase in the gate voltage does not immediately achieve its steady-state value. Instead, the drain current achieves a low value and slowly increases toward its steady-state maximum as the trapped electrons are released through thermal emission. The profile of the drain current is dependent on the density of traps, trap energy level, gate and drain voltages, and device construction.

Buffer trapping is commonly associated with drain lag, which is a delayed response of the drain current to a drain excitation, as illustrated in Figure 2.5. During a large drain bias, acceptor traps in the buffer capture electrons from the 2DEG and form a concentrated negative charge beneath the gate [83]. Because of this trapped charge, the response of the drain current to a step decrease in the drain voltage does not immediately achieve its steady-state value. Instead, the drain current achieves a low value and slowly increases toward its steady-state maximum as the trapped electrons are released through thermal emission. Provided that there is a sufficient density of deep-level acceptor traps in the buffer, the profile of the drain current is dependent on trap energy level, peak drain voltage, and device geometry (namely the gate–drain capacitance) [83].

2.3 Characterization of Charge-Trapping Phenomena

In this section we describe the main types of experimental methods for the characterization of charge-trapping phenomena in GaN HEMTs. Generally, these methods are followed by a parameter-extraction or curve-fitting procedure executed over the obtained measurement data for estimating the time constants associated with charge-trapping phenomena. However, since these post-processing procedures are necessarily tied to a given model, we will not review them due to their limited usefulness.

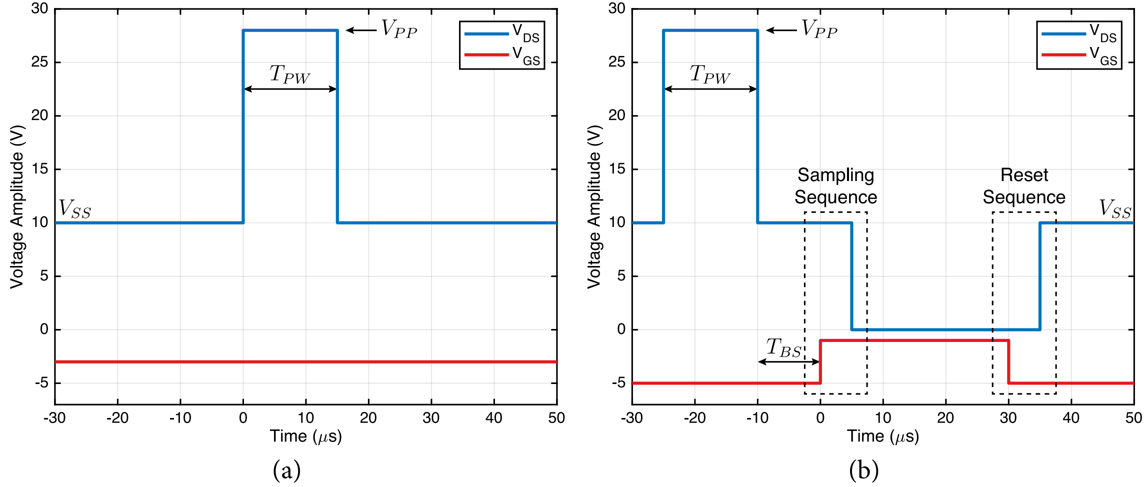

Figure 2.6 (a) Pulsed I-DLTS. (b) Isothermal double-pulsed I-DLTS.

2.3.1 Drain-Current Deep-Level Transient Spectroscopy

Drain-current deep-level transient spectroscopy (I-DLTS) consists in the measurement of the transient evolution of the dc drain current of a HEMT following an initial charge-trapping state that is forced on the HEMT. The forcing of the initial charge-trapping state can be done either in a pulsed configuration [87]–[89] or a double-pulsed configuration [90], [91].

In the case of pulsed I-DLTS, the drain-lag phenomenon can be characterized by setting the gate of the HEMT at a constant voltage such that the quiescent drain current is low (to minimize device self-heating), and then briefly pulsing the drain from the sampling voltage V_{SS} to the peak voltage V_{PP}, as illustrated in Figure 2.6(a). As a result of the drain voltage pulse, there is a sudden decrease in the quiescent drain current that is greater for higher peak drain voltages V_{PP} or for longer pulse durations T_{PW}. The recovery of the drain current is then measured for as long as necessary. For the characterization of the gate-lag phenomenon, it is the gate that is pulsed while the drain is kept at a constant low voltage.

The major drawback of pulsed I-DLTS is that different peak voltages or peak durations lead to different powers dissipated in the HEMT, and thus different levels of device self-heating. For this reason, the isothermal double-pulsed I-DLTS method [91], illustrated in Figure 2.6(b), is preferred. In this method, the gate voltage is set at an initial voltage such that the channel of the HEMT is completely pinched off. Then, the drain is prepulsed to a peak voltage V_{PP} for a prepulse duration of T_{PW}. This sets the charge-trapping state without heating the HEMT, as no current flows through the drain and no power is dissipated in the HEMT. After a time-before-sampling T_{BS}, the gate voltage is pulsed for the minimum duration necessary for measuring one sample of the drain current, after which a reset sequence is performed to prepare for the next measurement. This method allows for

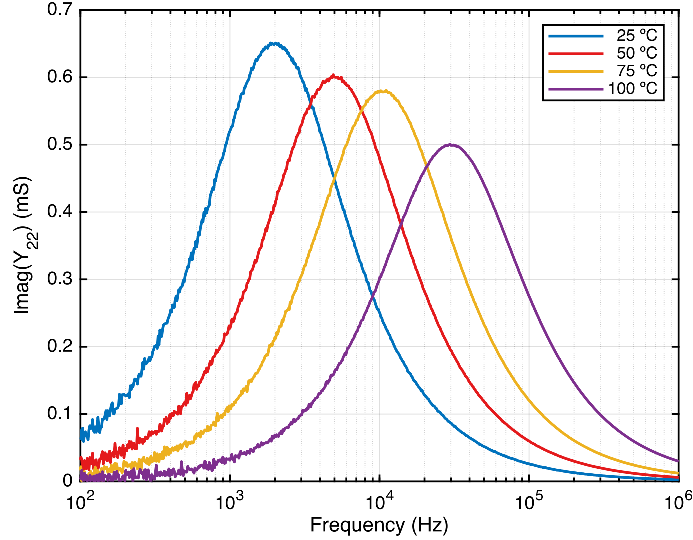

Figure 2.7 Typical low-frequency admittance measurement results.

the accurate characterization of the charge-capture process by setting $T_{BS} = 0$, or the charge-emission process by setting $T_{BS} > 0$.

2.3.2 Low-Frequency Admittance Measurements

Another common charge-trapping characterization method consists in measuring the low-frequency (less than 1 MHz) drain susceptance of a HEMT by measuring its output admittance and isolating the imaginary part [92], [93]. This typically results in a pronounced peak, as in Figure 2.7, which, for a single-time-constant model as in (2.1), indicates the time constant τ defined in (2.2). This time constant is usually attributed to the charge-emission process only [94], [95]; however, recent publications have clarified that it may actually be related to a balance between capture and emission [96]. By repeating this measurement at various temperatures, the apparent activation energy and apparent capture cross-section of the traps can be determined easily based on the Arrhenius equation by calculating the slope and intercept of the $\log(\tau T^2)$-versus-$1/(kT)$ plot, where T is the absolute measurement temperature and k is the Boltzmann constant [93].

$$Y_{22} = \left(g_d + \frac{g_0(\omega\tau)^2}{1 + (\omega\tau)^2} \right) + j\,\frac{g_0(\omega\tau)}{1 + (\omega\tau)^2} \tag{2.1}$$

$$\tau = \frac{C_0}{g_0} = \frac{1}{2\pi f_{\text{peak}}} \tag{2.2}$$

2.3.3 Pulse-Modulated RF Measurements

In order to characterize GaN HEMTs closer to their target operating conditions, pulse-modulated RF active load-pull measurements from hot bias conditions were proposed in

[97]. In this method, the multiharmonic terminations presented by the source and load matching networks are tuned to maximize the efficiency of the HEMT while maintaining its gain over the dynamic range of the output power [98]. Then, the time-domain large-signal pulse response of the HEMT is recorded as a function of bias voltages, pulse amplitude, and pulse duration.

Since all previously described characterization methods are performed on the discrete HEMT and require very specialized equipment (e.g., fast high-power pulsers), alternative methods targeting fully assembled GaN HEMT-based RF PAs have also been proposed. These only require equipment commonly available in most RF laboratories, such as a vector signal generator (VSG) and a vector signal analyzer (VSA), and can be performed much closer to the target operating conditions of the PA under test than the pulsed-dc and low-frequency measurements-based procedures. The most straightforward RF characterization method simply consists in measuring the transient response of a GaN HEMT-based PA to a large-signal pulsed-RF excitation with a given peak available power and pulse width. Typical results are shown in Figure 2.8(a).

Despite being simpler to execute than pulsed-dc methods, these characterization methods provide data that is more difficult to relate to the physical phenomena of charge trapping. This is because the RF nature of the test excitations leads to an inevitable combination of gate lag, drain lag and thermal phenomena, as both the gate and the drain of the HEMT are always—and simultaneously—under large excitations (at the time scales of the envelopes). Thus, these methods are preferable for the behavioral modeling of the effects of charge trapping on the nonlinear behavior of GaN HEMT-based PAs, and not necessarily the physical modeling of charge-trapping phenomena in GaN HEMTs.

2.3.4 Two-Tone-Modulated RF Measurements

A perhaps more interesting characterization method consists in measuring the steady-state response of a GaN HEMT-based PA to a series of large-signal two-tone excitations with varying frequency separation [99]. After recording the two-tone response of the PA, the small-signal gain is sampled at specific instants of the measured complex-envelope time series. These instants are t_{ss}, defined in (2.3), where Δf is the two-tone frequency separation, V_{pk} is the peak amplitude of the two-tone input excitation, and V_{ss} is a reference small-signal amplitude level. This method provides a more comprehensive characterization of the nonlinear long-term memory of the PA because the input excitation varies continuously across multiple amplitude levels at different rates, instead of switching nearly instantly between two discrete amplitude levels as in the case of the pulsed characterization methods. Figure 2.8(b) illustrates the typical results obtained from this characterization method.

$$t_{ss} = \frac{1}{\Delta f}\left[1 - \frac{1}{\pi}\arcsin\left(\frac{V_{ss}}{V_{pk}}\right)\right] \tag{2.3}$$

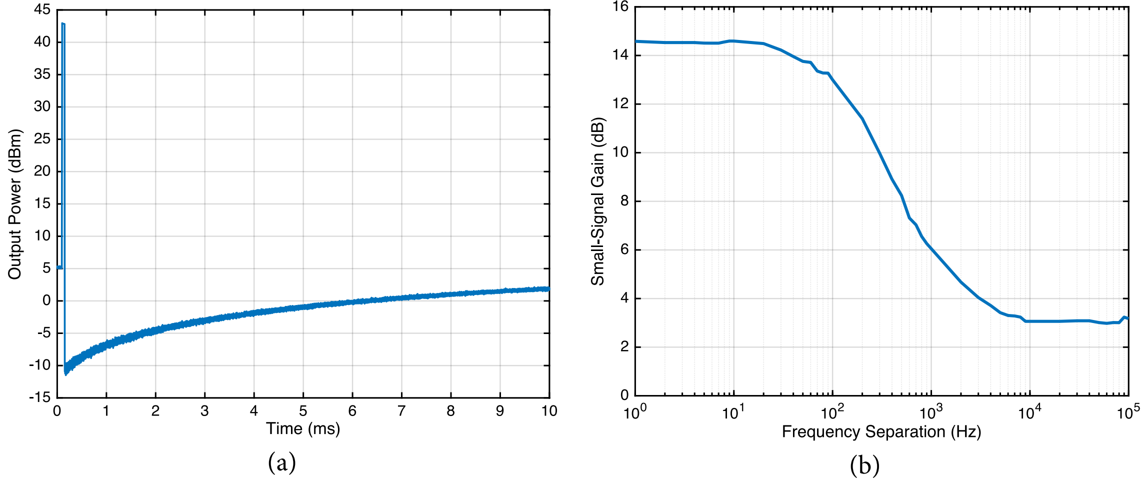

Figure 2.8 Typical (a) pulse-modulated and (b) two-tone-modulated RF measurements-based charge-trapping characterization results.

2.4 Modeling of Charge-Trapping Phenomena

2.4.1 Single-Time-Constant Jardel Model

The Jardel model [89] establishes a relationship between the threshold voltage of a HEMT and its intrinsic drain–source voltage. Although this relationship cannot be directly applied to the RF envelope measurements performed throughout this thesis, its dynamics (or mathematical formulation) certainly can, as shown in [13], [99]. Thus, throughout this thesis, we will use "the Jardel model" as a shorthand for the dynamics expressed by the mathematical formulation proposed in [89] when applied to RF envelope measurements, rather than the literal physical phenomena described by this formulation.

The Jardel model, whose equivalent circuit is illustrated in Figure 2.9, is characterized by an asymmetric charge (capture) and discharge (emission) process with different—but fixed—charge and discharge time constants, $\tau_c \approx R_c C$ and $\tau_e = R_e C$ respectively. This model, with a parameter set $\Psi_M = \{\tau_c,\, \tau_e,\, \kappa\}$, is defined as follows.

Let $v_x(t)$ denote the amplitude of the envelope of the PA's input excitation. Moreover, let $\Delta V_{GS}(t) = \kappa\, v_y(t)$ denote the threshold voltage variation predicted by the model, where κ is a scaling factor and $v_y(t)$ is the voltage at the capacitor in Figure 2.9. Finally, let $f_D(\cdot)$ denote the transfer function, defined in (2.4), of the ideal diode in Figure 2.9.

$$f_D(x) = \begin{cases} x, & x \geq 0 \\ 0, & x < 0 \end{cases} \tag{2.4}$$

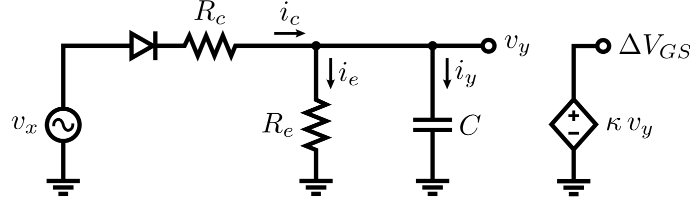

Figure 2.9 Equivalent circuit of the Jardel model.

Then, the capture current $i_c(t)$ is defined as in (2.5), the emission current $i_e(t)$ is defined as in (2.6), and the net capacitor current $i_y(t)$ is defined as in (2.7).

$$i_c(t) = f_D\left(\frac{v_x(t) - v_y(t)}{R_c}\right) \tag{2.5}$$

$$i_e(t) = \frac{v_y(t)}{R_e} \tag{2.6}$$

$$i_y(t) = i_c(t) - i_e(t) \tag{2.7}$$

The voltage at the capacitor $v_y(t)$ is defined as in (2.8) and, using Euler's method, it can be discretized as in (2.9), where n denotes the sample index and f_s denotes the sampling frequency.

$$v_y(t) = \frac{1}{C}\int_{t_0}^{t} i_y(\tau)\, d\tau + v_y(t_0) \tag{2.8}$$

$$v_y(n+1) = v_y(n) + \frac{1}{f_s\, C}\, i_y(n) \tag{2.9}$$

2.4.2 Multiple-Time-Constant Jardel Model

For large gate or drain voltage swings, the transient evolution of the drain current of a GaN HEMT under charge-trapping effects is revealed to have a profile that is not exactly exponential [91], [100]—instead, it is initially much faster than the best-fit exponential and becomes much slower over time. For this reason, many authors choose to fit the transient drain current using a weighted sum of multiple exponentials with different time constants [11], [88], [89], [101]–[103]. This can be trivially integrated with the Jardel model to realize a new model that features a multi-exponential capture and/or emission process that is described by multiple concurrent time constants. In this thesis, we call this the "Multi-Jardel" model, as it is simply the weighted sum of multiple independent nonlinear resistor-capacitor networks described by the Jardel model.

The Multi-Jardel model with N capture time constants and N emission time constants, with a parameter set $\Psi_M = \{\tau_{c,1}, \cdots, \tau_{c,N},\ \tau_{e,1}, \cdots, \tau_{e,N},\ \kappa_1, \cdots, \kappa_N\}$, is defined as follows. Let $\kappa\, J(v_x(t), \tau_c, \tau_e)$ denote the response of the Jardel model (with a capture time constant τ_c, an emission time constant τ_e, and a scaling factor κ) to an input excitation with an envelope

amplitude $v_x(t)$. Then, the threshold voltage variation $\Delta V_{GS}(t)$ predicted by the Multi-Jardel model is defined as in (2.10).

$$\Delta V_{GS}(t) = \sum_{n=1}^{N} \kappa_n \, J(v_x(t),\, \tau_{c,n},\, \tau_{e,n}) \tag{2.10}$$

2.4.3 Shockley–Read–Hall Statistics-Based Model

While the Jardel model (and its multiple-time-constant variant) does support asymmetric capture and emission time constants, these time constants are fixed. However, in [104] (and later [91]) the authors demonstrated, based on Shockley–Read–Hall (SRH) statistics, that the capture process can be more accurately modeled with a time constant that varies with the instantaneous trapping state, becoming exponentially larger as the accumulated charge increases. Similar to the model proposed by Jardel *et al.* in [89], this model establishes a relationship between the threshold voltage of a HEMT and its intrinsic drain–source voltage. Again, for simplicity, we will use "the SRH model" as a shorthand for the mathematical formulation of the dynamics described by this model, since our target applications in this thesis are the modeling and compensation of RF PAs and not the intrinsic characteristics of discrete HEMTs.

The SRH model, whose equivalent circuit is illustrated in Figure 2.10, is also characterized by an asymmetric charge (capture) and discharge (emission) process. However, whereas the capture rate in the Jardel model is defined by a fixed time constant, in the SRH model it is defined as a nonlinear function of the trapping state—or, for simplicity, as a time constant that varies with the trapping state. As in the Jardel model, the emission is modeled by a fixed time constant. This model, with a parameter set $\Psi_M = \{V_0,\, \omega_0,\, k_0,\, k_1,\, k_2\}$, is defined as follows.

Let $v_x(t)$ denote the amplitude of the envelope of the PA's input excitation. Moreover, let $\Delta V_{GS}(t) = v_y(t)$ denote the threshold voltage variation predicted by the model, where $v_y(t)$ is the voltage at the capacitor in Figure 2.10. Then, the capture current $i_c(t)$ is defined as in (2.11), where $v_I(t) = k_0 + k_1\, v_x(t) - k_2\, v_y(t)$ and V_T is the thermal voltage; the emission current $i_e(t)$ is defined as in (2.12); and the net capacitor current $i_y(t)$ is defined as in (2.13).

$$i_c(t) = \omega_0\,(V_0 - v_y(t)) \exp\left(\frac{v_I(t)}{V_T}\right) \tag{2.11}$$

$$i_e(t) = \omega_0\, v_y(t) \tag{2.12}$$

$$i_y(t) = i_c(t) - i_e(t) \tag{2.13}$$

The voltage at the capacitor $v_y(t)$ is defined as in (2.14) and, using Euler's method, it can be discretized as in (2.15), where n denotes the sample index, f_s denotes the sam-

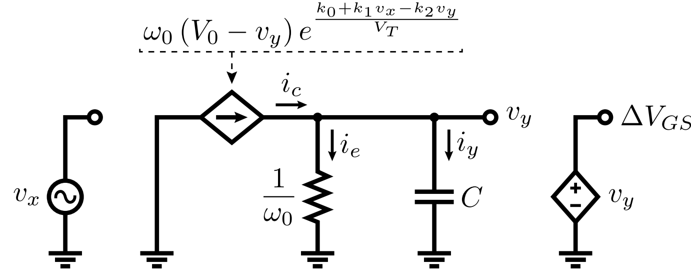

Figure 2.10 Equivalent circuit of the SRH model.

pling frequency, and $C = 1$ F is merely an auxiliary variable for the equivalent-circuit representation in Figure 2.10.

$$v_y(t) = \frac{1}{C}\int_{t_0}^{t} i_y(\tau)\,d\tau + v_y(t_0) \tag{2.14}$$

$$v_y(n+1) = v_y(n) + \frac{1}{f_s\,C}\,i_y(n) \tag{2.15}$$

2.5 Prevention of Charge-Trapping Phenomena

Charge trapping is universally recognized as one of the main challenges and detrimental aspects of current GaN HEMT technology [8], [24], [105]. For this reason, significant research activity has been directed toward preventing the onset of charge-trapping phenomena in GaN HEMTs, either through the development of improved material systems or the optimization of manufacturing processes. In spite of these efforts, current state-of-the-art GaN HEMT technology still suffers from significant long-term memory effects that degrade the microwave and dc power performance of these transistors. In fact, the commercially available GaN HEMTs used throughout the work reported in this thesis are known to employ two of the most prevalent charge-trapping prevention mechanisms [8]—surface passivation and field plating, detailed in this section—, and they still present extremely pronounced nonlinear long-term memory that is demonstrably caused by charge-trapping phenomena.

2.5.1 Passivation

The most common technique for the suppression of current collapse induced by surface charge trapping is the passivation of the topmost layer of the HEMT (either the AlGaN barrier layer or, if present, the GaN cap layer) with a dielectric such as SiN [66], [67], MgCaO [70], or AlN [71]. It is as yet unclear precisely how these surface treatments influence surface states, with possibilities including strain-induced polarization charges due to the passivation layer [70], positive charges present in the passivation layer [47], or the alteration of the nature of the surface traps [66] through either the reduction of their density

[67], [71] or their distance from the conduction band [74]. In spite of the demonstrated effectiveness of the passivation layer to suppress undue surface charge trapping, this layer results in a significant increase in the gate–drain capacitance (as well as the gate–source capacitance), limiting the high-frequency operation of the HEMT [42], [66]. Moreover, the effectiveness of the passivation layer to suppress surface trapping-related current collapse is diminished after high-electric-field stress [67]; however, dielectrics such as AlN with a high dielectric constant offer greater resilience to stress and increased gate–drain breakdown voltage than the more common SiN [71], [75].

2.5.2 Field Plates

Field plates are extensions of the gate or source metalization over the gate–drain access region. By modifying the electric field profile between the gate and the drain and decreasing its peak value [73], field plates not only increase the breakdown voltage of the HEMT but also reduce surface-related trapping effects. The reduction of charge-trapping effects is understood to be due to the reduction of the lateral electric field at the gate edge, which results in a lower injection of electrons into ionized donor-like surface states [68], [79].

2.6 Analog Predistortion

Following Arthur C. Clarke's 1945 article on "Extra-Terrestrial Relays" [106] and John R. Pierce's 1955 article on "Orbital Radio Relays" [107], efforts toward global communications escalated along with a demand for higher transmission bandwidths at lower costs, leading to an increased interest in higher-order modulation techniques such as quadrature phase-shift keying and quadrature amplitude modulation, as well as multiple-access schemes such as time-division multiple access. In order to achieve acceptable bit error rates and to meet the increasingly stringent spectral purity requirements of these data rate-increasing schemes, much attention was given between the late 1970s and the early 1980s to problems such as the linearization of high-power microwave amplifiers used in satellite earth stations [108] and traveling-wave tube amplifiers used in satellite transponders [109]. Due to the limited capabilities of contemporary digital signal-processing circuits, most linearization techniques consisted in analog electronic circuits that predistorted either the RF input of the PA [109] or, less frequently, its baseband components [108]. Regardless of the idiosyncrasy of each implementation, the great majority of the linearizers adhered to two main classes of predistortion circuits: series-diode predistorters, and cubic predistorters [110].

2.6.1 Series-Diode Predistorters

Series-diode predistorters (Figure 2.11) consist of a single forward-biased series diode, which may be modeled as a nonlinear resistor with a parasitic capacitance. The principle

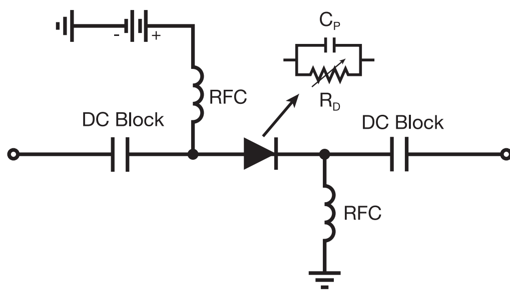

Figure 2.11 Series-diode predistorter.

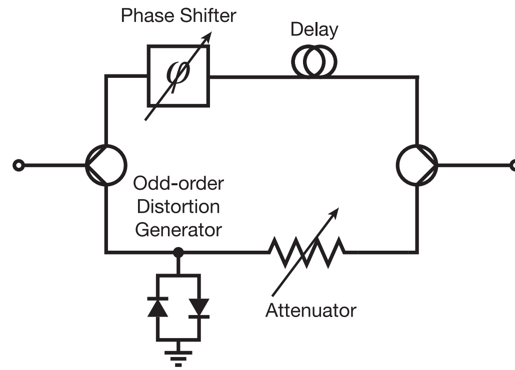

Figure 2.12 Cubic predistorter.

of operation is fairly straightforward: as per Shockley's diode equation, an increase in forward dc current (caused by an increasing incident RF signal power) results in a decrease in the equivalent series resistance of the diode. This, in turn, provided that the diode is properly biased and terminated, results in an expanding gain and a decreasing phase shift that counter the undesired amplitude-to-amplitude modulation (AM–AM) and amplitude-to-phase modulation (AM–PM) characteristics of the PA. Series-diode predistorters have been entirely superseded by other types of predistorters due to their very poor linearization performance: typical values of third-order intermodulation distortion (IMD) suppression do not exceed 3 dB [111].

2.6.2 Cubic Predistorters

In cubic predistorters (Figure 2.12), the input signal is coupled into a distortion generator—a pair of shunt antiparallel diodes—that produces exclusively odd-order harmonics of the input signal [111]. A variable phase shifter is used to guarantee a 180° phase difference between the input signal and the distortion signal, and a delay line is used to equalize the group delays of the two signal paths. Finally, a variable attenuator ensures the amplitude of the generated distortion matches that of the harmonic distortion produced by the pre-distorted PA. This amplitude matching, along with the 180° phase difference between the delayed signal and the generated distortion, results in an appreciable suppression of the spurious odd-order tones produced by the predistorted PA. Typical state-of-the-art cubic predistorters improve third-order IMD performance by approximately 10 dB [112], [113].

2.6.3 Generalized IMD Generators

With the advent of high-speed digital computing, analog predistortion plummeted into near oblivion and was swiftly replaced by more capable and more configurable DPD schemes. Still, some research was done, mainly in the early 2000s, and not only did old analog pre-distortion technology improve, some new interesting ideas also came to light. The first major advancement in analog predistortion was the refinement of the cubic predistorter,

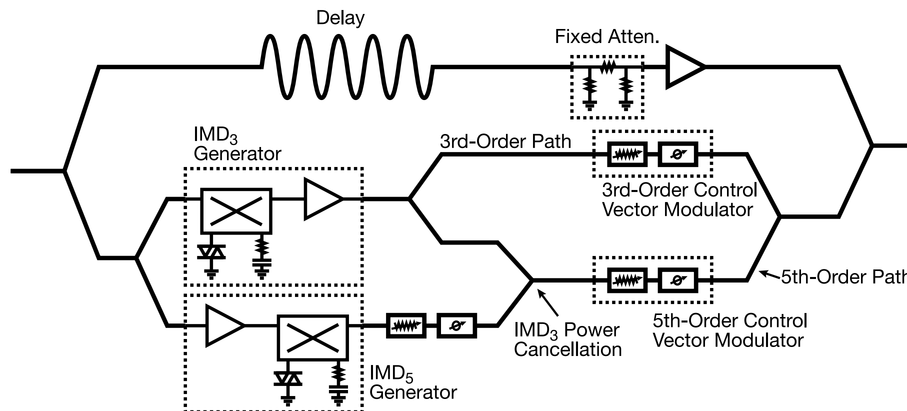

Figure 2.13 Fifth-order generalized IMD generator predistorter [115].

which led to the development of fully configurable independently controllable generalized IMD generators [114]–[117], that is, branched versions of the cubic predistorter (or similar structures) that generate third-order and fifth-order IMD tones that can be independently scaled in magnitude and shifted in phase—see Figure 2.13 for an example. Reported combined third-order and fifth-order IMD suppression performance has some variance: in [117], third-order IMD is improved by 20 dB and fifth-order IMD by 10 dB; in [118], both third-order and fifth-order IMD components are improved by 25 dB; finally, in [119], third-order IMD is improved by 43 dB and fifth-order IMD by 24 dB.

2.6.4 Polynomial Predistorters

The second major advancement in analog predistortion came from the realization that the transfer characteristics of an amplifier can be modeled using polynomial functions. These polynomials, in turn,—or, rather, their inverse—can be approximated using active circuits based on Howard Jones's analog four-quadrant multiplier [120], illustrated in Figure 2.14. A new class of monolithic microwave integrated circuits was therefore designed to implement high-order polynomials with freely configurable coefficients, and thus synthesize the inverse transfer characteristics of an amplifier [121], [122]. State-of-the-art polynomial predistorters are reported to have the following linearization performance results. In [123], the authors present an analog polynomial predistorter fabricated in a 0.35 μm silicon germanium bipolar complementary metal–oxide–semiconductor (CMOS) process that achieves a third-order IMD suppression of over 20 dB and an adjacent-channel leakage ratio (ACLR) improvement of 8 dB for a 5 MHz wideband code-division multiple access (WCDMA) signal. In [124], the author presents an analog temperature-compensated eleventh-order four-tap memory polynomial predistorter fabricated in a 0.18 μm CMOS process which improves the ACLR of a Doherty PA by up to 25 dB for a two-carrier 10 MHz WCDMA signal and by over 15 dB for a 20 MHz LTE signal. See Section 2.7.1 for more details on memory polynomials.

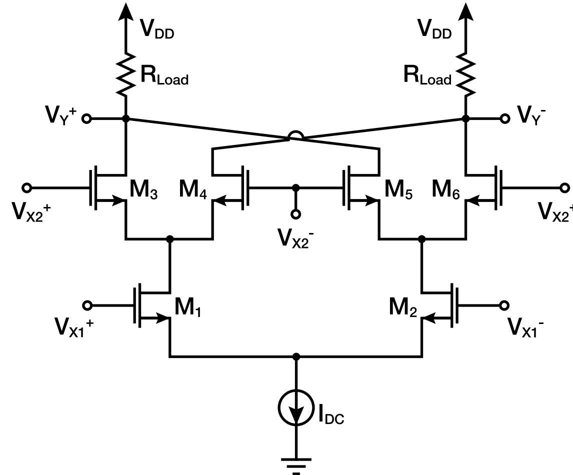

Figure 2.14 Four-quadrant analog multiplier.

2.6.5 Artificial Neural Networks

Recent technological advances have brought the possibility of reliably implementing artificial neural networks (ANNs) as analog circuits. Further advances, such as the commercial availability of memristors, are expected to lead to even more robust, dense, and higher-performing analog ANNs. Currently, there are still very few publications on the use of ANNs for the analog predistortion of RF PAs. Actually, most of them are by Gatet *et al.*, though they are lacking in terms of detailed experimental data. In [125], the authors describe the design of an analog feedforward ANN implemented in a 0.6 µm CMOS process. The ANN is composed of one input, one hidden layer of ten neurons, and one output. The synaptic weights and biases are set by external voltages, which are multiplied with the input signals using improved four-quadrant analog multipliers [126]; the sigmoid activation functions are implemented with simple differential pairs. In [127], the authors describe a predistortion scheme where two analog ANNs predistort the magnitude and phase of the baseband input signal of a PA. The weights of the ANNs are set by a field-programmable gate array. The PA is assumed to be static; however, memory is known to have an important impact on the linearizability of RF PAs, as detailed in Section 2.7.1. Finally, in [128], the authors linearize a memoryless Saleh model of an 80 W Ka-band traveling-wave tube amplifier using a procedure similar to that of [127].

2.7 Digital Predistortion

DPD has been the standard PA linearization technique since its inception. As such, the number of different DPD models reported in the literature is essentially uncountable. For this reason, in this section we only describe the three types of DPD models that were especially relevant for producing the work reported in this thesis.

2.7.1 Memory Polynomial

Originally proposed in [129], the memory polynomial (MP) is a pruned (narrowband) generalization of the Hammerstein model structure [130] where different finite-impulse-response (FIR) filters apply to different polynomial orders of the nonlinear expansion of an input signal. Due to the FIR structure of the filters in the MP model, practical realizations of this model for the linearization of RF PAs only support short-term memory [13], [131], [132], which is useful for the modeling of the effects of filter group delays, the frequency response of matching networks, nonlinear capacitances of the transistors, and the response of the bias networks of a PA [129]. The MP model is defined as in (2.16), where P is the polynomial order; M is the sample memory depth; $h_p(m)$ is the set of model parameters, with a total of $(P+1) \times (M+1)$ parameters; $x(n)$ is the input complex-envelope signal; and n is the sample index.

$$y_{\text{MP}}(n) = \sum_{p=0}^{P} \sum_{m=0}^{M} h_p(m)\, x(n-m)\, |x(n-m)|^p \tag{2.16}$$

2.7.2 Generalized Memory Polynomial

Originally proposed in [130], the generalized memory polynomial (GMP) combines the MP model with cross terms between the input signal and its lagging and/or leading exponentiated terms. This results in a formulation that offers significantly improved modeling capability, though at the cost of an increased number of parameters. Due to its flexibility, the GMP model is considered one of the default go-to models for accurate wideband linearization; however, just like the MP model, the GMP model only supports short-term memory. The GMP model is defined as in (2.17), where P is the polynomial order; M is the sample memory depth; K is the polynomial cross order; L is the cross-memory depth; $h_p(m,0)$ and $h_k(m,\pm l)$ form the set of model parameters, with a total of $(P+1) \times (M+1) + 2 \times K \times (M+1) \times L$ parameters; $x(n)$ is the input complex-envelope signal; and n is the sample index.

$$\begin{aligned} y_{\text{GMP}}(n) &= \sum_{p=0}^{P} \sum_{m=0}^{M} h_p(m,0)\, x(n-m)\, |x(n-m)|^p \\ &+ \sum_{k=1}^{K} \sum_{m=0}^{M} \sum_{l=1}^{L} h_k(m,l)\, x(n-m)\, |x(n-m-l)|^k \\ &+ \sum_{k=1}^{K} \sum_{m=0}^{M} \sum_{l=1}^{L} h_k(m,-l)\, x(n-m)\, |x(n-m+l)|^k \end{aligned} \tag{2.17}$$

2.7.3 Parametric Generalized Memory Polynomial

In [13], the authors proposed a DPD model where the parameters of a conventional GMP model change, over time, as a function of the input signal envelope. The principle of operation of this model follows the rationale that, when the long-term behavior of a PA is excited, the PA slowly suffers a slight change in its characteristics through time. If the long-term behavior can be described by a state vector $\vec{\alpha}(n)$, then the PA can be linearized using a conventional GMP model with slightly different parameter values at each step of the temporal evolution of $\vec{\alpha}(n)$. Thus, the GMP core of this model allows for the compensation of the static nonlinearity and short-term memory of the PA, and the dynamic variation of the GMP parameters allows for the compensation of its long-term memory—though at the cost of a very large number of model parameters and a very complex extraction procedure. This model is defined as in (2.18), where P, M, K and L are the GMP hyperparameters; $h_p(m, 0, \vec{\alpha}(n))$ and $h_k(m, \pm l, \vec{\alpha}(n))$ form the set of model parameters, with a total number of parameters A times greater than that of the GMP model, where A is the number of long-term state variables in $\vec{\alpha}(n)$; $x(n)$ is the input complex-envelope signal; and n is the sample index.

$$
\begin{aligned}
y_{\text{P-GMP}}(n) \;=\; & \sum_{p=0}^{P}\sum_{m=0}^{M} h_p(m, 0, \vec{\alpha}(n))\, x(n-m)\, |x(n-m)|^p \\
+ & \sum_{k=1}^{K}\sum_{m=0}^{M}\sum_{l=1}^{L} h_k(m, l, \vec{\alpha}(n))\, x(n-m)\, |x(n-m-l)|^k \\
+ & \sum_{k=1}^{K}\sum_{m=0}^{M}\sum_{l=1}^{L} h_k(m, -l, \vec{\alpha}(n))\, x(n-m)\, |x(n-m+l)|^k
\end{aligned}
\tag{2.18}
$$

For the compensation of the long-term memory effects in GaN HEMT-based PAs, the variation of the GMP parameters is informed by a physics-level understanding of thermal and charge-trapping phenomena. In [13], this information is provided by two auxiliary models—a linear first-order low-pass filter preceded by a nonlinear function for the thermal effects, and the Jardel model for the trapping effects—that operate over the amplitude of the input complex-envelope signal. Together, these two auxiliary models produce the two long-term state variables that define the long-term state vector $\vec{\alpha}(n) = [\alpha_{\text{th}}(n), \alpha_{\text{trap}}(n)]$. Having defined the long-term state vector, the variation of the GMP parameters is done as in (2.19).

$$
\begin{aligned}
h_p(m, 0, \vec{\alpha}(n)) \;&\equiv\; h_p(m, 0) \;+\; \frac{\Delta h_p(m, 0)}{\Delta \vec{\alpha}(n)}\, \vec{\alpha}(n) \\
h_k(m, \pm l, \vec{\alpha}(n)) \;&\equiv\; h_k(m, \pm l) \;+\; \frac{\Delta h_k(m, \pm l)}{\Delta \vec{\alpha}(n)}\, \vec{\alpha}(n)
\end{aligned}
\tag{2.19}
$$

CHAPTER 3

Hybrid Analog/Digital Linearization of GaN HEMT-Based PAs

Synopsis — In this chapter we describe a novel hybrid analog/digital linearization scheme for GaN HEMT-based PAs that consists of an analog electronic circuit and a conventional low-complexity digital predistorter. The analog electronic circuit compensates the long-term memory of the PA by dynamically modulating the gate–source voltage of the GaN HEMT as a nonlinear function of the PA's input excitation. Simultaneously, the digital predistorter compensates the remaining short-term memory and static nonlinearity of the PA. Experimental tests demonstrate that this linearization scheme achieves a level of IMD 6.8 dB better than what can be achieved with just the use of the digital predistorter, allowing for the compliance with the linearity specifications for multicarrier GSM base station transmitters. The contents of this chapter have been published in [J2].

3.1 Introduction

With the recent maturity of GaN HEMT technology, RF PA designers have benefited from the semiconductor's material properties to develop PAs with unprecedented output power capabilities, high power efficiencies, and wide bandwidths of operation [8], [24]. While these are some of the desirable attributes of any PA, they more often than not come at the expense of linearity: a characteristic that is compulsory in applications such as base station transmitters for cellular telecommunications. For this reason, PAs are typically accompanied by DPD units that compensate their nonlinear behavior and thus complete an amplification chain that features all of the aforementioned benefits [133].

While this has been a general solution for obtaining highly linear and efficient PAs for over a decade—preceding them with a DPD unit—, GaN HEMT-based PAs have proved to be uniquely challenging in being linearized due to their highly unusual nonlinear behavior. This nonlinear behavior is mainly attributed to charge-trapping phenomena that produce long-term memory effects not captured by most conventional DPD schemes [134]: the time constants associated with these effects are 3 to 6 orders of magnitude larger than those associated with short-term memory effects. This has prevented the reliable compliance with the linearization levels enforced in the cellular telecommunications industry even with state-of-the-art DPD schemes such as the GMP of Morgan *et al.* [130].

There have been several proposals for modeling and compensating the multiple-time-scale nonlinear behavior of RF PAs (not necessarily based on GaN HEMTs) [131], [134]–[137]. However, only in 2017 did Barradas *et al.* [13] publish the first DPD scheme capable of linearizing a GaN HEMT-based PA to a level that meets the linearity specifications for multicarrier signals in the Global System for Mobile Communications (GSM) standard: IMD components that do not exceed −60 dBc and a noise floor that does not exceed −70 dBc [138]. The DPD scheme proposed in [13] consisted in a conventional GMP model whose coefficients change, over time, as a function of the input signal envelope in order to counteract the long-term memory effects experienced by the GaN HEMT due to both thermal and charge-trapping phenomena. It is a physics-level understanding of these phenomena that is used to relate the change of the DPD coefficients to the input signal envelope.

In this chapter, we present an entirely different approach to the linearization of GaN HEMT-based PAs. Instead of coercing a conventional DPD model into operating over a time scale that is much longer than what it was initially intended for, in this chapter we describe a hybrid analog/digital linearization scheme where an analog electronic circuit compensates the long-term memory of the PA and a completely unmodified conventional DPD model compensates the remaining short-term memory and static nonlinearity of the PA. This scheme is demonstrated to be capable of linearizing a GaN HEMT-based PA up to a level that is in compliance with the exceptionally stringent multicarrier GSM standard. The hybrid analog/digital linearization scheme described herein is thus an important step away from the ever more complex DPD schemes; rather, its implementation is simple and its performance, as we demonstrate in this chapter, is comparable (or better) to that of previous works.

3.2 Compensation Strategy

Charge trapping is the primary cause of long-term memory effects in GaN HEMT-based PAs. While the physical mechanisms behind it are still not completely established, it is generally accepted that this phenomenon arises from the existence of localized electronic

states at energy levels between the conduction and valence bands, that is, deep-level traps near the center of the GaN band gap. In deep-level traps, the energy required to liberate a trapped charge (to either the valence or conduction band) is high, which means that the probability of it happening through thermal emission is low [139]. Under large electric fields, this leads to an accumulation of charge in trapped states and the formation of a net-negative electric potential that depletes the GaN channel and dynamically modulates its conductivity [83].

Charge trapping can be modeled as the charging and discharging of a virtual gate and/or virtual back gate that produces a self-biasing effect [82], [139]. Moreover, it has been demonstrated that this self-biasing effect is so severe that a GaN HEMT-based PA biased in class B can easily degenerate into a deep class C under normal operating conditions [140]. Since the time constants associated with the charging and discharging of these virtual gates can range from under one microsecond to over one minute [89], [91], and considering that the envelopes of modern communications and radar waveforms vary within these time frames, it follows that the long-term memory effects caused by charge-trapping phenomena are a major contribution to the seemingly intractable post-linearization residual distortion observed in communications applications [13] and the severe deterioration of the pulse-to-pulse stability in radar applications [14], [C3].

Even though there are methods for preventing the accumulation of trapped charge in GaN HEMTs, this phenomenon is unlikely to be completely eliminated in the near future. The reason for this is that some of the mechanisms that lead to charge trapping in GaN HEMTs are believed to be the same mechanisms that allow these transistors to function in the first place. For instance, surface states in the AlGaN barrier are understood to be a source of traps that induce gate lag [103], [141], [142]. While this phenomenon can be mitigated through the use of field plates and various passivation techniques [67], [70], [71], there is indication that these same surface states are responsible for the formation of the 2DEG that constitutes the GaN channel [47], [52]. Furthermore, extrinsic dopants in the GaN buffer are believed to be a source of traps that induce drain lag [83], [105]. However, these dopants are necessary to improve buffer isolation and prevent short-channel effects such as punch-through (sub-threshold current leakage) [36], [39].

In order to compensate the long-term memory effects caused by thermal and charge-trapping phenomena, we present in this chapter an analog electronic circuit that dynamically modulates the gate bias voltage of a GaN HEMT-based PA as a function of its input excitation. The modulation of the gate bias voltage of the PA allows for the compensation of the long-term memory effects caused by charge-trapping phenomena because, as we previously established, these effects are the result of a dynamic virtual gate and/or virtual back gate voltage (or, equivalently, a variation of the HEMT's threshold voltage). By canceling out this virtual gate voltage (or the variation of the threshold voltage), our circuit compensates both gate-lag and drain-lag effects simultaneously—because, in spite of the two effects

having different points of origin (the gate or drain terminal, respectively), both lead to a similar net variation of the HEMT's threshold voltage. This reasoning is supported by physical simulations in [83] and successful behavioral modeling efforts in [134]. It should be noted that, by modulating the gate bias voltage of the PA, this circuit also allows for the compensation of the long-term memory effects caused by thermal phenomena because, from a behavioral point of view, these effects correspond to a variation of the gain of the PA, which is similarly dependent on its quiescent (or, in this case, dynamic) gate–source voltage operating point. A similar approach to the compensation of thermal-related effects was adopted in [13] in the context of DPD.

3.3 Charge-Trapping Model

In this chapter, we use the Jardel model defined in Section 2.4.1 to account for the different capture and emission time constants. This model can be represented as in Figure 3.1, a physically meaningful nonlinear circuit with different charge and discharge time constants first deduced in [139], later overhauled in [89], and finally adapted in [13]. This circuit, whose dynamics are defined in (3.1), models the (negative) back gate voltage, V_{BG}, as a nonlinear function of the amplitude of the input envelope, V_E. Thanks to the diode, assumed to be an ideal switch (forward voltage equal to 0 V), the circuit works much like a peak detector with different charge and discharge time constants. Since the discharge time constant is typically much greater than the charge time constant (3 to 6 orders of magnitude), the charge time constant is approximately equal to $\tau_1 = R_1\,C$ and the discharge time constant is equal to $\tau_2 = R_2\,C$. The parameter $-K$ is a scaling factor.

$$\frac{dV_C}{dt} = \begin{cases} \dfrac{1}{R_1\,C}\,V_E - \dfrac{R_1 + R_2}{R_1\,R_2\,C}\,V_C \quad , & V_E \geq V_C \\[2ex] -\dfrac{1}{R_2\,C}\,V_C \quad , & V_E < V_C \end{cases} \tag{3.1}$$

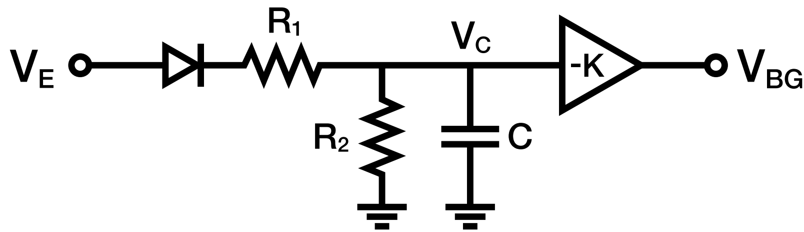

Figure 3.1 Nonlinear multiple-time-constant model of the self-biasing caused by charge trapping in GaN HEMTs. V_E is the amplitude of the input envelope; V_{BG} is the back gate voltage. The diode is assumed to be ideal ($V_f = 0$ V).

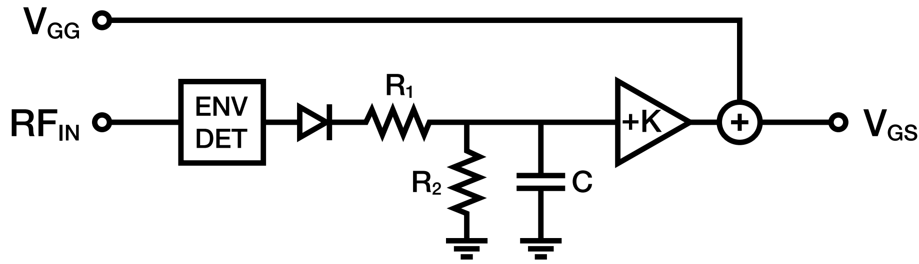

Figure 3.2 Diagram of the analog feedforward circuit for the compensation of long-term memory effects due to the self-biasing caused by charge trapping in GaN HEMTs.

3.4 Analog Compensation Circuit

In order to compensate the long-term memory effects caused by charge trapping in GaN HEMT-based PAs, we developed a feedforward circuit that corrects the self-biasing behavior observed in these devices using analog components. This analog compensation circuit (ACC); illustrated in Figure 3.2, pictured in Figure 3.3, and laid out in Appendix A (actually, Appendix A is an improved version of this ACC); implements the charge-trapping model described in Section 3.3 and adds the back gate voltage, with opposite sign, to the intended (constant) HEMT gate bias voltage, V_{GG}. This results in the compensated (modulated) gate–source voltage, V_{GS}, that is used to bias the GaN HEMT. The input envelope is extracted from the coupled PA excitation signal, RF_{IN}, using a commercially available envelope detector. The ideal diode is implemented using a Schottky diode whose forward voltage is compensated by an operational amplifier in a local feedback loop [143].

In summary, our ACC achieves the following. Suppose the HEMT is biased at a gate–source voltage V_{GS} that is initially equal to V_{GG}. When the HEMT is excited by an input signal, a drain–source voltage is generated and charge carriers (electrons) in the vicinity of the GaN channel become trapped for a mean time of $\tau_2 = R_2\,C$, thus creating an electric field that constricts the channel [140]. This is equivalent to there being a virtual back gate with a negative voltage V_{BG} which varies with the amplitude of the input envelope. In order to counteract the constrictive action of the back gate, the gate bias voltage is modulated in direct opposition to V_{BG}, producing the compensated V_{GS}. The result is a net gate voltage that is always equal to V_{GG} and the absence of long-term memory effects due to charge trapping—provided, that is, that the charge-trapping model is accurate and the usual large-value bypass capacitor at the gate bias terminal of the PA is removed (otherwise the modulated V_{GS} would be bypassed to ground).

The initial estimation of the parameters of the model (and of the implemented circuit) closely followed the procedure described in [99]. This included the characterization of the small-signal gain of the PA as a function of the gate bias voltage, the measurement of the PA's small-signal response to large-signal two-tone inputs of various frequency separations, and the optimization of the trap discharge time constant, τ_2, for obtaining the best

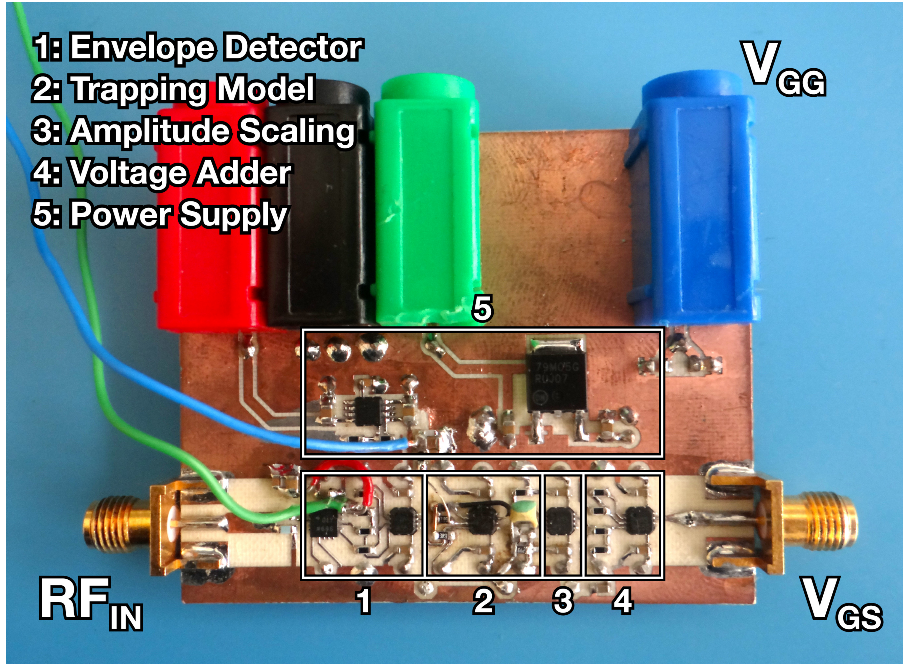

Figure 3.3 Photograph of the analog compensation circuit.

agreement between the frequency-dependent back gate voltage derived from the measurements and the one modeled using the charge-trapping model of Section 3.3. In order to accelerate the initial estimation procedure, trap charge was considered to be instantaneous, resulting in the following first estimates: $\tau_1 = 0$ µs, $\tau_2 = 145$ µs and $K = 242$ mV/V ($R_1 = 0\ \Omega$, $R_2 = 27$ kΩ and $C = 5.1$ nF). After manually tuning the circuit parameters for obtaining optimum results (see Section 3.6), we obtained $\tau_1 = 0.14$ µs, $\tau_2 = 58$ µs and $K = 90$ mV/V ($R_1 = 27\ \Omega$, $R_2 = 11$ kΩ and $C = 5.1$ nF).

3.5 Practical Validation

3.5.1 Validation Procedure

After implementing the ACC, we set out to verify whether it could compensate the long-term memory effects of a GaN HEMT-based PA and improve its linearizability. In order to do this, we devised the following two-part procedure. First, the PA was linearized using a GMP DPD model with the ACC disconnected; V_{GS} was therefore constant and equal to V_{GG}. Then, the PA was linearized using both the ACC, which modulated V_{GS}, and a GMP DPD model with the same complexity as the one used in the first test (parameter set $\{P, M, K, L\} = \{9, 4, 5, 4\}$, according to the GMP model definition in Section 2.7.2). A sampling frequency of 100 MHz was assumed to be sufficient to properly capture the dynamics of the PA and thus sufficient to generate an inverse model (the GMP DPD model).

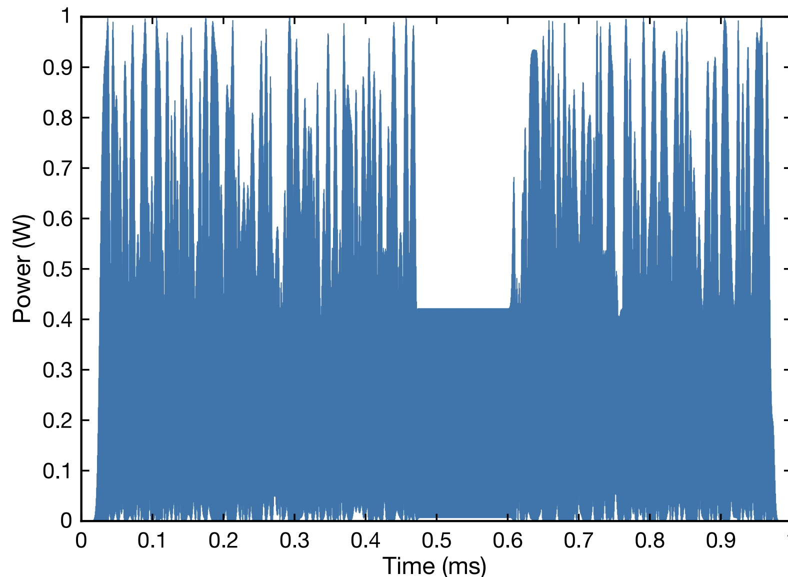

Figure 3.4 Envelope amplitude of the 4-carrier GSM PA input signal.

For this procedure, we selected a waveform that would excite not only the short-term characteristics of the PA but the long-term characteristics as well: the 4-carrier GSM signal illustrated in Figure 3.4. This baseband signal was sampled at 100 MHz, centered at 2.47 GHz, and scaled so that its peak envelope amplitude would be equal to 30 dBm. Observe that not only is this a slotted signal, it also features a low-amplitude training sequence between the 0.46 ms and the 0.60 ms marks. These two aspects, as well as the fast modulation of the instantaneous envelope amplitude, contribute to an excitation that is rich in both short-term dynamics (which a conventional GMP model can account for) and long-term dynamics. These long-term dynamics, namely the wide—but slow—variation of the mean envelope amplitude, produce a rich set of charge-trapping states that a conventional GMP model could not possibly account for (it would require a memory depth in the order of 10^3 to 10^6 samples).

After performing this procedure, the validation of our hypothesis was done by comparing, between the two linearization tests (without and with the ACC), a measure of the long-term memory of the PA and its linearity. This measure refers to a residual signal $r(n)$ calculated as in (3.2), where $\widetilde{w}(n)$ is the measured output complex envelope of the predistorted PA, $\widetilde{w}_{\text{GMP}}(n)$ is the output complex envelope of the predistorted PA computed using a forward GMP model of the PA, and n is the sample index. Since the modeled PA output captures not only the static nonlinearity of the PA but its short-term memory characteristics as well, the residual signal that remains from the subtraction with the measured PA output is, by definition, a result of the long-term memory characteristics of the PA that the GMP model cannot predict. Thus, any deviation of $r(n)$ from a value of 0 V indicates a time period in which the GMP DPD model would have failed to linearize the PA because of long-term memory effects.

$$r(n) = |\widetilde{w}(n)| - |\widetilde{w}_{\mathrm{GMP}}(n)| \tag{3.2}$$

Since the training sequence of the 4-carrier GSM input signal has a duration that is long enough for the charge-trapping state to vary greatly (in the form of charge emission, or trap discharge), we expect to see, during this period, a very noticeable increase in the magnitude of $r(n)$ when the ACC is not being used. When the ACC is being used, however, we expect the residual signal not to deviate very much from 0 V and, as a consequence, we expect the level of distortion at the output of the PA to be lower. If both of these expectations are verified, then we can state unequivocally that the ACC improves the linearizability of the GaN HEMT-based PA by compensating the long-term memory effects due to the self-biasing caused by charge-trapping phenomena.

3.5.2 Laboratory Setup

In order to test our hypothesis, we assembled the laboratory setup schematized in Figure 3.5 and pictured in Figure 3.6. The PA, illustrated in Figure 3.7, was based on the 10 W Wolfspeed CGH40010 GaN HEMT and was biased in class B with $V_{GG} = -2.68$ V, leading to a quiescent drain current of 20 mA ($\sim 1\%$ of I_{DSS}). The PA was kindly provided by Dr. P. M. Cabral.

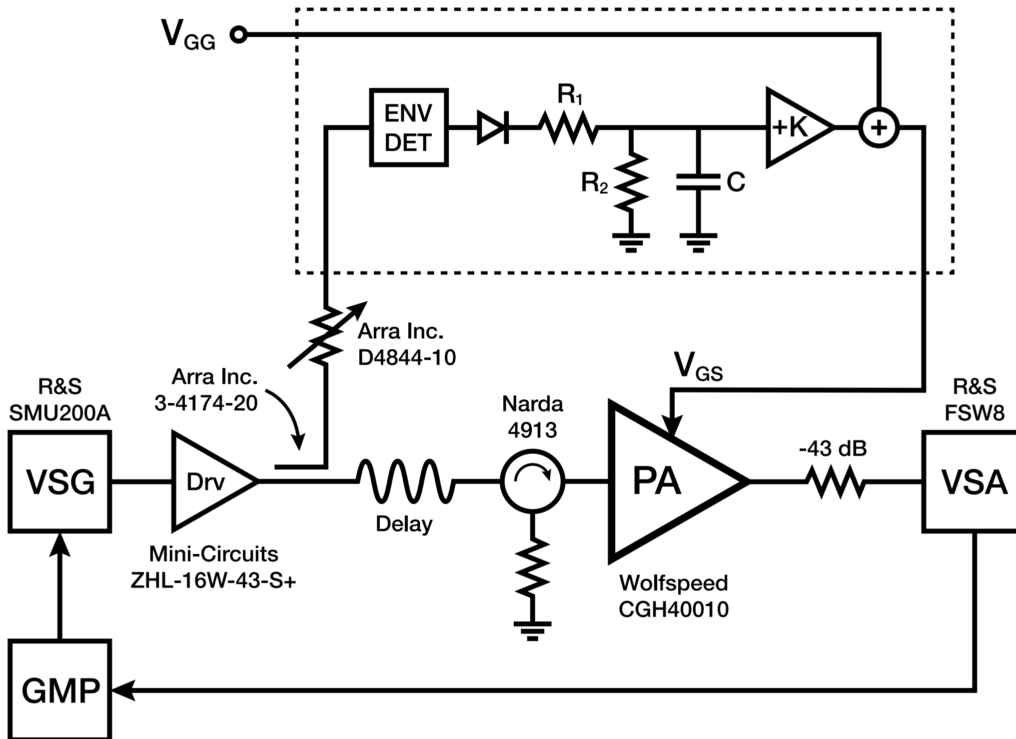

Figure 3.5 Diagram of the laboratory setup.

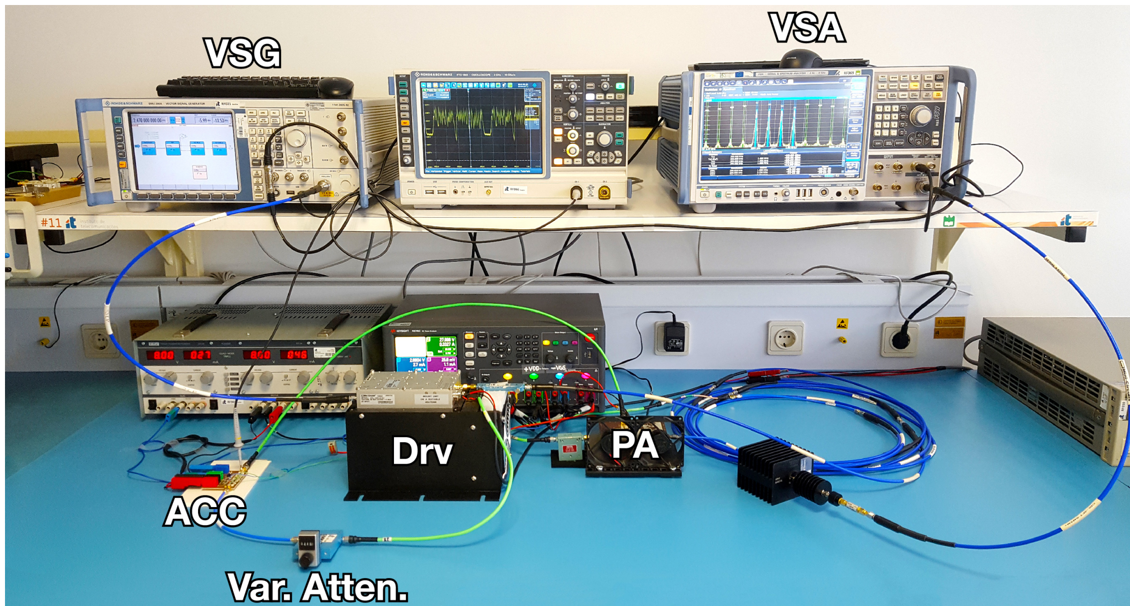

Figure 3.6 Photograph of the laboratory setup.

The PA input chain consisted of a Rohde & Schwarz SMU200A VSG followed by a Mini-Circuits ZHL-16W-43-S+ driver and a Narda 4913 isolator. The PA output chain consisted of a fixed −43 dB attenuator and a Rohde & Schwarz FSW8 VSA. Moreover, in order to source and measure the dc power of the PA, a Keysight N6705C dc power analyzer was used. For increased measurement accuracy, the internal 10 MHz oscillator of the VSA was used as the reference for both the VSA and the VSG, and a baseband trigger signal was provided by the VSG to the VSA.

The input signal of the ACC was extracted from the input of the PA using an Arra Inc. 3-4174-20 directional coupler, and an 8.9 m coil of coaxial cable was used to compensate the group delay of the ACC (measured at 46.8 ns using a Tektronix MSO71604C oscilloscope). In order to more easily tune the parameters of the ACC, K was made constant and, instead, an Arra Inc. D4844-10 mechanically variable attenuator was used to set the amplitude of the input signal.

All instruments were connected, through a local area network, to a personal computer that uploaded input signal envelopes, downloaded output signal envelope and drain current measurements, and implemented the GMP DPD model. All measurements were done at a controlled ambient temperature of 23 °C, and the PA was provided with some auxiliary ventilation.

3.5.3 Setup Calibration

The setup was calibrated at the PA input plane using a Keysight E9301A average power sensor connected to a Keysight N1913A power meter (PM). The calibration procedure consisted in sweeping the power level of the VSG, measuring the power level at the PA

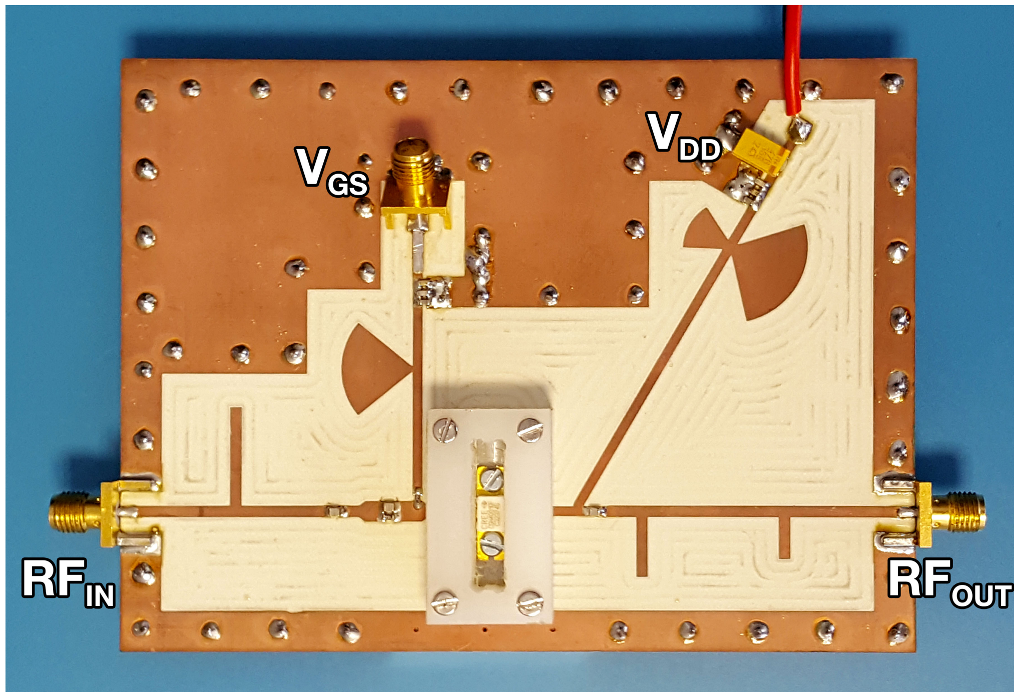

Figure 3.7 Photograph of the GaN HEMT-based PA.

input plane with the PM, and computing a calibration factor equal to the mean power gain.

Before doing this, however, the average power sensor was first calibrated using the reference power source built into the PM and a −20 dB attenuator whose S-parameters were measured using a Keysight N5242A vector network analyzer (VNA) (which was calibrated using the standard short–open–load–through procedure). This was a necessary preliminary step because the E9301A average power sensor toggles between two measurement ranges which feature a strong discontinuity even after completing the built-in calibration procedure.

After being calibrated, the PA input chain (including the delay line) was used as a reference power source to calibrate the PA output chain at the PA output plane in a way similar to that used in the calibration of the PA input chain.

3.6 Results

In Section 3.3 we established that charge-trapping phenomena in GaN HEMTs produce an effect equivalent to that of a back gate voltage V_{BG} that adds to the gate bias voltage V_{GG} and generates strong long-term nonlinearities by driving the net gate bias voltage toward more negative values. To counteract this effect, we developed an ACC that models V_{BG} and adds it, with opposite sign, to V_{GG}, resulting in a compensated V_{GS} (see Figure 3.8 for an example output). By biasing the gate with this varying V_{GS} instead of the constant V_{GG}, the HEMT should produce no long-term memory effects and therefore should be more easily linearizable.

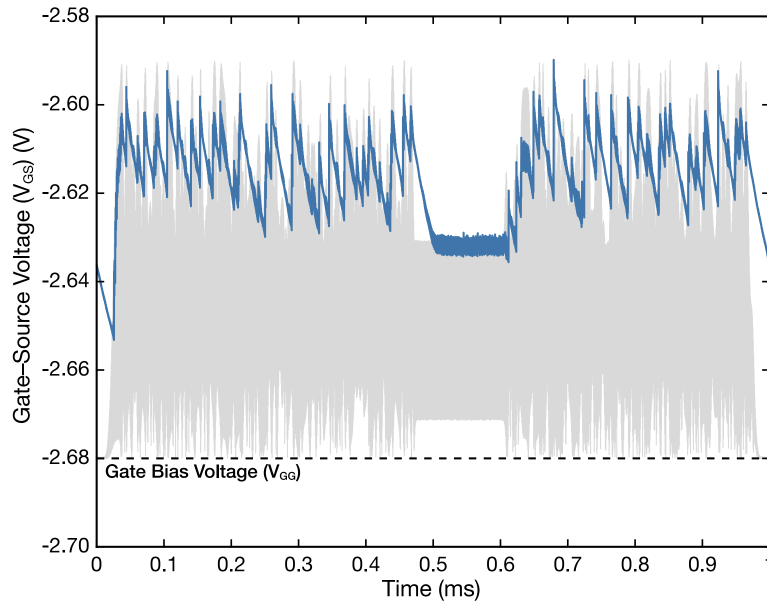

Figure 3.8 Output of the ACC—the compensated gate bias voltage of the GaN HEMT—and, in the background, a representation of the input envelope amplitude (for visual reference).

To demonstrate this, we computed the residual signal defined in (3.2) for the two linearization tests (without and with the ACC) and plotted it in Figure 3.9. This signal, which was filtered by a sharp $1/\tau_2 \approx 17$ kHz low-pass filter, is essentially the difference (the error) between the PA output that was measured and the PA output that can be predicted by a GMP model. As such, the residual is a direct result of the long-term memory effects that the GMP DPD model does not compensate—if it did, there would be no residual (error). As expected, in the linearization test where the ACC is not used we can observe a massive increase in the magnitude of the residual during the training sequence of the 4-carrier GSM input excitation. Also as expected, we can observe a very significant reduction of this residual when the ACC is used, as well as a slight overall correction of the ultra-slow deviation from 0 mV. We can, therefore, conclude that the ACC does, indeed, compensate the long-term memory effects due to the self-biasing behavior caused by charge-trapping phenomena in GaN HEMT-based PAs.

Having confirmed that the ACC compensates the long-term memory of the PA, it only remains to be shown that this translates into an improvement in the linearizability of the PA. Figure 3.10 reveals that, indeed, it does. For a 4-carrier GSM input excitation with a peak available power of 30 dBm (mean available power of 23.7 dBm), the PA produced an output signal with an intermodulation distortion ratio (IMR) of −58.95 dB when being linearized with a conventional GMP DPD model, and an IMR of −65.77 dB when being linearized with our ACC and a GMP DPD model with the same parameter set (the same complexity). Despite this 6.82 dB improvement in linearity, the power-added efficiency (PAE) only decreased by 0.5 p.p.: from 29.1 % in the former case to 28.6 % in the latter.

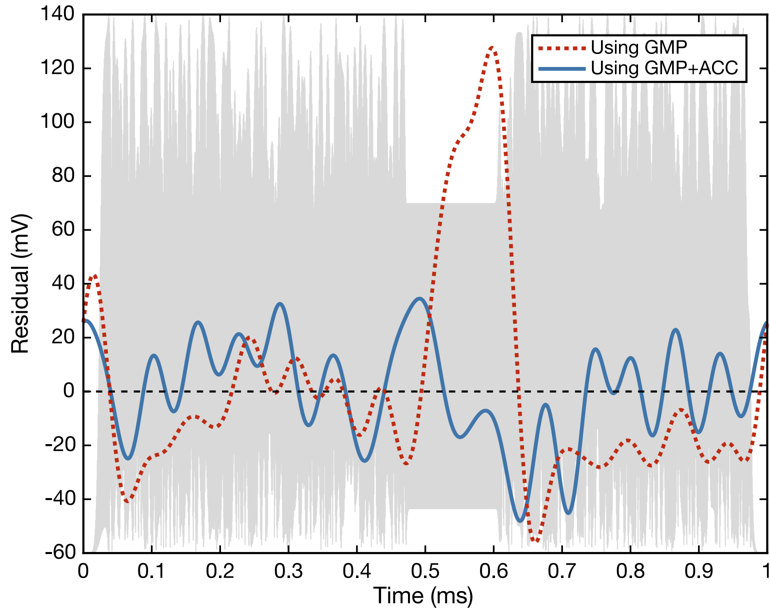

Figure 3.9 Long-term residual error signal of the predistorted PA output when the ACC is disabled and when the ACC is enabled. Also, in the background, a representation of the input envelope amplitude is shown for visual reference.

The peak output power in both cases was, respectively, 40.85 dBm and 40.78 dBm. These results are summarized in Table 3.1.

Figure 3.11 illustrates the AM–AM and AM–PM profiles of the PA under three circumstances: when no linearization is being done, when the ACC is being used to compensate the self-biasing of the HEMT due to charge trapping, and when the complete hybrid analog/digital linearization scheme is being employed. In Section 3.5.2 we mentioned that the PA was initially biased in class B, yet this figure reveals that the PA is still operating in class C even when the ACC is being used. While it might seem that the ACC failed to accomplish its objective—to compensate the self-biasing of the HEMT due to charge-trapping phenomena—, not pushing the class of operation of the PA to a textbook class B was a deliberate decision of ours. In reality, we could have chosen τ_2 and K so large that the PA would be effectively biased in class A. However, while this would have resulted in a complete absence of long-term memory effects and an ultra-linear response, the PAE would have been catastrophically degraded. In fact, our tuning of the ACC parameters was done not just with the improvement of the linearizability of the PA in mind, but also with the preservation of its PAE. The resulting gain profile reflects the compromise between increased linearizability and reduced PAE that we deemed adequate. To demonstrate that the ACC does have the ability to compensate not only the dynamic self-biasing of the GaN HEMT (as shown in Figure 3.9 and Figure 3.10) but its static self-biasing as well, we also show in Figure 3.11 the AM–AM and AM–PM profiles of the PA for a case in which the ACC was used to drive the operation of the PA into class B.

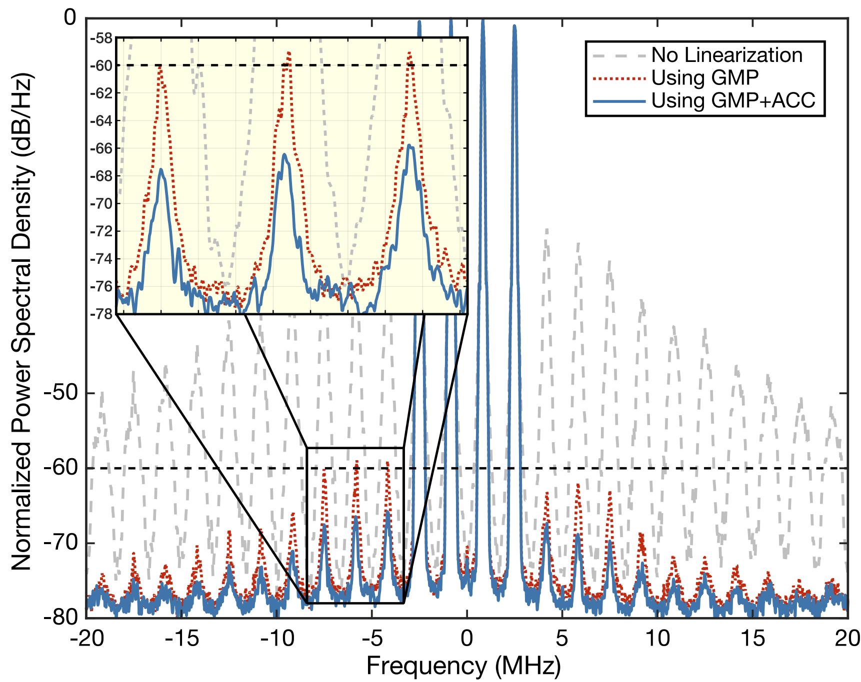

Figure 3.10 Spectra of the PA output without any compensation, with linearization using a GMP, and after being linearized using our hybrid analog/digital linearization scheme.

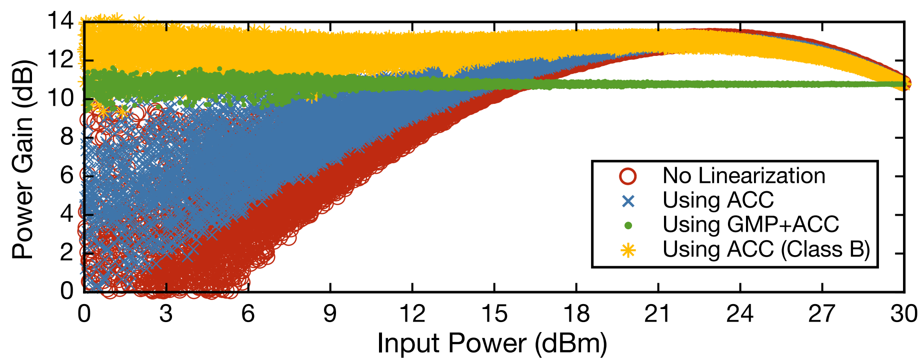

(a)

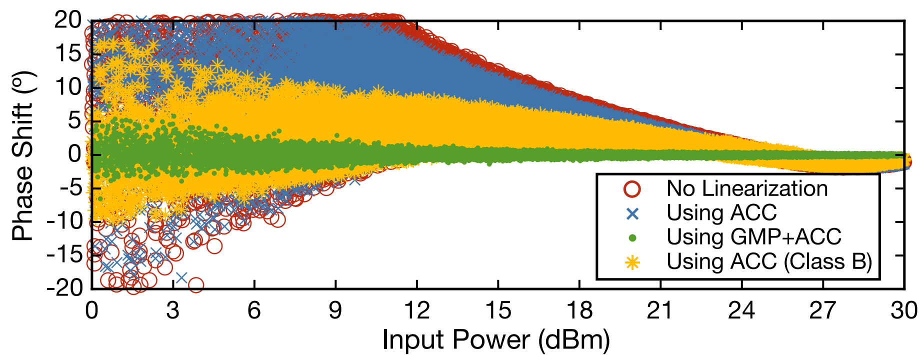

(b)

Figure 3.11 (a) AM–AM and (b) AM–PM profiles of the PA without any compensation, with compensation of trapping effects using the ACC, and after being linearized using the hybrid analog/digital linearization scheme.

Table 3.1 Summary of the linearization results.

	IMR	PAE	P_{out}	I_{dc}
GMP	−58.95 dB	29.1 %	34.60 dBm	334.0 mA
GMP+ACC	−65.77 dB	28.6 %	34.52 dBm	334.6 mA

P_{out} is the mean output power.
I_{dc} is the mean dc drain current.

3.7 Conclusion

In this chapter we identified that the model for the effects of charge trapping in GaN HEMT-based PAs can be implemented as a simple feedforward analog circuit that dynamically changes the bias voltage of the HEMT's gate. Having implemented the inverse model, we compensated these long-term memory effects and improved the linearizability of a 10 W GaN HEMT-based PA by 6.82 dB, achieving an IMR of −65.77 dBc at the cost of a decrease in PAE of just 0.5 p.p. for a 4-carrier GSM signal with a training sequence.

These results are in compliance with the exceptionally stringent linearization masks for multicarrier GSM transmitters. While other works have achieved similar results, their all-digital approach led to DPD solutions that are extremely complex to implement. Using our hybrid analog/digital solution, however, similar results can be obtained using a simple analog circuit and a conventional, completely unmodified GMP DPD model.

CHAPTER 4

Charge Emission as a Multiple-Time-Scale Phenomenon

Synopsis — In this chapter we present a novel charge-trapping behavioral model and its implementation as an analog electronic circuit for the compensation of long-term memory effects in GaN HEMT-based PAs. Rather than a fixed emission time constant as in Chapter 3, this model features a state-dependent variable emission time constant. This allows not only for the more accurate modeling and compensation of the nonlinear long-term memory effects experienced by GaN HEMT-based PAs, but also for the adaptation of the dynamics of the ACC to varying operating conditions, such as the ambient temperature. We demonstrate that the proposed ACC is able to successfully eliminate any multiple-time-scale transient symptom of current collapse following a high-power RF pulse or two-tone excitation and accurately preserve the class of operation of a GaN HEMT-based PA. Moreover, we also demonstrate that the proposed ACC can aid the linearization of GaN HEMT-based PAs for 5G NR communications, allowing for the reduction in the complexity of the DPD model. For a 5G NR TDD signal with a bandwidth of 20 MHz, the inclusion of the ACC improved out-of-band emissions by over 15 dB and improved the error-vector magnitude by over 10 p.p. at essentially no cost to the PA's power-added efficiency. The contents of this chapter have been published in [J4].

4.1 Introduction

Despite their remarkable power capabilities, the deployment of GaN HEMT-based PAs in the mobile communications infrastructure is often ruled out in favor of alternative silicon-based technologies. One of the reasons for this is the pervasiveness of long-term memory effects in GaN HEMT technology caused by thermal and charge-trapping phenomena.

While these effects can be compensated for using DPD algorithms [13], their implementation and model-extraction complexity—as well as the power necessary to execute them in real time—make them unsuitable for modern small cells and large-scale MIMO transceivers, where the power necessary for the linearization of each amplification element is of great concern.

In order to address these issues, we present in this chapter a feedforward analog circuit for the compensation of long-term memory effects in GaN HEMT-based PAs. Similarly to the ACC presented in Chapter 3, this circuit models, in real time and for an arbitrary input excitation, the multiple-time-scale dynamics of charge trapping and generates a time-varying signal that, when applied to the gate bias terminal of a GaN HEMT-based PA, compensates the nonlinear long-term memory effects that would otherwise be observable. For communications applications, the remaining short-term memory and static nonlinearity of the PA can then be compensated using a complementary low-complexity DPD algorithm.

Contrary to previous works in which the emission time constant was fixed, such as Chapter 3 and [13], [J2], the ACC presented in this chapter is supported on a model that considers a state-dependent variable time constant for the compensation of charge-trapping effects related to charge emission. This provides two major benefits over previous works. First, our variable-time-constant model greatly improves the accuracy of the predicted dynamic trapping state for larger PA input signal excursions, allowing for the reduction in the complexity of the complementary DPD linearizer. Second, the proposed circuit allows for the online adaptation of the parameters of the implemented trapping model in response to any need, e.g., due to process, supply voltage, or ambient temperature variations. This allows for an arbitrarily large variation of the dynamics of the ACC in order to meet even the most stringent field conditions that affect the trapping dynamics of the GaN HEMT.

As an external compensation method, the proposed circuit does not prevent the accumulation of trapped charge inside the HEMT, but instead masks the effects resulting from this accumulation. In spite of this, in this chapter we demonstrate that our improved compensation circuit is able to successfully eliminate any transient symptom of current collapse following a high-power pulse or two-tone excitation and accurately preserve the class of operation of a GaN HEMT-based PA. Moreover, we also demonstrate an application scenario where our proposed compensation circuit is used in conjunction with a reduced-order memory-polynomial DPD model to linearize a GaN HEMT-based PA for 5G NR communications.

4.2 Compensation Model

4.2.1 Qualitative Operation

At the core of every charge-trapping model lies a variation of a peak detector or a switchable resistor–capacitor network with different charge and discharge time constants [89], [101],

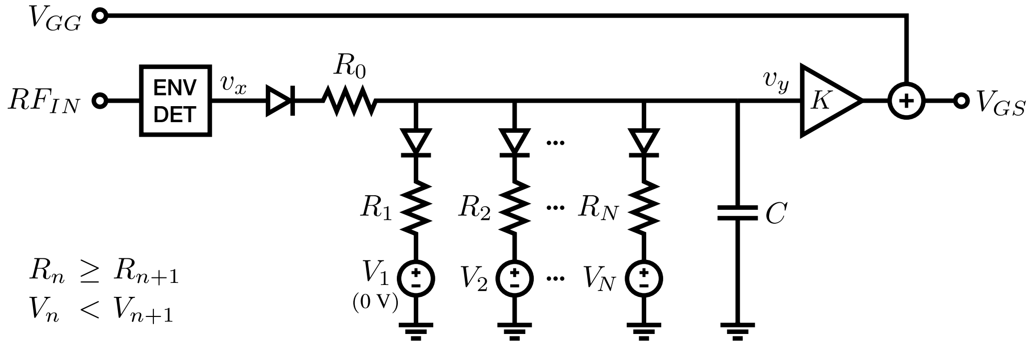

Figure 4.1 Nonlinear multiple-time-scale variable-emission-time-constant model for the compensation of long-term memory effects in GaN HEMT-based PAs. All diodes are assumed to be ideal ($V_f = 0$ V).

[144]. This is a direct consequence of the seminal work of Kunihiro and Ohno [139], who established that charge capture in deep-level traps occurs at a much faster rate than charge emission. While this has led to the assumption that each of these processes can be accurately modeled using only one time constant, simple RF pulse measurements show that this is not the case for sufficiently large signal excursions [91]. In reality, both capture and emission processes are known to have a complex dynamic behavior that starts off very fast and becomes much slower over time [91].

In order to accurately compensate the long-term memory effects caused by charge-trapping phenomena in GaN HEMT-based PAs, we devised the model illustrated in Figure 4.1, which captures the complex dynamics of charge trapping by varying the emission time constant as a function of the trapping state. As established in Section 3.2 and demonstrated in [J2], [C3], the compensation strategy consists in modulating the gate bias voltage of the GaN HEMT-based PA by adding the output of the trapping model to the constant voltage V_{GG} that sets the quiescent state of the PA. This results in the gate–source voltage V_{GS} that compensates the long-term memory effects caused by charge-trapping phenomena when applied to the gate bias terminal of the PA.

The core of the proposed compensation model works in the following way. Suppose that a pulse-modulated carrier is applied to the RF_{IN} input of the model shown in Figure 4.1. First, the capacitor charges through R_0 for the duration of the pulse and reaches a voltage v_y. Then, the capacitor discharges through all parallel R_n branches where $v_y > V_n$, $n = 1, 2, \cdots, N$. As the capacitor discharges toward $v_y = 0$ V, larger-n branches are disabled until R_1 is the only enabled branch (note that $V_n < V_{n+1}$ and V_1 is always equal to 0 V). This translates into a net discharge conductance that decreases as the charge of the capacitor decreases, resulting in a discharge rate that starts fast but becomes slower over time.

While the proposed model features an emission time constant that varies with the instantaneous trapping state, the capture time constant is fixed and approximately equal

to $R_0 C$ (because $R_0 \ll R_1, \cdots, R_N$). Since the PA is much less sensitive to variations in its operating point during large-signal excitations (as evidenced by the AM–AM profiles of self-biased GaN HEMT-based PAs in [140]), the modeling of charge capture with a fixed time constant was deemed sufficiently accurate for the purposes of our compensation model. This trade-off between capture modeling accuracy and circuit implementation complexity is further supported by the work in [C3], where we report, for a self-biased GaN HEMT-based PA, a decrease in the large-signal gain of less than 1 dB and a decrease in the small-signal gain of over 20 dB.

Besides regulating the switching between different emission time constants by enabling or disabling the different conductance branches, breakpoints (the V_n sources in Figure 4.1) also contribute to the smoothness of the model. This is because each conductance branch n actually discharges toward V_n and not toward ground. There is, therefore, a smooth handover from one time constant to another, which improves the accuracy of our compensation model.

4.2.2 Comparison With Other Models

Figure 4.2(a) illustrates, in blue, the response of our model to a pulsed-envelope excitation. In this example, our model features a near-instantaneous (with respect to the signal envelope) capture time constant $\tau_0 = R_0 C = 1$ µs, a two-branch emission time constant with $\tau_1 = R_1 C = 10$ ms and $\tau_2 = R_2 C = 1$ ms, and a breakpoint $V_2 = 0.5$ V. As intended, the charge and discharge rates of the capacitor are widely different. Moreover, the discharge of the capacitor is very fast while the model output is greater than the breakpoint at 0.5 V and becomes much slower thereafter.

Besides illustrating the response of our model to a pulsed envelope, Figure 4.2(a) also shows, in red, the response of a model that is repeatedly mentioned in the literature as being an obvious solution for the modeling of multiple-time-scale emission profiles. This model, defined in Section 2.4.2 as the "Multi-Jardel" model, which is based on the model of Jardel *et al.* with a fixed capture time constant and a fixed emission time constant [89], consists in simply summing the outputs (with a given set of scaling factors) of multiple independent Jardel models with different emission time constants. For instance, let $J(v_x(t), \tau_c, \tau_e)$ denote the response of the Jardel model, with a capture time constant τ_c and an emission time constant τ_e, to an input excitation with an envelope amplitude $v_x(t)$. Then, the response of the Multi-Jardel model in Figure 4.2(a) is $y(t) = \frac{1}{2} J(v_x(t), 1\ \mu s, 1\ ms) + \frac{1}{2} J(v_x(t), 1\ \mu s, 10\ ms)$. For reference, the contribution of each individual Jardel model to the response of the Multi-Jardel model is also shown in Figure 4.2(a).

While the pulsed-envelope responses shown in Figure 4.2(a) seem to indicate that our model is very similar to the Multi-Jardel model, more complex input excitations reveal that this is not the case. For instance, Figure 4.2(b) illustrates the response of our model

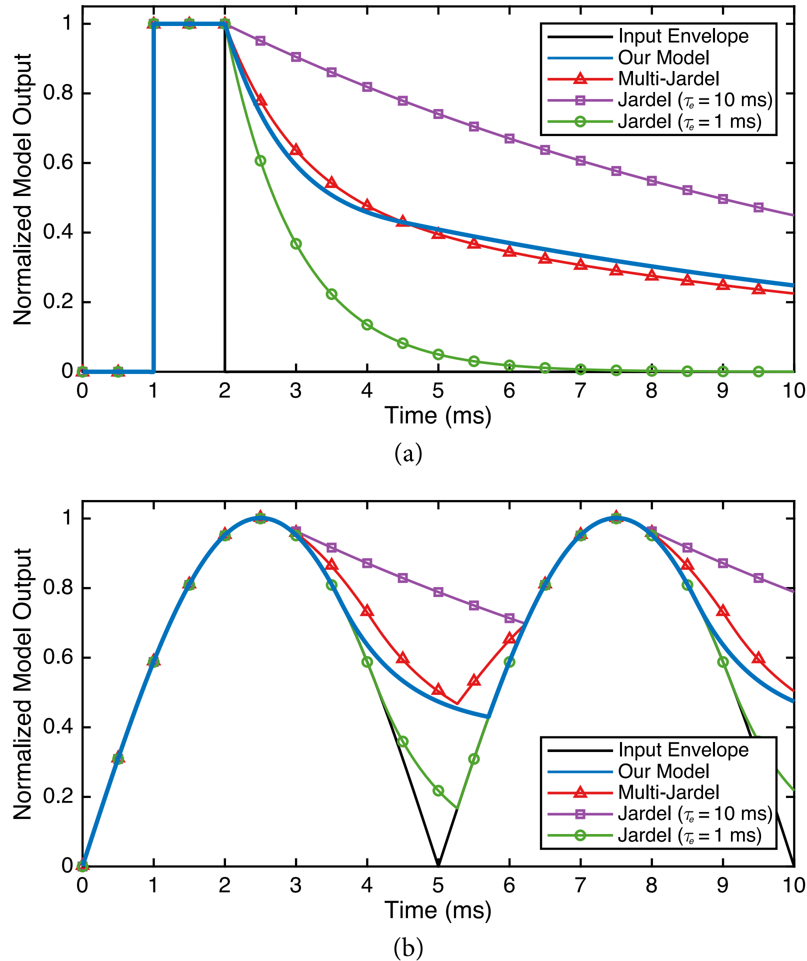

Figure 4.2 Comparison between the output of our model with a variable two-branch emission time constant, a model with two independent emission time constants (1 ms and 10 ms), a model with one fixed emission time constant equal to 10 ms, and a model with one fixed emission time constant equal to 1 ms for (a) a pulsed excitation and (b) a two-tone excitation.

and the Multi-Jardel model (with the same parameters as in Figure 4.2(a)) to an input excitation with a sinusoidal (two-tone) envelope; for reference, the contribution of each individual Jardel model to the response of the Multi-Jardel model is also shown. Clearly, the response of the Multi-Jardel model is not physically reasonable, since there is a strong discontinuous inversion of its derivative during the emission phase. This is due to the fact that the Jardel model with $\tau_e = 1$ ms resumes its charging phase before the Jardel model with $\tau_e = 10$ ms (because, naturally, it discharges much faster). In contrast, our model produces a reasonable response. The accurate modeling of measured emission profiles should, therefore, consider one single variable emission time constant (as in our model), and not multiple time constants (or the scaled sum of the individual contributions of fixed emission time constants).

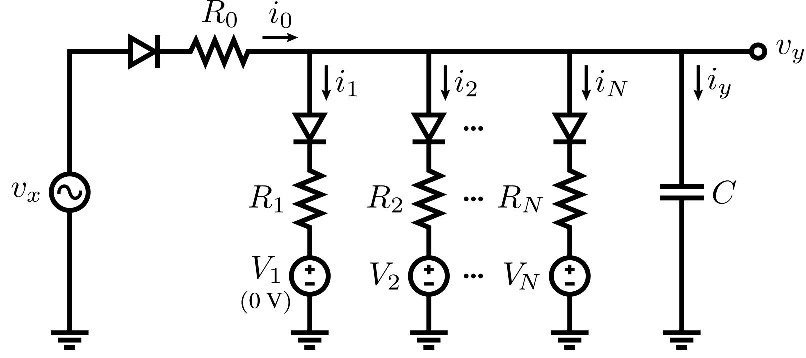

Figure 4.3 Trapping core of the variable-emission-time-constant compensation model.

4.2.3 Mathematical Formulation

The extraction of the parameters of the compensation model consists in fitting its output to measured data. This optimization process benefits from a fast digital representation of the model, so, instead of relying on an analog electronic circuit simulator, we developed the following discrete-time mathematical description of our charge-trapping model.

Referring to Figure 4.3, let $v_x(t)$ denote the amplitude of the envelope of the PA's input excitation and $v_y(t)$ the output of the charge-trapping model with N parallel conductance branches. Furthermore, let $f_D(\cdot)$, defined in (4.1), denote the transfer function of the diodes, which are assumed to be ideal.

$$f_D(x) = \begin{cases} x, & x \geq 0 \\ 0, & x < 0 \end{cases} \tag{4.1}$$

By applying Kirchhoff's current law to the output node, the current through the capacitor $i_y(t)$ can be defined as in (4.2) and (4.3). For clarity, in (4.4) we group the currents responsible for the charging and discharging of the capacitor as $i_c(t) = i_0(t)$ and $i_e(t) = \sum_{n=1}^{N} i_n$. These currents model, respectively, the processes of charge capture and charge emission.

$$\begin{aligned} i_y(t) &= i_0(t) - i_1(t) - i_2(t) - \cdots - i_N(t) &(4.2)\\ &= f_D\left(\frac{v_x(t) - v_y(t)}{R_0}\right) - \sum_{n=1}^{N} f_D\left(\frac{v_y(t) - V_n}{R_n}\right) &(4.3)\\ &= i_c(t) - i_e(t) &(4.4)\end{aligned}$$

Since $v_y(t)$ is the voltage at the capacitor's terminals, it can be calculated as in (4.5).

$$v_y(t) = \frac{1}{C}\int_{t_0}^{t}\Big(i_c(\tau) - i_e(\tau)\Big)\, d\tau + v_y(t_0) \tag{4.5}$$

Finally, using Euler's method, this model can be discretized as follows. Let (4.6). Then, $v_y(t)$ can be approximated in discrete time as in (4.7), where k denotes the discrete-time

sample index, $i_c(k)$ and $i_e(k)$ denote the discrete-time samples of $i_c(t)$ and $i_e(t)$, and f_s denotes the sampling frequency.

$$\frac{d}{dt}v_y(t) = \frac{1}{C}\Big(i_c(t) - i_e(t)\Big) \tag{4.6}$$

$$v_y(k+1) = v_y(k) + \frac{1}{f_s\,C}\Big(i_c(k) - i_e(k)\Big) \tag{4.7}$$

4.2.4 Temperature Considerations

Since the voltage breakpoints act as time-constant interpolation nodes rather than strict time-constant switching points, the emission time constant can be modified by varying the parameters V_n even with a fixed set of resistors R_n. This feature is a major advancement over previous works where the time constants were fixed, such as Chapter 3 and [J2], since it allows for the online adaptation of the parameters and dynamics of the charge-trapping compensation circuit in response to any need (e.g., due to process, supply voltage, or ambient temperature variations) without changing the set of resistors R_n, as exemplified in Figure 4.4 (and later confirmed in Table 4.1 and Table 4.2).

For more particular applications, even the resistors R_n can be adapted without modifying the compensation circuit (i.e., without physically substituting the resistors). This is because a conductance branch n can be entirely disabled by applying a sufficiently high voltage to its respective V_n breakpoint. For instance, for operation at two distinct temperature ranges, one set of model parameters with N_1 emission resistors (conductance branches) can be extracted for one temperature range, and a different set of model parameters with N_2 emission resistors can be extracted for the other temperature range. Then, both param-

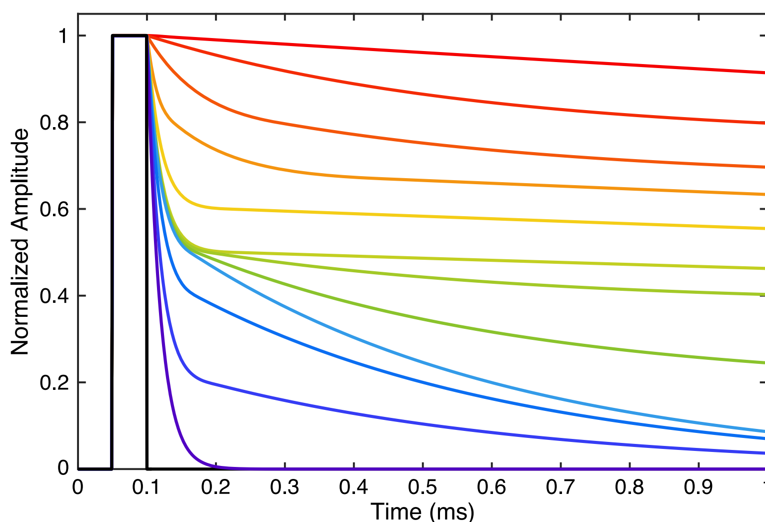

Figure 4.4 Variability of the pulse response of our compensation model with a state-dependent variable emission time constant for a fixed set of resistors R_n and various sets of breakpoint voltages V_n.

eter sets can be incorporated into one compensation circuit with $N_1 + N_2$ total emission resistors. Finally, depending on the temperature range of operation, all undesired emission resistors can be disabled simply by pulling the respective breakpoint voltages high (e.g., to the positive power rail of the circuit).

The dynamics of the proposed charge-trapping model (and the analog circuit that implements it) can, therefore, be modified either by adapting the breakpoint voltages V_n (allowing for a fine tuning of the state-dependent variable emission time constant) or by selecting entirely different sets of resistors R_n by pulling the V_n of undesired conductance branches high. This allows for an arbitrarily large (or fine) variation of the dynamics of the compensation circuit in order to meet even the most stringent field conditions that affect the trapping dynamics of the GaN HEMT.

4.3 Analog Compensation Circuit

In order to compensate the long-term memory effects caused by charge-trapping phenomena in GaN HEMT-based PAs, we designed the ACC pictured in Figure 4.5 and laid out in Appendix B. This circuit is a direct implementation of the compensation model detailed in Section 4.2 using analog electronic components, and it features three parallel conductance branches. Figure 4.6 shows a simplified schematic of the trapping core of the ACC. As illustrated, the ideal diodes were implemented using a diode whose forward voltage is compensated by an operational amplifier in a local feedback loop [143].

Figure 4.6 also indicates two potential pitfalls when implementing the compensation model: the input bias currents of the operational amplifiers and the reverse-bias currents of the diodes. Since the capacitor C is required to be relatively small because of the output current limit of the operational amplifiers, these parasitic currents should be as small as possible to preserve a good agreement between the model and its circuit implementation. Otherwise, these currents may lead to two undesirable outcomes: a disruption of the output signal's dynamics by altering the charge of the capacitor, and a large voltage offset imposed by R_n (e.g., 1 μA $\times$ 1 MΩ $=$ 1 V). The input bias current of the operational amplifiers immediately puts a restriction on the internal architecture of the operational amplifier used in the input ideal diode: it must not be a current-feedback amplifier because these have low-impedance inverting inputs. Furthermore, the voltage offset created at the R_n resistors also leads to variations in the output signal's dynamics. This is because this offset voltage is dependent on the number of enabled parallel conductance branches (it depends on the instantaneous output voltage), and also because it causes the undue switching between the charging and discharging of the capacitor by biasing the input diode. Because of the switching nature of the ideal-diode subcircuits, the parallel capacitance of the diodes should also be as small as possible to minimize the coupling between the outputs of the operational amplifiers and the capacitor C.

Our implementation consists of the following components. The envelope detector is an Analog Devices ADL5511 integrated circuit that operates from dc to 6 GHz. All operational amplifiers are Texas Instruments OPA659 voltage-feedback operational amplifiers with a typical input bias current of 10 pA. All diodes are Toshiba 1SS307E silicon switching diodes with a typical reverse-bias current of 200 fA and a total capacitance of 800 fF (at a reverse voltage of 4 V). Capacitor C is a 6.8 nF $\pm$ 1 % C0G/NP0 KEMET ceramic capacitor. Finally, the gain K is implemented using an Analog Devices AD8336 variable gain amplifier controlled by a pair of Analog Devices ADR510 precision voltage references.

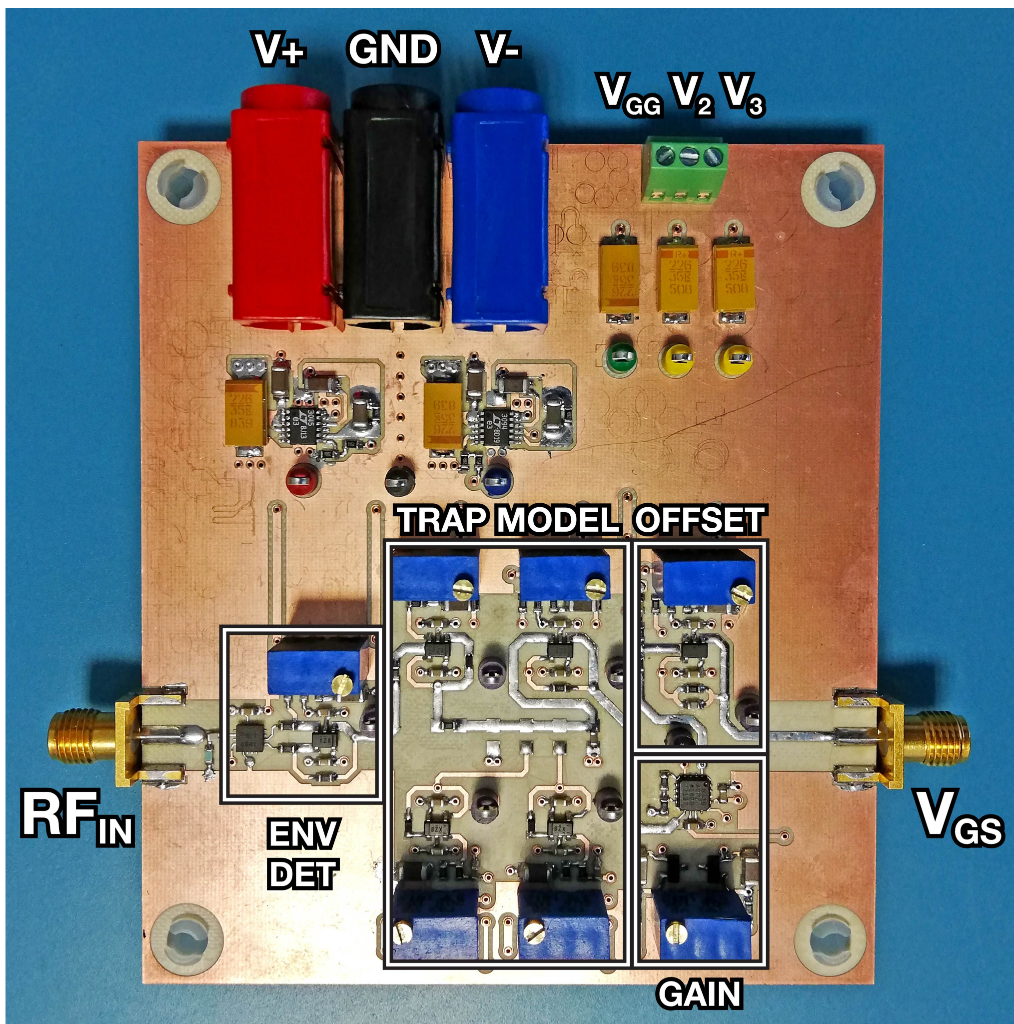

Figure 4.5 Photograph of the variable-emission-time-constant ACC.

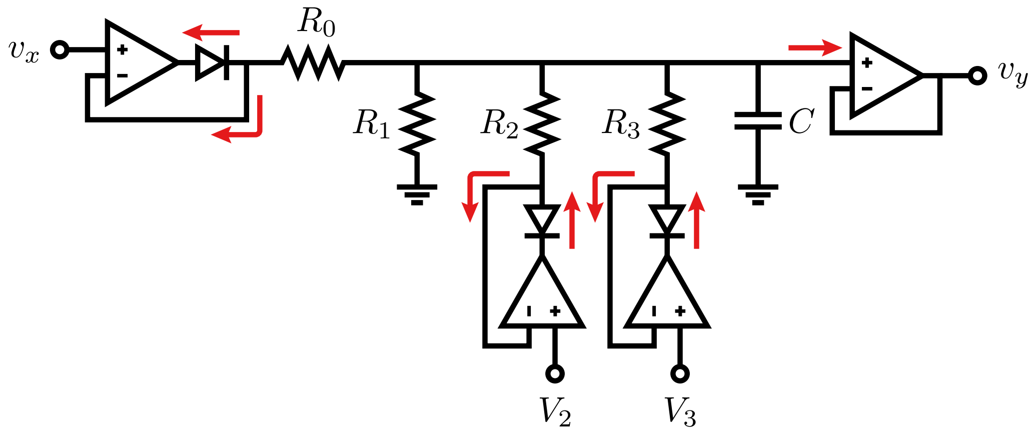

Figure 4.6 Simplified schematic of the trapping core of the ACC. Red arrows indicate potential sources of discrepancies between the model and its practical implementation. v_x is the input envelope amplitude.

4.4 Measurement Setup

In order to conduct the measurements for the validation of the ACC, we assembled the laboratory setup schematized in Figure 4.7 and pictured in Figure 4.8. The 2.2 GHz single-ended PA, illustrated in Figure 4.9, was based on the 15 W 28 V Wolfspeed CGH27015F GaN HEMT and was biased in class B (at the root of g_{m3} [145]). The PA was kindly provided by Dr. L. C. Nunes.

The input excitation of the PA was generated using a Rohde & Schwarz SMW200A VSG followed by a Mini-Circuits ZHL-16W-43-S+ driver. The output of the PA was measured using a Rohde & Schwarz FSW8 VSA. The input excitation of the ACC was extracted from the input of the PA using an Arra Inc. 3-4174-20 20 dB directional coupler. For increased measurement accuracy, the internal 10 MHz oscillator of the VSA was used as the reference for the VSA and VSG, and a baseband trigger signal was provided by the VSG to the VSA.

Other instruments include a Keysight N6705C dc power analyzer for the sourcing of the dc power of the PA, a Keysight E9301A average power sensor connected to a Keysight N1913A PM for absolute power calibration, a Keysight 34461A digital multimeter for the verification of the breakpoint voltages of the ACC, a Keysight DSOS804A oscilloscope for the monitoring of ACC signals, and various power supplies for the sourcing of the power and breakpoint voltages of the ACC. All measurements were carried out at a controlled ambient temperature of 24 °C, and the PA was provided with some auxiliary ventilation.

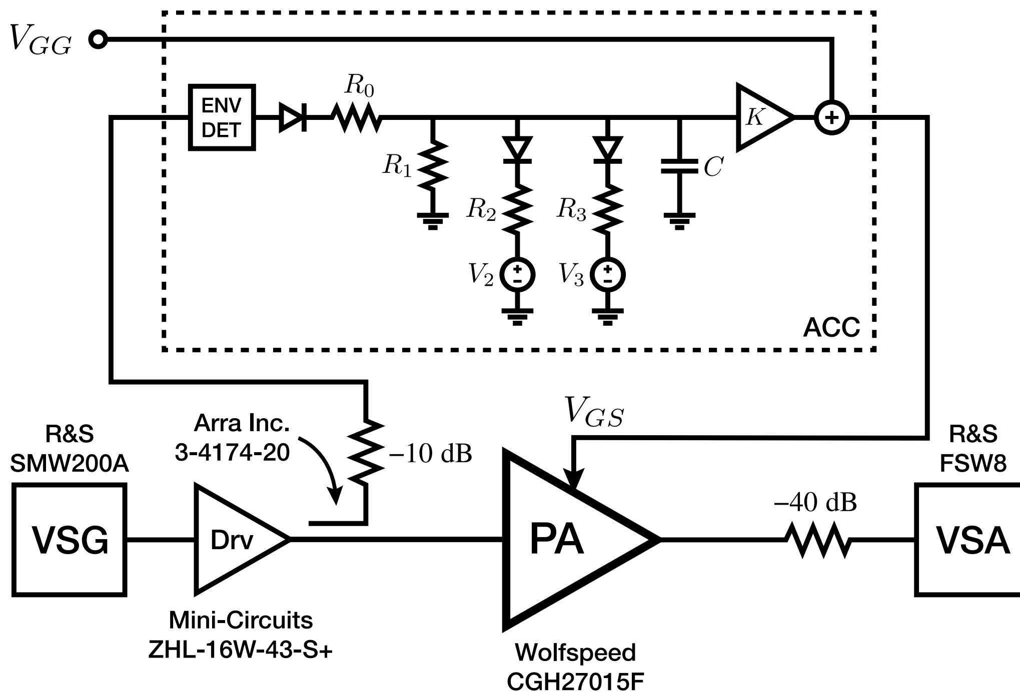

Figure 4.7 Diagram of the measurement setup.

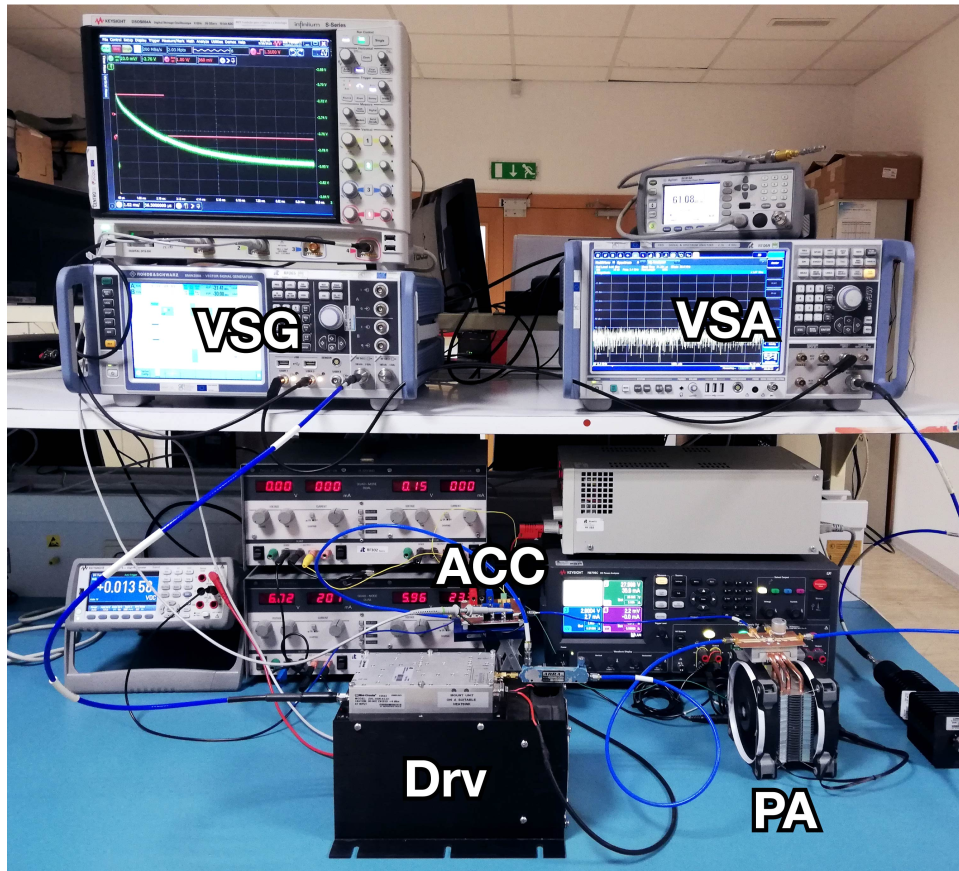

Figure 4.8 Photograph of the measurement setup.

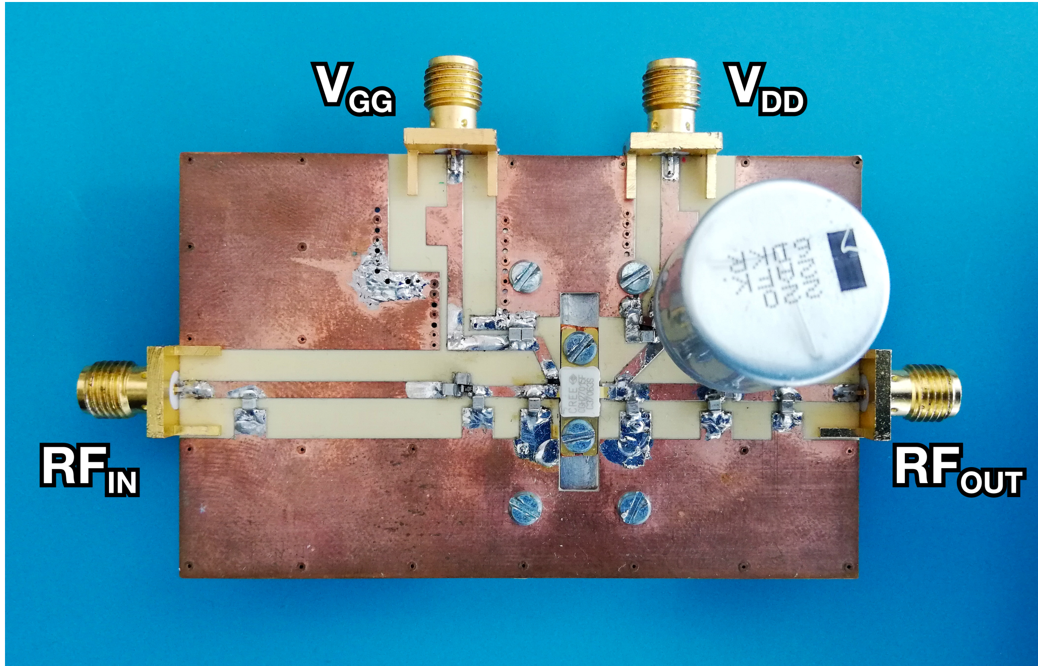

Figure 4.9 Photograph of the GaN HEMT-based PA.

4.5 Pulse Response Compensation

In this section we explore the first set of measurements that were made to verify the ability of our ACC to compensate the long-term memory effects caused by charge-trapping phenomena in GaN HEMT-based PAs. In short, we measured the transient response of a GaN HEMT-based PA to an RF pulse and observed a sudden decrease in the small-signal gain followed by a slow recovery of said gain. We then repeated the same procedure with the ACC connected to the PA and verified that the small-signal gain did not decrease after the pulse was applied.

4.5.1 Setup Calibration

Before any measurements were made, the laboratory setup was calibrated as follows. First, the PM was connected to the output of the directional coupler at the PA input plane and the VSG was set to continuously generate a train of high-power pulses. An input-plane absolute-power calibration factor was then obtained by iteratively comparing the expected average power at the PA input plane with the one measured using the PM. Having calibrated the signal source at the input plane of the PA, the PM was disconnected and the signal analyzer (attenuated VSA) was connected in its stead. An output-plane absolute-power calibration factor was then obtained by comparing the average power measured by the VSA with the known average power at the output of the calibrated signal source.

In order to preserve the waveforms of the test signals generated at the PA input plane and compensate any distortion caused by the output stage of the VSG (e.g., the inductive

response of the driver's biasing network), all input signal envelopes used throughout the rest of this section were predistorted using the iterative error-integration algorithm defined in (4.8), where $z(t)$ is the predistorted signal envelope, $w(t)$ is the measured signal envelope at the driver output, $x(t)$ is the target signal envelope, and λ is a learning-rate parameter [146], [147].

$$z(t) \; := \; z(t) \; - \; \lambda \left(w(t) - x(t) \right) \tag{4.8}$$

4.5.2 Measurement Procedure

After the setup was calibrated, the GaN HEMT-based PA was preheated [C3] and its small-signal gain G_{SS} was measured as a function of the gate–source voltage V_{GS}. This was done by sweeping V_{GS} using the dc power analyzer and measuring G_{SS} in response to a continuous-wave (CW) −10 dBm excitation. From this preliminary measurement resulted the $V_{GS}(G_{SS})$ map, which is required for the extraction of the parameters of the ACC. Note that V_{GS} is only required to be swept from the PA's bias point to increasingly negative voltages. Unless the PA is intended to be biased in class A, the power dissipated due to the quiescent drain current will vary very little throughout the sweep. Thus, the temperature of the HEMT throughout the sweep will be approximately constant.

Finally, the PA was biased in class B and its transient response to a series of large-signal RF pulses was measured. The pulse response was measured first with a constant-voltage source biasing the PA (without the ACC), and then with the ACC connected to the PA (after its parameters had been extracted). The measurements were sequenced by configuring the VSG so that it would output a constant small-signal level and, once triggered, generate one single large-signal pulse and immediately fall back to outputting a constant small-signal level. This guaranteed that the initial charge-trapping conditions were the same before each pulse, allowing for fast and repeatable measurements. The large-signal level of the pulsed excitations ranged from 20 dBm to 30 dBm and the small-signal level was constant at −10 dBm. The pulses had a duration of 50 µs. All signal envelopes were generated and measured at a sampling frequency of 200 MHz.

4.5.3 Circuit Parameter Extraction

The extraction of the parameters of the ACC was done as follows. First, the time-varying gate–source voltage $V_{GS}(t)$ of the PA was estimated by calculating the time-varying small-signal gain $G_{SS}(t)$ of the PA for each pulse-response time series and interpolating it over the $V_{GS}(G_{SS})$ map obtained from the preliminary measurement [99]. Then, the dynamic virtual back gate voltage $V_{BG}(t)$ of the GaN HEMT was estimated by postulating that $V_{GS}(t) = V_{GG} + V_{BG}(t)$. Finally, the signals $\Delta V_{GS}(t)$ that compensate the dynamic virtual back gate voltage for each measured pulse-response time series were trivially derived ($\Delta V_{GS}(t) = -V_{BG}(t)$) and the target output of the ACC for each excitation was determined.

After estimating the target pulse response of the trapping core of the ACC ($\Delta V_{GS}(t)$, defined as $\Delta V_{GS}(t) = K\, v_y(t)$), the parameters of the nonlinear model defined in Section 4.2.3 were extracted, for each measured pulse-response time series, by minimizing the mean squared error (MSE) between the target pulse response and the model's pulse response using the covariance matrix adaptation evolution strategy (CMA-ES) [148]. This was done separately for each measured pulse-response time series, resulting in the parameters listed in Table 4.1.

Table 4.1 Pulse response compensation parameters.

P_{pk}	R_0	R_1	R_2	R_3	V_2	V_3
20 dBm	91 Ω	3.6 MΩ	2.0 MΩ	330 kΩ	5 mV	42 mV
22 dBm	91 Ω	3.6 MΩ	2.0 MΩ	330 kΩ	5 mV	100 mV
24 dBm	91 Ω	3.6 MΩ	2.0 MΩ	330 kΩ	5 mV	162 mV
26 dBm	91 Ω	3.6 MΩ	2.0 MΩ	330 kΩ	5 mV	227 mV
28 dBm	91 Ω	3.6 MΩ	2.0 MΩ	330 kΩ	5 mV	295 mV
29 dBm	91 Ω	3.6 MΩ	2.0 MΩ	330 kΩ	22 mV	331 mV
30 dBm	91 Ω	3.6 MΩ	2.0 MΩ	330 kΩ	106 mV	371 mV

4.5.4 Compensation Results

After extracting the parameters of the charge-trapping model, these were programmed into the ACC by soldering the required resistors (R_0–R_3) and setting the breakpoint voltages (V_2 and V_3) with an external power supply. Then, the ACC was connected to the PA and the following results were obtained.

Figure 4.10(b) shows the response of the uncompensated GaN HEMT-based PA to a series of pulses with increasing peak power. These results can be explained through our understanding of the charge-trapping mechanism as follows. During a large-signal pulse there is a fast accumulation of charge in trapped states that depletes the channel and reduces the small-signal gain of the GaN HEMT-based PA as if there was an increasingly negative virtual back gate voltage. As this charge slowly dissipates through thermal emission and the virtual back gate voltage rises back toward zero, the small-signal gain of the PA recovers to its initial value. Since pulses with higher peak powers lead to a larger accumulation of trapped charge, the small-signal gain of the PA is reduced from 2 dB (for a 20 dBm pulse) up to over 15 dB (for a 30 dBm pulse).

Figure 4.10(c) shows the response of the GaN HEMT-based PA to the same series of pulses, but while being compensated by the ACC. This figure reveals that, by dynamically modulating the gate bias voltage of the PA, the ACC cancels out the virtual back gate voltage of the GaN HEMT and the small-signal gain collapse experienced by the PA is compensated.

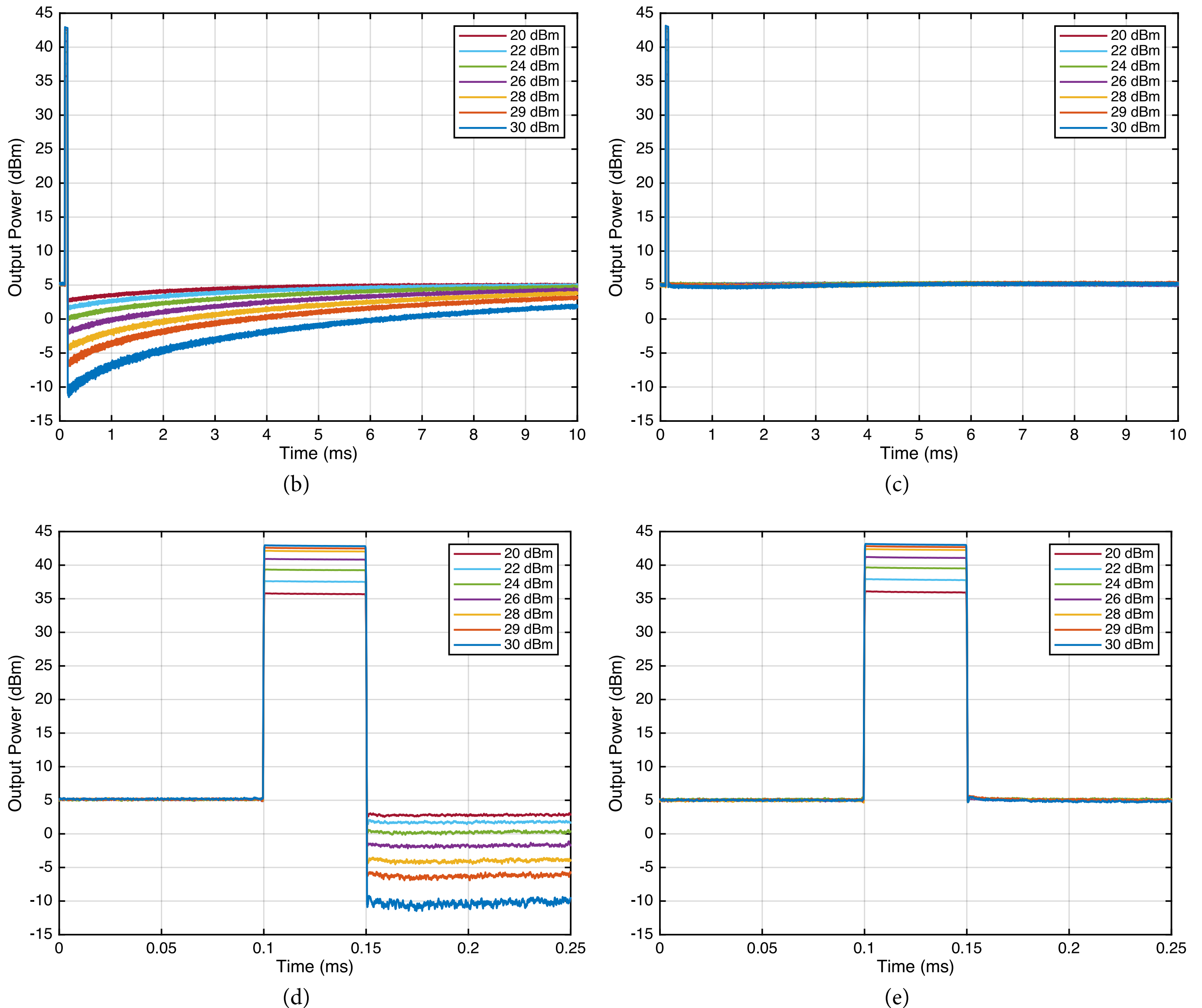

Figure 4.10 Pulse response of the GaN HEMT-based PA (a) without compensation and (b) with compensation using our ACC. A zoomed-in view of the same data can also be seen in (c) for the case without compensation and (d) for the case with compensation.

The phenomenon of charge emission, or the recovery of the small-signal gain, is known to have a multiple-time-constant (or variable-time-constant) dynamic behavior [91]. Contrary to an exponential increase with one single time constant, the actual rate of recovery of the small-signal gain of a GaN HEMT-based PA starts very fast but becomes slower and slower as the trapped charge is released. This is why our variable-time-constant ACC is able to accurately compensate not just the long-term gain collapse, but also—and simultaneously—the short-term gain collapse immediately following the end of each pulse. Figure 4.10(d) and Figure 4.10(e) prove this by showing the first 250 μs of the same data plotted in Figure 4.10(b) and Figure 4.10(c).

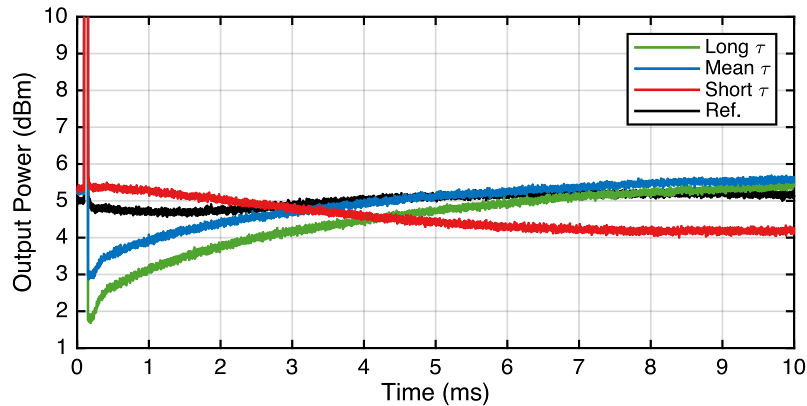

Figure 4.11 Compensation of the response to a 30 dBm pulse using an ACC with one fixed emission time constant.

In order to compare our variable-time-constant ACC with an ACC that implements a fixed emission time constant (as in Section 3.2), we compensated the response of the PA to a pulse with a peak power of 30 dBm using just one emission time constant, as illustrated in Figure 4.11. Since the emission phenomenon results in a variable-time-constant small-signal gain recovery, there are three reasonable ways of compensating for its effects using just one time constant, or, in other words, there are three time constants that can be extracted: one that compensates the short-term gain collapse immediately following the pulse, but fails to compensate the long-term gain collapse; one that compensates the long-term gain collapse, but fails to compensate the short-term gain collapse; and one that balances the compensation between the two time scales, but fails to compensate either of them without severely overcompensating (overshooting) the long-term gain collapse. For reference, Figure 4.11 also shows the response of the variable-time-constant ACC to a 30 dBm pulse (from Figure 4.10).

4.6 Two-Tone Response Compensation

In this section we explore the second set of measurements that were made to verify the ability of our ACC to compensate the long-term memory effects caused by charge-trapping phenomena in GaN HEMT-based PAs. In short, we measured the steady-state response of a GaN HEMT-based PA to a series of two-tone RF excitations with increasing tone frequency separation and observed a decrease in the small-signal gain as the tone separation increased. We then repeated the same procedure with the ACC connected to the PA and verified that the small-signal gain was constant regardless of the tone separation. This frequency-domain method for the characterization of charge-trapping phenomena was first proposed in [99] and, as we established in Section 4.2, it is much stricter than the pulse-response method in terms of model structure and accuracy.

4.6.1 Setup Calibration

The calibration of the laboratory setup followed the same procedure as that of the pulse-response measurements, albeit with a few differences. First, the input excitation used for the calibration was a large-signal two-tone signal. Second, the setup was predistorted using a third-order four-tap memory polynomial. A memory-polynomial model was used instead of the iterative error-integration algorithm described in Section 4.5 because it provided better linearization results in a shorter time. In fact, the error-integration algorithm was only used for the linearization of the pulsed excitations because the driver presented a slow transient inductive response to the pulses, and its compensation would have required a model with an extremely large sample memory depth (assuming a FIR memory structure). Since the two-tone excitations are measured in steady state, a memory polynomial proved to be sufficient for the measurements detailed in this section.

4.6.2 Measurement Procedure

After the setup was calibrated, the $V_{GS}(G_{SS})$ map required for the extraction of the parameters of the ACC was measured as explained in Section 4.5.2. Then, the PA was biased in class B and its steady-state response to a series of two-tone excitations was measured. These measurements were done first with a constant-voltage source biasing the PA (without the ACC), and then with the ACC connected to the PA (after its parameters had been extracted). The two-tone input envelopes had a frequency separation that ranged from 1 Hz to 100 kHz and a peak power that ranged from 24 dBm to 29 dBm.

In order to accommodate the record-length limitations of the VSG and VSA, the generated and captured signal envelopes were sampled at different sampling frequencies. Depending on the two-tone frequency separation, the sampling frequencies ranged from 5 kHz to 200 MHz. Moreover, in order to preserve an accurate sinusoidal waveform while accommodating the sampling-frequency limitations of the instruments, the sampling frequencies and record lengths were set so that the total number of unique envelope samples was always greater than or equal to 10^4. For instance, the two-tone envelope with a tone separation of 100 kHz was generated at 125.0125 MHz in order to obtain 10001 unique samples over four envelope periods; if it had been generated at 200 MHz (the maximum sampling frequency of the VSG), the number of unique samples would only have been 4000. This sampling scheme greatly improves the signal resolution at the small-signal portions of the continuously generated sinusoidal envelopes, which is beneficial for the extraction of the parameters of the ACC.

4.6.3 Circuit Parameter Extraction

The extraction of the parameters of the ACC was done as follows. First, each measured PA output time series was filtered in the frequency domain by computing the discrete Fourier

transform and selecting all tones whose frequency was an odd integer multiple of $\Delta f/2$, where Δf is the frequency separation of the input two-tone excitation. This resulted in the filtered PA output time series $y_f(t)$ defined in (4.9), where α_m and ϕ_m are the amplitude and phase of the selected tones and f_m is their corresponding frequency.

$$y_f(t) = \sum_{m=1}^{M} \alpha_m \exp(2\pi f_m t + \phi_m) \tag{4.9}$$

Computing $y_f(t)$ is useful for two reasons: first, it greatly reduces the noise of the PA output time series; second, it provides a mathematical equation for the measured PA output. This equation can then be used to align the output of the PA with its input excitation (i.e., remove the group delay of the measurement setup and PA) with a precision much better than one sampling period. Since $y_f(t)$ is periodic (it is the steady-state response of the PA) and its waveform is that of a distorted sinusoid, then time alignment can be done by finding the instant t_0 at which $|y_f(t)|$ is minimum and declaring it as the zero-phase instant. To obtain t_0 we used a multiple-start nonlinear least-squares optimization algorithm. The filtered PA output signal aligned to the PA input signal is then $y_a(t)$, defined in (4.10).

$$y_a(t) = y_f(t - t_0) \tag{4.10}$$

Having filtered and aligned the PA output to the PA input, the gain $g(t)$ of the PA can then be accurately calculated as in (4.11), where $x(t)$ is the envelope of the input two-tone signal.

$$g(t) = \left|\frac{y_a(t)}{x(t)}\right| \tag{4.11}$$

The small-signal gain g_{ss} was then obtained by evaluating $g(t)$ at an instant t_{ss} where the PA input can be considered a small-signal excitation. Since the $V_{GS}(G_{SS})$ map was obtained in the preliminary measurements for a small-signal CW input of −10 dBm, then it is convenient that t_{ss} be the instant at which the input excitation has an amplitude of −10 dBm. In general, g_{ss} is given by (4.12), where V_{ss} is the small-signal level and V_{pk} is the peak amplitude of the two-tone input (in linear units).

$$\begin{aligned} g_{ss} &= g(t_{ss}), \\ \text{where } t_{ss} &= \frac{1}{\Delta f}\left[1 - \frac{1}{\pi}\arcsin\left(\frac{V_{ss}}{V_{pk}}\right)\right] \end{aligned} \tag{4.12}$$

Finally, the compensation voltage ΔV_{GS} that cancels out the virtual back gate voltage at time t_{ss} was estimated by interpolating g_{ss} over the $V_{GS}(G_{SS})$ map. This was done for all measurements across all two-tone frequency separations Δf, resulting in a $\Delta V_{GS}(\Delta f, t_{ss})$ profile. This frequency-domain profile was then used to extract the parameters of the trapping model of the ACC by minimizing the MSE between the measured $\Delta V_{GS}(\Delta f, t_{ss})$ profile and the one generated by the trapping model using the CMA-ES optimization algorithm. The resulting parameters are listed in Table 4.2.

Table 4.2 Two-tone response compensation parameters.

P_{pk}	R_0	R_1	R_2	R_3	V_2	V_3
24 dBm	91 Ω	9.1 MΩ	330 kΩ	220 kΩ	24 mV	24 mV
26 dBm	91 Ω	9.1 MΩ	330 kΩ	220 kΩ	30 mV	30 mV
27 dBm	91 Ω	7.5 MΩ	1.1 MΩ	390 kΩ	33 mV	34 mV
28 dBm	91 Ω	7.5 MΩ	1.1 MΩ	390 kΩ	24 mV	36 mV
29 dBm	91 Ω	7.5 MΩ	1.1 MΩ	390 kΩ	23 mV	25 mV

4.6.4 Compensation Results

After extracting the parameters of the charge-trapping model, these were programmed into the ACC by soldering the required resistors (R_0–R_3) and setting the breakpoint voltages (V_2 and V_3) with an external power supply. Then, the ACC was connected to the PA and the following results were obtained.

Figure 4.12(a) shows the $g_{ss}(\Delta f)$ profiles obtained from the steady-state response of the uncompensated GaN HEMT-based PA to a series of two-tone excitations with increasing two-tone frequency separation and for different peak input powers (24 dBm to 29 dBm). These results can be explained through our understanding of the charge-trapping mechanism as follows. As the amplitude of the sinusoidal input envelope rises from zero to its peak value, the GaN HEMT accumulates charge in trapped states. Furthermore, as the amplitude descends from the peak toward zero, the trapped charge is released. If the envelope is much slower than the time constants associated with the charge-emission process (i.e., for low values of Δf), then all trapped charge has been released by the time the envelope has descended from its peak amplitude to a small-signal level, and the small-signal gain remains unchanged. However, if the envelope is fast enough (i.e., for sufficiently large values of Δf), then some charge remains trapped by the time the envelope has descended from its peak amplitude to a small-signal level, resulting in a decrease of the small-signal gain. If the input envelope is much faster than the charge-emission process (i.e., for very large values of Δf), then barely any charge is released during the descent of the input envelope from its peak amplitude to a small-signal level, resulting in a saturated decrease of the small-signal gain. Naturally, as was demonstrated with the pulse-response measurements in Section 4.5, if the peak power of the input envelope is increased, then more charge is accumulated and the collapse of the small-signal gain is greater.

Figure 4.12(b) shows the $g_{ss}(\Delta f)$ profiles of the same GaN HEMT-based PA, but while being compensated by the ACC. This figure reveals that the frequency-dependent small-signal gain collapse experienced by the PA due to charge-trapping phenomena is completely compensated by the ACC.

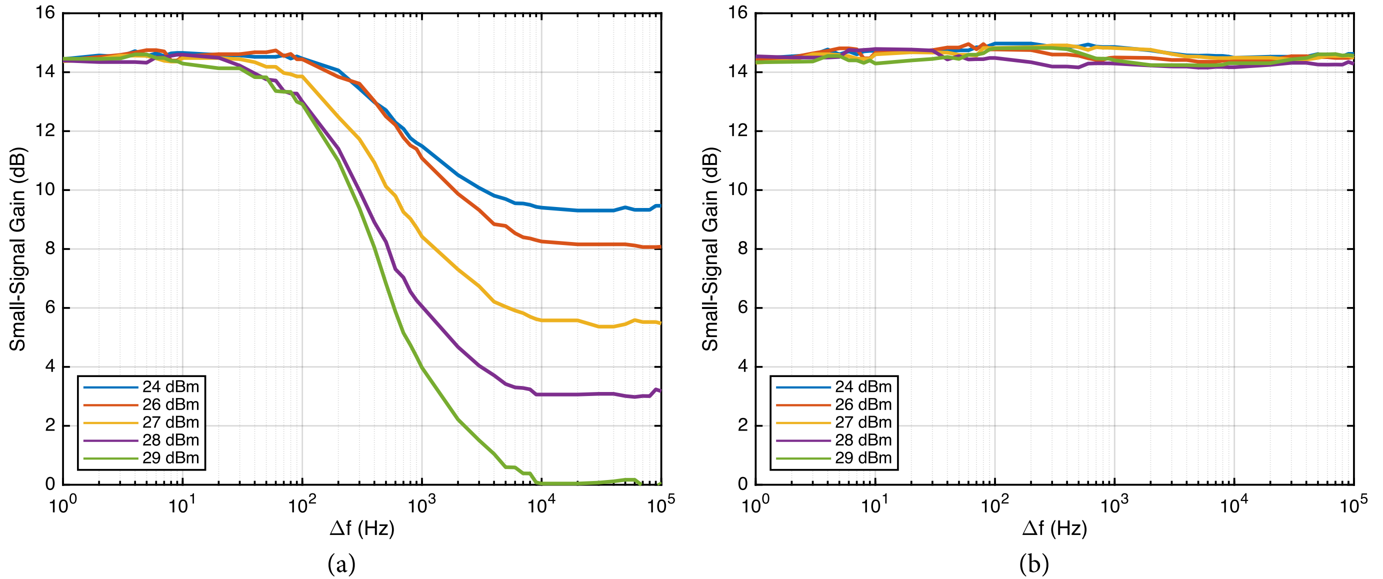

Figure 4.12 Two-tone response of the GaN HEMT-based PA (a) without compensation and (b) with compensation using our ACC.

4.7 Self-Biasing Compensation

In this section we describe the third set of measurements that were made to verify the ability of the ACC to compensate the long-term memory effects caused by charge-trapping phenomena in GaN HEMT-based PAs. These measurements serve as the definitive validation of the working principle of the ACC, since they provide the most conclusive evidence of the back-gating mechanism the ACC aims to compensate [140].

In this test, we measured the steady-state response of the PA (with and without compensation) to a series of two-tone excitations with a peak envelope power increasing from 0 dBm to 29 dBm. The tone separation was constant and equal to 100 kHz, which was shown in Figure 4.12 to be much faster than the emission process of the GaN HEMT. The setup calibration was done as in Section 4.6.1, and the parameters of the ACC were the ones extracted in Section 4.6.3 for the small-signal gain profile with a peak input power of 29 dBm. After measuring the response of the PA, its gain was computed as in Section 4.6.3 and the following results were obtained.

Figure 4.13(a) illustrates the dynamic gain-versus-input-power profile of the uncompensated PA. These results can be explained through our understanding of the charge-trapping mechanism as follows. During the first measurements, while the peak power of the input envelope is low, the gain profile is flat in accordance with the class-B biasing of the PA. However, as the peak input power increases, an increasing amount of charge is captured by deep-level traps in the GaN HEMT. Since there is not enough time during the 10 μs period of the input envelope amplitude for a significant amount of captured charge to be emitted, there is an accumulation of trapped charge that contributes to the depletion of

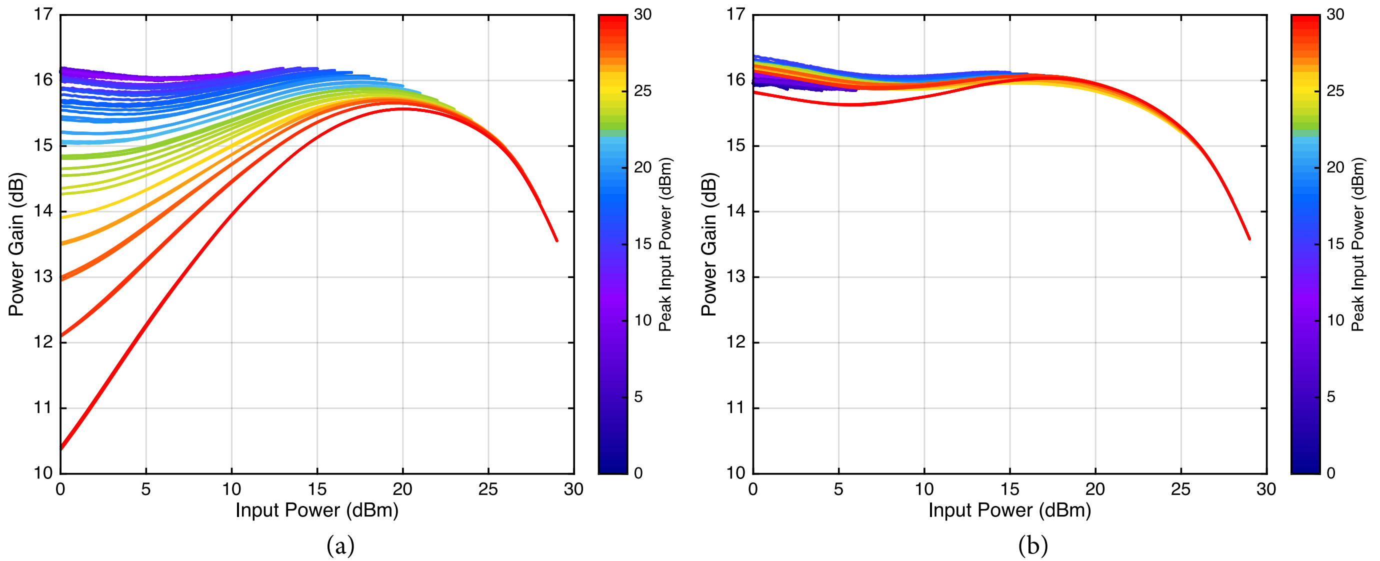

Figure 4.13 Dynamic gain profile of the GaN HEMT-based PA (a) without compensation and (b) with compensation using our ACC.

the GaN channel, reducing the gain of the PA. As discussed throughout this chapter, this accumulation of trapped charge can be likened to the charging of a virtual back gate that biases the GaN HEMT. Accordingly, the gain profile of the PA is gradually shifted toward an increasingly deep class-C profile as the peak input power increases. In the end, the PA had effectively biased itself from class B to class C and demonstrated a gain expansion of over 15 dB.

Figure 4.13(b) illustrates the dynamic gain profile of the PA when being compensated by the ACC. Evidently, the ACC corrected the gain collapse caused by the charging of the virtual back gate of the GaN HEMT, proving not only that the ACC is able to compensate the self-biasing of GaN HEMT-based PAs, but also that the charge-trapping compensation model it implements is congruent with the physical behavior of GaN HEMTs.

4.8 5G NR Linearization

With emerging standards for cellular communications such as 5G NR, the deployment of small-cell and massive-MIMO technology to enhance network coverage and capacity is expected to place new restrictions on the power available for the linearization of each individual PA in a transmitter array. Thus, existing DPD algorithms for the linearization of GaN HEMT-based PAs, which are very power-demanding and do not scale with antenna count due to their outstanding complexity, will necessarily be phased out in favor of simpler, more efficient linearization schemes. Moreover, the flexible frame structure specified in 5G NR for the efficient multiplexing of services with diverse requirements—e.g., low latency and high reliability (short subframes), or delay tolerance and high spectral efficiency (long subframes)—, as well as the dynamic TDD scheme for access to the air interface, will excite

long-term memory with a greater variety of time scales in transmitting PAs. This places even more emphasis on the accurate modeling and compensation of the long-term memory effects experienced by GaN HEMT-based PAs.

Following this rationale, in this section we demonstrate that our proposed ACC can be used in conjunction with a low-complexity DPD model to linearize a GaN HEMT-based PA for 5G NR communications. Moreover, we demonstrate that our proposed variable-time-constant charge-trapping model is especially suited for GaN HEMT-based PAs under highly variable charge-trapping conditions, and that the modeling of the charge-emission process with a fixed time constant may not be sufficiently accurate for the linearization of GaN HEMT-based PAs for 5G NR communications.

4.8.1 Measurement Procedure

After the absolute power of the setup detailed in Section 4.4 was calibrated and the GaN HEMT-based PA was biased in class B, the PA was linearized under three different configurations: with a DPD, with a DPD and an ACC with one fixed emission time constant (as in Chapter 3 and [J2]), and with a DPD and the proposed ACC with a state-dependent variable emission time constant (with three conductance branches). In all cases, the DPD was a simple fifth-order one-tap memory polynomial. Naturally, while the structure of the DPD was maintained between each test, its coefficients were different for all tests.

The PA input test signal was based on the NR-FR1-TM2 waveform defined in a 3GPP technical specification for 5G NR base station conformance testing [149]. This signal, whose envelope is illustrated in Figure 4.14, was generated for TDD applications and includes an additional synchronization signal burst at the start of each radio frame (every 10 ms). By featuring different time-varying levels of average signal amplitude, we expect this waveform to reveal the complex dynamics of charge trapping in the form of a slow dynamic residual nonlinearity that persists despite the DPD linearization. Moreover, by compensating the long-term memory induced by charge-trapping phenomena with the ACC, we expect the residual nonlinearity to be reduced. The PA input signal had a bandwidth of 20 MHz and a peak available power of 30 dBm, which led to an initial gain compression of 2.4 dB.

4.8.2 Compensation Results

Figure 4.15 illustrates the spectra of the PA input, the PA output without linearization, and the PA output after the three different linearization tests: with the adopted 5th-order 1-tap memory-polynomial DPD, with the same DPD complemented by an ACC with a fixed emission time constant, and with the same DPD complemented by our proposed ACC with a state-dependent variable emission time constant. As the figure reveals, this simple DPD is not capable of linearizing the PA by itself up to an acceptable level due to its limited memory depth. In reality, for any DPD model to be able to successfully linearize a GaN HEMT-

based PA excited by a waveform with a similar or higher level of long-term variability, it would either require a memory depth in the order of 10^3 to 10^6 samples or a highly complicated (and nonscalable) long-term formulation such as the one in [13]. Figure 4.15 also demonstrates that the fixed-time-constant ACC provided some improvement in the suppression of out-of-band emissions over the DPD-only linearization—an improvement of 6.5 dB, which was very consistent with the results obtained in Chapter 3 and [J2]. Finally, this reported experimental data also confirms that the proposed variable-time-constant ACC achieves the best level of linearization, over 15 dB better than the DPD-only scheme.

Figure 4.16 illustrates the temporal evolution of the per-symbol error-vector magnitude (EVM) obtained for each test, in both root mean square (RMS) and maximum values. This figure is particularly effective at revealing the slow dynamic residual nonlinearity of the GaN HEMT-based PA that remains even after the linearization with the DPD unit, in Figure 4.16(a), and the slightly better linearization with the DPD unit and the fixed-time-constant ACC, in Figure 4.16(b). More specifically, it evidences the sudden—but transient—increase in the level of nonlinearity during the small-signal instants following large-signal input excitations, as discussed at length throughout this thesis. Moreover, Figure 4.16(c) demonstrates that the proposed variable-time-constant ACC is able to completely compensate the long-term memory effects of the PA and provide, in conjunction with the low-complexity DPD unit, exceptional levels of linearity and signal quality. The overall EVM was 2.4 % RMS and 16.1 % peak for the test with only the DPD unit, 1.6 % RMS and 10.8 % peak for the test with the DPD unit and the fixed-time-constant ACC, and 0.9 % RMS and 3.6 % peak for the test with the DPD unit and the proposed variable-time-constant ACC.

Finally, we measured the PAE of the GaN HEMT-based PA with and without using the proposed ACC. For the 5G NR linearization tests detailed in this section, the results were an average PAE of 6.9 % without the ACC and a PAE of 6.5 % with the ACC. Since the obtained PAE was so low because of the very large peak-to-average power ratio (PAPR) of the 5G NR test signal, we repeated the measurement of the PAE for a different input

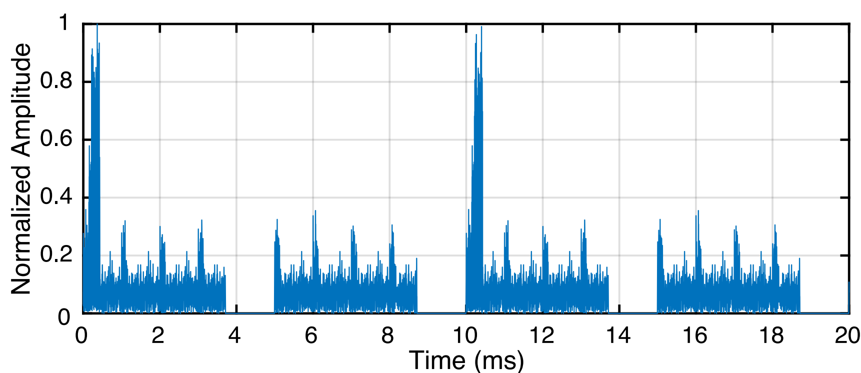

Figure 4.14 Envelope of the PA input signal.

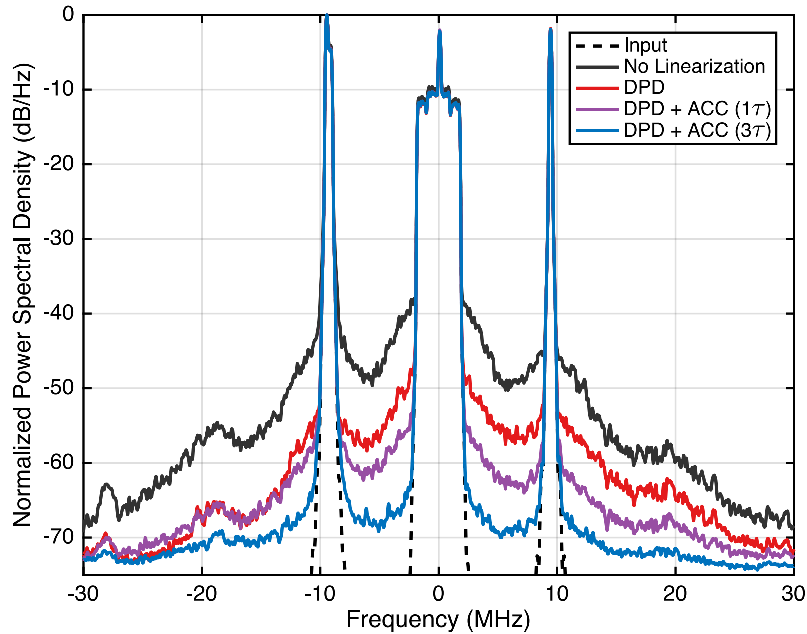

Figure 4.15 Spectra of the PA input, the PA output without linearization, the PA output with linearization using a simple memory-polynomial DPD, the PA output with linearization using this same DPD and an ACC with a fixed emission time constant, and the PA output with linearization using the DPD and our proposed ACC with a state-dependent variable emission time constant.

excitation (and without the DPD unit—only the PA by itself, or the PA when compensated by the ACC) in order to rule out any observation problems that might have arisen from our initial choice of input excitation. Thus, we synthesized a frequency-flat multi-tone signal with a bandwidth of 20 MHz, a peak available power of 30 dBm, and a PAPR of 3 dB. The results were a PAE of 55.7 % without the ACC and a PAE of 55.8 % with the ACC. Finally, as a validity check, we measured the PAE for a two-tone input excitation with a frequency separation of 100 kHz and a peak available power of 30 dBm. The results were a PAE of 55.2 % without the ACC and a PAE of 55.1 % with the ACC.

4.9 Conclusion

In this chapter we presented a charge-trapping model with a variable emission time constant and its implementation as a feedforward analog circuit for the compensation of long-term memory effects in GaN HEMT-based PAs. The behavioral nature of the adopted model allows it to capture both charge-trapping and electro-thermal long-term memory phenomena simultaneously and grants it the advantage of being simple to implement as an analog electronic circuit. Compared to previous models with a fixed emission time constant, the proposed model and its analog implementation provide the ability to more accurately predict and compensate the dynamic trapping state for a wider range of time

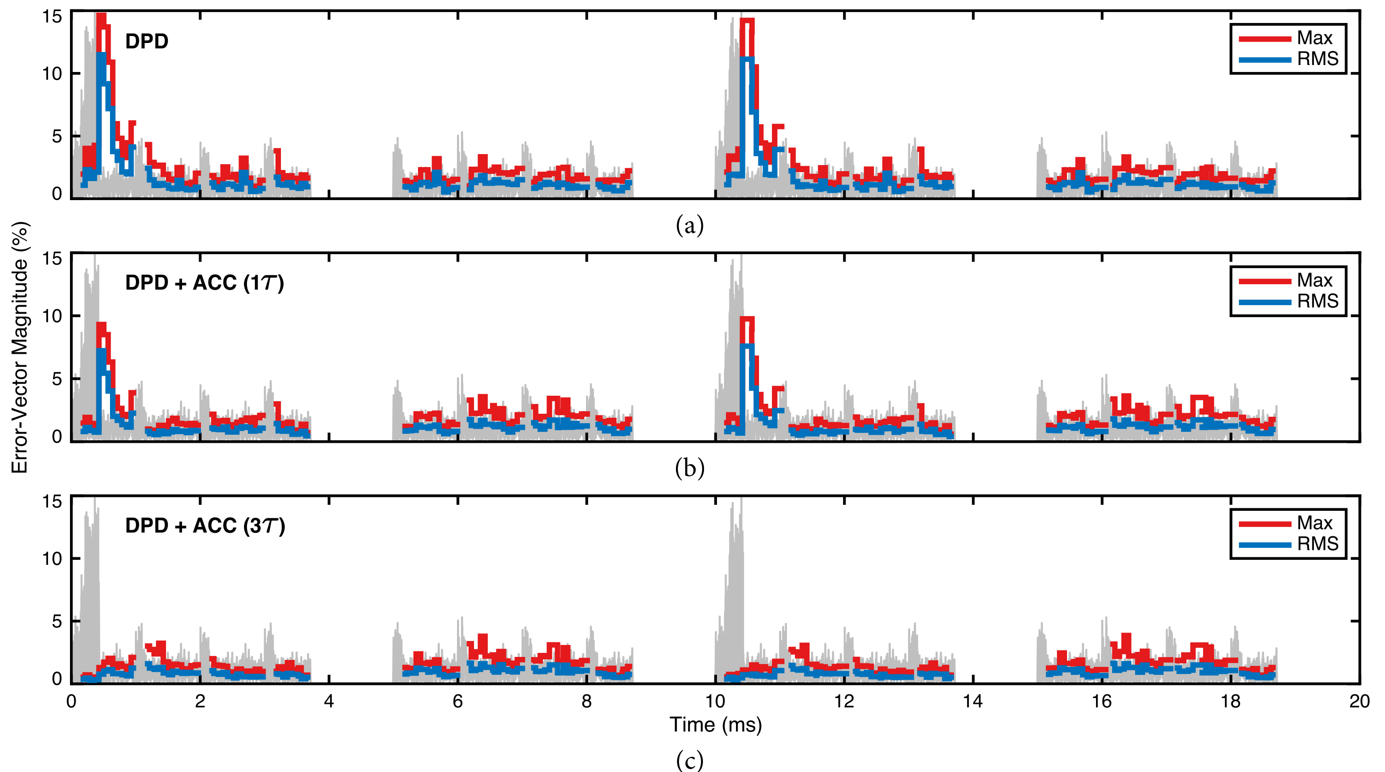

Figure 4.16 Temporal evolution of the EVM of the PA output after (a) linearization using a simple memory-polynomial DPD unit, (b) linearization using this same DPD unit and an ACC with a fixed emission time constant, and (c) linearization using the DPD unit and our proposed ACC with a state-dependent variable emission time constant. In the background, a representation of the input envelope is shown for visual reference.

scales (from microseconds to milliseconds and beyond) and larger PA signal excursions (where the variability of the emission time constant is greater). This is especially relevant for GaN HEMT-based PAs targeted for 5G NR communications, which feature very flexible frame structures with highly variable signal durations. Moreover, the proposed ACC allows for the adaptation of its parameters and the adjustment of its compensation dynamics to better accommodate the operating conditions of the GaN HEMT-based PA.

In order to demonstrate and validate the effectiveness of the model and the ACC, we performed three independent sets of measurements: the transient pulse response, the two-tone response, and the dynamic gain profile of a 2.2 GHz PA based on a 15 W 28 V GaN HEMT. All of these observations were consistent in demonstrating the desired compensation of the long-term PA dynamics. Finally, we demonstrated a hybrid analog/digital 5G NR linearization scenario where our proposed ACC was used in conjunction with a low-complexity memory-polynomial DPD unit to successfully linearize a GaN HEMT-based PA. When compared to a DPD-only linearization scheme, the introduction of our proposed ACC led to an improvement of the out-of-band emissions by over 15 dB and an improvement of the peak EVM by over 10 p.p. at essentially no cost to the PAE of the GaN HEMT-based PA.

CHAPTER 5

Pulse-to-Pulse Instability of GaN HEMT-Based PAs

Synopsis — In this chapter we describe a method for compensating the pulse-to-pulse instability caused by thermal and charge-trapping phenomena in GaN HEMT-based PAs. The method consists in dynamically modulating the gate–source voltage of the HEMT in order to offset its dynamic threshold voltage variation. The compensation signal is obtained iteratively based on measured data. This method was verified with a pulsed radar waveform for moving target indication on a GaN HEMT-based PA, achieving an improvement of the peak output power of 0.85 dB and an improvement of the pulse-to-pulse amplitude stability of over 20 dB. The contents of this chapter have been published in [C3] and [J3].

5.1 Introduction

Modern radars use bursts of pulsed RF electromagnetic waves to irradiate a region of interest and detect the delayed reflections from targets in that region. Pulsed waveforms are especially interesting for moving target indication (MTI)—the distinction between moving targets (e.g., an aircraft) and stationary targets (e.g., the sea)—because equal transmitted signals result in equal reflected signals from stationary targets [150]. Thus, by analyzing the variations between successive pulses in the received waveforms, moving targets can be detected while stationary targets, or clutter, are suppressed [14].

Considering that MTI consists in analyzing the variations between the received pulses, all pulse variations caused by the radar system itself (as opposed to a moving target) negatively impact the suppression of clutter and may lead to false detections. Pulse-to-pulse stability, a measure of the envelope amplitude and phase variations between the transmitted pulses, is therefore a critical parameter for characterizing the performance of a pulsed radar.

Because pulsed radars require very high transmission power levels, GaN HEMT technol-

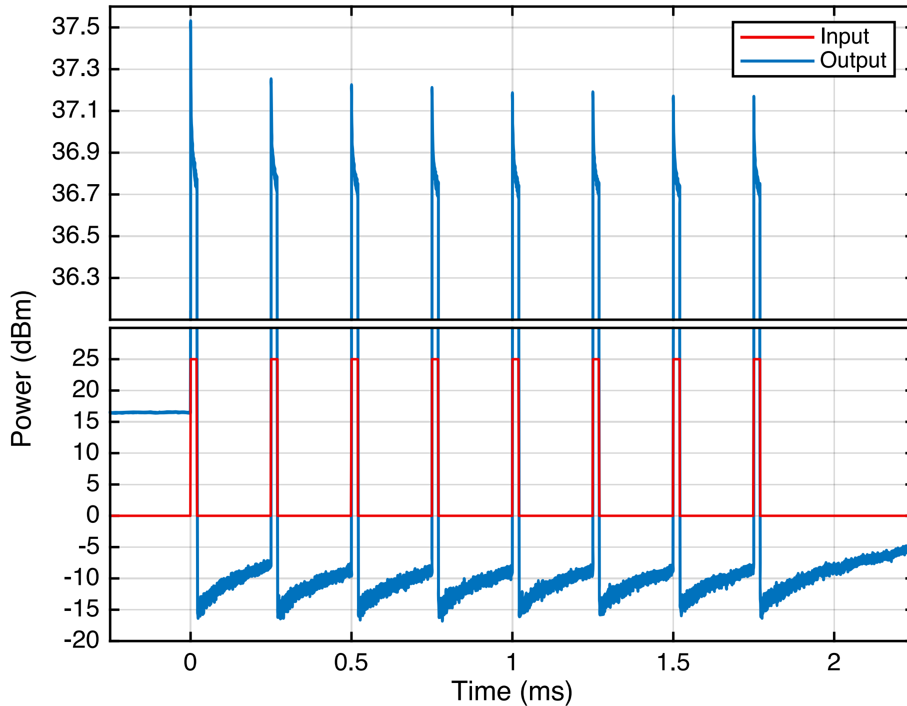

Figure 5.1 Measured response of a GaN HEMT-based PA to a burst of square pulses with equal amplitude.

ogy constitutes an appealing solution for their solid-state implementation [151]. However, it is well known that GaN HEMT-based PAs suffer from long-term memory effects caused by thermal and charge-trapping phenomena that severely deteriorate their linearity and, more specifically, their pulse-to-pulse stability [152]. To address this issue, in this chapter we present a method for compensating these effects and improving the pulse-to-pulse amplitude stability of GaN HEMT-based PAs.

5.2 Pulse-to-Pulse Stability

The typical response of a GaN HEMT-based PA to a burst of square pulses with equal envelope amplitude is presented in Figure 5.1. Note how the pulses output by the PA are far from being square and not of equal amplitude. This is due to charge-trapping phenomena that dynamically change the threshold voltage of the HEMT (and consequently its gain) over three very distinct time scales: the pulse duration (20 µs), the pulse repetition period (250 µs), and the burst repetition period (7 ms).

During the on-times of the pulses in Figure 5.1, the high voltage swings at the drain of the HEMT cause its traps to charge at a very fast rate. This produces an effect similar to a dynamic variation of the HEMT's threshold voltage [139], which explains the drops in output power. Moreover, during the off-times of the pulses, the traps are allowed to discharge and the threshold voltage of the HEMT begins its recovery toward its initial state.

This is why the small-signal output is always ascending and why the output power at the beginning of each pulse's on-time is always higher than the output power at the end of the previous pulse's on-time.

As evidenced in Figure 5.1, the long-term memory effects caused by charge-trapping phenomena have several undesirable consequences: extreme nonlinearity, the loss of peak output power (over 0.8 dB in this case), and poor pulse-to-pulse amplitude stability—the output power varies not only within each pulse, but also within a burst from pulse to pulse and even between different bursts.

The pulse-to-pulse amplitude stability S_A of B pulse bursts, each composed of P pulses, can be defined as in (5.1), where $x_{p,b}$ denotes the complex envelope of the p-th pulse of the b-th burst, $|x_0|$ denotes the peak amplitude over all pulses (for normalization), and n denotes sampled time. This metric quantifies the amplitude variations of all pulses across all bursts. Therefore, as a measure of variation (or error), a lower value of S_A implies a greater stability (less error).

$$\begin{aligned} S_A(n) &= \frac{1}{P-1} \sum_{p=1}^{P-1} \left[\overline{X_{p+1}}(n) - \overline{X_p}(n) \right]^2, \\ \text{where } \overline{X_p}(n) &= \frac{1}{B} \sum_{b=1}^{B} \frac{|x_{p,b}(n)|}{|x_0|} \end{aligned} \tag{5.1}$$

5.3 Compensation Method

In order to compensate the pulse-to-pulse amplitude instability of GaN HEMT-based PAs, the proposed method consists in varying the transconductance of the HEMT by applying a variable gate–source voltage $V_{GS} = V_{GG} + \Delta V_{GS}$, where V_{GG} is the constant gate bias voltage that sets the quiescent drain current and ΔV_{GS} is the compensation signal. Different transconductance modulation techniques have been shown to compensate other nonlinear effects caused by charge-trapping phenomena in GaN HEMTs [J2].

To determine the compensation signal, we devised the following methodology. First, the small-signal (Figure 5.2(a)) and large-signal (Figure 5.2(b)) gains of the PA were measured as a function of the gate–source voltage. These measurements provide a mapping between the instantaneous PA output power level and the variation of the HEMT's threshold voltage under small-signal or large-signal excitations. Then, the response of the PA to a pulse train was measured and the corresponding variation of the threshold voltage was computed by linearly interpolating the measured small-signal and large-signal gain profiles at query points determined by the measured PA output response. Finally, the compensation signal was obtained by inverting the sign of the threshold voltage variation.

By applying this compensation signal to the gate of the HEMT, the variation of the threshold voltage is counteracted by an opposite variation of the gate–source voltage. This

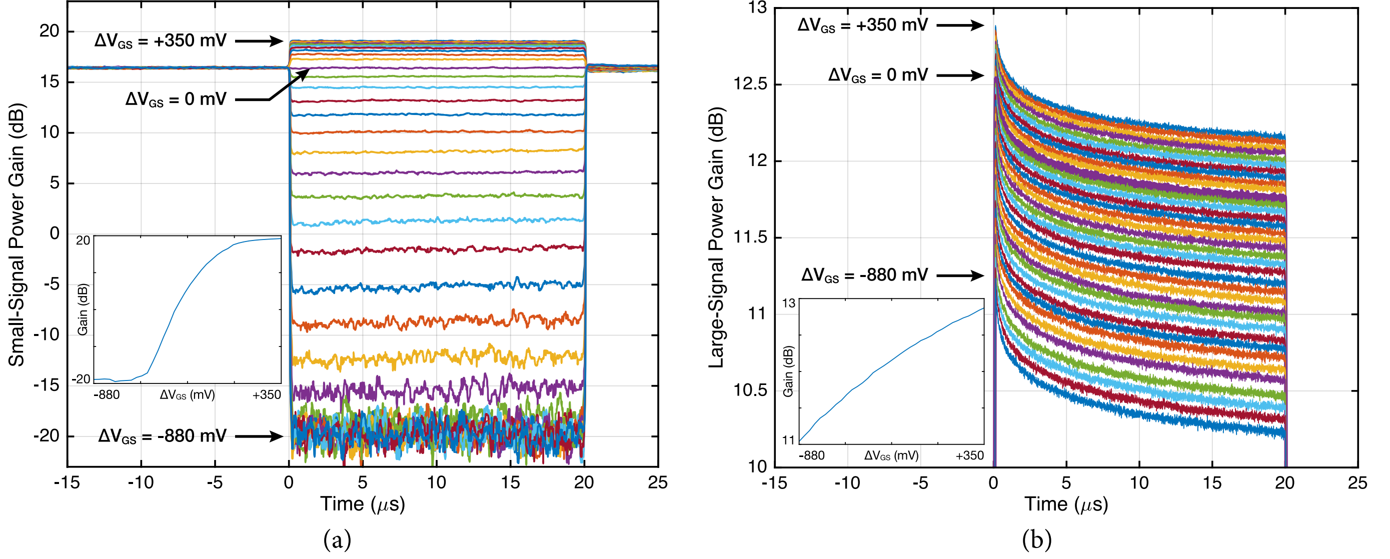

Figure 5.2 Variation of (a) the small-signal power gain and (b) the large-signal gain of the GaN HEMT-based PA for various values of the gate–source voltage. Also, as plot inserts, the actual (a) G^{SS} and (b) G^{LS} gain profiles used for interpolation.

results in a new output response (to the same pulse train) that is much more linear than the first and thus features a much improved pulse-to-pulse amplitude stability. To further improve the pulse-to-pulse amplitude stability, we recalculated the compensation signal using the new output response of the PA and added the difference to the previous compensation signal. This process is summarized in Algorithm 1, where G^{SS} and G^{LS} are the small-signal and large-signal gain profiles, ΔV_{GS}^{SS} and ΔV_{GS}^{LS} are the corresponding gate–source voltage variations, and λ is an optional learning-rate parameter. Typically, only 1 to 5 iterations are necessary for an improvement of 20 dB.

Algorithm 1 Determination of the compensation signal ΔV_{GS}

Input: $\Delta V_{GS}^{SS}, G^{SS}, \Delta V_{GS}^{LS}, G^{LS}, PA_{in}$
Output: ΔV_{GS}

1: $\Delta V_{GS} := 0$
2: **while** necessary **do**
3: Measure PA_{out} in response to PA_{in} and ΔV_{GS}
4: ΔV_T := interpolation of $(x, y) = \left(\{G^{SS}, G^{LS}\}, \{\Delta V_{GS}^{SS}, \Delta V_{GS}^{LS}\}\right)$ over $x = PA_{out}/PA_{in}$
5: $\Delta V_{GS} := \Delta V_{GS} - \lambda \Delta V_T$
6: **end while**
7: **return** ΔV_{GS}

5.4 Implementation Details

The laboratory setup used to measure and compensate the pulse-to-pulse amplitude stability of a 1.6 GHz 15 W GaN HEMT-based PA biased in class B ($I_{DQ} \approx 2\ \%\ I_{DSS}$) is illustrated in Figure 5.3 and pictured in Figure 5.4. The instrumentation consisted of a Rohde & Schwarz SMU200A VSG for the generation of the PA input signal, a Tektronix AWG70002A arbitrary waveform generator (AWG) for the generation of the compensation signal, and a Rohde & Schwarz FSW VSA for the measurement of the PA output signal.

In order to successfully reproduce this work, it is critically important to ensure the repeatability of all measurements. This entails the setting of an initial thermal state by (1) biasing the HEMT at the desired quiescent point, (2) preheating the HEMT using a continuous train of large-signal pulses (for 3 minutes in our case), (3) waiting for the "hot" quiescent point to settle (1 minute in our case), and (4) adjusting the bias voltage to match the desired quiescent point. After setting the HEMT to this temperature-stable state, we ensured that all measurements were performed at the same charge-trapping state by using the sequencing capabilities of the VSG: contrary to usual practice, instead of continuously repeating a signal (e.g., one pulse, or a burst of pulses), the VSG was set up so that it would generate one single instance of that signal and immediately fall back to outputting a constant small-signal level. This guaranteed that two consecutive measurements always started at the same charge-trapping state, since there was enough time for the traps to discharge between the two measurements.

Another important aspect is the generation of the compensation signal by the AWG. For it to mimic the described behavior of the VSG, we connected one of the VSG's marker outputs to one of the AWG's external trigger inputs and set the AWG to single-shot external-trigger mode. Finally, we advanced all AWG output waveforms (by 2475 ns in our case) to ensure that both the VSG and the AWG provided synchronous excitations to the PA.

For the measurement of the PA output, a marker signal from the VSG should be connected to the trigger input of the VSA. Moreover, the VSA should be instructed to start the signal capture before the output of the VSG is enabled. Only this way can we be sure to measure the start of the very first pulse output by the PA: the one that is guaranteed to have no (additional) charge-trapping effects.

An inverting voltage-adder circuit was used to combine the constant gate bias voltage V_{GG} with the compensation signal ΔV_{GS}, resulting in the compensated gate–source voltage V_{GS}. The inverting topology of the voltage-adder is necessary to isolate the dc-coupled output of the AWG and the V_{GG} voltage source. Also, the typical large-value bypass capacitor at the gate bias terminal of the PA must be removed, otherwise the modulated V_{GS} would be bypassed to ground.

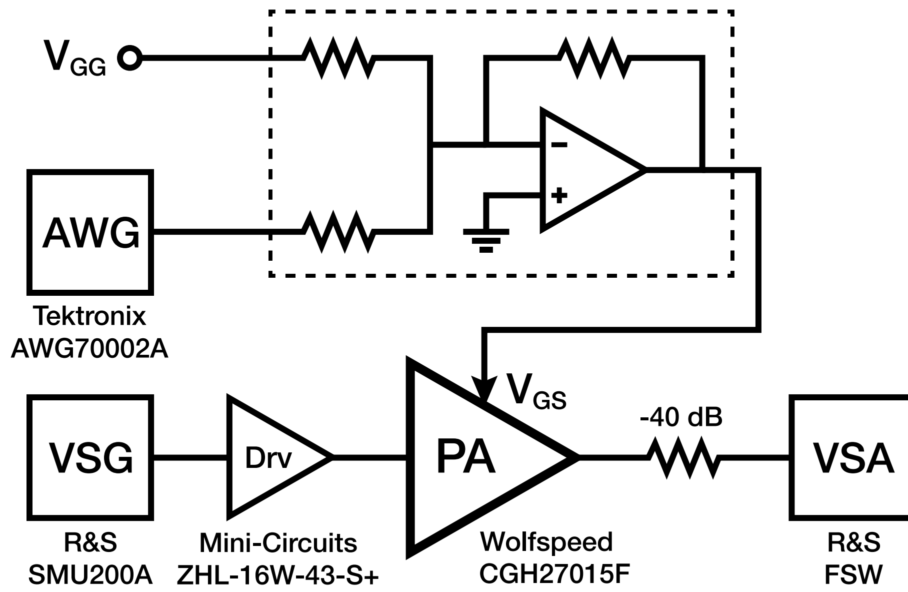

Figure 5.3 Diagram of the laboratory setup.

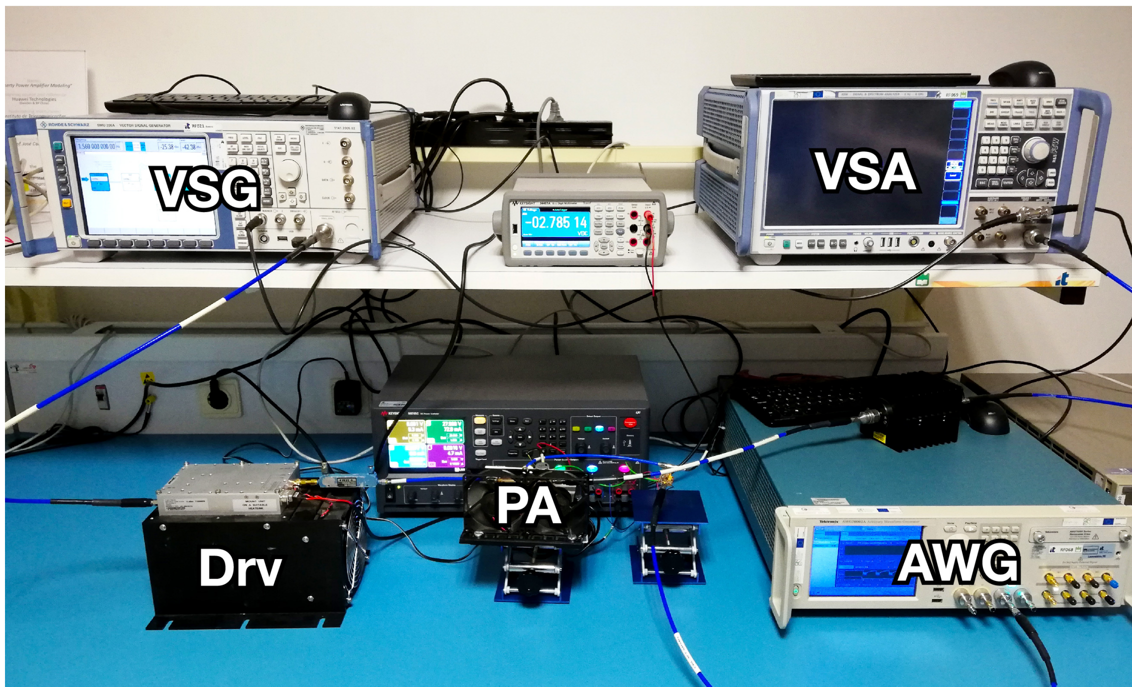

Figure 5.4 Photograph of the laboratory setup.

5.5 Results

Figure 5.2(a) and Figure 5.2(b) illustrate the measurements made for the extraction of the small-signal and large-signal gains of the PA as a function of the gate–source voltage. In order to obtain the former, the VSG was set up to output a constant power level of 0 dBm and the AWG was set up to output single pulses with a duration of 20 µs and varying amplitudes. In order to obtain the latter, the VSG was set up to output single pulses with a duration of 20 µs, a low-level of 0 dBm, and a high-level of 25 dBm; the AWG was set up as in the first set of measurements.

As these figures reveal, the gain of the PA varies during the duration of the pulses: it increases for the small-signal test set and decreases for the large-signal test set. As explained, this is due to the discharging and charging of the HEMT's traps and the consequent decrease or increase of the threshold voltage. Thus, the true gain of the PA (under the initial conditions established before) corresponds to the very first instant of each pulse, when the traps are "discharged" (they were actually charged to the state corresponding to a constant 0 dBm input at the biasing conditions of the PA).

After extracting the small-signal and large-signal gain profiles, the PA was submitted to an input signal that resembles those of pulsed radars: four bursts of eight pulses, with a pulse duration of 20 µs, a pulse repetition period of 250 µs, a burst repetition period of 7 ms, a low-level of 0 dBm, and a high-level of 25 dBm. After executing Algorithm 1, the compensation signal illustrated in Figure 5.5 was obtained and, as Figure 5.6 demonstrates, the PA was linearized.

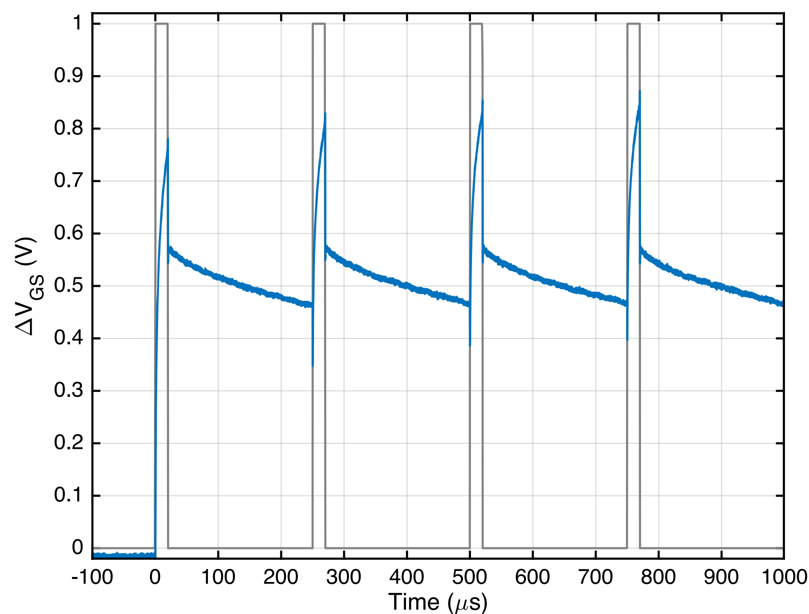

Figure 5.5 The first millisecond of the signal that compensates the pulse-to-pulse instability of the GaN HEMT-based PA. Also, in the background, a representation of the first four input pulses is shown for visual reference.

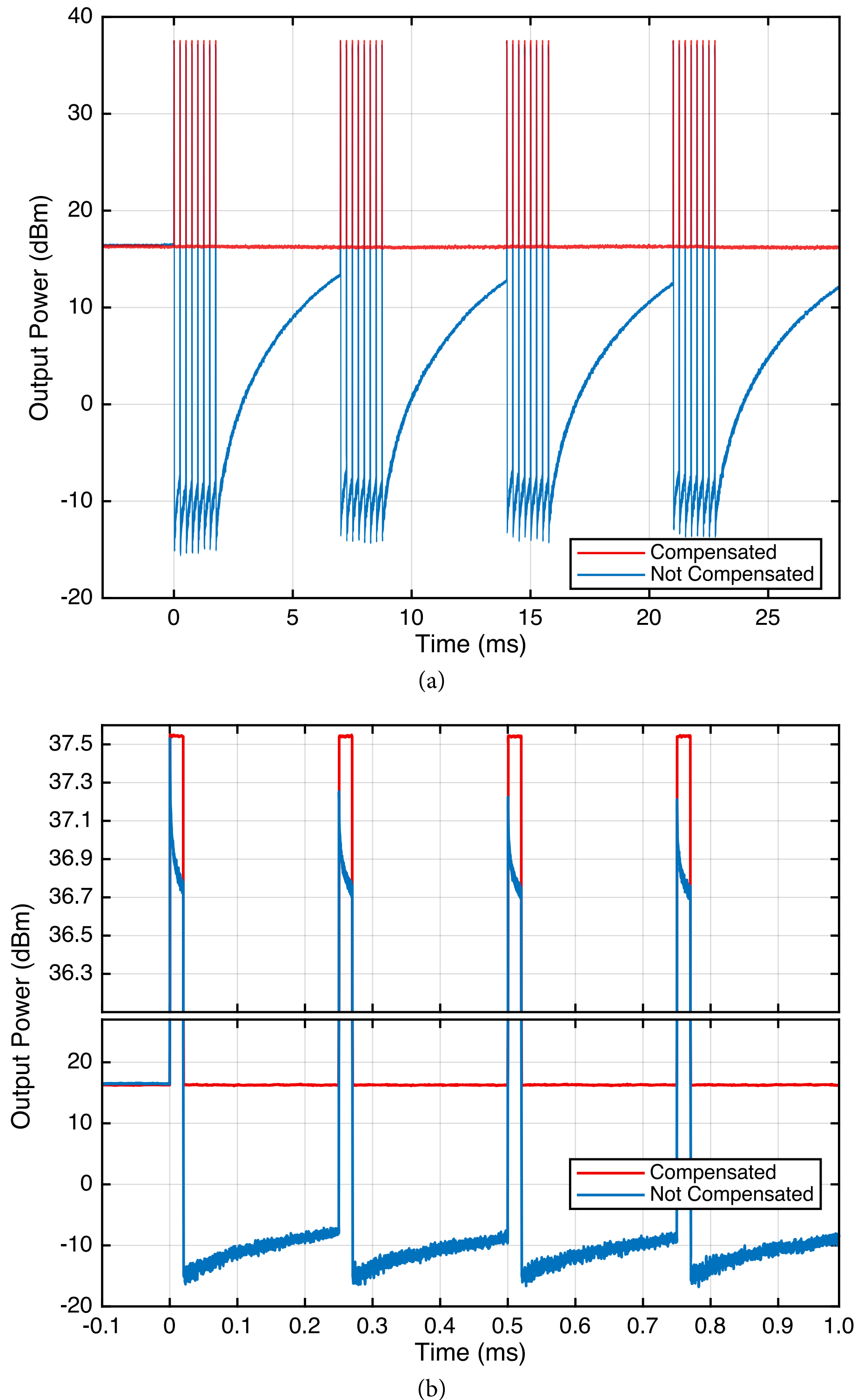

Figure 5.6 (a) Complete and (b) zoomed-in view of the compensated and uncompensated responses of the GaN HEMT-based PA to a pulsed waveform.

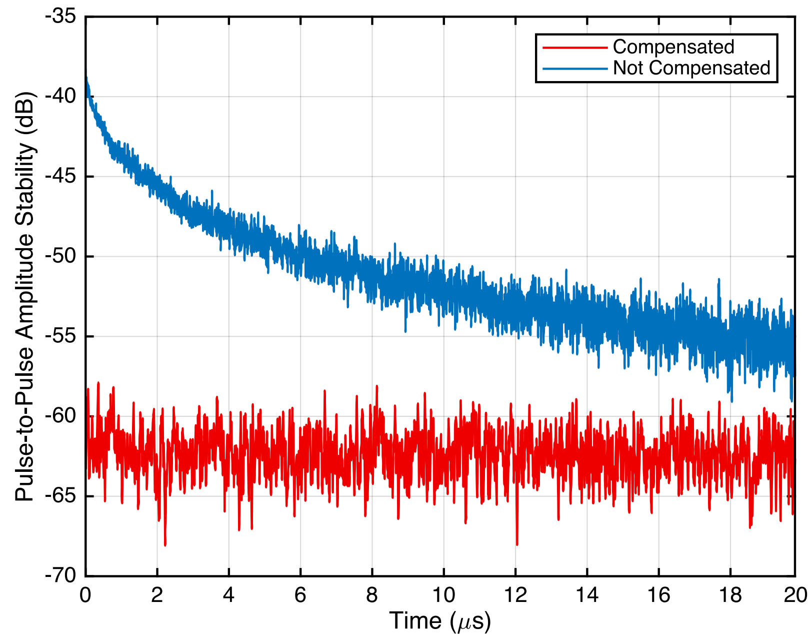

Figure 5.7 Pulse-to-pulse amplitude stability of the compensated and uncompensated responses of the GaN HEMT-based PA to a pulsed waveform.

Figure 5.7 shows the pulse-to-pulse amplitude stability of the uncompensated and compensated PA outputs over all 32 pulses. As evidenced, a greater than 20 dB improvement was obtained.

5.6 Conclusion

In this chapter we presented a method for compensating the pulse-to-pulse amplitude instability of GaN HEMT-based PAs for their incorporation in pulsed radars for MTI. The method consists in measuring the small-signal and large-signal gains of the PA and iteratively computing a compensation signal based on the distorted response of the PA to a pulsed input excitation. This compensation signal is then used to correct output power variations over all excitation time scales simultaneously: within each pulse, between pulses in a burst, and between different pulse bursts. Our method was demonstrated to improve the peak output power of a 15 W GaN HEMT-based PA by 0.85 dB and the pulse-to-pulse amplitude stability by over 20 dB.

In general, pulsed radar transmitters do not operate at back-off powers as in this chapter—they are either at full power or completely turned off. In this case, only the large-signal parts of the pulsed excitations need to be compensated, since there are no small-signal parts. This is a much simpler problem than the one explored in this chapter, as only one iteration of Algorithm 1 (with $\lambda = 1$) is required to obtain a compensation signal that massively improves the pulse-to-pulse amplitude stability. In fact, the determination of the compensation signal is only required to be iterative when there is both a large-signal

level and a small-signal level that need be compensated. This is because the compensation of the large-signal level leads to a significant increase in the amount of trapped charge, since the compensated output produces a larger drain voltage throughout the duration of the pulses (as illustrated in Figure 5.6(b)). As a result of this additional charge, the GaN HEMT self-biases toward a deeper class C, leading to a change in the small-signal recovery transients that is not accounted for by the (now out-of-date) compensation signal. It is, therefore, not possible to obtain (through this method) a compensation signal that linearizes both the large-signal and small-signal parts of a pulsed excitation in one single iteration. As we discussed, however, this is not an issue in more realistic pulsed radar transmitters.

While a given compensation signal is specific to the input signal for which it was extracted, simple solutions for a more generalized compensation strategy could be realized, e.g., a lookup table of compensation signals for various pulse duty cycles.

CHAPTER 6

Dynamic Self-Biasing Behavior of GaN HEMT-Based PAs

Synopsis — In this chapter we describe a method for the accurate characterization of the capture and emission dynamics of charge-trapping phenomena in GaN HEMT-based PAs using transient two-tone large-signal RF measurements. Then, we demonstrate that the accurate modeling of these phenomena is contingent on the capture process being described by a state-dependent variable time constant, rather than a fixed near-instantaneous time constant as is typically assumed. Finally, we present an analog electronic circuit that implements a piecewise-linear approximation of the SRH model for the compensation of the dynamic self-biasing behavior of GaN HEMT-based PAs.

6.1 Introduction

As reviewed in Section 2.3, several experimental procedures have been proposed for the characterization of charge-trapping phenomena and the extraction of the parameters of relevant models. Among these, the most prevalent are based on pulsed [87]–[89] or double-pulsed [90] I-DLTS, low-frequency admittance measurements [93], and pulsed-RF active load-pull measurements [98]. Since these characterization procedures are performed on the discrete HEMT and require very specialized equipment, alternative methods targeting fully assembled GaN HEMT-based PAs have also been proposed. These include pulse-modulated [153] and two-tone-modulated [99] RF measurements-based procedures that only require equipment commonly available in most RF laboratories, such as a VSG and a VSA, and that can be performed much closer to the target operating conditions of the PA under test.

Charge trapping is characterized by highly asymmetric charge capture and emission

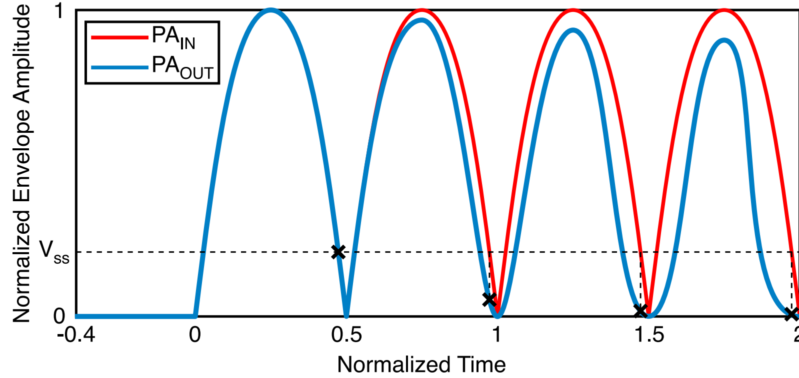

Figure 6.1 Typical transient response of a GaN HEMT-based PA to a two-tone envelope excitation. Due to charge trapping, the PA gradually self-biases toward a deep class C and loses most of its small-signal gain.

processes [139]. While charge capture has traditionally been dismissed as a nearly instantaneous process, recent developments in the characterization and modeling of charge-trapping phenomena have shown that the time constants associated with charge capture can be comparable to the slow-varying envelopes of modern radar or wireless communications signals, ranging from less than a microsecond up to a few tens of milliseconds [91]. This has uncovered the outstanding importance of the multiple-time-constant dynamic behavior of charge trapping in the pulse-to-pulse stability of GaN HEMT-based PAs for radar applications and in the linearization of GaN HEMT-based PAs for cellular base station transmitters. For this reason, in this chapter we describe a new method where transient two-tone RF measurements are used to accurately characterize the dynamics of charge-trapping capture and emission processes in GaN HEMT-based PAs by tracking their dynamic self-biasing behavior across both the frequency and time domains, as illustrated in Figure 6.1.

Moreover, in this chapter we also demonstrate that the dynamic self-biasing behavior caused by charge-trapping phenomena—and the resulting long-term memory effects—can be compensated using an external analog circuit whose parameter extraction is based on our transient two-tone RF characterization method. Our proposed ACC, which features a state-variable capture time constant and a fixed emission time constant, implements an approximation of a state-of-the-art physical model of charge trapping based on SRH statistics [91] and works by canceling out, in real time and based on the model-predicted trapping state, the threshold voltage variation experienced by the GaN HEMT in a GaN HEMT-based PA.

6.2 Theoretical Background

Charge trapping refers to an accumulation of charge in deep-level traps with energy levels near the middle of the band gap of a semiconductor. In GaN HEMTs, this is understood to

be caused by large electric fields at the gate terminal (gate lag), the drain terminal (drain lag), or a combination of both. As a result of the accumulated charge, an equivalent net-negative gate electric potential is created and the conductivity of the GaN channel is decreased until the charge is released through thermal emission [83]. Charge-trapping phenomena in GaN HEMTs inherently present highly asymmetric capture and emission times [91], [139]. However, while it is generally believed that the asymmetry between the time constants associated with charge capture and emission is so great that the capture process can be considered nearly instantaneous, in [91] the authors demonstrated that this is not an accurate assumption. In reality, the time constants associated with charge capture can be comparable to the slow-varying envelopes of modern radar or wireless communications signals, ranging from less than a microsecond up to a few tens of milliseconds.

The most common abstraction for charge-trapping phenomena in GaN HEMTs is a virtual back gate that charges and discharges at different rates [139], dynamically offsetting the threshold voltage of the HEMT and producing a self-biasing effect [82]. This self-biasing effect has been demonstrated to be so severe that a GaN HEMT-based PA biased in class B can easily degenerate into deep class C under normal operating conditions [140]. Since this effect depends on the long-term characteristics of the signal being transmitted by the PA, it is not surprising that conventional DPD algorithms are not capable of delivering sufficient levels of linearization, as the transfer characteristics of the PA are continuously changing in time at a rate much slower than the observable time span of these algorithms (limited by the available sample memory), but also much faster than the rate at which the DPD model parameters are adapted [13], [J2].

In spite of the virtual back gate being just an abstraction, drift-diffusion simulations of AlGaN/GaN heterostructures suggest that there may indeed be an actual accumulation of charge beneath the gate of the HEMT [83]. Furthermore, the principle of a virtual back gate has been exploited to successfully compensate long-term memory effects in GaN HEMT-based PAs employing commercial GaN HEMTs throughout this thesis. Thus, there are strong indications that the dynamic self-biasing behavior of GaN HEMT-based PAs can be attributed to charge-trapping phenomena and that an accurate characterization of these phenomena is essential for the compensation of this behavior.

6.3 Characterization

Previous efforts to characterize trapping-related time constants using large-signal two-tone excitations (e.g., [99], Section 2.3.4, and Section 4.6) identified that, for very low two-tone frequency separations Δf (<10 Hz), the small-signal gain of a GaN HEMT-based PA remains unchanged. This happens because, while there is a very significant accumulation of trapped charge during the large-signal portion of the envelope, the envelope is so slow that there is enough time for most of the trapped charge to be released through thermal emission

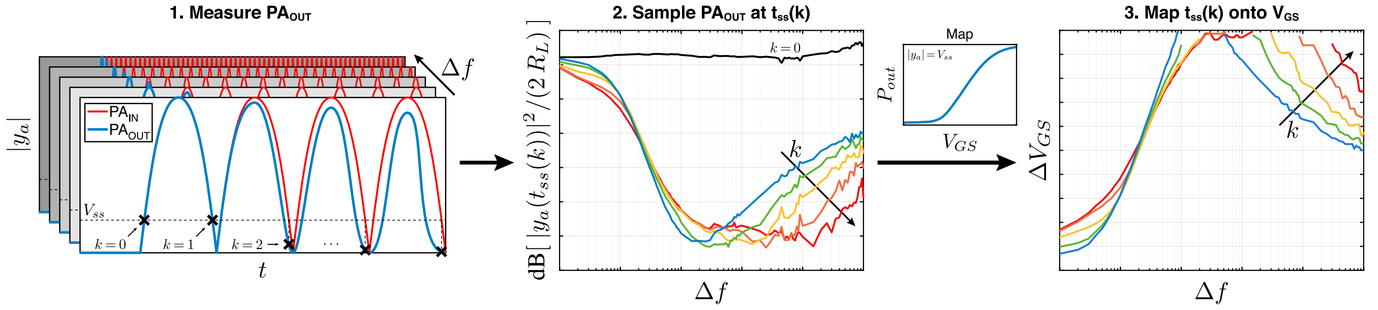

Figure 6.2 Diagram of the proposed characterization method. First, the transient response of the PA to a series of large-signal two-tone excitations is measured. Then, specific small-signal points are selected at $t = t_{ss}(k)$. Finally, the equivalent gate–source voltage variation is estimated by mapping these points onto V_{GS} through the measured $P_{out}(V_{GS}, V_{ss})$ map. $y_a(t)$ is the PA output envelope, time-aligned with the corresponding two-tone input signal.

by the time the envelope reaches a small-signal level. However, for larger Δf (0.1–1 kHz), it is found that the small-signal gain decreases because there is not enough time for the trapped charge to be released during the short period between the large-signal and small-signal parts of the sinusoidal envelope. For much larger Δf (>10 kHz), the envelope is too fast for there to be any significant emission of trapped charge, so the small-signal gain remains very low at a constant level.

Even though the method detailed in [99], Section 2.3.4 and Section 4.6 is sufficient for the characterization of the steady-state balance between the capture and emission processes (as all measurements are done in steady-state conditions), it provides very little information on each process separately. For this reason, in this chapter we detail a new transient two-tone RF characterization method that allows for the accurate characterization of both capture and emission processes. Through this method, the gradual self-biasing of a GaN HEMT-based PA can be tracked at each envelope half-cycle and the dynamic variation of the HEMT's threshold voltage (or virtual back gate voltage) can be more comprehensively characterized. We assume that, in a realistic PA, the time constants associated with the bias networks are much shorter than those associated with thermal and charge-trapping phenomena, otherwise the efficiency of the PA would be extremely low for wideband excitations [154]. Our proposed method is graphically summarized in Figure 6.2 and detailed as follows.

6.3.1 Transient Two-Tone RF Characterization Method

Measurements: First, the response of the PA under test to a constant small-signal CW excitation is measured as a function of the gate–source voltage. From this preliminary measurement results the map $P_{out}(V_{GS}, V_{ss})$, where P_{out} is the measured PA output power, V_{GS} is the gate–source voltage, and V_{ss} is the amplitude of the small-signal CW excitation. This map, which is assumed to be static, is used at a later stage to estimate the trapping state of the PA in the form of an equivalent variation of the HEMT's threshold voltage. Note that

V_{GS} is only required to be swept from the PA's target bias point to increasingly negative voltages, since charge trapping always leads to an increase of the threshold voltage. Thus, unless the PA is intended to be biased in class A, the temperature throughout the sweep will be approximately constant, as the power dissipated due to the quiescent drain current will vary very little throughout the sweep.

Then, the transient response of the PA to a series of large-signal two-tone RF excitations with frequency separation Δf is measured, where Δf is a swept parameter. This can be done using a VSG and a VSA. The VSG should be configured to generate one single instance of each waveform and to trigger the VSA measurement at the start of each waveform playback. In order to maintain the same initial conditions for all measurements (i.e., the same baseline trapping state), the charge accumulated as a result of each measurement should be allowed to be released through thermal emission prior to triggering the next measurement. Some strategies for achieving this include, e.g., waiting 30 s to 100 s between each measurement with the PA under a small-signal excitation, tracking the recovery of the PA's small-signal gain, or tracking the recovery of the PA's quiescent current. From these measurements results a dataset containing the transient responses of the PA to large-signal two-tone excitations with different frequency separations Δf.

Post-Processing: After performing the required measurements, all recorded time series must be aligned with their respective excitations in order to compensate the group delay introduced by the measurement setup. Since we consider that the measurements are performed using a VSG and a VSA, then the input excitation is never actually measured—it only exists as a digital set of samples in a computer. Thus, aligning the measured PA output with the input excitation consisted, in our case, in sliding the input excitation across time in order to maximize the cross-correlation between the two signals.

For optimal results, the alignment should not be done simply by cyclically shifting the samples of the input excitation vector, as this would limit the time resolution to the duration of one sampling period. Instead, a new input excitation vector should be generated by introducing a double-precision phase shift or time delay to the sampling of the respective sinusoid. Thus, optimum alignment requires an optimization process for finding t_0 such that $|x(n, t_0)| = |\sin(2\pi \cdot \Delta f/2 \cdot (n/f_s - t_0))|$ has maximum cross-correlation with the amplitude of the measured PA response $|y(n)|$, where $n = 0,\ 1,\ \cdots,\ N-1$ is the sample index and f_s is the sampling frequency. This can be done in an expedient fashion by minimizing the cost function $\lambda(t_0)$ defined in (6.1) using, e.g., gradient descent techniques or the more advanced CMA-ES algorithm [148]. In the end, the adjusted time vector $t(n) = n/f_s - t_0$ is obtained.

$$\lambda(t_0) \;=\; \sum_{n=0}^{N-1} \left[\log\left(\frac{|y(n)|}{\max\{|y(n)|\}}\right) \;-\; \log(|x(n,t_0)|)\right]^2 \tag{6.1}$$

Note that the alignment process can be improved (and greatly accelerated) by considering just the first envelope cycle of each recorded time series, as this is the cycle with the most clearly defined (steepest) zero-crossing, as illustrated in Figure 6.1. This is because the PA has not yet self-biased to a deep class C, where the zero-crossings of the sinusoidal envelope are flattened. Thus, for each time series, we determine t_0 using the first envelope cycle and delay/advance the whole time series by that amount. Furthermore, note that proper alignment is most critical at the small-signal parts of the envelope, as this is where the slope of the envelope amplitude is steepest. It is for this reason that $\lambda(t_0)$ includes the logarithm function—to magnify the small-signal amplitudes and prevent their squared errors from being outweighed by those of the large-signal parts of the envelope. For an example of how the logarithm function impacts the alignment results, see Figure 6.3, where a zoomed-in view of an envelope zero-crossing is shown after alignment considering $\lambda(t_0)$ as defined in (6.1) (black and blue markers), and after alignment considering the more obvious—but less adequate—cost function defined in (6.2) (black and red markers).

$$\widehat{\lambda}(t_0) = \sum_{n=0}^{N-1} \left[\frac{|y(n)|}{\max\{|y(n)|\}} - |x(n,t_0)| \right]^2 \tag{6.2}$$

After obtaining the aligned transient response $y_a(t)$ of the PA (in reality, the response is the same and it is the time vector that is shifted by t_0), it is sampled through linear interpolation at the instants where the amplitude of the respective two-tone excitation is equal to that of the small-signal CW excitation used in the preliminary measurement of the $P_{out}(V_{GS}, V_{ss})$ map (as represented in Figure 6.1 by the black markers). In other words, the values of $y_a(t_{ss}(k))$ are recorded, where t_{ss} is defined in (6.3), $k = 1,\ 2,\ \cdots,\ K$ is the

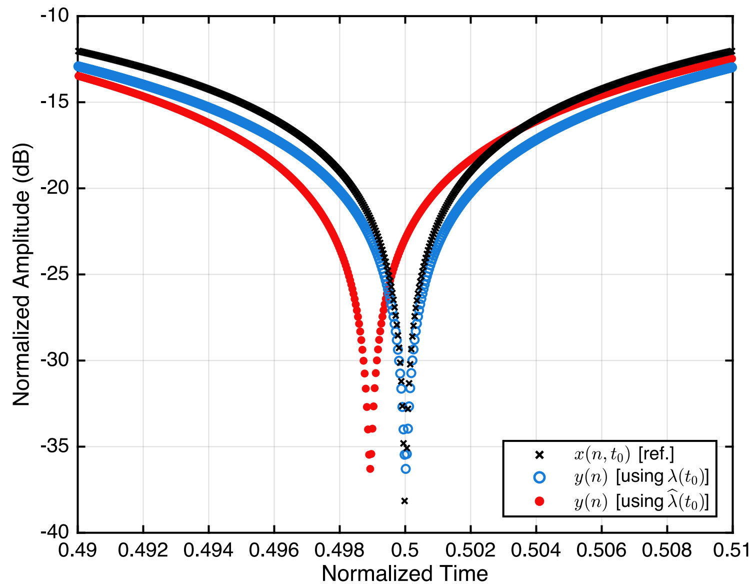

Figure 6.3 Comparison between the envelope alignment results obtained with different optimization cost functions.

index of each half-cycle of the two-tone input excitation with frequency separation Δf (up to a total of K envelope half-cycles or amplitude periods), V_p is the peak amplitude of the two-tone input excitation, and V_{ss} is the amplitude of the CW excitation at which the $P_{out}(V_{GS}, V_{ss})$ map was measured. This results in a dataset that provides a comprehensive characterization of the gradual self-biasing experienced by a GaN HEMT-based PA for a wide variety of amplitude-modulated excitation dynamics.

$$t_{ss}(k) = \frac{1}{\Delta f}\left[k - \frac{1}{\pi}\arcsin\left(\frac{V_{ss}}{V_p}\right)\right] \tag{6.3}$$

6.3.2 Experimental Results

Measurement Setup: In order to characterize the dynamic self-biasing of a GaN HEMT-based PA, we assembled the measurement setup illustrated in Figure 6.4(a). The in-phase and quadrature baseband waveforms of the transient two-tone input signals were generated using a Tektronix AWG70002A AWG, which was connected to a Keysight E8267D PSG VSG for RF up-conversion. A Mini-Circuits ZHL-16W-43-S+ driver scaled the output of the VSG and provided the input excitations to the PA. The output of the PA was measured using a Keysight N9041B UXA VSA, which was preceded by an attenuator for the adequate adjustment of the VSA input power level. The dc power of the PA was sourced from a Keysight N6705C dc power analyzer, which was also used for sweeping V_{GS} during the measurement of the $P_{out}(V_{GS}, V_{ss})$ map.

Using this setup, we characterized the dynamic self-biasing behavior of a 1.6 GHz single-ended PA based on the 15 W 28 V Wolfspeed CGH27015F GaN HEMT. The PA, whose CW PAE was measured as greater than 56 %, was biased in class B at the root of g_{m3} [145], leading to a quiescent drain current of 40 mA. The bias voltages were, therefore, V_{GG} = −2.7 V and V_{DD} = 28 V. The two-tone excitations provided a peak available input power of 29 dBm and their frequency separation was varied from 10 Hz to 1 MHz. The $P_{out}(V_{GS}, V_{ss})$ map and the transient response of the PA at $t_{ss}(k)$ were measured for an input power level of 0 dBm (i.e., V_{ss} = 316 mV). The PA was measured for 100 periods of each input excitation, the last of which corresponded to a near-steady-state condition. In order to minimize the spurious effects of inevitable temperature drifts, all measurements were carried out at a controlled ambient temperature of 24 °C and the PA was provided with ample auxiliary active cooling.

Setup Calibration: Before performing the characterization procedure, the measurement setup was calibrated at the RF-input and RF-output planes of the PA (α and β in Figure 6.4). First, the scattering parameters of a directional coupler were measured at its input port (1:IN), output port (2:OUT) and coupled port (3:CPL) using an Anritsu MS4647B VNA. Then, the PA was disconnected from the measurement setup and the directional coupler was connected in its stead at the same α and β planes of calibration (i.e., between the output

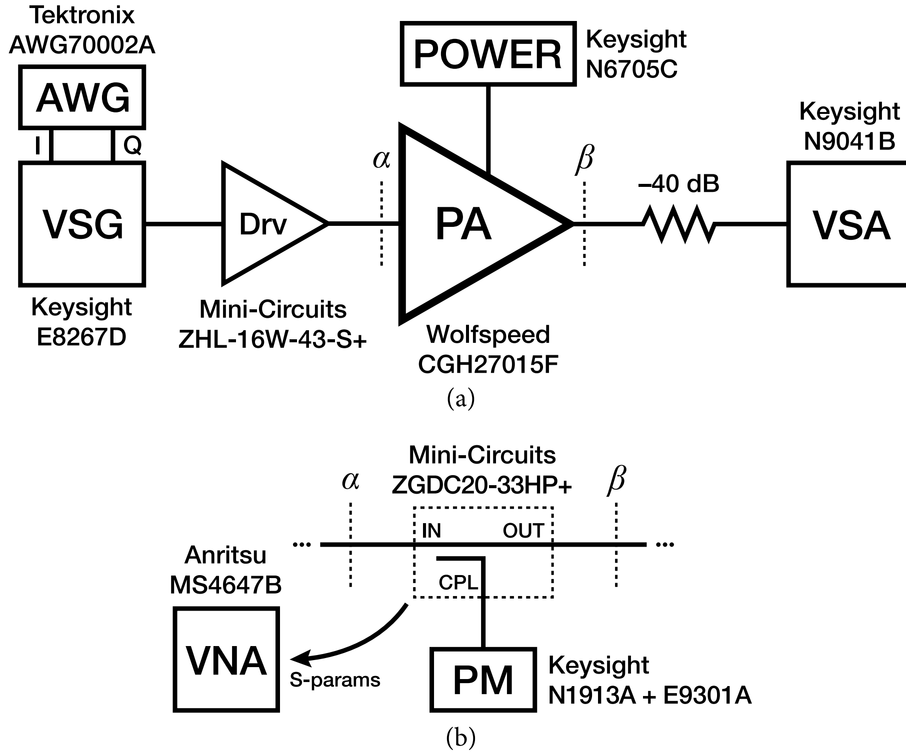

Figure 6.4 Diagram of (a) the measurement setup for the characterization of the dynamic self-biasing behavior of a GaN HEMT-based PA, and (b) the calibration equipment. During calibration, the PA is disconnected from the measurement setup and the calibration equipment is connected in its stead at the α and β planes.

of the driver and the input of the VSA attenuator). As shown in Figure 6.4(b), the coupled port of the directional coupler was connected to a Keysight N1913A PM through a Keysight E9301A average power sensor. This calibration setup allows for an accurate assessment of the absolute power levels at both calibration planes simultaneously by combining the average power measurement of the PM (traceable to an internal absolute-power standard), the scattering parameters of the directional coupler (traceable to a short-open-load-through standard), and the waveform measurement of the VSA (not traceable, but sufficiently accurate).

Finally, an iterative procedure was executed to obtain a set of calibration factors—Γ_{VSG}, defined in (6.4), and Γ_{VSA}, defined in (6.5)—that corrected the absolute peak power at both calibration planes up to an error of less than 0.01 dB. The procedure consisted in measuring the average power at the PM $P_{av}^{(\text{PM})}$; measuring the waveform at the VSA $y(n)$; and obtaining the calibration factors based on the peak power at the α-plane $P_{pk}^{(\alpha)}$, defined in (6.6); the peak power at the β-plane $P_{pk}^{(\beta)}$, defined in (6.7); and the peak power at the VSA $P_{pk}^{(\text{VSA})}$, defined in (6.8). In these equations, S is the scattering matrix of the directional coupler, $P_{pk,\text{dBm}}^{(\text{Target})} = 29$ dBm is the target peak power at the α-plane, $\sigma \leq 1$ is a learning-rate parameter, cf is the crest factor of $y(n)$, N is the number of samples of $y(n)$, and $R_L = 50\ \Omega$. The iterative calibration procedure was executed for each target excitation (i.e., for each

Δf) until the desired level of accuracy was reached. After obtaining the calibration factors, the directional coupler was disconnected from the measurement setup and the PA was reconnected.

$$\Gamma_{\text{VSG}} := \Gamma_{\text{VSG}} - \sigma\Big[10\log_{10}\Big(10^3\, P_{pk}^{(\alpha)}\Big) - P_{pk,\text{dBm}}^{(\text{Target})}\Big] \tag{6.4}$$

$$\Gamma_{\text{VSA}} := \sqrt{P_{pk}^{(\beta)} \,/\, P_{pk}^{(\text{VSA})}} \tag{6.5}$$

$$P_{pk}^{(\alpha)} = \frac{cf^2}{(1-|S_{11}|^2)\,|S_{31}|^2}\, P_{av}^{(\text{PM})} \tag{6.6}$$

$$P_{pk}^{(\beta)} = \Big(1-|S_{11}|^2\Big)\,|S_{21}|^2\, P_{pk}^{(\alpha)} \tag{6.7}$$

$$P_{pk}^{(\text{VSA})} = \frac{cf^2}{2\,NR_L}\sum_{n=0}^{N-1}|y(n)|^2 \tag{6.8}$$

Characterization Results: In Figure 6.5(a) we present the $P_{out}(V_{GS}, V_{ss})$ map resulting from the preliminary measurements at a CW input power level of 0 dBm. Moreover, in this figure we also show an example of the estimated trajectory of the gate–source voltage as a result of the gradual accumulation of trapped charge due to the large-signal two-tone excitation at $\Delta f = 100$ kHz (detailed in Section 6.4).

Finally, Figure 6.5(b) illustrates the result of the characterization of the dynamic self-biasing behavior of the GaN HEMT-based PA. In this figure, the output power of the PA when measured at the instants where the level of the input large-signal two-tone excitation is 0 dBm (i.e., $|y_a(t_{ss}(k))|$, or the black markers in Figure 6.1) is plotted as a function of two variables: the two-tone frequency separation Δf (the horizontal axis), and time (color-coded). Thus, Figure 6.5(b) shows the temporal evolution of the small-signal output power of the PA for each transient two-tone large-signal excitation with frequency separation Δf: from an initial CW steady-state condition in black; to an output power level in blue following the very first input period (measured at $t = t_{ss}(1)$); and up to an output power level in red at the near-steady-state final condition following the one-hundredth input period (measured at $t = t_{ss}(100)$).

The results shown in Figure 6.5(b) can be explained based on our understanding of the charge-trapping mechanism as follows. As the amplitude of the envelope of a two-tone excitation rises from zero to its peak value, the rate of capture of charge carriers by deep-level traps in the GaN HEMT exceeds the rate of emission, leading to an accumulation of trapped charge and a consequent reduction in the conductivity of the GaN channel. Conversely, as the amplitude descends from the peak toward zero, the rate of capture decreases below the rate of emission, leading to a net release of trapped charge and the consequent recovery of the conductivity of the GaN channel toward its initial state. For very low values of Δf, the envelope is slow enough for all trapped charge to be released between each input period, resulting in an unchanging small-signal PA output power. However, for larger values of

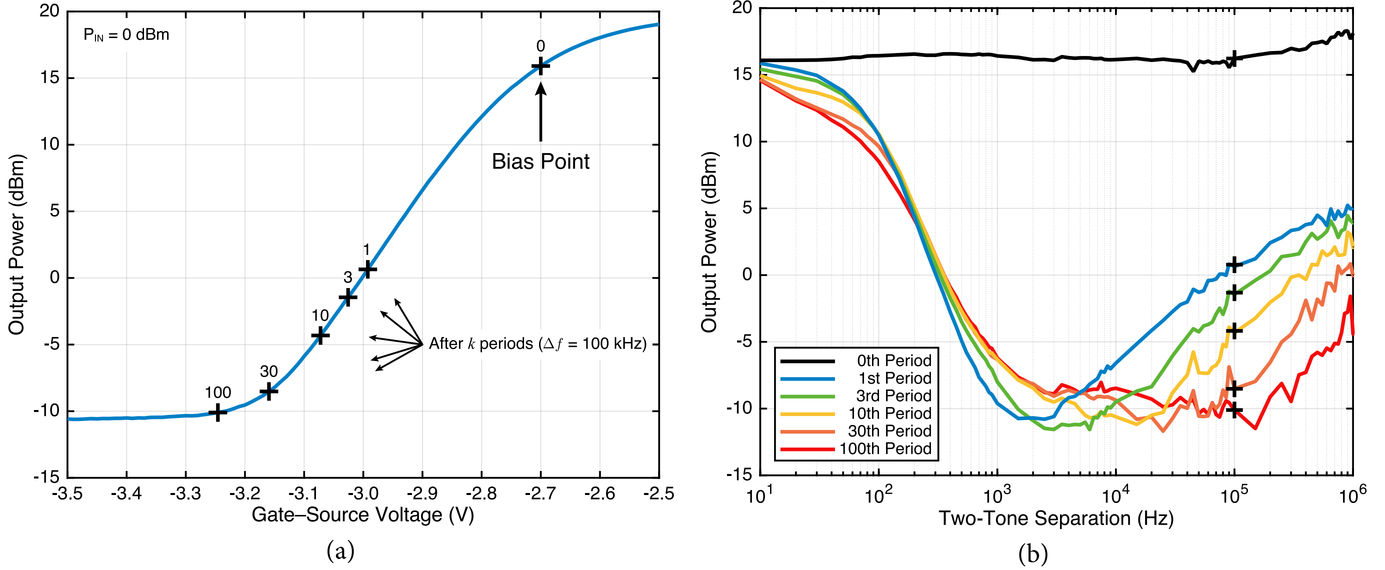

Figure 6.5 (a) Variation of the PA output power as a function of the gate–source voltage V_{GS} for a constant 0 dBm CW excitation. (b) Variation of the PA output power measured at the small-signal-input instants $t_{ss}(k)$ as a function of the two-tone frequency separation Δf. Also, in black markers, an example of the gradual self-biasing for $\Delta f = 100$ kHz.

Δf, the envelope is fast enough for some charge to remain trapped between input periods, resulting in a reduction of the output power of the PA. As the results demonstrate, this small-signal output power reduction can be as large as 25 dB, indicating a complete collapse of the small-signal transfer characteristics of the GaN HEMT and a clear degeneration of the operation of the GaN HEMT-based PA from class B to a deep class C.

In addition to evidencing the dynamic change in the class of operation of the PA, Figure 6.5(b) also reveals the temporal evolution of this self-biasing behavior: from the very first input period to the last. This provides valuable information on the net state of the deep-level traps of the GaN HEMT at various stages of the descent from class B to class C. For instance, if the capture process were nearly instantaneous (as commonly assumed), then the deep-level traps would reach a maximum of trapped charge in the very first input period for all Δf considered, and the characterization results would present coincident temporal profiles. However, at higher Δf, the successive profiles in Figure 6.5(b) indicate a progressively lower PA output power for the same PA input power, demonstrating that the first periods of the input excitation may not be sufficient to fully charge the deep-level traps of the GaN HEMT. This is further evidence that the capture process in charge-trapping phenomena is much slower than what is commonly assumed, as explained in [91].

6.4 Modeling

Now that the dynamic self-biasing behavior of GaN HEMT-based PAs can be accurately characterized, the next step toward its compensation consists in identifying the mechanism

that causes it. In the previous sections, we suggested that this behavior can be attributed to the dynamic variation of the HEMT's threshold voltage. In this section, we demonstrate not only that our hypothesis is supported by physical models of charge trapping in GaN HEMTs, but also that the accurate prediction of the dynamic self-biasing behavior of GaN HEMT-based PAs is contingent on the accurate modeling of the charge-capture process.

Regardless of the internal structure (or mathematical formulation) of the model that is used for the compensation of the dynamic self-biasing behavior of a GaN HEMT-based PA, our compensation strategy—canceling out the dynamic variation of the HEMT's threshold voltage—dictates that the output of the model should be the instantaneous threshold voltage variation $\Delta V_{GS}(t)$. Moreover, since the compensation shall be carried out by an analog circuit, it is preferable that this model have a feedforward structure, so that the input signal of the model can be extracted from the input of the PA rather than from its output. Thus, the model should be of the form $\Delta V_{GS}(t) = f_M[v_x(t), \Psi_M]$, where $v_x(t)$ denotes the amplitude of the envelope of the PA's input excitation, and $f_M[\cdot]$ is an operator that denotes the dynamic model-defined mapping between $v_x(t)$ and $\Delta V_{GS}(t)$ using the set of model parameters Ψ_M.

6.4.1 Model Extraction

In order to extract the set of parameters Ψ_M for a given model, the target mapping between $v_x(t)$ and $\Delta V_{GS}(t)$ should first be obtained from the characterization results as follows. Referring back to Section 6.3.1, recall that $y_a(t_{ss}(k))$ (shown in Figure 6.5(b)) is the output of the PA at the instants where the input of the PA has an amplitude of V_{ss}. Since we measured a map $P_{out}(V_{GS}, V_{ss})$ (shown in Figure 6.5(a)) that relates P_{out} and V_{GS} for an input excitation with amplitude V_{ss}, then this map can be used to estimate the equivalent V_{GS} for each measured $y_a(t_{ss}(k))$—for instance, through linear interpolation of $|y_a(t_{ss}(k))|^2/(2\,R_L)$, where $R_L = 50\ \Omega$. This results in a vector $V_{GS}(t_{ss}(k))$ that contains an estimate of the equivalent gate–source voltage at each period of the transient response of the PA to a given large-signal two-tone excitation. Note that some estimates resulting from the interpolation may be indeterminate due to the sigmoid shape of the map; in these cases, we choose to discard the estimates. Finally, the variation of the threshold voltage due to charge trapping can be calculated by subtracting the gate bias voltage V_{GG} from all estimated $V_{GS}(t_{ss}(k))$. This results in a dataset $\Delta V_{GS}(\Delta f, k)$ that contains the variation of the threshold voltage of the GaN HEMT, for a two-tone excitation with frequency separation Δf, estimated at each period k, and under the biasing conditions imposed during the characterization (in our case, $V_{GG} = -2.7$ V and $V_{DD} = 28$ V).

Since $\Delta V_{GS}(\Delta f, k)$ provides a comprehensive characterization of the transient variation of the threshold voltage for a wide variety of amplitude-modulated excitation dynamics, it is suitable for the extraction of model parameters. This extraction can be done by employing an algorithm (e.g., CMA-ES) for the minimization of the MSE between $\Delta V_{GS}(\Delta f, k)$ and

$\Delta V_{GS}^{M}(\Delta f, k)$, for all Δf and all k, where $\Delta V_{GS}^{M}(\Delta f, k)$ is the threshold voltage variation predicted by the model. The predicted threshold voltage variation can be obtained by calculating the transient response of the model to the same set of two-tone excitations with varying frequency separation Δf, and then sampling it at $t_{ss}(k)$.

6.4.2 Model Definition

Jardel Model: Serving as the baseline comparison charge-trapping model throughout this chapter, the Jardel model [89] establishes a relationship between the threshold voltage of a HEMT and its intrinsic drain–source voltage. Although this relationship cannot be directly applied to the RF envelope measurements proposed in the characterization method detailed in Section 6.3, its dynamics (or mathematical formulation) certainly can, as shown in [13], [99]. Thus, throughout the rest of this chapter, we will use "the Jardel model" as a shorthand for the dynamics expressed by the mathematical formulation proposed in [89] when applied to RF envelope measurements, rather than the literal physical phenomena described by this formulation. The equivalent circuit and the mathematical definition of the dynamics described by the Jardel model can be found in Section 2.4.1.

SRH Model: While the Jardel model does support asymmetric capture and emission time constants, these time constants are fixed. However, in [91] the authors demonstrated, based on SRH statistics and the works of [104], [139], that the capture process can be more accurately modeled with a time constant that varies with the instantaneous trapping state, becoming exponentially larger as the accumulated charge increases. Similar to the model proposed by Jardel *et al.* in [89], this model establishes a relationship between the threshold voltage of a HEMT and its intrinsic drain–source voltage. Again, for simplicity, we will use "the SRH model" as a shorthand for the mathematical formulation of the dynamics described by this model, since our target application is the modeling and compensation of an RF PA, and not the intrinsic characteristics of a discrete HEMT. The equivalent circuit and the mathematical definition of the dynamics described by the SRH model can be found in Section 2.4.3.

6.4.3 Experimental Results

Figure 6.6(a) illustrates the result of the extraction of the parameters of the Jardel model, as well as the target dataset $\Delta V_{GS}(\Delta f, k)$ that resulted from the characterization measurements. The extracted parameters were $\tau_c = 29.2$ µs, $\tau_e = 3.47$ ms, and $\kappa = 1.54$ V/V. As is shown by the red curve representing the one-hundredth envelope period (a near-steady-state condition)—and as has been previously demonstrated in [99] and Section 4.6—, the Jardel model fits the estimated variation of the threshold voltage quite well under steady-state conditions. However, the figure also reveals that this model is not capable of predicting

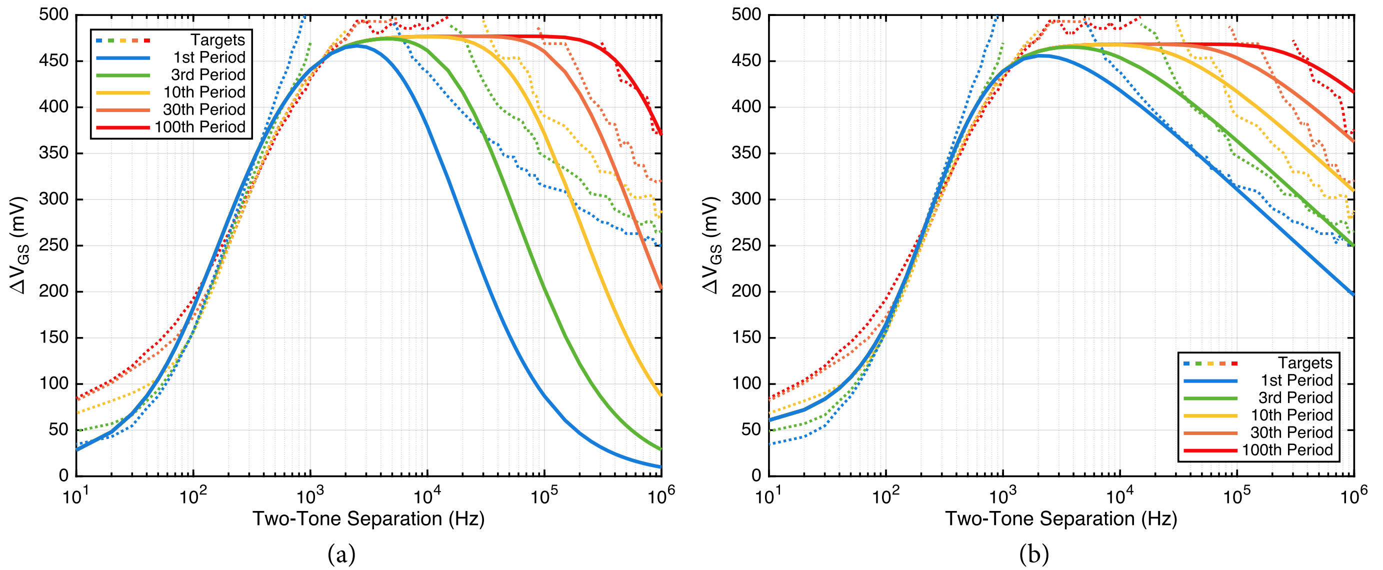

Figure 6.6 Result of the extraction of (a) the Jardel model and (b) the SRH model. In the background, the estimated variation of the threshold voltage of the GaN HEMT is also shown.

the transient behavior with sufficient accuracy because of the modeling of the capture process as a single fixed time constant.

Figure 6.6(b) illustrates the result of the extraction of the parameters of the SRH model, as well as the target dataset $\Delta V_{GS}(\Delta f, k)$ also displayed in Figure 6.6(a). The extracted parameters (for $V_T = 25.9$ mV and $V_0 = 1.00$ V) were $\omega_0 = 446$ rad/s, $k_0 = -63.7$ mV, $k_1 = 36.0$ mV/V, and $k_2 = 475$ mV/V. As the figure reveals, the state-variable time constant used to model the capture process greatly improves the ability of the model to predict the measured (estimated) transient ΔV_{GS} curves, especially at higher Δf. In addition, there is some agreement between the Jardel and SRH models, as the time constants associated with the emission process are relatively similar ($1/\omega_0 = 2.24$ ms).

Naturally, there is a limit to how accurate of a fit can be obtained with these models. First, because these models, despite being state-of-the-art, still do not provide a complete and accurate description of the dynamics of charge-trapping phenomena—for instance, we've demonstrated in Chapter 4 and [C3], [J4] that the single fixed emission time constant considered by both the Jardel and the SRH models is a gross simplification of the actual emission dynamics observed through transient current measurements. Second, because these models were originally conceived for the prediction of either gate-lag or drain-lag phenomena, and not both phenomena simultaneously, as that would require a greater number of model parameters for the distinction between the different contributions of the gate and drain potentials. Third, because the response of these models is altered by our use of the PA's input envelope amplitude as their input signal, instead of the intrinsic voltage waveform that the original authors established. Fourth, because the RF measurements-based characterization results themselves are an inevitable combination of gate-lag phenomena,

drain-lag phenomena, and thermal phenomena as well. Finally, because there may be other effects caused by charge-trapping phenomena that we are not taking into account (e.g., dynamic on-resistance). In any case, and in spite of these apparent limitations, in the next section we show that excellent compensation results can still be obtained using the SRH model when extracted based on our characterization method.

6.5 Analog Compensation

In the previous sections, we demonstrated how the dynamic self-biasing behavior of GaN HEMT-based PAs can be characterized and predicted in real time using the SRH physical model of charge trapping. In this section, we demonstrate that an approximation of this model can be implemented as a fully analog electronic circuit and used to compensate the dynamic self-biasing behavior of a GaN HEMT-based PA. For comparison purposes, we also implemented the Jardel model as an analog circuit and measured how well it compensates the dynamic self-biasing behavior of the same PA under the same conditions.

In order to compensate the dynamic self-biasing behavior of a GaN HEMT-based PA, our ACC employed the compensation strategy detailed in Chapter 3 and Chapter 4 for mobile communications applications and in Chapter 5 for pulsed radar applications. This strategy consists in canceling out the dynamic variation of the HEMT's threshold voltage by modulating the gate–source voltage. As illustrated in Figure 6.7, the modulation is done by superimposing a compensation signal $\Delta V_{GS}(t)$ over the gate bias voltage V_{GG}, resulting in the compensated gate–source voltage $V_{GS}(t)$. The compensation signal is obtained by coupling the PA's input RF excitation into the input port of the ACC, demodulating it with an envelope detector, and finally processing it through a nonlinear filter, which is an analog implementation of a charge-trapping model. Naturally, the typical large-value bypass capacitor at the gate bias terminal of the PA should be removed, otherwise the V_{GS} modulation would be bypassed to ground.

6.5.1 Analog Compensation Circuit

Piecewise-SRH Model: While the SRH model does provide a very good fit to the dynamic threshold voltage variation estimated from the characterization results, its definition of the charge-capture process does not exactly lend itself to a direct implementation as

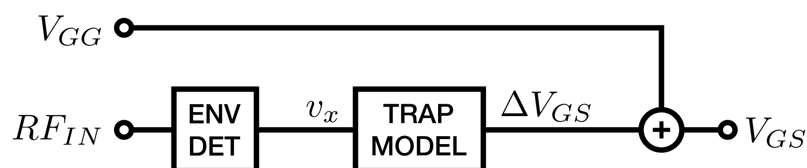

Figure 6.7 Block diagram of the analog compensation circuit.

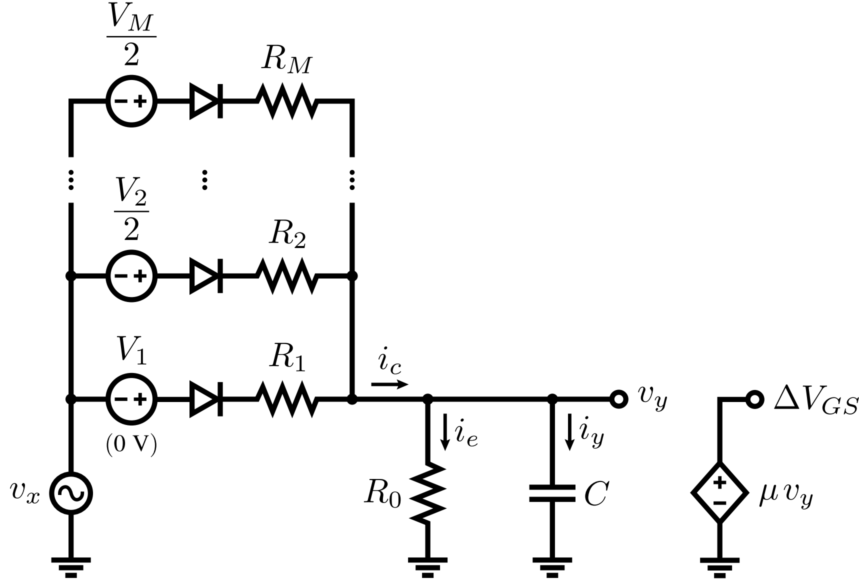

Figure 6.8 Equivalent circuit of the piecewise-SRH model.

an analog circuit. For this reason, we developed a new behavioral model that preserves the SRH model's characteristic state-variable capture time constant, yet whose analog implementation is straightforward.

In this model—the piecewise-SRH model, whose equivalent circuit is illustrated in Figure 6.8—, the complex charge-capture process defined in the SRH model is approximated by a piecewise-linear function. In this function, the time constant of the charge-capture process is switched (or, more accurately, interpolated) between M different values, depending on the instantaneous trapping state and input excitation. The time-constant switching is carried out by a set of ideal diodes that are biased at the switching breakpoint voltages $V_m/2$, where $V_1 = 0$ V and $V_m < 0$ for all $m = 2, 3, \cdots, M$. By charging the capacitor C through every resistor R_m such that $v_x(t) - v_y(t) > -V_m/2$, this configuration allows for the interpolation between time constants rather than a hard switching between them, contributing to the smoothness of the model. As in the SRH model (as well as the Jardel model), the emission process is modeled by a fixed time constant $\tau_e = R_0\, C$. The piecewise-SRH model, with a parameter set $\Psi_M = \{R_0, R_1, \cdots, R_M, V_2, \cdots, V_M, C, \mu\}$, is defined as follows.

Let $v_x(t)$ denote the amplitude of the envelope of the PA's input excitation. Moreover, let $\Delta V_{GS}(t) = \mu\, v_y(t)$ denote the threshold voltage variation predicted by the model, where μ is a scaling factor and $v_y(t)$ is the voltage at the capacitor in Figure 6.8. Finally, let $f_D(\cdot)$ denote the transfer function, defined in (6.9), of the ideal diodes in Figure 6.8.

$$f_D(x) = \begin{cases} x, & x \geq 0 \\ 0, & x < 0 \end{cases} \tag{6.9}$$

Then, the capture current $i_c(t)$ is defined as in (6.10), the emission current $i_e(t)$ is defined as in (6.11), and the net capacitor current $i_y(t)$ is defined as in (6.12).

$$i_c(t) = \sum_{m=1}^{M} f_D\left(\frac{v_x(t) + V_m/2 - v_y(t)}{R_m}\right) \tag{6.10}$$

$$i_e(t) = \frac{v_y(t)}{R_0} \tag{6.11}$$

$$i_y(t) = i_c(t) - i_e(t) \tag{6.12}$$

The voltage at the capacitor $v_y(t)$ is defined as in (6.13) and, using Euler's method, it can be discretized as in (6.14), where n denotes the sample index and f_s denotes the sampling frequency.

$$v_y(t) = \frac{1}{C}\int_{t_0}^{t} i_y(\tau)\, d\tau + v_y(t_0) \tag{6.13}$$

$$v_y(n+1) = v_y(n) + \frac{1}{f_s\, C}\, i_y(n) \tag{6.14}$$

Implementation Details: In both the Jardel ACC, shown in Figure 2.9 and laid out in Appendix A, and the piecewise-SRH ACC, shown in Figure 6.8 and laid out in Appendix C, the ideal diodes were implemented as precision rectifier circuits where an operational amplifier compensates the forward voltage of a diode in a local feedback loop [143]. In the piecewise-SRH ACC, the $V_m/2$ voltage sources in the charge-capture path were implemented as conventional non-inverting summing-amplifier circuits based on an operational amplifier—it is for this reason that the breakpoint voltages are multiplied by a factor of 1/2.

In both ACCs, the envelope detector was implemented using an Analog Devices ADL5511 integrated circuit. The ideal diodes were implemented using Texas Instruments OPA659 voltage-feedback operational amplifiers with ultra-low input bias currents (to prevent the parasitic loading of the trapping state integrator—the capacitor C) and Toshiba 1SS307E silicon switching diodes with ultra-low reverse-bias current and total capacitance. The scaling factors κ and μ were implemented using an Analog Devices AD8336 variable gain amplifier controlled by a pair of Analog Devices ADR510 precision voltage references. Finally, a 6.8 nF $\pm$ 1 % C0G/NP0 KEMET ceramic capacitor was chosen for the capacitor C. The implemented Jardel ACC and piecewise-SRH ACC are pictured in Figure 6.9 and Figure 6.10, respectively.

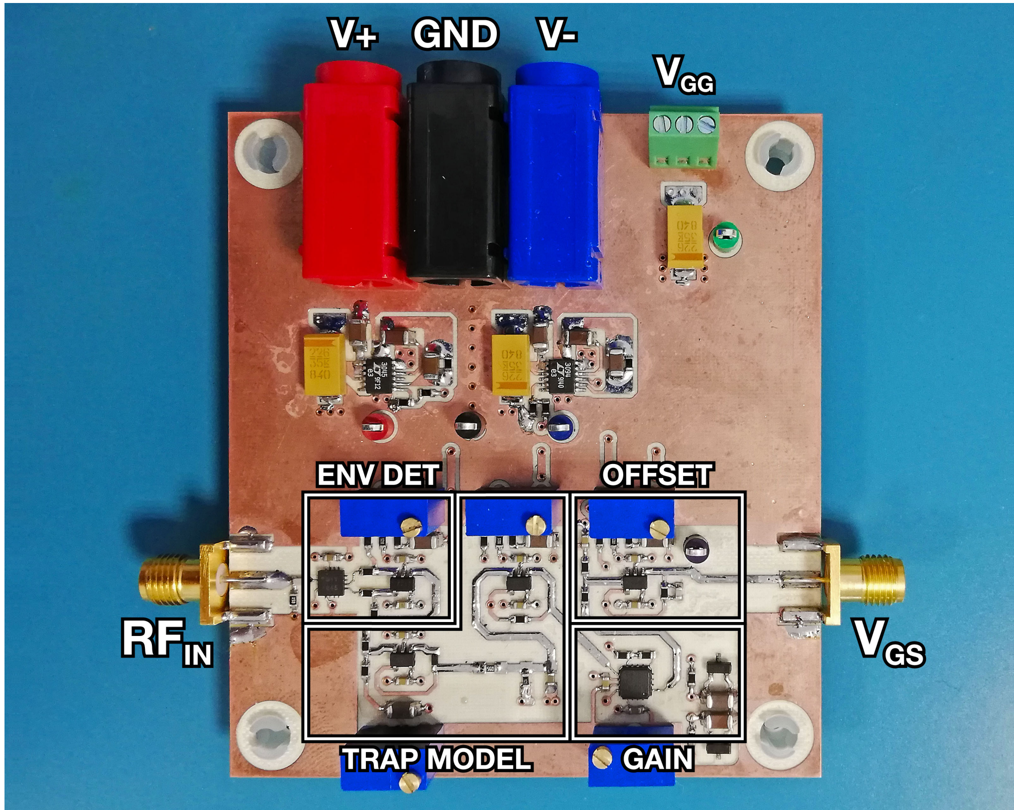

Figure 6.9 Photograph of the Jardel ACC.

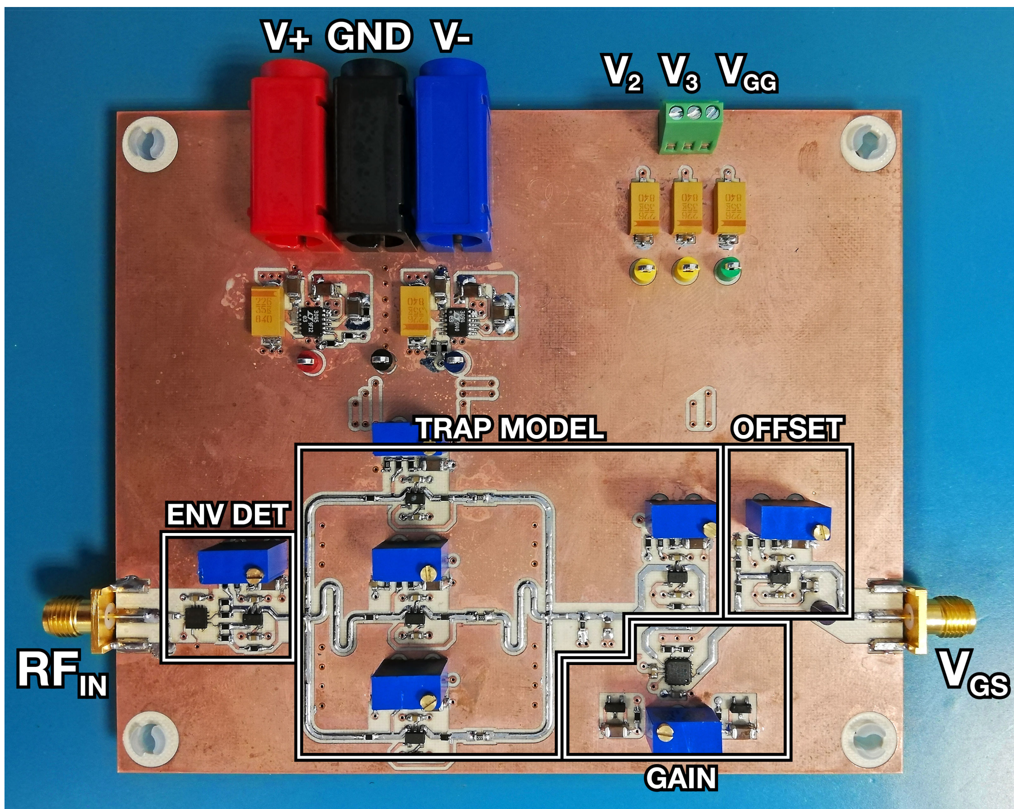

Figure 6.10 Photograph of the piecewise-SRH ACC.

6.5.2 Experimental Results

Figure 6.11 illustrates the result of the extraction of the parameters of the piecewise-SRH model. The extracted parameters were $R_0 = 330$ kΩ, $R_1 = 7.50$ kΩ, $R_2 = 1.80$ kΩ, $R_3 = 43.0$ Ω, $V_2 = -204$ mV, $V_3 = -330$ mV, $C = 6.80$ nF, and $\mu = 1.57$ V/V. For comparison with the parameters of the Jardel ACC ($\tau_e = 3.47$ ms and $\tau_c = 29.2$ µs), the time constants τ_m, defined as $\tau_m = R_m C$, were $\tau_0 = 2.24$ ms, $\tau_1 = 51.0$ µs, $\tau_2 = 12.2$ µs, and $\tau_3 = 292$ ns. Figure 6.11 demonstrates, once again, that the state-variable capture time constant of the SRH model provides excellent agreement with the measured (estimated) threshold voltage variation—even when simplified as a piecewise-linear function.

In order to validate the ability of the ACCs to compensate the dynamic self-biasing behavior of a GaN HEMT-based PA, we assembled the measurement setup illustrated in Figure 6.12. This setup is similar to the one used for the characterization of the PA (Figure 6.4(a)); however, instead of biasing the PA with a constant-voltage source, it was biased by the output of the ACC, whose input was extracted from the PA's input excitation with a directional coupler. After repeating the calibration procedure detailed in Section 6.3.2, the dynamic self-biasing behavior of the ACC-assisted GaN HEMT-based PA was characterized and the following results were obtained.

Figure 6.13(a) illustrates the result of the characterization of the PA when compensated by the Jardel ACC. As the model-fitting results indicated, the Jardel model does not provide a sufficiently accurate prediction of the instantaneous charge-trapping state for the dynamic self-biasing behavior of the GaN HEMT-based PA to be compensated at larger two-tone

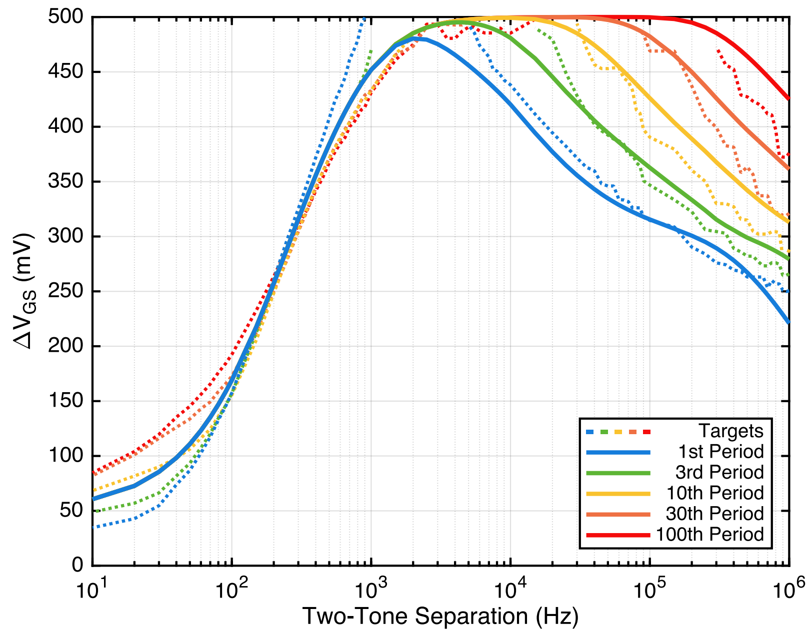

Figure 6.11 Result of the extraction of the piecewise-SRH model and, in the background, the estimated variation of the threshold voltage of the GaN HEMT.

Figure 6.12 Diagram of the measurement setup for the compensation of the dynamic self-biasing behavior of a GaN HEMT-based PA.

frequency separations. This is because the process of charge capture does not occur with a fixed time constant, but rather with a time constant that varies with the instantaneous charge-trapping state, becoming larger as the accumulated charge increases.

Figure 6.13(b) illustrates the result of the characterization of the PA when compensated by the piecewise-SRH ACC. In contrast to the Jardel ACC, the piecewise-SRH ACC was able to compensate the dynamic self-biasing behavior of the PA across both frequency and time domains. These results demonstrate definitively that a model featuring a dynamic state-variable capture time constant is able to provide much more accurate information on the transient variation of a GaN HEMT's threshold voltage, allowing for the instantaneous correction (rather than an eventual steady-state correction) of the current collapse that would otherwise occur.

6.6 Conclusion

In this chapter we detailed a method for the characterization of the dynamic self-biasing behavior of GaN HEMT-based PAs using transient two-tone large-signal RF measurements. This method, which can be performed using conventional RF laboratory equipment, not only provides comprehensive measured data on the capture and emission dynamics of charge-trapping phenomena, but also reveals that the charge-capture process can be much slower than what is traditionally assumed. This result is in agreement with recent publications on this topic [91].

After presenting our characterization method, we demonstrated that the accurate modeling of the dynamic self-biasing behavior of GaN HEMT-based PAs is contingent on the capture process being described by a state-variable time constant—more specifically, a time constant that increases with the accumulation of trapped charge, as formulated by the SRH physical model of charge trapping. This result underscores the importance of

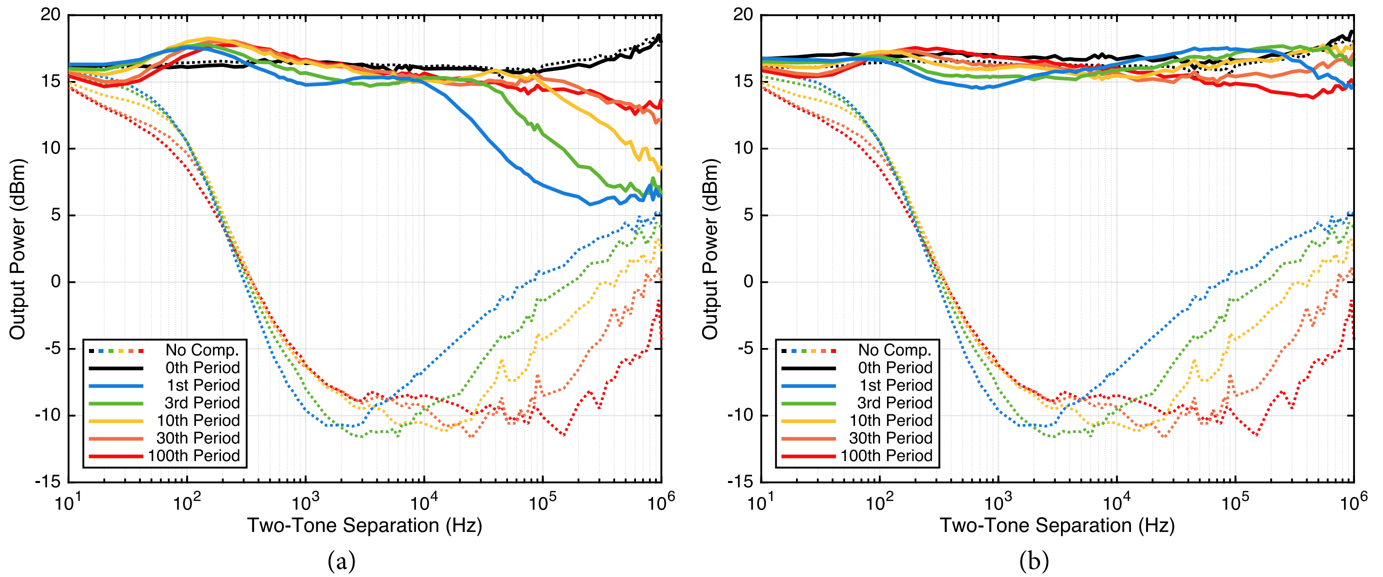

Figure 6.13 Dynamic variation of the small-signal PA output power when compensated by (a) the Jardel ACC and (b) the piecewise-SRH ACC.

accurately characterizing and modeling the dynamics of charge capture: while previous works have found moderate success in modeling charge-trapping phenomena in pulsed or steady-state conditions by dismissing the process of charge capture as a near-instantaneous event, this work (in accordance with [91]) demonstrates that the charge-capture process has an important contribution to the transient behavior of charge-trapping phenomena and the long-term memory effects caused by them—a contribution that cannot be accurately predicted with a fixed capture time constant.

Finally, we developed a behavioral model that approximates the SRH model with a piecewise-defined state-variable capture time constant, and implemented it as a fully analog electronic circuit for the compensation of the dynamic self-biasing behavior of a GaN HEMT-based PA. For comparison purposes, we also implemented the conventional charge-trapping model with a fixed capture time constant as an analog circuit. After characterizing the dynamic self-biasing behavior of the PA-under-test with and without the assistance of each of the ACCs, we verified that only the circuit based on the piecewise-SRH model was able to accurately preserve the class of operation of the PA and completely eliminate any transient symptom of current collapse during the transient evolution of the GaN HEMT's internal trapping state. Based on the work reported in Chapter 3 and Chapter 4, where an ACC was paired with a DPD unit to create a hybrid analog/digital linearization scheme, this result has important implications on the linearizability of GaN HEMT-based PAs for communications applications.

CHAPTER 7

Conclusion

Synopsis — In this chapter we summarize the main contributions of the work reported in this thesis and propose relevant avenues for future research.

7.1 Summary of Main Contributions

In this thesis, we reported our work on the characterization, modeling and compensation of the nonlinear long-term memory effects caused by thermal and charge-trapping phenomena in GaN HEMT-based RF PAs. In Chapter 3, we proposed a novel hybrid analog/digital linearization scheme where an analog electronic circuit compensates the long-term memory of a GaN HEMT-based PA and a low-complexity DPD unit compensates the remaining short-term memory and static nonlinearity. In Chapter 4, we proposed a novel behavioral model that considers a variable emission time constant and detailed its implementation as an analog electronic circuit for integration in hybrid analog/digital linearization schemes for 5G NR communications. In Chapter 5, we demonstrated that the working principle of our proposed ACCs—the modulation of the gate–source voltage of the HEMT—has the potential of completely compensating the nonlinear long-term memory effects that degrade the linearity of GaN HEMT-based PAs. Moreover, in this chapter we provided one of the earliest evidences of the slow dynamics associated with charge capture. Finally, in Chapter 6 we proposed a novel experimental method for the characterization of the dynamic self-biasing behavior of GaN HEMT-based PAs. This simple method provides arguably the most complete characterization of the charge capture and emission dynamics close to the actual operating conditions of GaN HEMT-based PAs. Moreover, in this chapter we proposed a novel behavioral model that considers a variable capture time constant and detailed its implementation as an analog electronic circuit for integration in hybrid analog/digital linearization schemes.

While charge-trapping phenomena remain pervasive in GaN HEMT technology and the resulting long-term memory effects prevent it from being deployed in many applications, external circuit-level solutions such as our ACCs can be used to further increase the deployment of high-power-density high-efficiency GaN HEMT-based PAs. Although our proposed ACC implementations were just proofs of concept, they were sufficient for demonstrating not only that these long-term memory effects can indeed be compensated, but also that their compensation may lead to exceptional increases in PA linearizability. We envision, then, a high-power-density high-efficiency GaN HEMT-based PA with an integrated and co-designed low-power analog signal-processing unit responsible for the compensation of the long-term memory effects caused by thermal and charge-trapping phenomena. For the linearization of this augmented PA with no apparent long-term memory effects, only a low-complexity low-power DPD unit should be required.

7.2 Future Research

Throughout this work we developed two charge-trapping behavioral models that demonstrated excellent agreement with estimated threshold voltage variation profiles under emission-dominant and capture-dominant situations. As explained in Chapter 4 and Chapter 6, respectively, these models featured either a fixed capture time constant and a variable emission time constant, or a variable capture time constant and a fixed emission time constant. While it would be possible to combine these two models and obtain an undoubtedly superior (i.e., more accurate) model with a variable capture time constant and a variable emission time constant, as illustrated in Figure 7.1 and defined in Appendix D, this would not constitute as big of an improvement as our two models did over the Jardel model with fixed capture and emission time constants. This is due to the lack of what we believe to be the next required breakthrough in the modeling and compensation of charge-trapping phenomena: generality.

In the context of this thesis, a general model of charge trapping is a model that can accurately predict the threshold voltage variation in all tests performed throughout this thesis—i.e., as a result of transient pulsed excitations, steady-state two-tone excitation, and transient two-tone excitations—with a fixed set of model parameters. For instance, in Chapter 4 we demonstrated that our model with a fixed capture time constant and a variable emission time constant is able to very accurately predict the threshold voltage variation as a result of a pulse with a given peak power. However, for our model, different pulses with different peak powers require different sets of model parameters to obtain (very) accurate estimations.

The main reason why our model with a variable emission time constant does not accurately predict the threshold voltage variation resulting from pulses with a wide range of peak powers is the fact that the emission time constant, τ_e, only varies with the instantaneous

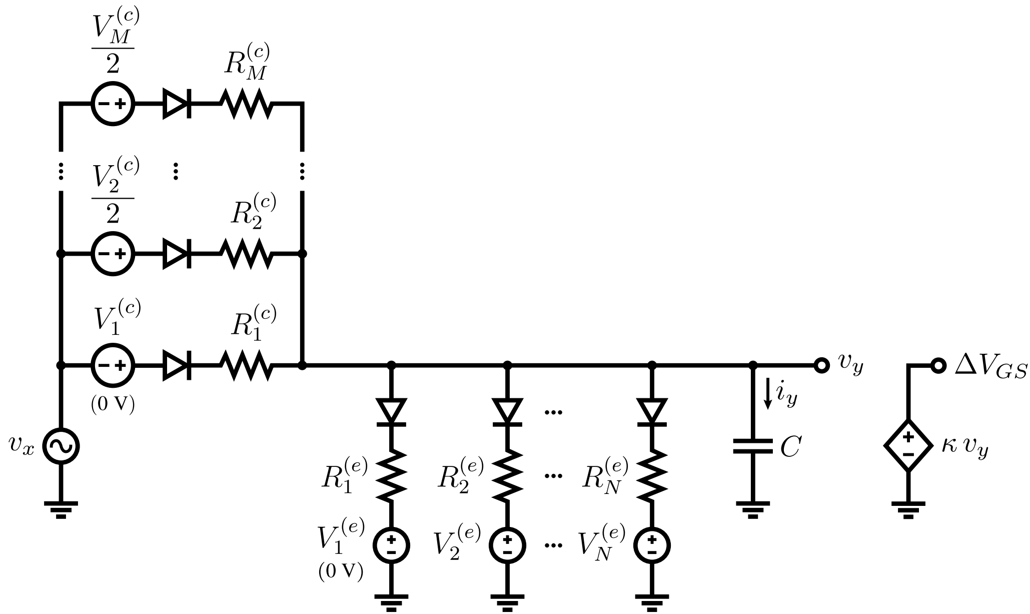

Figure 7.1 Multiple-time-scale charge-trapping behavioral model with state-variable capture and emission time constants.

output of the model, ΔV_{GS}. In other words, our model assumes that there is a one-to-one correspondence between ΔV_{GS} and τ_e. While this is true during the emission phase of a pulse with a given peak power (because the process of charge emission is monotonic), as we demonstrated in Chapter 4, it is not true when considering a range of possible pulse peak powers—i.e., it is not general. This is easily demonstrated by analyzing the recovery of the threshold voltage during the emission phase of pulses with different peak powers. For instance, Figure 7.2 illustrates the estimated threshold voltage variation following one pulse with a peak power of 30 dBm and one pulse with a peak power of 26 dBm (these results are taken from the measurements detailed in Section 4.5). The second recovery is time-shifted for visual comparison purposes. As these results indicate, the rate of emission does not have a static dependency with ΔV_{GS}, since the slope of the profile corresponding to the 26 dBm pulse is much steeper than that of the profile corresponding to the 30 dBm pulse at $\Delta V_{GS} \approx 150$ mV. Thus, contrary to what our model with a variable emission time constant assumes, the emission time constant is not statically and monotonically dependent on the instantaneous threshold voltage variation.

A general model should therefore be able to accurately estimate, with a fixed set of model parameters, the threshold voltage variation for a wide range of PA input power levels. By providing a more accurate prediction and compensation of the threshold voltage variation of a GaN HEMT, a general model as we described would constitute a major breakthrough toward the achievement of GaN HEMT-based PAs with no apparent long-term memory effects. These PAs would therefore provide all the benefits of GaN HEMT technology (high power density and efficiency) without the severe drawbacks resulting from their long-term

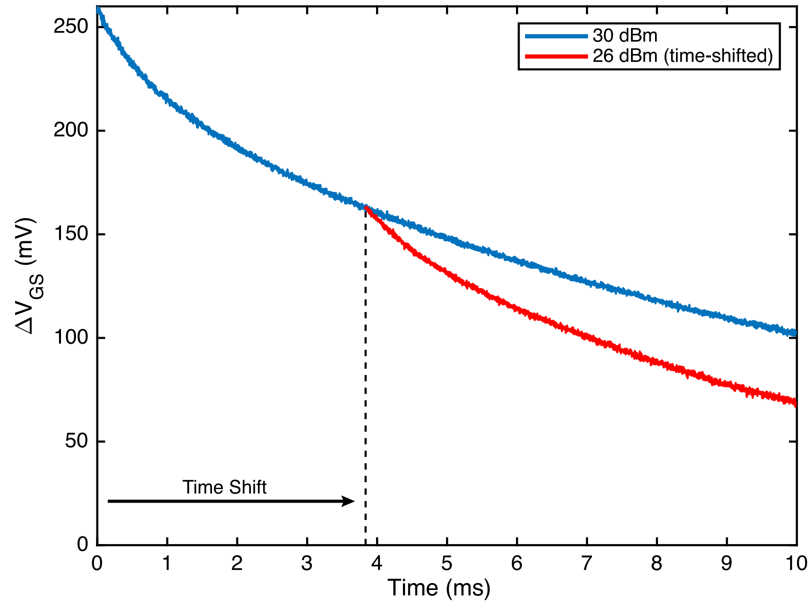

Figure 7.2 Compensation signal during the emission phase for a pulsed excitation with a peak power of 30 dBm and 26 dBm. The signal corresponding to the 26 dBm pulse is time-shifted to demonstrate that the rate of discharge is not solely dependent on the instantaneous output state.

memory. For this reason, future research should focus on understanding exactly how and why the capture and emission time constants vary (from a behavioral point of view) and developing a generalized model of charge trapping that is able to completely eliminate the long-term memory of GaN HEMT-based PAs. Moreover, future research should analyze the impact of our compensation models and ACCs on the linearizability of more advanced PA topologies, e.g., Doherty amplifiers and envelope-tracking amplifiers.

APPENDIX A

Schematic of the Jardel ACC

1. Power Supply

Input: ±6-20 V
Output: ±5 V 500 mA

U1 LT3045: IN, EN/UV, PG, SET, GND, ILIM, PGFB, OUTS, OUT
+6V; C1 22 uF; C2 4.7 uF; C3 4.7 uF; R2 49.9k; R3 715k; R4 49.9k; C4 10 uF, 20 mΩ max, 2 nH max; TP1; +5V; GND

U2 LT3094: IN, EN/UV, PG, SET, GND, ILIM, PGFB, OUTS, OUT
-6V; C5 22 uF; C6 4.7 uF; C7 4.7 uF; R5 49.9k; R6 715k; R7 49.9k; C8 10 uF, 20 mΩ max, 2 nH max; TP3; -5V; TP2; GND

2. Envelope Detector

R8: MCT06030C7509FP500
C9: GQM1875C2E101JB12D

RFIN; TX Line, W: 2.2 mm, L: 5.4 mm; C9 100 pF; R8 75

Isola IS680 substrate:
Er: 3.38
H: 1.52 mm
T: 35 um

U3 ADL5511ACPZ-R7: RFIN, ENBL, VPOS, EREF, VENV, FLT1, FLT2, FLT3, FLT4, COMM, VRMS; +VU3

R9 510; R10 510; R11 510; U4 OPA659IDBVT; +VU4; -VU4; TP4; ENVA; R12 390; R13 120; R14 22k; RP1 20k; C10 4.7 uF; +5V; -5V

C11 100 nF (+5V, +VU3); C12 100 nF (+5V, +VU4); C13 100 nF (-5V, -VU4); GND

Unit-Gain Differential Amplifier

Used because U3.VENV is referred to U3.EREF. The true envelope amplitude is equal to U3.VENV - U3.EREF.

4. Gate Voltage Adder

VTRAP; VGG; R25 510; R26 510; U10 OPA659IDBVT; +VU10; -VU10; VGS; TP7; C24 4.7 pF; R27 510; R28 390; R29 120; R30 22k; RP5 20k; C25 4.7 uF; +5V; -5V; GND

C26 100 nF (+5V, +VU10); C27 100 nF (-5V, -VU10)

Unit-Gain Voltage Adder

3. GaN Trapping Model

ENVA; R15 510; U5 OPA659IDBVT; +VU5; -VU5; D1 1SS307E; R16 22k; RP2 20k; C14 4.7 uF; +5V; -5V; GND

Precision Half-Wave Rectifier ("Super Diode")

R0 10 Ω or greater; R1; C0G/NP0 6.8 nF ±1% C; GND

U6 OPA659IDBVT; +VU6; -VU6; R17 510; R18 390; R19 120; R20 22k; RP3 20k; C15 4.7 uF; TP5

U7 AD8336: PRAO, INPN, INPP, VGAI, PWRA, VNEG, VCOM, VPOS, BIAS, -60 dB to 0 dB, +34 dB, GAIN CONTROL, GPOS, GNEG, VOUT; R21 510; R22 510; -VU7; +VU7; VTRAP; TP6

RP4 20k; U8 ADR510; U9 ADR510; R23 3.9k; R24 3.9k; C16 4.7 uF; C17 4.7 uF

±1.000 V Voltage Reference

C18 100 nF (+5V, +VU5); C19 100 nF (-5V, -VU5); C20 100 nF (+5V, +VU6); C21 100 nF (-5V, -VU6); C22 100 nF (+5V, +VU7); C23 100 nF (-5V, -VU7)

5. Interface

J1 Banana Jack, Red: +6V
J2 Banana Jack, Black: GND
J3 Banana Jack, Blue: -6V
J4 Screw Terminal: 1, 2, 3; TP8; VGG; C28 22 uF; C29 100 nF; GND
J5 SMA Jack: RFIN, GND
J6 SMA Jack: VGS, GND

Title	An Analog Implementation of the Jardel Model for the Compensation of Trapping Effects in GaN HEMT-Based PAs	
Size: A3	Number: Pedro M. Tomé	Revision: H
Date: 27/01/2020		Sheet of 1 / 1
File: D:\Dropbox\..\RevH_SCH.SchDoc		Drawn By:

APPENDIX B

Schematic of the Variable-Time-Constant Emission ACC

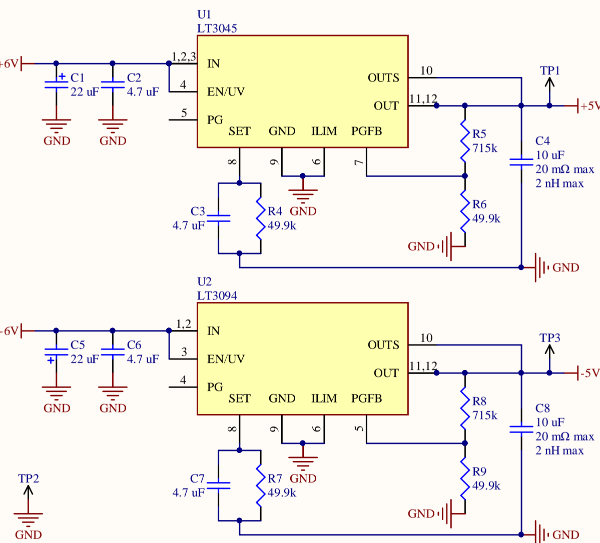

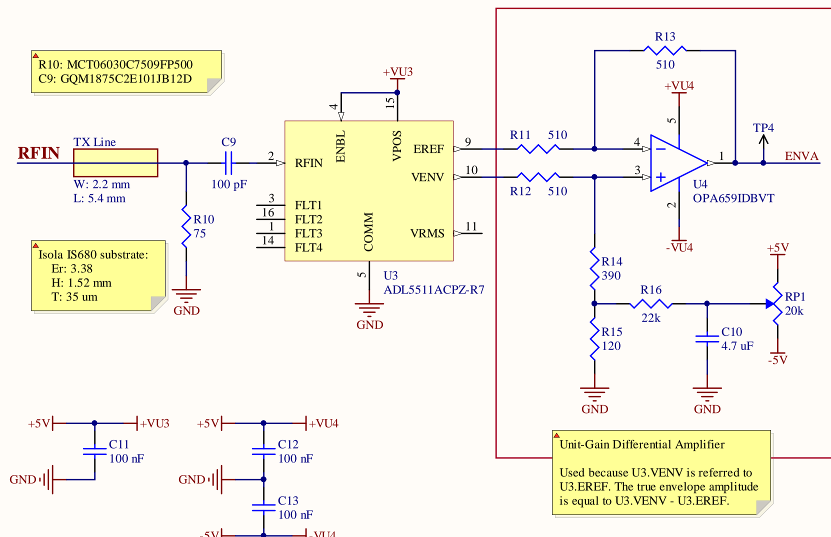

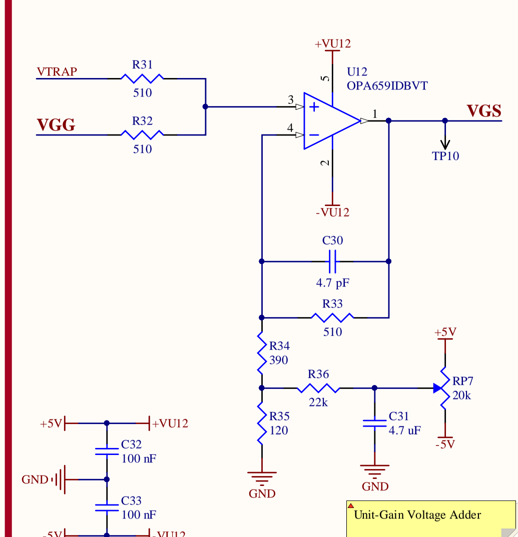

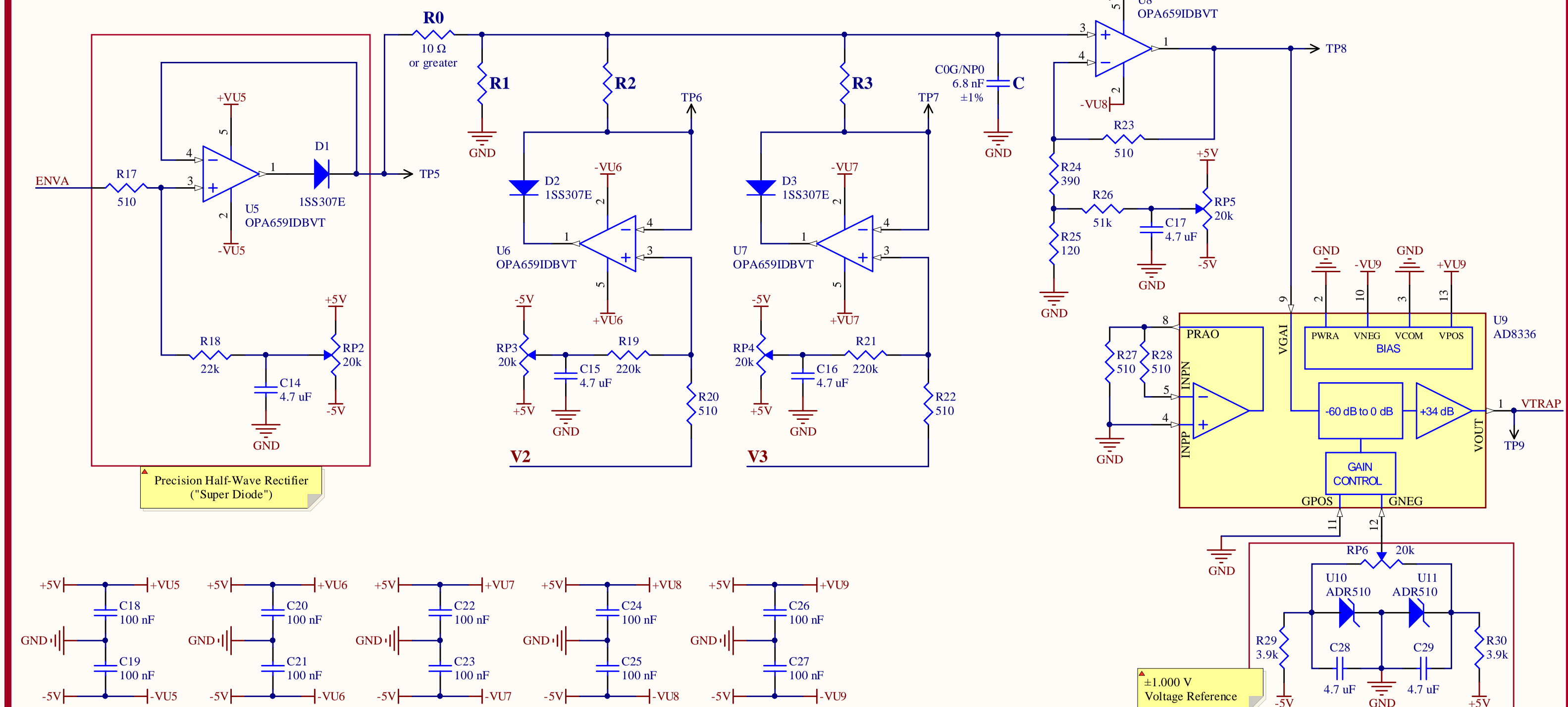

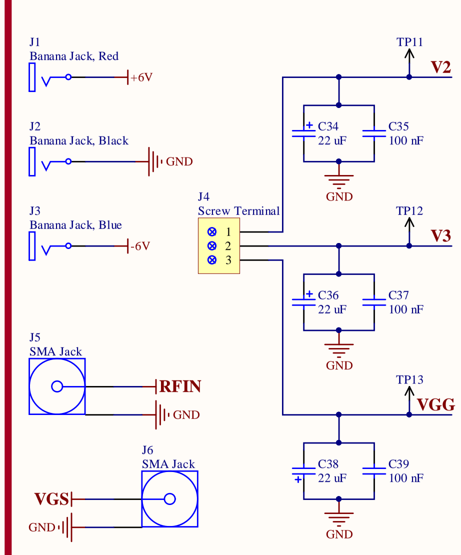

Title	An Analog Circuit for the Multiple-Time-Scale Compensation of GaN Trapping Effects	
Size: A3	Number: Pedro M. Tomé	Revision: B
Date: 29/08/2020	Sheet of 1 / 1	
File: D:\Dropbox\..\RevB_SCH.SchDoc	Drawn By:	

APPENDIX C

Schematic of the Piecewise-SRH ACC

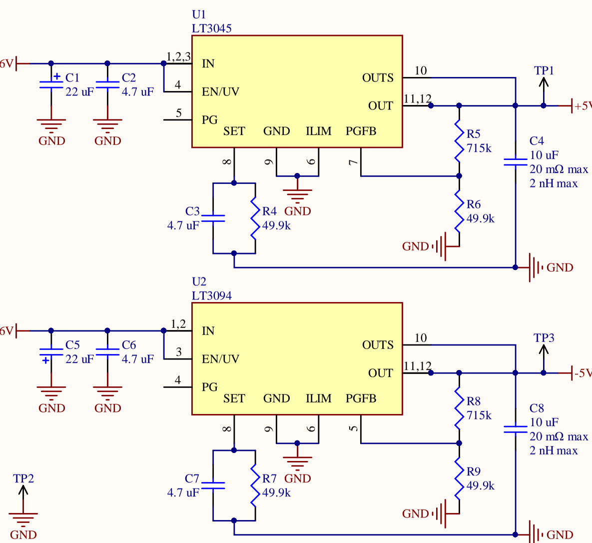

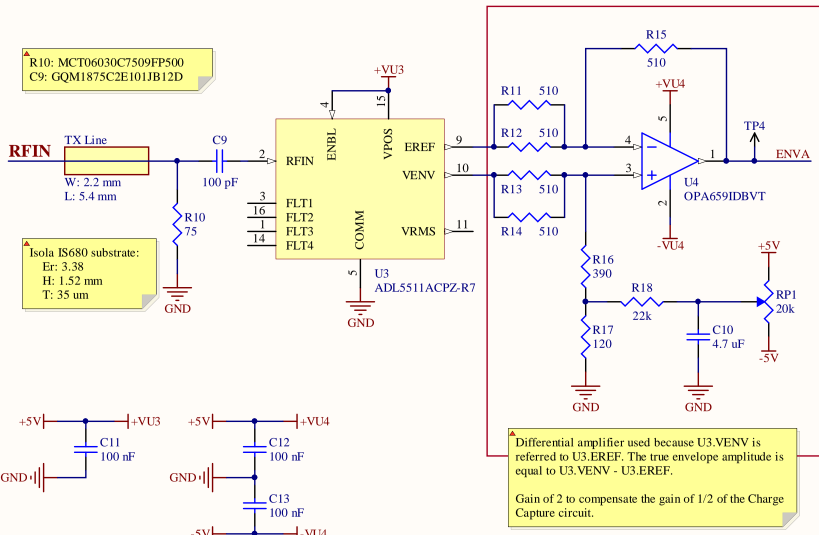

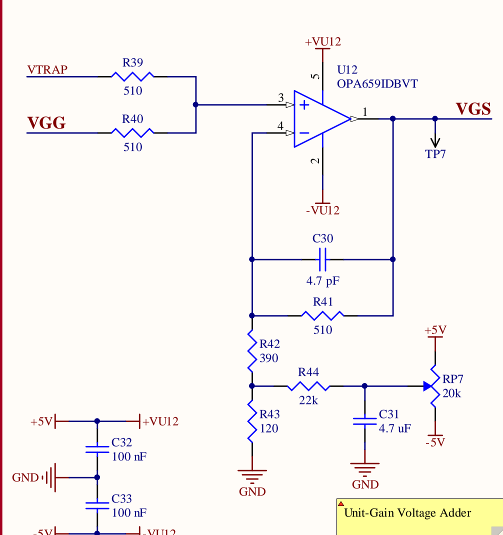

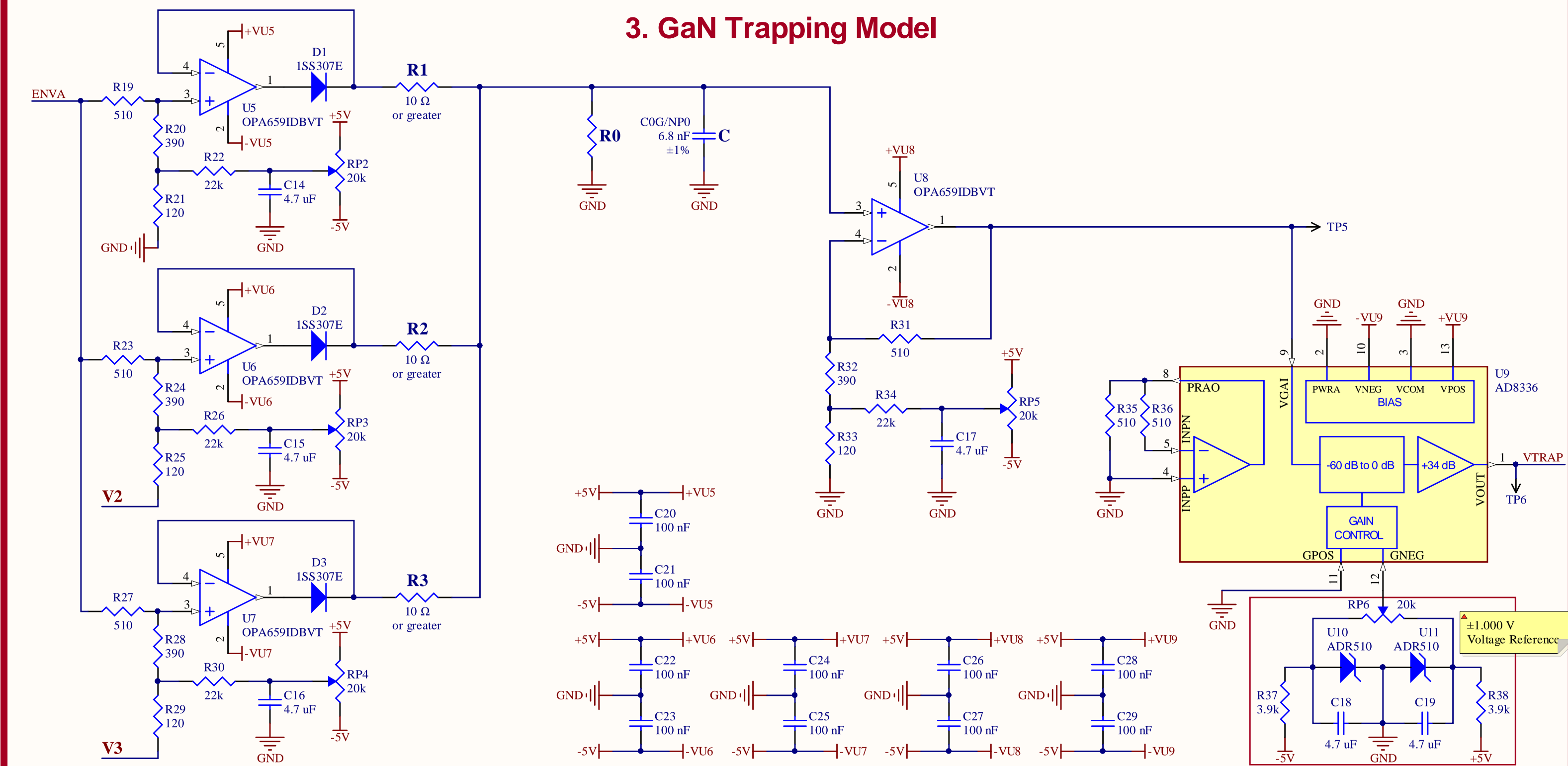

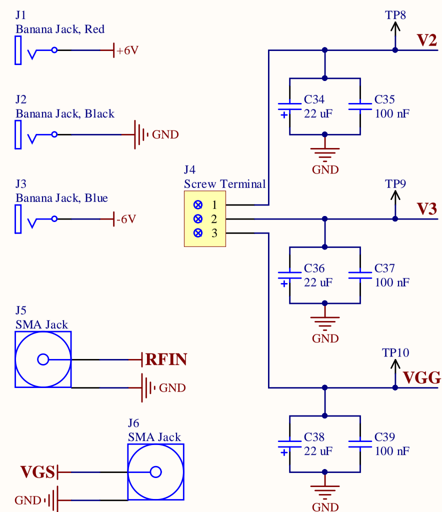

Title	An Analog Implementation of the SRH Model for the Compensation of Trapping Effects in GaN HEMT-Based PAs	
Size: A3	Number: Pedro M. Tomé	Revision: A
Date: 27/01/2020		Sheet of 1 / 1
File: D:\Dropbox\..\RevA_SCH.SchDoc		Drawn By:

APPENDIX D

Extended Variable-Time-Constant Charge-Trapping Model

The charge-trapping model with variable capture and emission time constants illustrated in Figure 7.1 is defined as follows. Let $v_x(t)$ denote the amplitude of the envelope of the PA's input excitation. Moreover, let $\Delta V_{GS}(t) = \kappa\, v_y(t)$ denote the threshold voltage variation predicted by the model, where κ is a scaling factor and $v_y(t)$ is the voltage at the capacitor. Finally, let $f_D(\cdot)$ denote the transfer function, defined in (D.1), of the ideal diodes.

$$f_D(x) \;=\; \begin{cases} x, & x \geq 0 \\ 0, & x < 0 \end{cases} \tag{D.1}$$

Then, the net capacitor current $i_y(t)$ is defined as in (D.2); the voltage at the capacitor $v_y(t)$ is defined as in (D.3); and, using Euler's method, $v_y(t)$ can be discretized as in (D.4), where n denotes the sample index and f_s denotes the sampling frequency.

$$i_y(t) \;=\; \sum_{m=1}^{M} f_D\!\left(\frac{v_x(t) + V_m^{(c)}/2 - v_y(t)}{R_m^{(c)}}\right) \;-\; \sum_{n=1}^{N} f_D\!\left(\frac{v_y(t) - V_n^{(e)}}{R_n^{(e)}}\right) \tag{D.2}$$

$$v_y(t) \;=\; \frac{1}{C}\int_{t_0}^{t} i_y(\tau)\, d\tau \;+\; v_y(t_0) \tag{D.3}$$

$$v_y(n+1) \;=\; v_y(n) \;+\; \frac{1}{f_s\, C}\; i_y(n) \tag{D.4}$$

APPENDIX E

Paper J2

Hybrid Analog/Digital Linearization of GaN HEMT-Based Power Amplifiers

Pedro M. Tomé, Filipe M. Barradas, Telmo R. Cunha, and José C. Pedro

Published In: IEEE Transactions on Microwave Theory and Techniques (Vol. 67, No. 1, Jan. 2019)

Pages: 288–294

Date of Publication: 05 December 2018

DOI: 10.1109/TMTT.2018.2880911

This is the authors' version of an article that has been published in the IEEE TRANSACTIONS ON MICROWAVE THEORY AND TECHNIQUES. Changes were made to this version by the publisher prior to publication.
The final version of the record is available at https://doi.org/10.1109/TMTT.2018.2880911.

Hybrid Analog/Digital Linearization of GaN HEMT-Based Power Amplifiers

Pedro M. Tomé, *Student Member, IEEE,* Filipe M. Barradas, *Member, IEEE,* Telmo R. Cunha, *Member, IEEE,* and José C. Pedro, *Fellow, IEEE*

***Abstract*—In this work we describe a hybrid analog/digital linearization scheme for GaN HEMT-based power amplifiers that consists of a novel analog feedforward circuit and a conventional generalized memory polynomial (GMP) digital predistorter (DPD). The analog circuit implements a nonlinear filter that compensates the long-term memory effects observed in GaN HEMTs due to the self-biasing behavior caused by electron trapping phenomena. Experimental tests demonstrate that this linearization scheme achieves a level of intermodulation distortion 6.8 dB better than what can be achieved with just the use of the GMP DPD. This level of distortion is in compliance with the linearity specifications for multicarrier GSM base station transmitters.**

***Index Terms*—Analog linearization, digital predistortion (DPD), electron trapping, GaN HEMT, long-term memory effects, power amplifier linearization.**

I. INTRODUCTION

WITH the recent maturity of GaN high-electron-mobility transistor (HEMT) technology, radio-frequency (RF) power amplifier (PA) designers have benefited from the semiconductor's material properties to develop PAs with unprecedented output power capabilities, high power efficiencies, and wide bandwidths of operation [1], [2]. While these are some of the desirable attributes of any PA, they more often than not come at the expense of linearity: a characteristic that is compulsory in applications such as base station transmitters for cellular telecommunications. For this reason, PAs are typically accompanied by digital predistortion (DPD) units that compensate their nonlinear behavior and thus complete an amplification chain that features all of the aforementioned benefits [3].

While this has been a general solution for obtaining highly linear and efficient PAs for over a decade—preceding them with a DPD—, GaN HEMT-based PAs have proved to be uniquely challenging in being linearized due to their highly unusual nonlinear behavior. This nonlinear behavior is mainly attributed to electron trapping phenomena that produce long-term memory effects not captured by most traditional DPD schemes [4]: the time constants associated with these effects are 3 to 6 orders of magnitude larger than those associated with short-term memory effects. This has prevented the reliable compliance with the linearization levels enforced in the cellular telecommunications industry even with state-of-the-art DPD schemes such as the generalized memory polynomial (GMP) of Morgan *et al.* [5].

While there have been several proposals for modeling and compensating the multiple-time-scale nonlinear behavior of RF PAs (not necessarily based on GaN HEMTs) [4], [6]–[9], only in 2017 did Barradas *et al.* [10] publish the first DPD scheme capable of linearizing a GaN HEMT-based PA to a level that meets the linearity specifications for multicarrier signals in the Global System for Mobile Communications (GSM) standard: intermodulation components that do not exceed −60 dBc and a noise floor that does not exceed −70 dBc [11]. The DPD scheme proposed in [10] consisted in a conventional GMP model whose coefficients change, over time, as a function of the input signal envelope in order to counteract the long-term memory effects experienced by the GaN HEMT due to both thermal and electron trapping phenomena—this is, then, a parametric model. It is a physics-level understanding of these phenomena that is used to relate the change of the DPD coefficients to the input signal envelope.

Our approach is very different from all of these former works. Instead of coercing a traditional DPD model into operating over a time scale that is much longer than what it was initially intended for, in this work we first compensate the long-term memory effects of a GaN HEMT-based PA using a novel analog solution—thus rendering the PA effectively memoryless (in the long term)—and then use a completely unmodified GMP DPD to linearize it up to a level that is in compliance with the exceptionally stringent multicarrier GSM standard. The hybrid analog/digital linearization scheme proposed herein is thus an important step away from the ever more complex DPD schemes; rather, its implementation is simple and its performance, as we demonstrate in this paper, is comparable (or better) to that of previous works.

Equally important is the distinction between the application—e.g., the linearization of a multicarrier GSM transmitter—and our actual contribution to the state of the art in GaN HEMT linearization: a fully analog compensator of the long-term memory effects caused by electron trapping. It is our understanding that this contribution should provide great benefits not only to GaN HEMT-based PAs used in multicarrier GSM transmitters, but also to those used in communications systems employing time-division duplexing

Manuscript submitted June 22, 2018.
This work was funded by FCT/MEC through national funds under the project UID/EEA/50008/2013 (APIC) and the project PTDC/EEI-TEL/7049/2014 (Lin5GPA). The work of P. M. Tomé was supported by FCT/MEC under Ph.D. Grant PD/BD/128198/2016.
The authors are with DETI, Instituto de Telecomunicações, Universidade de Aveiro, 3810–193 Aveiro, Portugal (e-mail: tome.p.m@ua.pt; filipebarradas@ua.pt; trcunha@ua.pt; jcpedro@ua.pt)

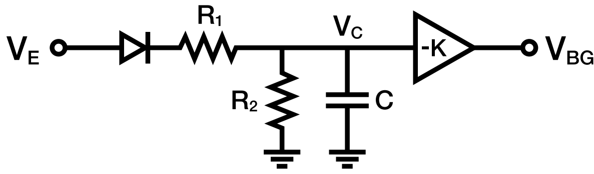

Fig. 1. Nonlinear multiple-time-constant model of the self-biasing caused by electron trapping in GaN HEMTs. V_E is the amplitude of the input envelope; V_{BG} is the back gate voltage. The diode is assumed to be ideal ($V_f = 0$ V).

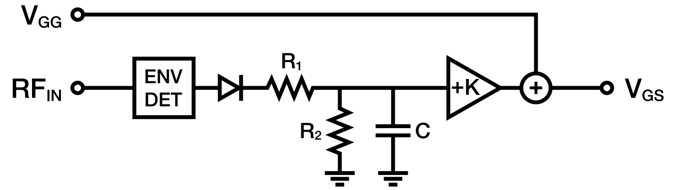

Fig. 2. Diagram of the analog feedforward circuit for the compensation of long-term memory effects due to the self-biasing caused by electron trapping in GaN HEMTs.

schemes, new multi-level waveforms such as 802.11ay, and radars.

This paper is organized as follows. In Section II we review the electron trapping model from which we based our solution. In Section III we describe our analog feedforward circuit that compensates the long-term memory effects caused by electron trapping in GaN HEMTs. In Section IV we detail our methodology and experimental setup for demonstrating that the analog compensation circuit works as hypothesized. In Section V we present the results. Finally, in Section VI we present our final remarks and conclusions regarding this work.

II. Electron Trapping Model

The main cause of long-term memory effects in GaN HEMT-based PAs is electron trapping. While the exact physics responsible for electron trapping are still not entirely understood, it has been shown that this phenomenon can be interpreted as the charging and discharging of a virtual back gate which produces a self-biasing effect [12], [13]. Moreover, in [14] Kunihiro and Ohno used the Shockley–Read–Hall formulation for carrier generation and recombination in deep-level traps to demonstrate that electron capture and emission—or, on a larger scale, trap charge and discharge—happen at very different rates: from nanoseconds, for the charge process, to microseconds or even milliseconds for the discharge process.

From a modeling perspective, these results translate into Fig. 1, a physically meaningful nonlinear circuit with different charge and discharge time constants first deduced in [14], later overhauled in [15], and finally adapted in [10]. This circuit, whose dynamics are defined in (1), models the (negative) back gate voltage, V_{BG}, as a nonlinear function of the amplitude of the input envelope, V_E. Thanks to the diode, assumed to be an ideal switch (forward voltage equal to 0 V), the circuit works much like a peak detector with different charge and discharge time constants. Since the discharge time constant is typically much greater than the charge time constant (3 to 6 orders of magnitude), the charge time constant is approximately equal to $\tau_1 = R_1 C$ and the discharge time constant is equal to

$$\frac{dV_C}{dt} = \begin{cases} \dfrac{1}{R_1 C} V_E - \dfrac{R_1 + R_2}{R_1 R_2 C} V_C & , \quad V_E \geq V_C \\ -\dfrac{1}{R_2 C} V_C & , \quad V_E < V_C \end{cases} \tag{1}$$

$\tau_2 = R_2 C$. The parameter $-K$ is merely a constant of proportionality—for easier model extraction, V_E is typically normalized to a peak value of 1 V.

As the authors of [10] note, this model is only an accurate approximation of the self-biasing behavior caused by electron trapping if there is a linear relation between the input envelope amplitude and the output drain voltage. Since this model is mostly dependent on the peaks of the signal, we agree (and our results demonstrate) that this is a reasonable assumption.

III. Analog Compensation Circuit

In order to compensate the long-term memory effects caused by electron trapping in GaN HEMT-based PAs, we developed a feedforward circuit that corrects the self-biasing behavior evident in these devices using analog components. This analog compensation circuit (ACC), illustrated in Fig. 2 and pictured in Fig. 3, implements the electron trapping model reviewed in Section II and adds the back gate voltage, with opposite sign, to the intended (constant) HEMT gate bias voltage, V_{GG}. This results in the compensated (modulated) gate–source voltage, V_{GS}, that is used to bias the GaN HEMT. The input envelope is extracted from the coupled PA excitation signal, RF_{IN}, using a commercially available envelope detector. The ideal diode is implemented using a Schottky diode whose forward voltage is compensated by an operational amplifier in a local feedback loop [16].

In summary, our ACC achieves the following. Suppose the HEMT is biased at a gate–source voltage V_{GS} that is initially equal to V_{GG}. When the HEMT is excited by an input signal, a drain–source voltage is generated and charge carriers (e.g., electrons) in the vicinity of the GaN channel become trapped for a mean time of $\tau_2 = R_2 C$, thus creating an electric field that constricts the channel [17]. This is equivalent to there being a virtual back gate with a negative voltage V_{BG} which varies with the amplitude of the input envelope. In order to counteract the constrictive action of the back gate, the gate bias voltage is modulated in direct opposition to V_{BG}, producing V_{GS}. The result is a net gate voltage that is always equal to V_{GG} and the absence of long-term memory effects due to electron trapping—provided, that is, that the usual large-value bypass capacitor at the gate bias terminal of the PA is removed (otherwise the modulated V_{GS} would be bypassed to ground).

The initial estimation of the parameters of the model (and thus of the implemented circuit) closely followed the procedure described in [18]. This included the characterization of the small-signal gain of the PA as a function of the gate bias voltage, the measurement of the PA's small-signal response to

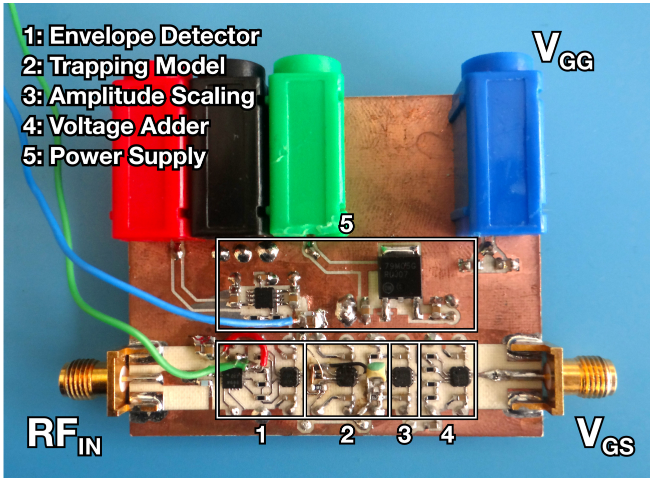

Fig. 3. Photograph of the analog compensation circuit.

large-signal two-tone inputs of various frequency separations, and the optimization of the trap discharge time constant, τ_2, for obtaining the best agreement between the frequency-dependent back gate voltage derived from the measurements and the one modeled using the electron trapping model of Section II. In order to accelerate the initial estimation procedure, trap charge was considered to be instantaneous, resulting in the following first estimates: $\tau_1 = 0$ µs, $\tau_2 = 145$ µs ($R_2 = 27$ kΩ, $C = 5.1$ nF), and $K = 242$ mV/V. After manually tuning the circuit parameters for obtaining optimum results (see Section V), we obtained $\tau_1 = 0.14$ µs ($R_1 = 27$ Ω), $\tau_2 = 58$ µs, and $K = 90$ mV/V.

IV. Practical Validation

A. Validation Procedure

After implementing the ACC, we set out to verify whether it could compensate the long-term memory effects of a GaN HEMT-based PA and improve its linearizability. In order to do this, we devised the following two-part procedure. First, the PA was linearized using a GMP DPD with the ACC disconnected; V_{GS} was therefore constant and equal to V_{GG}. Then, the PA was linearized using both the ACC, which modulated V_{GS}, and a GMP DPD with the same complexity as the one used in the first test (parameter set $\{P, M, K, L\} = \{9, 4, 5, 4\}$, according to the GMP model definition in [5]).

For this procedure, we selected a waveform that would excite not only the short-term characteristics of the PA, but its long-term ones as well: the 4-carrier GSM signal illustrated in Fig. 4. This baseband signal was sampled at 100 MHz, centered at 2.47 GHz, and scaled so that its peak envelope amplitude would be equal to 30 dBm. Observe that not only is this a slotted signal, it also features a low-amplitude training sequence between the 0.46 ms and the 0.60 ms marks. These two aspects, as well as the fast modulation of the instantaneous envelope amplitude, contribute to an excitation that is rich in both short-term dynamics (which a conventional GMP can account for) and long-term dynamics. These long-term dynamics, namely the wide—but slow—variation of the mean envelope amplitude, produce a rich set of electron trapping states that a conventional GMP could not possibly account for (it would require a memory depth in the order of 10^3 to 10^6 samples).

After performing this procedure, the validation of our hypothesis was done by comparing, between the two linearization tests (without and with the ACC), a measure of the long-term memory of the PA and its linearity. This measure refers to a residual signal $r(n)$ calculated as in (2), where $\widetilde{w}(n)$ is the measured output complex envelope of the predistorted PA, $\widetilde{w}_{\text{GMP}}(n)$ is the output complex envelope of the predistorted PA computed using a forward GMP model of the PA, and n is the sample index. Since the modeled PA output captures not only the static gain of the PA but its short-term memory characteristics as well, the residual signal that remains from the subtraction with the measured PA output is, by definition, a result of the long-term memory characteristics of the PA that the GMP model cannot predict. Thus, any deviation of $r(n)$ from a value of 0 V indicates a time period in which the GMP DPD would have failed to linearize the PA because of long-term memory effects.

Since the training sequence of the 4-carrier GSM input signal has a duration that is long enough for the electron trapping state to vary greatly (in the form of electron emission, or trap discharge), we expect to see, during this period, a very noticeable increase in the magnitude of $r(n)$ when the ACC is not being used. When the ACC is being used, however, we expect the residual signal not to deviate very much from 0 V and, as a consequence, we expect the level of distortion at the output of the PA to be lower. If both of these expectations are verified, then we can state unequivocally that the ACC improves the linearizability of the GaN HEMT-based PA by compensating the long-term memory effects due to the self-biasing caused by electron trapping phenomena.

$$r(n) = |\widetilde{w}(n)| - |\widetilde{w}_{\text{GMP}}(n)| \tag{2}$$

We note that in this paper we adopted the following convention: $x(t) = \text{Re}\{\widetilde{x}(t)\exp(j2\pi f_c t)\}$, where $x(t)$ is a real RF signal, $\widetilde{x}(t)$ is the corresponding baseband complex envelope, f_c is the center frequency, and $\text{Re}\{\widetilde{z}\}$ is the real part of $\widetilde{z}$. We also assumed that the sampling frequency of 100 MHz was sufficient to properly characterize the dynamics of the PA and thus sufficient to generate an inverse model (the GMP DPD).

B. Laboratory Setup

In order to test our hypothesis, we assembled the laboratory setup schematized in Fig. 5 and pictured in Fig. 6. The PA, built in-house for demonstration purposes, was based on the 10 W Wolfspeed CGH40010 GaN HEMT and was biased in class B with $V_{GG} = -2.68$ V, leading to a quiescent current of 20 mA ($\sim$1% of I_{DSS}).

The PA input chain consisted of a Rohde & Schwarz SMU200A vector signal generator (VSG) followed by a Mini-Circuits ZHL-16W-43-S+ driver and a Narda 4913 isolator. The PA output chain consisted of a fixed −43 dB attenuator and a Rohde & Schwarz FSW8 vector signal analyzer (VSA). Moreover, in order to source and measure the dc power of

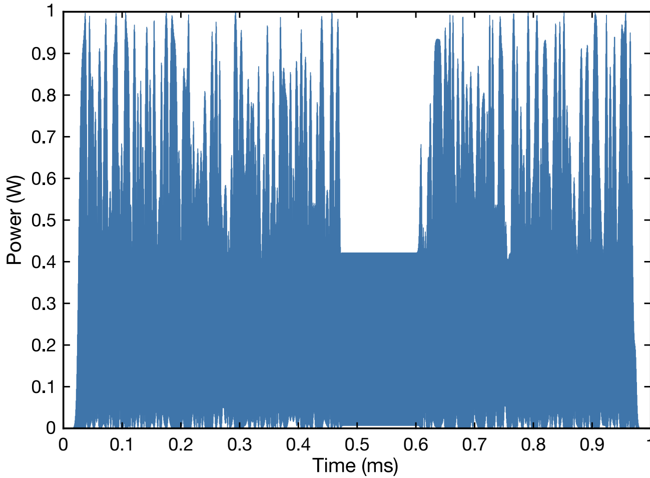

Fig. 4. Envelope amplitude of the 4-carrier GSM PA input signal.

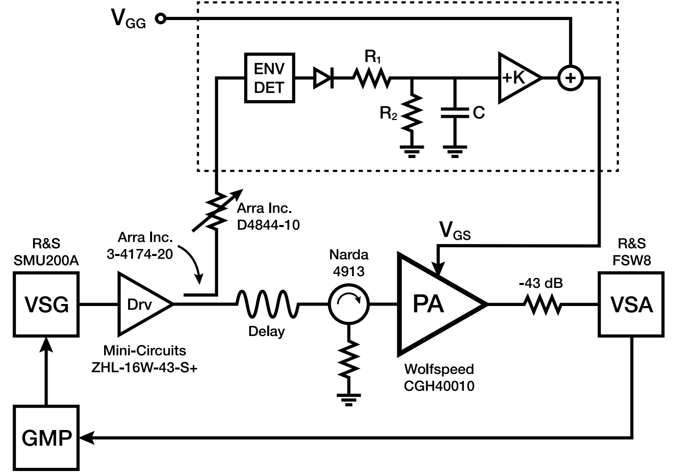

Fig. 5. Diagram of the laboratory setup.

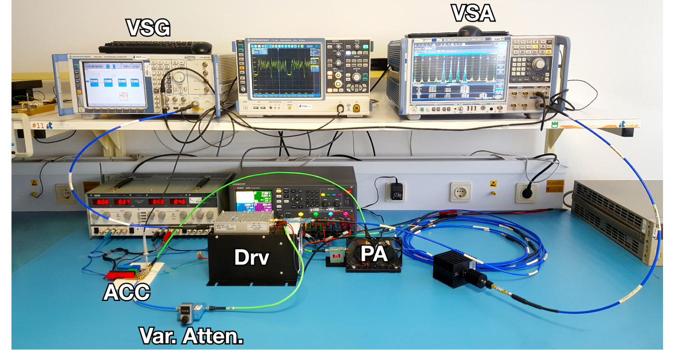

Fig. 6. Photograph of the laboratory setup.

the PA, a Keysight N6705C dc power analyzer was used. For increased measurement accuracy, the internal 10 MHz oscillator of the VSA was used as the reference for both the VSA and the VSG, and a baseband trigger signal was provided by the VSG to the VSA.

The input signal of the ACC was extracted from the input of the PA using an Arra Inc. 3-4174-20 directional coupler, and an 8.9 m coil of coaxial cable was used to compensate the group delay of the ACC (measured at 46.8 ns using a Tektronix MSO71604C oscilloscope). In order to more easily tune the parameters of the ACC, K was made constant and, instead, an Arra Inc. D4844-10 mechanically variable attenuator was used to set the amplitude of the input signal.

All instruments were connected, through a local area network, to a personal computer that uploaded input signal envelopes, downloaded output signal envelope and drain current measurements, and implemented the GMP DPD. All measurements were done at a controlled ambient temperature of 23 °C, and the PA was provided with some auxiliary ventilation.

C. Setup Calibration

The setup was calibrated at the PA input plane using a Keysight E9301A average power sensor connected to a Keysight N1913A power meter. The calibration procedure consisted in sweeping the power level of the VSG, measuring the power level at the PA input plane with the power meter, and computing a calibration factor equal to the mean power gain.

Before doing this, however, the average power sensor and the power meter were first calibrated using the reference power source built into the power meter and a −20 dB attenuator whose S-parameters were measured using a Keysight N5242A network analyzer (which was calibrated using the standard open–short–load–through procedure). This was a necessary preliminary step because the E9301A average power sensor toggles between two measurement ranges which feature a strong discontinuity even after completing the built-in calibration procedure.

After being calibrated, the PA input chain (including the delay line) was used as a reference power source to calibrate the PA output chain at the PA output plane in a way similar to that used in the calibration of the PA input chain.

V. Results

In Section II we established that the electron trapping phenomenon in GaN HEMTs produces an effect equivalent to that of a back gate voltage V_{BG} that adds to the gate bias voltage V_{GG} and generates strong long-term nonlinearities by driving the net gate bias voltage towards more negative values. To counteract this effect, we developed an ACC that models V_{BG} and adds it, with opposite sign, to V_{GG}, resulting in a compensated V_{GS} (see Fig. 7 for an example output). By biasing the gate with this varying V_{GS} instead of the constant V_{GG}, the HEMT should produce no long-term memory effects and therefore should be more easily linearizable.

To demonstrate this, we computed the residual signal defined in (2) for the two linearization tests (without and with the ACC) and plotted it in Fig. 8. This signal, which was filtered by a sharp $1/\tau_2 \approx 17$ kHz low-pass filter, is essentially the difference (the error) between the PA output that was measured and the PA output that can be predicted by a GMP. As such, the residual is a direct result of the long-term memory effects that the GMP DPD does not compensate—if it did, there would

be no residual (error). As expected, in the linearization test where the ACC is not used we can observe a massive increase in the magnitude of the residual during the training sequence of the 4-carrier GSM input excitation. Also as expected, we can observe a very significant reduction of this residual when the ACC is used, as well as a slight overall correction of the ultra-slow deviation from 0 mV. We can, therefore, conclude that the ACC does, indeed, compensate the long-term memory effects due to the self-biasing behavior caused by electron trapping phenomena in GaN HEMT-based PAs.

Having confirmed that the ACC compensates the long-term memory of the PA, it only remains to be shown that this translates into an improvement in the linearizability of the PA. Fig. 9 reveals that, indeed, it does. For a 4-carrier GSM input excitation with a peak power of 30 dBm (mean power of 23.7 dBm), the PA produced an output signal with an intermodulation distortion ratio (IMR) of −58.95 dB when being linearized with a conventional GMP DPD, and an IMR of −65.77 dB when being linearized with our ACC and a GMP DPD with the same parameter set (the same complexity). Despite this 6.82 dB improvement in linearity, the power-added efficiency (PAE) only decreased by 0.5 p.p.: from 29.1 % in the former case to 28.6 % in the latter. The peak output power in both cases was, respectively, 40.85 dBm and 40.78 dBm. These results are summarized in Table I.

Fig. 10 illustrates the power gain (AM–AM) and phase shift (AM–PM) profiles of the PA under three circumstances: when no linearization is being done, when the ACC is being used to compensate the self-biasing of the HEMT due to electron trapping, and when the complete hybrid analog/digital linearization scheme is being employed. In Section IV-B we mentioned that the PA was initially biased in class B, yet this figure reveals that the PA is still operating in class C even when the ACC is being used. While it might seem that the ACC failed to accomplish its objective—to compensate the self-biasing of the HEMT due to electron trapping—, not pushing the class of operation of the PA to a textbook class B was a deliberate decision of ours. In reality, we could have chosen τ_2 and K so large that the PA would be effectively biased in class A; while this would have resulted in a complete absence of long-term memory effects and an ultra-linear response, the power efficiency would have been catastrophically degraded. In fact, our tuning of the ACC parameters was done not just with the improvement of the linearizability of the PA in mind, but also with the preservation of its power efficiency. The resulting gain profile reflects the compromise between increased linearizability and reduced power efficiency that we deemed adequate. To demonstrate that the ACC does have the ability to compensate not only the dynamic self-biasing of the GaN HEMT (as shown in Figs. 8 and 9) but its static self-biasing as well, we also show in Fig. 10 the gain and phase shift profiles of the PA for a case in which the ACC was used to drive the operation of the PA into class B.

VI. Conclusion

In this work we identified that the model for the effects of electron trapping in GaN HEMT-based PAs could be implemented as a simple feedforward analog circuit that dynamically changes the bias voltage of the HEMT's gate. Having implemented the inverse model, we compensated these long-term memory effects and improved the linearizability of a 10 W GaN HEMT-based PA by 6.82 dB, achieving a level of intermodulation distortion of −65.77 dBc at the cost of a decrease in PAE of just 0.5 p.p. for a 4-carrier GSM signal with a training sequence.

These results are in compliance with the exceptionally stringent linearization masks for multicarrier GSM transmitters. While other works have achieved similar results, their all-digital approach led to DPD solutions that are extremely complex to implement. Using our hybrid analog/digital solution, however, similar results can be obtained using a simple analog circuit and a conventional, completely unmodified GMP DPD.

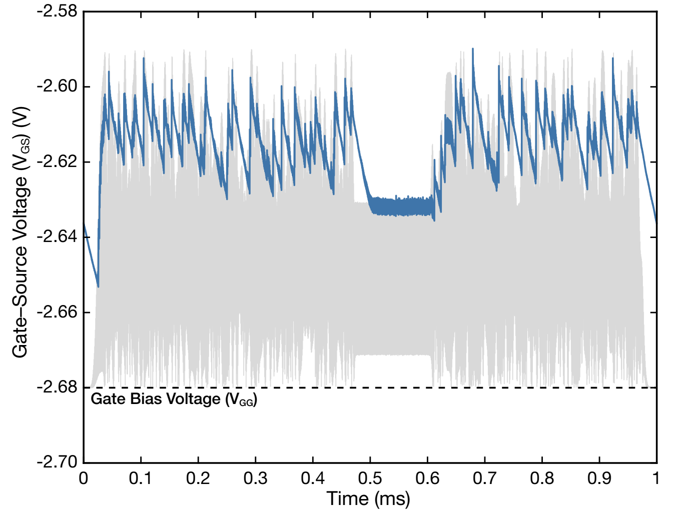

Fig. 7. Output of the ACC—the compensated gate bias voltage of the GaN HEMT—and, in the background, a representation of the input envelope amplitude (for visual reference).

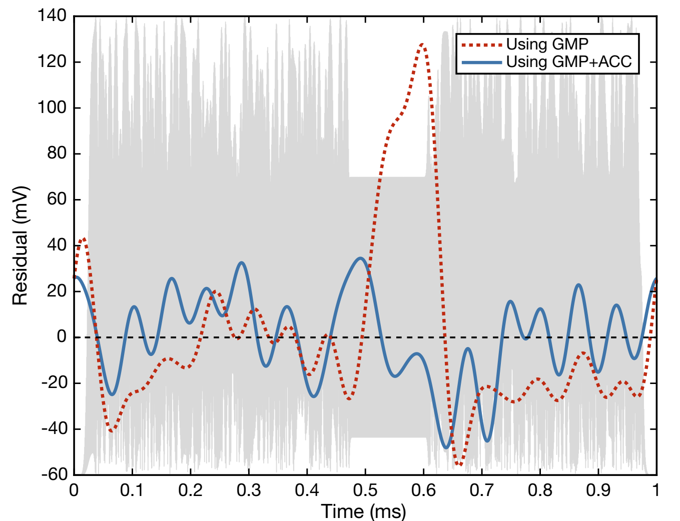

Fig. 8. Long-term residual error signal of the predistorted PA output when the ACC is disabled and when the ACC is enabled. Also, in the background, a representation of the input envelope amplitude is shown for visual reference.

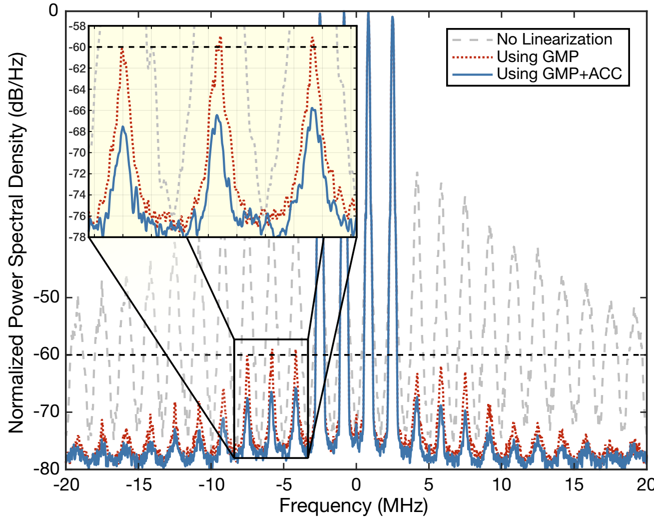

Fig. 9. Spectra of the PA output without any compensation, with linearization using a GMP, and after being linearized using our hybrid analog/digital linearization scheme.

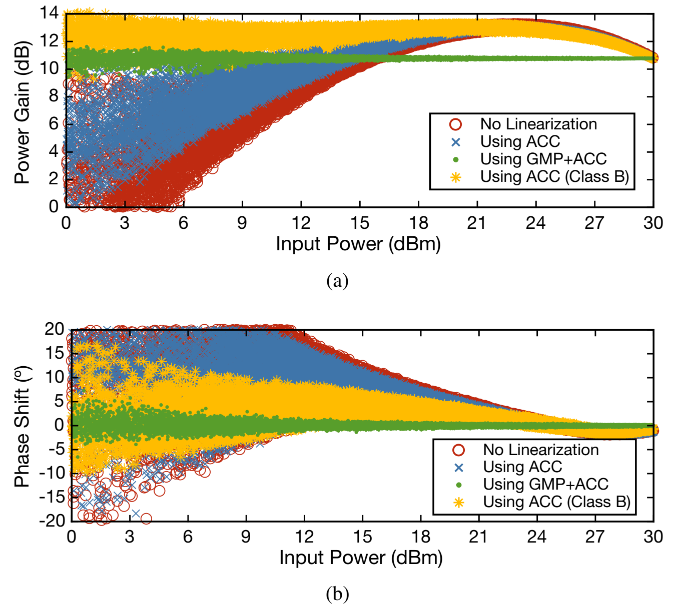

Fig. 10. (a) Power gain and (b) phase shift profiles of the PA without any compensation, with compensation of trapping effects using the ACC, and after being linearized using the hybrid analog/digital linearization scheme.

TABLE I
SUMMARY OF THE LINEARIZATION RESULTS

	IMR	PAE	P_{out}	I_{dc}
GMP	−58.95 dB	29.1 %	34.60 dBm	334.0 mA
GMP+ACC	−65.77 dB	28.6 %	34.52 dBm	334.6 mA

P_{out} is the mean output power.
I_{dc} is the mean dc drain current.

REFERENCES

[1] R. S. Pengelly, S. M. Wood, J. W. Milligan, S. T. Sheppard, and W. L. Pribble, "A review of GaN on SiC high electron-mobility power transistors and MMICs," *IEEE Trans. Microw. Theory Techn.*, vol. 60, no. 6, pp. 1764–1783, Jun. 2012.

[2] U. K. Mishra, L. Shen, T. E. Kazior, and Y.-F. Wu, "GaN-based RF power devices and amplifiers," *Proc. IEEE*, vol. 96, no. 2, pp. 287–305, Feb. 2008.

[3] A. Katz, J. Wood, and D. Chokola, "The evolution of PA linearization: From classic feedforward and feedback through analog and digital predistortion," *IEEE Microw. Mag.*, vol. 17, no. 2, pp. 32–40, Feb. 2016.

[4] J. C. Pedro, P. M. Cabral, T. R. Cunha, and P. M. Lavrador, "A multiple time-scale power amplifier behavioral model for linearity and efficiency calculations," *IEEE Trans. Microw. Theory Techn.*, vol. 61, no. 1, pp. 606–615, Jan. 2013.

[5] D. R. Morgan, Z. Ma, J. Kim, M. G. Zierdt, and J. Pastalan, "A generalized memory polynomial model for digital predistortion of RF power amplifiers," *IEEE Trans. Signal Process.*, vol. 54, no. 10, pp. 3852–3860, Oct. 2006.

[6] C. Maziere, A. Soury, E. Ngoya, and J. M. Nebus, "A system level model of solid state amplifiers with memory based on a nonlinear feedback loop principle," in *Proc. Eur. Microw. Conf.*, Paris, France, Oct. 2005, pp. 1–4.

[7] E. Ngoya, C. Quindroit, and J.-M. Nebus, "Improvements on long term memory modeling in power amplifiers," in *Proc. IEEE MTT-S Int. Microw. Symp.*, Boston, MA, USA, Jun. 2009, pp. 1–4.

[8] S. Boumaiza and F. M. Ghannouchi, "Thermal memory effects modeling and compensation in RF power amplifiers and predistortion linearizers," *IEEE Trans. Microw. Theory Techn.*, vol. 51, no. 12, pp. 2427–2433, Dec. 2003.

[9] A. S. Tehrani, T. Eriksson, and C. Fager, "Modeling of long term memory effects in RF power amplifiers with dynamic parameters," in *Proc. IEEE MTT-S Int. Microw. Symp.*, Montreal, QC, Canada, Jun. 2012, pp. 1–3.

[10] F. M. Barradas, L. C. Nunes, T. R. Cunha, P. M. Lavrador, P. M. Cabral, and J. C. Pedro, "Compensation of long-term memory effects on GaN HEMT-based power amplifiers," *IEEE Trans. Microw. Theory Techn.*, vol. 65, no. 9, pp. 3379–3388, Sep. 2017.

[11] *Digital cellular telecommunications system (Phase 2+) (GSM); GSM/EDGE radio transmission and reception*, Eur. Telecommun. Standards Inst. (std.) ETSI TS 145 005, Jan. 2018.

[12] N. Scheinberg, R. Bayruns, and R. Goyal, "A low-frequency GaAs MESFET circuit model," *IEEE J. Solid-State Circuits*, vol. 23, no. 2, pp. 605–608, Apr. 1988.

[13] R. Vetury, N. Q. Zhang, S. Keller, and U. K. Mishra, "The impact of surface states on the DC and RF characteristics of AlGaN/GaN HFETs," *IEEE Trans. Electron Devices*, vol. 48, no. 3, pp. 560–566, Mar. 2001.

[14] K. Kunihiro and Y. Ohno, "A large-signal equivalent circuit model for substrate-induced drain-lag phenomena in HJFETs," *IEEE Trans. Electron Devices*, vol. 43, no. 9, pp. 1336–1342, Sep. 1996.

[15] O. Jardel, F. D. Groote, T. Reveyrand, J.-C. Jacquet, C. Charbonniaud, J.-P. Teyssier, D. Floriot, and R. Quere, "An electrothermal model for AlGaN/GaN power HEMTs including trapping effects to improve large-signal simulation results on high VSWR," *IEEE Trans. Microw. Theory Techn.*, vol. 55, no. 12, pp. 2660–2669, Dec. 2007.

[16] P. Horowitz and W. Hill, *The Art of Electronics*, 3rd ed. New York, NY, USA: Cambridge University Press, 2015.

[17] J. C. Pedro, L. C. Nunes, and P. M. Cabral, "Soft compression and the origins of nonlinear behavior of GaN HEMTs," in *Proc. Eur. Microw. Integr. Circuit Conf.*, Rome, Italy, Oct. 2014, pp. 1–4.

[18] L. C. Nunes, J. L. Gomes, P. M. Cabral, and J. C. Pedro, "A simple method to extract trapping time constants of GaN HEMTs," in *Proc. IEEE MTT-S Int. Microw. Symp.*, Philadelphia, PA, USA, Jun. 2018, pp. 716–719.

Pedro M. Tomé (S'17) received the M.Sc. degree in electronic and telecommunications engineering from the University of Aveiro, Aveiro, Portugal, in 2016.

His master's thesis focused on analog neural predistortion of power amplifiers. He is currently a student of the MAP-tele Doctoral Program in telecommunications, a joint program between the University of Minho, Guimarães, Portugal, the University of Aveiro, and the University of Porto, Porto, Portugal. His previous research includes a student research grant on analog predistortion of power amplifiers in 2015 and a student research grant on the control of systems with delayed feedback in 2014. His current research interests include the study and compensation of performance-impairing phenomena in massive multi-input multi-output transmitters targeting fifth-generation wireless communications.

Telmo R. Cunha (M'05) received the Diploma and Ph.D. degrees in electronics and computer engineering from the Universidade do Porto, Porto, Portugal, in 1996 and 2003, respectively.

He was formerly involved with the Astronomical Observatory, University of Porto, and, afterward, with Geonav Lda., a private company near Porto. Since 2004, he is an Assistant Professor with the Department of Electronics, Telecommunications and Informatics, University of Aveiro, Aveiro, Portugal, and also a Senior Research Engineer with the Institute of Telecommunications, University of Aveiro. He has been lecturing in the fields of control theory and electronics, and he has been involved in several national and international research projects. His current research interests include behavioral modeling and linearization applied to radio frequency and microwave devices.

Dr. Cunha has been a reviewer for several IEEE journals.

Filipe M. Barradas (S'13-M'17) was born in Évora, Portugal, in July 1989. He received the M.Sc degree in electronics and telecommunications engineering from Universidade de Aveiro, Aveiro, Portugal, in 2012, and the PhD degree in electrical engineering at the same university in 2017.

He is currently a Research Assistant at Instituto de Telecomunicações, Aveiro, Portugal. His main interests include digital predistortion and behavioral modelling of RF PAs, as well as signal processing with applications on telecommunications. Other interests include design and analysis of nonlinear microwave circuits.

Dr. Barradas has been a reviewer for several IEEE journals.

José Carlos Pedro (S'90–M'95–SM'99–F'07) received the diploma, doctoral and habilitation degrees in electronics and telecommunications engineering, from University of Aveiro, Portugal, in 1985, 1993 and 2002, respectively, where he is now a Full Professor.

His main scientific interests include active device modeling and the analysis and design of various nonlinear microwave circuits. He is the leading author of two books and has authored or co-authored more than 200 papers in international journals and symposia. He has served the scientific community by acting as a reviewer and editor of several conferences and journals, namely the IEEE MTT TRANSACTIONS from which he is now the Editor-in-Chief.

Prof. Pedro received various prizes, namely the Marconi Young Scientist Award in 1993, the 2000 Institution of Electrical Engineers Measurement Prize, the 2015 EuMC Best Paper Microwave Prize and the Microwave Distinguished Educator Award. He is a Fellow of the IEEE since 2007.

APPENDIX F

Paper J4

A Multiple-Time-Scale Analog Circuit for the Compensation of Long-Term Memory Effects in GaN HEMT-Based Power Amplifiers

Pedro M. Tomé, Filipe M. Barradas, Telmo R. Cunha, and José C. Pedro

Published In: IEEE Transactions on Microwave Theory and Techniques

Date of Publication: 17 July 2020

DOI: 10.1109/TMTT.2020.3007713

This is the authors' version of an article that has been published in the IEEE TRANSACTIONS ON MICROWAVE THEORY AND TECHNIQUES. Changes were made to this version by the publisher prior to publication.
The final version of the record is available at https://doi.org/10.1109/TMTT.2020.3007713.

A Multiple-Time-Scale Analog Circuit for the Compensation of Long-Term Memory Effects in GaN HEMT-Based Power Amplifiers

Pedro M. Tomé, *Student Member, IEEE,* Filipe M. Barradas, *Member, IEEE,* Telmo R. Cunha, *Member, IEEE,* and José C. Pedro, *Fellow, IEEE*

***Abstract*—In this paper we present an analog circuit for the compensation of long-term memory effects in power amplifiers (PAs) based on GaN high-electron-mobility transistors (HEMTs). The analog compensation circuit (ACC) is supported on a charge-trapping behavioral model that features a state-dependent variable emission time constant, rather than a fixed emission time constant. This allows not only for the more accurate modeling and compensation of the nonlinear long-term memory effects experienced by GaN HEMT-based PAs, but also for the adaptation of the dynamics of the ACC to varying operating conditions, such as the ambient temperature. We demonstrate that the proposed ACC is able to successfully eliminate any multiple-time-constant transient symptom of current collapse following a high-power radio-frequency pulse or two-tone excitation and accurately preserve the class of operation of a GaN HEMT-based PA. Moreover, we also demonstrate that the proposed ACC can aid the linearization of GaN HEMT-based PAs for fifth-generation (5G) New Radio (NR) communications, allowing for the reduction in the complexity of the digital predistorter. For a 5G NR time-division duplexing signal with a bandwidth of 20 MHz, the inclusion of the ACC improved out-of-band emissions by over 15 dB and improved the error-vector magnitude by over 10 p.p. at essentially no cost to the PA's power-added efficiency.**

***Index Terms*—Analog linearization, charge trapping, GaN high-electron-mobility transistor, long-term memory effects.**

I. INTRODUCTION

GALLIUM nitride high-electron-mobility transistors (HEMTs) are well-known for their high breakdown field, power density and thermal conductivity, as well as a very low drain–source capacitance. Thanks to these properties, this technology has contributed to the emergence of power amplifiers (PAs) featuring very high output power levels, while maintaining high power efficiencies and wide bandwidths of operation. For these reasons, GaN HEMTs are generally regarded as the technology of choice for high-power radio-frequency (RF) applications such as cellular base station transmitters and radar [1].

Manuscript submitted January 8, 2020; revised May 8, 2020; accepted June 13, 2020.

This work was supported by FCT/MEC through National Funds under Project UID/EEA/50008/2013 (APIC) and Project PTDC/EEI-TEL/7049/2014 (Lin5GPA). The work of P. M. Tomé was supported by FCT/MEC under Ph.D. Grant PD/BD/128198/2016. *(Corresponding author: Pedro M. Tomé).*

The authors are with the Department of Electronics, Telecommunications and Informatics, Institute of Telecommunications, University of Aveiro, 3810–193 Aveiro, Portugal (e-mail: tome.p.m@ua.pt; filipebarradas@ua.pt; trcunha@ua.pt; jcpedro@ua.pt).

Despite their remarkable power capabilities, the deployment of GaN HEMT-based PAs in the mobile communications infrastructure is often ruled out in favor of alternative silicon-based technologies. One of the reasons for this is the pervasiveness of long-term memory effects in GaN HEMT technology caused by thermal and charge-trapping phenomena. These effects include commonly observed nonlinear behavior such as current collapse [2], knee walkout [3], and dc–RF dispersion [4]. While these effects can be compensated for using digital predistortion (DPD) algorithms [5], their implementation and model-extraction complexity—as well as the power necessary to execute them in real time—make them unsuitable for modern small cells and large-scale multiple-input multiple-output (MIMO) transceivers, where the power necessary for the linearization of each amplification element is of great concern.

In order to address these issues, we present in this paper a feedforward analog circuit for the compensation of long-term memory effects in GaN HEMT-based PAs. This circuit models, in real time and for an arbitrary input excitation, the multiple-time-scale dynamics of charge trapping and generates a time-varying signal that, when applied to the gate bias terminal of a GaN HEMT-based PA, compensates the nonlinear long-term memory effects that would otherwise be observable. For communications applications, the remaining short-term memory and static nonlinearity of the PA can then be compensated using a complementary low-complexity DPD algorithm.

Contrary to previous works in which the emission time constant was fixed [5], [6], our proposed circuit is supported on a model that considers a state-dependent variable time constant for the compensation of charge-trapping effects related to charge emission. This provides two major benefits over previous works. First, our variable-time-constant model greatly improves the accuracy of the predicted dynamic trapping state for larger PA input signal excursions, allowing for the reduction in the complexity of the complementary DPD linearizer. Second, the proposed circuit allows for the online adaptation of the parameters of the implemented trapping model in response to any need, e.g., due to process, supply voltage, or ambient temperature variations. This allows for an arbitrarily large variation of the dynamics of the ACC in order to meet even the most stringent field conditions that affect the trapping dynamics of the GaN HEMT.

As an external compensation method, the proposed circuit does not prevent the accumulation of trapped charge inside the HEMT, but instead masks the effects resulting from this accumulation. In spite of this, in this paper we demonstrate that our compensation circuit is able to successfully eliminate any transient symptom of current collapse following a high-power pulse or two-tone excitation and accurately preserve the class of operation of a GaN HEMT-based PA. Moreover, we also demonstrate an application scenario where our proposed compensation circuit is used in conjunction with a reduced-order memory-polynomial DPD model to linearize a GaN HEMT-based PA for fifth-generation (5G) New Radio (NR) communications.

This paper is organized as follows. In Section II, we establish the fundamental working principle of our analog compensation circuit. In Sections III and IV, we detail our variable-time-constant charge-trapping model and its implementation as an analog circuit. In Section V, we describe the laboratory setup for performing all relevant measurements. In Sections VI–VIII, we detail and analyze the results of three independent sets of measurements that validate the ability of our analog circuit to compensate the long-term memory effects in GaN HEMT-based PAs. In Section IX, we demonstrate an application scenario of the linearization of a 5G NR transmitter based on a hybrid analog/digital linearization scheme. Finally, in Section X, we provide some concluding remarks.

II. Compensation Strategy

Charge trapping is the primary cause of long-term memory effects in GaN HEMT-based PAs. While the physical mechanisms behind it are still not completely established, it is generally accepted that this phenomenon arises from the existence of localized electronic states at energy levels between the conduction and valence bands, that is, deep-level traps near the center of the GaN band gap. In deep-level traps, the energy required to liberate a trapped charge (to either the valence or conduction band) is high, which means that the probability of it happening through thermal emission is low [7]. Under large electric fields, this leads to an accumulation of charge in trapped states and the formation of a net-negative electric potential that depletes the GaN channel and dynamically modulates its conductivity [8].

Charge trapping can be modeled as the charging and discharging of a virtual back gate that produces a self-biasing effect [7], [9]. Moreover, it has been demonstrated that this self-biasing effect is so severe that a GaN HEMT-based PA biased in class B can easily degenerate into a deep class C under normal operating conditions [10]. Since the time constants associated with the charging and discharging of this virtual back gate can range from under one microsecond to over one minute [11], [12], and considering that the envelopes of modern communications and radar waveforms vary within these time frames, it follows that the long-term memory effects caused by charge-trapping phenomena are a major contribution to the seemingly intractable post-linearization residual distortion observed in communications applications [5] and the severe deterioration of the pulse-to-pulse stability in radar applications [13], [14].

Even though there are methods for preventing the accumulation of trapped charge in GaN HEMTs, this phenomenon is unlikely to be completely eliminated in the near future. The reason for this is that some of the mechanisms that lead to charge trapping in GaN HEMTs are believed to be the same mechanisms that allow these transistors to function in the first place. For instance, surface states in the AlGaN barrier are understood to be a source of traps that induce gate lag [15]–[17]. While this phenomenon can be mitigated through the use of field plates and various passivation techniques [18]–[20], there is indication that these same surface states are responsible for the formation of the two-dimensional electron gas that constitutes the GaN channel [21], [22]. Furthermore, extrinsic dopants in the GaN buffer are believed to be a source of traps that induce drain lag [8], [23]. However, these dopants are necessary to improve buffer isolation and prevent short-channel effects such as punch-through (sub-threshold current leakage) [24], [25].

In order to compensate the long-term memory effects caused by thermal and charge-trapping phenomena, we present in this paper an analog circuit that dynamically modulates the gate bias voltage of a GaN HEMT-based PA as a function of its input excitation. The modulation of the gate bias voltage of the PA allows for the compensation of the long-term memory effects caused by charge-trapping phenomena because, as we previously established, these effects are the result of a dynamic virtual back gate voltage (or, equivalently, a variation of the HEMT's threshold voltage). By canceling out this virtual back gate voltage (or the variation of the threshold voltage), the proposed circuit compensates both gate-lag and drain-lag effects simultaneously—because, in spite of the two effects having different points of origin (the gate or drain terminal, respectively), both contribute to the charging and discharging of the same virtual back gate that produces a net variation of the HEMT's threshold voltage. This reasoning is supported by physical simulations in [8] and successful behavioral modeling efforts in [26]. It should be noted that, by modulating the gate bias voltage of the PA, this circuit also allows for the compensation of the long-term memory effects caused by thermal phenomena because, from a behavioral point of view, these effects correspond to a variation of the gain of the PA, which is similarly dependent on its quiescent (or, in this case, dynamic) gate–source voltage operating point. A similar approach to the compensation of thermal-related effects was adopted in [5] in the context of digital predistortion.

III. Compensation Model

A. *Qualitative Operation*

At the core of every charge-trapping model lies a variation of a peak detector or a switchable resistor-capacitor network with different charge and discharge time constants [11], [27], [28]. This is a direct consequence of the seminal work of Kunihiro and Ohno [7], who established that charge capture in deep-level traps occurs at a much faster rate than charge emission. While this has led to the assumption that each of these processes can be accurately modeled using only one time constant, simple RF pulse measurements show that this

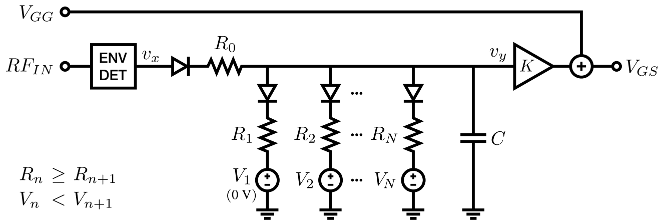

Fig. 1. Nonlinear multiple-time-scale variable-time-constant model for the compensation of long-term memory effects in GaN HEMT-based PAs. All diodes are assumed to be ideal ($V_f = 0$ V).

is not the case for sufficiently large signal excursions [12]. In reality, both capture and emission processes are known to have a complex dynamic behavior that starts off very fast and becomes much slower over time [12].

In order to accurately compensate the long-term memory effects caused by charge-trapping phenomena in GaN HEMT-based PAs, we propose the model illustrated in Fig. 1, which captures the complex dynamics of charge trapping by varying the emission time constant as a function of the trapping state. As established in Section II and demonstrated in [6], [14], the compensation strategy consists in modulating the gate bias voltage of the GaN HEMT-based PA by adding the output of the trapping model to the constant voltage V_{GG} that sets the quiescent state of the PA. This results in the gate–source voltage V_{GS} that compensates the long-term memory effects caused by charge-trapping phenomena when applied to the gate bias terminal of the PA.

The core of the proposed compensation model works in the following way. Suppose that a pulse-modulated carrier is applied to the RF_{IN} input of the model shown in Fig. 1. First, the capacitor charges through R_0 for the duration of the pulse and reaches a voltage v_y. Then, the capacitor discharges through all parallel R_n branches where $v_y > V_n,\ n = 1, 2, \cdots, N$. As the capacitor discharges toward $v_y = 0$ V, larger-n branches are disabled until R_1 is the only enabled branch (note that $V_n < V_{n+1}$ and V_1 is always equal to 0 V). This translates into a net discharge conductance that decreases as the charge of the capacitor decreases, resulting in a discharge rate that starts fast but becomes slower over time.

While the proposed model features an emission time constant that varies with the instantaneous trapping state, the capture time constant is fixed and approximately equal to $R_0\,C$ (because $R_0 \ll R_1, \cdots, R_N$). Since the PA is much less sensitive to variations in its operating point during large-signal excitations (as evidenced by the AM-AM profiles of self-biased GaN HEMT-based PAs in [10]), the modeling of charge capture with a fixed time constant was deemed sufficiently accurate for the purposes of the proposed compensation model. This trade-off between capture modeling accuracy and circuit implementation complexity is further supported by the work in [14], where the authors report, for a self-biased GaN HEMT-based PA, a decrease in the large-signal gain of less than 1 dB and a decrease in the small-signal gain of over 20 dB.

Besides regulating the switching between different emission time constants by enabling or disabling the different conductance branches, breakpoints (the V_n sources in Fig. 1) also contribute to the smoothness of the model. This is because each conductance branch n actually discharges toward V_n and not toward ground. There is, therefore, a smooth handover from one time constant to another, which improves the accuracy of our compensation model.

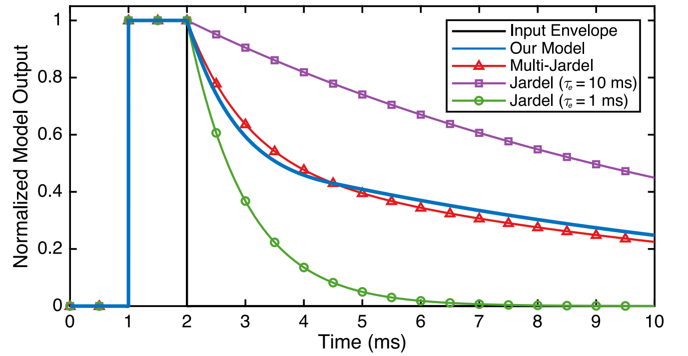

(a)

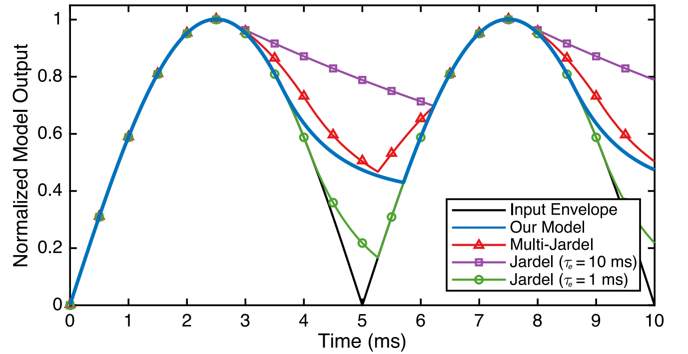

(b)

Fig. 2. Comparison between the output of our model with a variable two-branch emission time constant, a model with two independent emission time constants (1 ms and 10 ms), a model with one fixed emission time constant equal to 10 ms, and a model with one fixed emission time constant equal to 1 ms for (a) a pulsed excitation and (b) a two-tone excitation.

B. *Comparison With Other Models*

Fig. 2(a) illustrates, in blue, the response of our model to a pulsed-envelope excitation. In this example, our model features a near-instantaneous capture time constant $\tau_0 = R_0\,C = 1$ μs, a two-branch emission time constant with $\tau_1 = R_1\,C = 10$ ms and $\tau_2 = R_2\,C = 1$ ms, and a breakpoint $V_2 = 0.5$ V. As intended, the charge and discharge rates of the capacitor are widely different. Moreover, the discharge of the capacitor is very fast while the model output is greater than the breakpoint at 0.5 V and becomes much slower thereafter.

Besides illustrating the response of our model to a pulsed envelope, Fig. 2(a) also shows, in red, the response of a model that is repeatedly mentioned in the literature as being an obvious solution for the modeling of multiple-time-constant emission profiles. This model, which is based on the model of Jardel *et al.* with a fixed capture time constant and a fixed emission time constant [11], consists in simply summing the outputs (with a given set of scaling factors) of multiple independent Jardel models with different emission time constants. For instance, let $J(x(t), \tau_c, \tau_e)$ denote the

response of the Jardel model, with a capture time constant τ_c and an emission time constant τ_e, to an input excitation $x(t)$. Then, the response of the multi-Jardel model in Fig. 2(a) is $y(t) = \frac{1}{2}\,J(x(t), 1\ \mu s, 1\ ms) + \frac{1}{2}\,J(x(t), 1\ \mu s, 10\ ms)$. For reference, the contribution of each individual Jardel model to the response of the multi-Jardel model is also shown in Fig. 2(a).

While the pulsed-envelope responses shown in Fig. 2(a) seem to indicate that our model is very similar to the multi-Jardel model, more complex input excitations reveal that this is not the case. For instance, Fig. 2(b) illustrates the response of our model and the multi-Jardel model (with the same parameters as in Fig. 2(a)) to an input excitation with a sinusoidal (two-tone) envelope; for reference, the contribution of each individual Jardel model to the response of the multi-Jardel model is also shown. Clearly, the response of the multi-Jardel model is not physically reasonable, since there is a strong discontinuous inversion of its derivative during the emission phase. This is due to the fact that the Jardel model with $\tau_e = 1$ ms resumes its charging phase before the Jardel model with $\tau_e = 10$ ms (because, naturally, it discharges much faster). In contrast, our model produces a reasonable response. The accurate modeling of measured emission profiles should, therefore, consider one single variable emission time constant (as in our model), and not multiple time constants (or the scaled sum of the individual contributions of fixed emission time constants).

C. Mathematical Formulation

The extraction of the parameters of the compensation model consists in fitting its output to measured data. This optimization process benefits from a fast digital representation of the model, so, instead of relying on an analog electronic circuit simulator, we developed the following discrete-time mathematical description of the charge-trapping model.

Referring to Fig. 3, let $v_x(t)$ denote the amplitude of the envelope of the PA's input excitation and $v_y(t)$ the output of the charge-trapping model with N parallel conductance branches. Furthermore, let $f_D(\cdot)$, defined in (1), denote the transfer function of the diodes, which are assumed to be ideal.

$$f_D(x) = \begin{cases} x, & x \geq 0 \\ 0, & x < 0 \end{cases} \tag{1}$$

By applying Kirchhoff's current law to the output node, the current through the capacitor $i_y(t)$ can be defined as in (2) and (3). For clarity, in (4) we group the currents responsible for the charging and discharging of the capacitor as $i_c(t) = i_0(t)$ and $i_e(t) = \sum_{n=1}^{N} i_n$. These currents model, respectively, the processes of charge capture and charge emission.

$$i_y(t) = i_0(t) - i_1(t) - i_2(t) - \cdots - i_N(t) \tag{2}$$

$$= f_D\left(\frac{v_x(t) - v_y(t)}{R_0}\right) - \sum_{n=1}^{N} f_D\left(\frac{v_y(t) - V_n}{R_n}\right) \tag{3}$$

$$= i_c(t) - i_e(t) \tag{4}$$

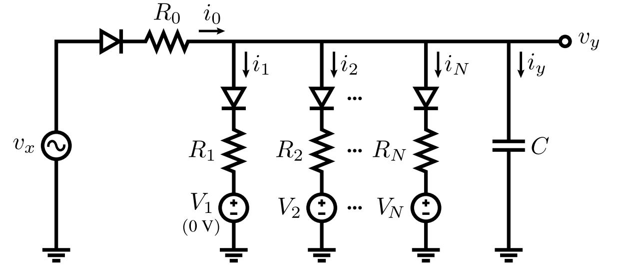

Fig. 3. Trapping core of the proposed compensation model.

Finally, since $v_y(t)$ is the voltage at the capacitor's terminals, it can be calculated as in (5).

$$v_y(t) = \frac{1}{C}\int_{t_0}^{t}\Big(i_c(\tau) - i_e(\tau)\Big)\,d\tau + v_y(t_0) \tag{5}$$

Using Euler's method, this model can be discretized as follows. Let (6). Then, $v_y(t)$ can be approximated in discrete time as in (7), where k denotes the discrete-time sample index, $i_c(k)$ and $i_e(k)$ denote the discrete-time samples of $i_c(t)$ and $i_e(t)$, and f_s denotes the sampling frequency.

$$\frac{d}{dt}v_y(t) = \frac{1}{C}\Big(i_c(t) - i_e(t)\Big) \tag{6}$$

$$v_y(k+1) = v_y(k) + \frac{1}{f_s\,C}\Big(i_c(k) - i_e(k)\Big) \tag{7}$$

D. Temperature Considerations

Since the voltage breakpoints act as time-constant interpolation nodes rather than strict time-constant switching points, the emission time constant can be modified by varying the parameters V_n even with a fixed set of resistors R_n. This feature is a major advancement over previous works where the time constants were fixed [6], since it allows for the online adaptation of the parameters and dynamics of the charge-trapping compensation circuit in response to any need (e.g., due to process, supply voltage, or ambient temperature variations) without changing the set of resistors R_n, as exemplified in Fig. 4 (and later confirmed in Tables I and II).

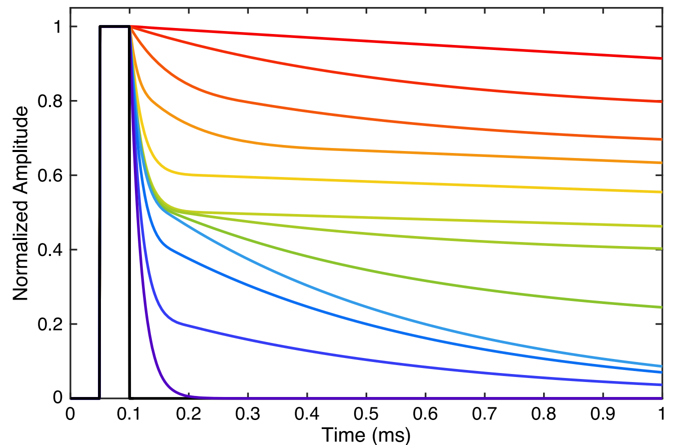

Fig. 4. Variability of the pulse response of the proposed compensation model with a fixed set of resistors R_n and various sets of breakpoint voltages V_n.

For more particular applications, even the resistors R_n can be adapted without modifying the compensation circuit (i.e., without physically substituting the resistors). This is because a conductance branch n can be entirely disabled by applying a sufficiently high voltage to its respective V_n breakpoint. For instance, for operation at two distinct temperature ranges, one set of model parameters with N_1 emission resistors (conductance branches) can be extracted for one temperature range, and a different set of model parameters with N_2 emission resistors can be extracted for the other temperature range. Then, both parameter sets can be incorporated into one compensation circuit with $N_1 + N_2$ total emission resistors. Finally, depending on the temperature range of operation, all undesired emission resistors can be disabled simply by pulling the respective breakpoint voltages high (e.g., to the positive power rail of the circuit).

The dynamics of the proposed charge-trapping model (and the analog circuit that implements it) can, therefore, be modified either by adapting the breakpoint voltages V_n (allowing for a fine tuning of the state-dependent variable emission time constant) or by selecting entirely different sets of resistors R_n by pulling the V_n of undesired conductance branches high. This allows for an arbitrarily large (or fine) variation of the dynamics of the compensation circuit in order to meet even the most stringent field conditions that affect the trapping dynamics of the GaN HEMT.

IV. Analog Compensation Circuit

In order to compensate the long-term memory effects caused by charge-trapping phenomena in GaN HEMT-based PAs, we designed the analog compensation circuit (ACC) pictured in Fig. 5. This circuit is a direct implementation of the compensation model detailed in Section III using analog electronic components, and it features three parallel conductance branches. Fig. 6 shows a simplified schematic of the trapping core of the ACC. As illustrated, the ideal diodes were implemented using a diode whose forward voltage is compensated by an operational amplifier in a local feedback loop [29].

Fig. 6 also indicates two potential pitfalls when implementing the compensation model: the input bias currents of the operational amplifiers and the reverse-bias currents of the diodes. Since the capacitor C is required to be relatively small because of the output current limit of the operational amplifiers, these parasitic currents should be as small as possible to preserve a good agreement between the model and its circuit implementation. Otherwise, these currents may lead to two undesirable outcomes: a disruption of the output signal's dynamics by altering the charge of the capacitor, and a large voltage offset imposed by R_n (e.g., $1\ \mu\text{A} \times 1\ \text{M}\Omega = 1$ V). The input bias current of the operational amplifiers immediately puts a restriction on the internal architecture of the operational amplifier used in the input ideal diode: it must not be a current-feedback amplifier because these have low-impedance inverting inputs. Furthermore, the voltage offset created at the R_n resistors also leads to variations in the output signal's dynamics. This is because this offset voltage is dependent on the number of enabled parallel conductance branches (it depends on the instantaneous output voltage), and also because it causes the undue switching between the charging and discharging of the capacitor by biasing the input diode. Because of the switching nature of the ideal-diode subcircuits, the parallel capacitance of the diodes should also be as small as possible to minimize the coupling between the outputs of the operational amplifiers and the capacitor C.

Our implementation consists of the following components. The envelope detector is an Analog Devices ADL5511 integrated circuit that operates from dc to 6 GHz. All operational amplifiers are Texas Instruments OPA659 voltage-feedback operational amplifiers with a typical input bias current of 10 pA. All diodes are Toshiba 1SS307E silicon switching diodes with a typical reverse-bias current of 200 fA and a total capacitance of 800 fF (at a reverse voltage of 4 V). Capacitor C is a 6.8 nF $\pm$ 1 % C0G/NP0 KEMET ceramic capacitor. Finally, the gain K is implemented using an Analog Devices AD8336 variable gain amplifier controlled by a pair of Analog Devices ADR510 precision voltage references.

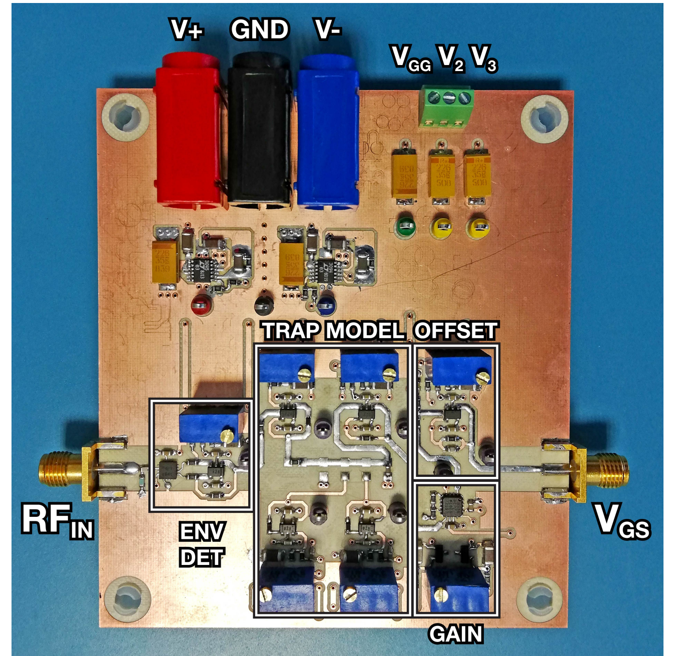

Fig. 5. Photograph of the ACC.

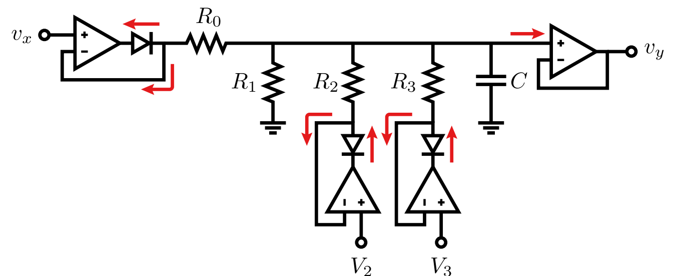

Fig. 6. Simplified schematic of the trapping core of the ACC. Red arrows indicate potential sources of discrepancies between the model and its practical implementation. v_x is the input envelope amplitude.

V. Measurement Setup

In order to conduct the measurements for the validation of the ACC, we assembled the laboratory setup pictured in Fig. 7 and schematized in Fig. 8. The 2.2 GHz single-ended PA was based on the 15 W 28 V Wolfspeed CGH27015F GaN HEMT and was biased in class B (at the root of g_{m3} [30]).

The input excitation of the PA was generated using a Rohde & Schwarz SMW200A vector signal generator (VSG) followed by a Mini-Circuits ZHL-16W-43-S+ driver. The output of the PA was measured using a Rohde & Schwarz FSW8 vector signal analyzer (VSA). The input excitation of the ACC was extracted from the input of the PA using an Arra Inc. 3-4174-20 20 dB directional coupler. For increased measurement accuracy, the internal 10 MHz oscillator of the VSA was used as the reference for the VSA and VSG, and a baseband trigger signal was provided by the VSG to the VSA.

Other instruments include a Keysight N6705C dc power analyzer for the sourcing of the dc power of the PA, a Keysight E9301A average power sensor connected to a Keysight N1913A power meter for absolute power calibration, a Keysight 34461A digital multimeter for the verification of the breakpoint voltages of the ACC, a Keysight DSOS804A oscilloscope for the monitoring of ACC signals, and various power supplies for the sourcing of the power and breakpoint voltages of the ACC.

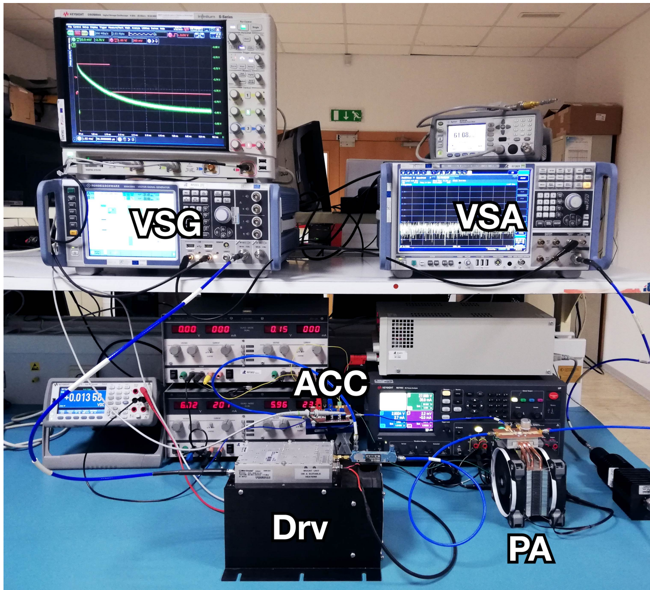

Fig. 7. Photograph of the measurement setup.

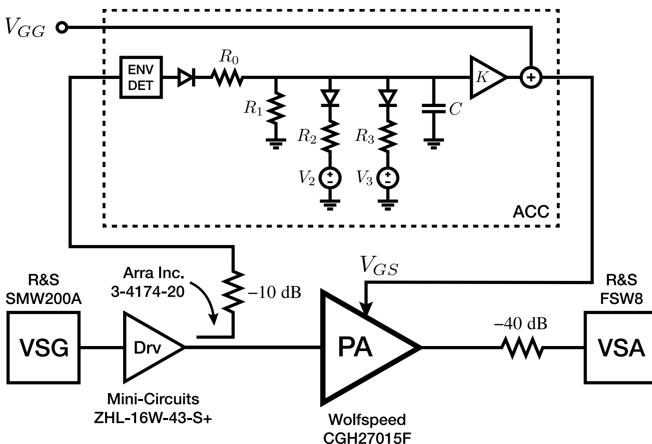

Fig. 8. Diagram of the measurement setup.

VI. Pulse Response Compensation

In this section we explore the first set of measurements that were made to verify the ability of our ACC to compensate the long-term memory effects caused by charge-trapping phenomena in GaN HEMT-based PAs. In short, we measured the transient response of a GaN HEMT-based PA to an RF pulse and observed a sudden decrease in the small-signal gain followed by a slow recovery of said gain. We then repeated the same procedure with the ACC connected to the PA and verified that the small-signal gain did not decrease after the pulse was applied.

A. Setup Calibration

Before any measurements were made, the laboratory setup was calibrated as follows. First, the power meter was connected to the output of the directional coupler at the PA input plane and the VSG was set to continuously generate a train of high-power pulses. An input-plane absolute-power calibration factor was then obtained by iteratively comparing the expected average power at the PA input plane with the one measured using the power meter. Having calibrated the signal source at the input plane of the PA, the power meter was disconnected and the signal analyzer (attenuated VSA) was connected in its stead. An output-plane absolute-power calibration factor was then obtained by comparing the average power measured by the VSA with the known average power at the output of the calibrated signal source.

In order to preserve the waveforms of the test signals generated at the PA input plane and compensate any distortion caused by the output stage of the VSG (e.g., the inductive response of the driver's biasing network), all input signal envelopes used throughout the rest of this section were predistorted using the iterative error-integration algorithm defined in (8), where $z(t)$ is the predistorted signal envelope, $w(t)$ is the measured signal envelope at the driver output, $x(t)$ is the target signal envelope, and λ is a learning-rate parameter [31].

$$z(t) \;:=\; z(t) \;-\; \lambda\,(w(t) - x(t)) \tag{8}$$

B. Measurement Procedure

After the setup was calibrated, the GaN HEMT-based PA was preheated [14] and its small-signal gain G_{SS} was measured as a function of the gate–source voltage V_{GS}. This was done by sweeping V_{GS} using the dc power analyzer and measuring G_{SS} in response to a continuous-wave (CW) −10 dBm excitation. From this preliminary measurement resulted the $V_{GS}(G_{SS})$ map, which is required for the extraction of the parameters of the ACC. Note that V_{GS} is only required to be swept from the PA's bias point to increasingly negative

voltages. Unless the PA is intended to be biased in class A, the power dissipated due to the quiescent drain current will vary very little throughout the sweep. Thus, the temperature of the HEMT throughout the sweep will be approximately constant.

Finally, the PA was biased in class B and its transient response to a series of large-signal RF pulses was measured. The pulse response was measured first with a constant-voltage source biasing the PA (without the ACC), and then with the ACC connected to the PA (after its parameters had been extracted). The measurements were sequenced by configuring the VSG so that it would output a constant small-signal level and, once triggered, generate one single large-signal pulse and immediately fall back to outputting a constant small-signal level. This guaranteed that the initial charge-trapping conditions were the same before each pulse, allowing for fast and repeatable measurements. The large-signal level of the pulsed excitations ranged from 20 dBm to 30 dBm and the small-signal level was constant at −10 dBm. The pulses had a duration of 50 µs. All signal envelopes were generated and measured at a sampling frequency of 200 MHz.

C. Circuit Parameter Extraction

The extraction of the parameters of the ACC was done as follows. First, the time-varying gate–source voltage $V_{GS}(t)$ of the PA was estimated by calculating the time-varying small-signal gain $G_{SS}(t)$ of the PA for each pulse-response time series and interpolating it over the $V_{GS}(G_{SS})$ map obtained from the preliminary measurement [32]. Then, the dynamic virtual back gate voltage $V_{BG}(t)$ of the GaN HEMT was estimated by postulating that $V_{GS}(t) = V_{GG} + V_{BG}(t)$. Finally, the signals $\Delta V_{GS}(t)$ that compensate the dynamic virtual back gate voltage for each measured pulse-response time series were trivially derived ($\Delta V_{GS}(t) = -V_{BG}(t)$) and the target output of the ACC for each pulsed excitation was determined.

After estimating the target pulse response of the trapping core of the ACC ($\Delta V_{GS}(t) \equiv K\, v_y(t)$), the parameters of the nonlinear model defined in Section III-C were extracted, for each measured pulse-response time series, by minimizing the mean squared error (MSE) between the target pulse response and the model's pulse response using the covariance matrix adaptation evolution strategy (CMA-ES) [33]. This was done separately for each measured pulse-response time series, resulting in the parameters listed in Table I.

D. Compensation Results

After extracting the parameters of the charge-trapping model, these were programmed into the ACC by soldering the required resistors (R_0–R_3) and setting the breakpoint voltages (V_2 and V_3) with an external power supply. Then, the ACC was connected to the PA and the following results were obtained.

Fig. 9(a) shows the response of the uncompensated GaN HEMT-based PA to a series of pulses with increasing peak power. These results can be explained through our understanding of the charge-trapping mechanism as follows. During a large-signal pulse there is a fast accumulation of charge in trapped states that depletes the channel and reduces the small-signal gain of the GaN HEMT-based PA as if there was an increasingly negative virtual back gate voltage. As this charge slowly dissipates through thermal emission and the virtual back gate voltage rises back toward zero, the small-signal gain of the PA recovers to its initial value. Since pulses with higher peak powers lead to a larger accumulation of trapped charge, the small-signal gain of the PA is reduced from 2 dB (for a 20 dBm pulse) up to over 15 dB (for a 30 dBm pulse).

Fig. 9(b) shows the response of the GaN HEMT-based PA to the same series of pulses, but while being compensated by the ACC. This figure reveals that, by dynamically modulating the gate bias voltage of the PA, the ACC cancels out the virtual back gate voltage of the GaN HEMT and the small-signal gain collapse experienced by the PA is compensated.

The phenomenon of charge emission, or the recovery of the small-signal gain, is known to have a multiple-time-constant (or variable-time-constant) dynamic behavior [12]. Contrary to an exponential increase with one single time constant, the actual rate of recovery of the small-signal gain of a GaN HEMT-based PA starts very fast but becomes slower and slower as the trapped charge is released. This is why our variable-time-constant ACC is able to accurately compensate not just the long-term gain collapse, but also—and simultaneously—the short-term gain collapse immediately following the end of each pulse. Figs. 9(c) and 9(d) prove this by showing the first 250 µs of the same data plotted in Figs. 9(a) and 9(b).

In order to compare our variable-time-constant ACC with an ACC that implements a fixed emission time constant [6], we compensated the response of the PA to a pulse with a peak power of 30 dBm using just one emission time constant, as illustrated in Fig. 10. Since the emission phenomenon results in a variable-time-constant small-signal gain recovery, there are three reasonable ways of compensating for its effects using just one time constant, or, in other words, there are three time constants that can be extracted: one that compensates the short-term gain collapse immediately following the pulse, but fails to compensate the long-term gain collapse; one that compensates the long-term gain collapse, but fails to compensate the short-term gain collapse; and one that balances the compensation between the two time scales, but fails to compensate either of them without severely overcompensating (overshooting) the long-term gain collapse. For reference, Fig. 10 also shows the response of the variable-time-constant ACC to a 30 dBm pulse (from Fig. 9).

TABLE I
PULSE RESPONSE COMPENSATION PARAMETERS

P_{pk}	R_0	R_1	R_2	R_3	V_2	V_3
20 dBm	91 Ω	3.6 MΩ	2.0 MΩ	330 kΩ	5 mV	42 mV
22 dBm	91 Ω	3.6 MΩ	2.0 MΩ	330 kΩ	5 mV	100 mV
24 dBm	91 Ω	3.6 MΩ	2.0 MΩ	330 kΩ	5 mV	162 mV
26 dBm	91 Ω	3.6 MΩ	2.0 MΩ	330 kΩ	5 mV	227 mV
28 dBm	91 Ω	3.6 MΩ	2.0 MΩ	330 kΩ	5 mV	295 mV
29 dBm	91 Ω	3.6 MΩ	2.0 MΩ	330 kΩ	22 mV	331 mV
30 dBm	91 Ω	3.6 MΩ	2.0 MΩ	330 kΩ	106 mV	371 mV

Fig. 9. Pulse response of the GaN HEMT-based PA (a) without compensation and (b) with compensation using our ACC. A zoomed-in view of the same data can also be seen in (c) for the case without compensation and (d) for the case with compensation.

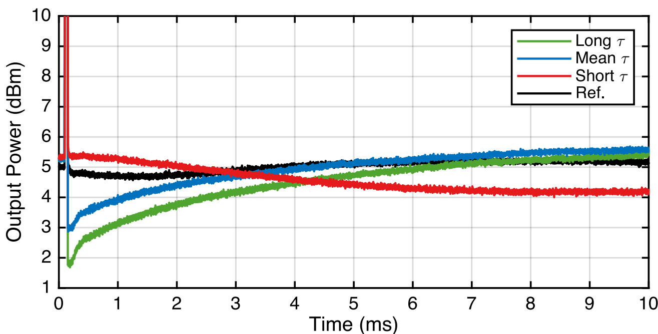

Fig. 10. Compensation of the response to a 30 dBm pulse using an ACC with one fixed emission time constant.

VII. Two-Tone Response Compensation

In this section we explore the second set of measurements that were made to verify the ability of our ACC to compensate the long-term memory effects caused by charge-trapping phenomena in GaN HEMT-based PAs. In short, we measured the steady-state response of a GaN HEMT-based PA to a series of two-tone RF excitations with increasing tone frequency separation, and observed a decrease in the small-signal gain as the tone separation increased. We then repeated the same procedure with the ACC connected to the PA and verified that the small-signal gain was constant regardless of the tone separation. This frequency-domain method for the characterization of charge-trapping phenomena was first proposed in [32] and, as we established in Section III, it is much stricter than the pulse-response method in terms of model structure and accuracy.

A. Setup Calibration

The calibration of the laboratory setup followed the same procedure as that of the pulse-response measurements, albeit with a few differences. First, the input excitation used for the calibration was a large-signal two-tone signal. Second, the

setup was predistorted using a third-order four-tap memory polynomial. A memory-polynomial model was used instead of the iterative error-integration algorithm described in Section VI because it provided better linearization results in a shorter time. In fact, the error-integration algorithm was only used for the linearization of the pulsed excitations because the driver presented a slow transient inductive response to the pulses, and its compensation would have required a model with an extremely large sample memory depth (assuming a finite-impulse-response memory structure). Since the two-tone excitations are measured in steady state, a memory polynomial proved to be sufficient for the measurements detailed in this section.

B. Measurement Procedure

After the setup was calibrated, the $V_{GS}(G_{SS})$ map required for the extraction of the parameters of the ACC was measured as explained in Section VI-B. Then, the PA was biased in class B and its steady-state response to a series of two-tone excitations was measured. These measurements were done first with a constant-voltage source biasing the PA (without the ACC), and then with the ACC connected to the PA (after its parameters had been extracted). The two-tone input envelopes had a frequency separation that ranged from 1 Hz to 100 kHz and a peak power that ranged from 24 dBm to 29 dBm.

In order to accommodate the record-length limitations of the VSG and VSA, the generated and captured signal envelopes were sampled at different sampling frequencies. Depending on the two-tone frequency separation, the sampling frequencies ranged from 5 kHz to 200 MHz. Moreover, in order to preserve an accurate sinusoidal waveform while accommodating the sampling-frequency limitations of the instruments, the sampling frequencies and record lengths were set so that the total number of unique envelope samples was always greater than or equal to 10^4. For instance, the two-tone envelope with a tone separation of 100 kHz was generated at 125.0125 MHz in order to obtain 10001 unique samples over four envelope periods; if it had been generated at 200 MHz (the maximum sampling frequency of the VSG), the number of unique samples would only have been 4000. This sampling scheme greatly improves the signal resolution at the small-signal portions of the continuously generated sinusoidal envelopes, which is beneficial for the extraction of the parameters of the ACC.

C. Circuit Parameter Extraction

The extraction of the parameters of the ACC was done as follows. First, each measured PA output time series was filtered in the frequency domain by computing the discrete Fourier transform and selecting all tones whose frequency was an odd integer multiple of $\Delta f/2$, where Δf is the frequency separation of the input two-tone excitation. This resulted in the filtered PA output time series $y_f(t)$ defined in (9), where α_m and ϕ_m are the amplitude and phase of the selected tones and f_m is their corresponding frequency.

$$y_f(t) = \sum_{m=1}^{M} \alpha_m \exp(2\pi f_m t + \phi_m) \tag{9}$$

Computing $y_f(t)$ is useful for two reasons: first, it greatly reduces the noise of the PA output time series; second, it provides a mathematical equation for the measured PA output. This equation can then be used to align the output of the PA with its input excitation (i.e., remove the group delay of the measurement setup and PA) with a precision much better than one sampling period. Since $y_f(t)$ is periodic (it is the steady-state response of the PA) and its waveform is that of a distorted sinusoid, then time alignment can be done by finding the instant t_0 at which $|y_f(t)|$ is minimum and declaring it as the zero-phase instant. To obtain t_0 we used a multiple-start nonlinear least-squares optimization algorithm. The filtered PA output signal aligned to the PA input signal is then $y_a(t)$, defined in (10).

$$y_a(t) = y_f(t - t_0) \tag{10}$$

Having filtered and aligned the PA output to the PA input, the gain $g(t)$ of the PA can then be accurately calculated as in (11), where $x(t)$ is the envelope of the input two-tone signal.

$$g(t) = \left| \frac{y_a(t)}{x(t)} \right| \tag{11}$$

The small-signal gain g_{ss} was then obtained by evaluating $g(t)$ at an instant t_{ss} where the PA input can be considered a small-signal excitation. Since the $V_{GS}(G_{SS})$ map was obtained in the preliminary measurements for a small-signal CW input of −10 dBm, then it is convenient that t_{ss} be the instant at which the input excitation has an amplitude of −10 dBm. In general, g_{ss} is given by (12), where V_{ss} is the small-signal level and V_{pk} is the peak amplitude of the two-tone input (in linear units).

$$\begin{aligned} g_{ss} &= g(t_{ss}), \\ \text{where } t_{ss} &= \frac{1}{\Delta f}\left[1 - \frac{1}{\pi}\arcsin\left(\frac{V_{ss}}{V_{pk}}\right)\right] \end{aligned} \tag{12}$$

Finally, the compensation voltage ΔV_{GS} that cancels out the virtual back gate voltage at time t_{ss} was estimated by interpolating g_{ss} over the $V_{GS}(G_{SS})$ map. This was done for all measurements across all two-tone frequency separations Δf, resulting in a $\Delta V_{GS}(\Delta f, t_{ss})$ profile. This frequency-domain profile was then used to extract the parameters of the trapping model of the ACC by minimizing the MSE between the measured $\Delta V_{GS}(\Delta f, t_{ss})$ profile and the one generated by the trapping model using the CMA-ES optimization algorithm. The resulting parameters are listed in Table II.

D. Compensation Results

After extracting the parameters of the charge-trapping model, these were programmed into the ACC by soldering the required resistors (R_0–R_3) and setting the breakpoint voltages (V_2 and V_3) with an external power supply. Then, the ACC was connected to the PA and the following results were obtained.

Fig. 11(a) shows the $g_{ss}(\Delta f)$ profiles obtained from the steady-state response of the uncompensated GaN HEMT-based PA to a series of two-tone excitations with increasing two-tone frequency separation and for different peak input powers (24 dBm to 29 dBm). These results can be explained

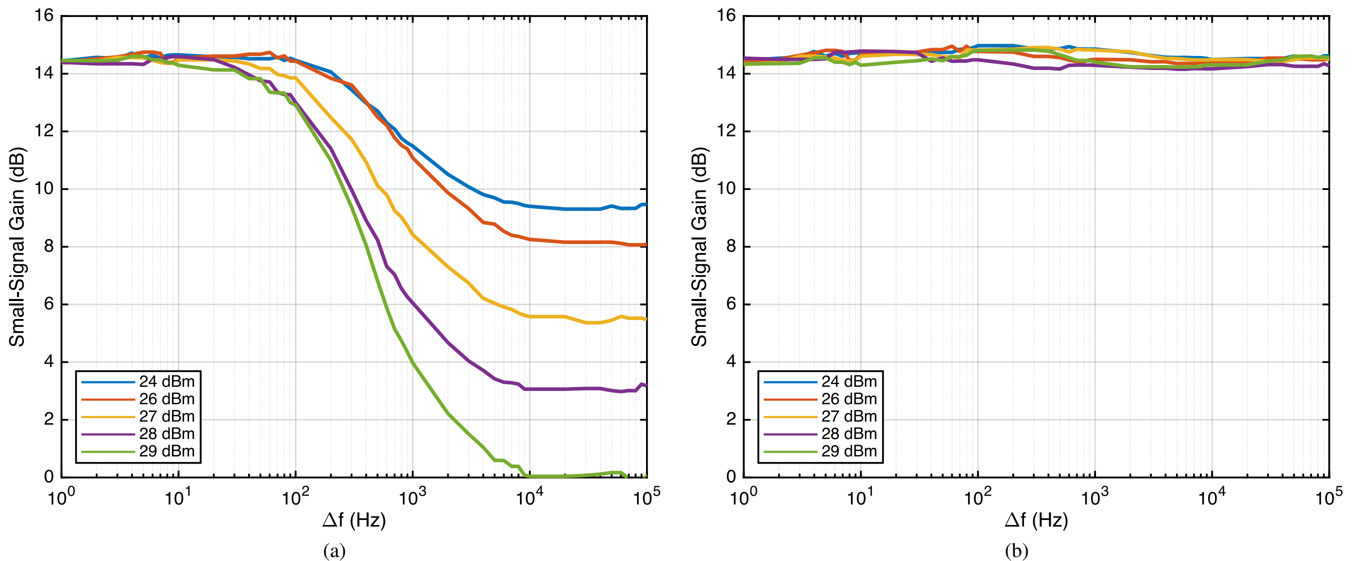

Fig. 11. Two-tone response of the GaN HEMT-based PA (a) without compensation and (b) with compensation using our ACC.

through our understanding of the charge-trapping mechanism as follows. As the amplitude of the sinusoidal input envelope rises from zero to its peak value, the GaN HEMT accumulates charge in trapped states. Furthermore, as the amplitude descends from the peak toward zero, the trapped charge is released. If the envelope is much slower than the time constants associated with the charge emission process (i.e., for low values of Δf), then all trapped charge has been released by the time the envelope has descended from its peak amplitude to a small-signal level, and the small-signal gain remains unchanged. However, if the envelope is fast enough (i.e., for sufficiently large values of Δf), then some charge remains trapped by the time the envelope has descended from its peak amplitude to a small-signal level, resulting in a decrease of the small-signal gain. If the input envelope is much faster than the charge emission process (i.e., for very large values of Δf), then barely any charge is released during the descent of the input envelope from its peak amplitude to a small-signal level, resulting in a saturated decrease of the small-signal gain. Naturally, as was demonstrated with the pulse-response measurements in Section VI, if the peak power of the input envelope is increased, then more charge is accumulated and the collapse of the small-signal gain is greater.

Fig. 11(b) shows the $g_{ss}(\Delta f)$ profiles of the same GaN HEMT-based PA, but while being compensated by the ACC. This figure reveals that the frequency-dependent small-signal gain collapse experienced by the PA due to charge-trapping phenomena is completely compensated by the ACC.

TABLE II
TWO-TONE RESPONSE COMPENSATION PARAMETERS

P_{pk}	R_0	R_1	R_2	R_3	V_2	V_3
24 dBm	91 Ω	9.1 MΩ	330 kΩ	220 kΩ	24 mV	24 mV
26 dBm	91 Ω	9.1 MΩ	330 kΩ	220 kΩ	30 mV	30 mV
27 dBm	91 Ω	7.5 MΩ	1.1 MΩ	390 kΩ	33 mV	34 mV
28 dBm	91 Ω	7.5 MΩ	1.1 MΩ	390 kΩ	24 mV	36 mV
29 dBm	91 Ω	7.5 MΩ	1.1 MΩ	390 kΩ	23 mV	25 mV

VIII. SELF-BIASING COMPENSATION

In this section we describe the third set of measurements that were made to verify the ability of the ACC to compensate the long-term memory effects caused by charge-trapping phenomena in GaN HEMT-based PAs. These measurements serve as the definitive validation of the working principle of the ACC, since they provide the most conclusive evidence of the back-gating mechanism the ACC aims to compensate [10].

In this test, we measured the steady-state response of the PA (with and without compensation) to a series of two-tone excitations with a peak envelope power increasing from 0 dBm to 29 dBm. The tone separation was constant and equal to 100 kHz, which was shown in Fig. 11 to be much faster than the emission process of the GaN HEMT. The setup calibration was done as in Section VII-A, and the parameters of the ACC were the ones extracted in Section VII-C for the small-signal gain profile with a peak input power of 29 dBm. After measuring the response of the PA, its gain was computed as in Section VII-C and the following results were obtained.

Fig. 12(a) illustrates the dynamic gain-versus-input-power profile of the uncompensated PA. These results can be explained through the theory of charge trapping as follows. During the first measurements, while the peak power of the input envelope is low, the gain profile is flat in accordance with the class-B biasing of the PA. However, as the peak input power increases, an increasing amount of charge is captured by deep-level traps in the GaN HEMT. Since there is not enough time during the 10 μs period of the input envelope amplitude for a significant amount of captured charge to be emitted, there is an accumulation of trapped charge that contributes to the depletion of the GaN channel, reducing the gain of the PA. As discussed throughout this paper, this accumulation of trapped charge can be likened to the charging of a virtual back gate that biases the GaN HEMT. Accordingly, the gain profile

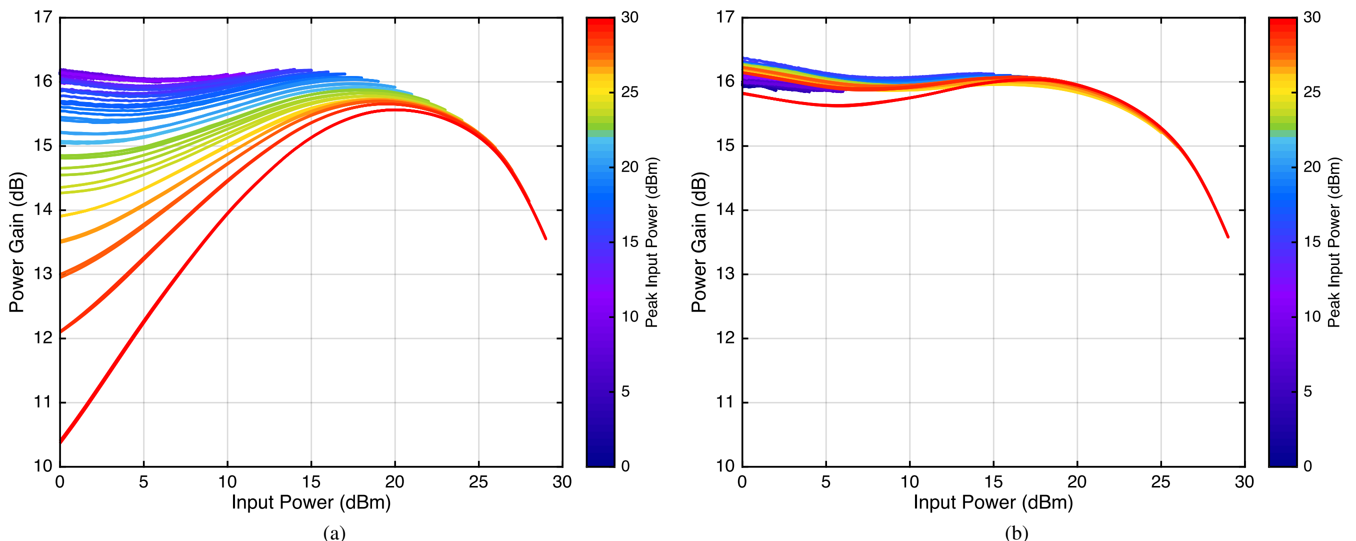

Fig. 12. Dynamic gain profile of the GaN HEMT-based PA (a) without compensation and (b) with compensation using our ACC.

of the PA is gradually shifted toward an increasingly deep class-C profile as the peak input power increases. In the end, the PA had effectively biased itself from class B to class C and demonstrated a gain expansion of over 15 dB.

Fig. 12(b) illustrates the dynamic gain profile of the PA when being compensated by the ACC. Evidently, the ACC corrected the gain collapse caused by the charging of the virtual back gate of the GaN HEMT, proving not only that the ACC is able to compensate the self-biasing of GaN HEMT-based PAs, but also that the charge-trapping compensation model it implements is congruent with the physical behavior of GaN HEMTs.

IX. 5G NR Linearization

With emerging standards for cellular communications such as 5G NR, the deployment of small-cell and massive-MIMO technology to enhance network coverage and capacity is expected to place new restrictions on the power available for the linearization of each individual PA in a transmitter array. Thus, existing DPD algorithms for the linearization of GaN HEMT-based PAs, which are very power-demanding and do not scale with antenna count due to their outstanding complexity, will necessarily be phased out in favor of simpler, more efficient linearization schemes. Moreover, the flexible frame structure specified in 5G NR for the efficient multiplexing of services with diverse requirements—e.g., low latency and high reliability (short subframes), or delay tolerance and high spectral efficiency (long subframes)—, as well as the dynamic time-division duplexing (TDD) scheme for access to the air interface, will excite long-term memory with a greater variety of time scales in transmitting PAs. This places even more emphasis on the accurate modeling and compensation of the long-term memory effects experienced by GaN HEMT-based PAs.

Following this rationale, in this section we demonstrate that our proposed ACC can be used in conjunction with a low-complexity DPD model to linearize a GaN HEMT-based PA for 5G NR communications. Moreover, we demonstrate that our proposed variable-time-constant charge-trapping model is especially suited for GaN HEMT-based PAs under highly variable charge-trapping conditions, and that the modeling of the charge-emission process with a fixed time constant may not be sufficiently accurate for the linearization of GaN HEMT-based PAs for 5G NR communications.

A. Measurement Procedure

After the absolute power of the setup detailed in Section V was calibrated and the GaN HEMT-based PA was biased in class B, the PA was linearized under three different configurations: with a DPD, with a DPD and an ACC with one fixed emission time constant (as in our previous work in [6]), and with a DPD and the proposed ACC with a state-dependent variable emission time constant (with three conductance branches). In all cases, the DPD was a simple fifth-order one-tap memory polynomial. Naturally, while the structure of the DPD was maintained between each test, its coefficients were different for all tests.

The PA input test signal was based on the NR-FR1-TM2 waveform defined in a 3rd Generation Partnership Project (3GPP) technical specification for 5G NR base station conformance testing [34]. This signal, whose envelope is illustrated in Fig. 13, was generated for TDD applications and includes an additional synchronization signal burst at the start of each radio frame (every 10 ms). By featuring different time-varying levels of average signal amplitude, we expect this waveform to reveal the complex dynamics of charge trapping in the form of a slow dynamic residual nonlinearity that persists despite the DPD linearization. Moreover, by compensating the long-term memory induced by charge-trapping phenomena with the ACC, we expect the residual nonlinearity to be reduced. The PA input signal had a bandwidth of 20 MHz and a peak available power of 30 dBm, which led to an initial gain compression of 2.4 dB.

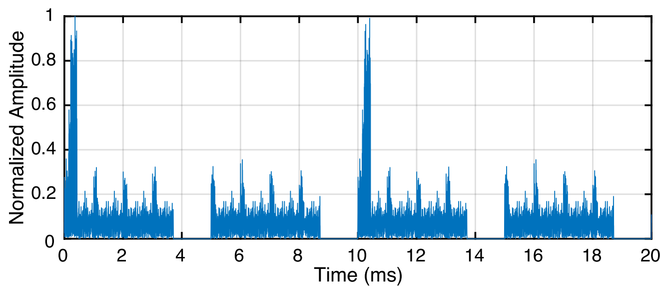

Fig. 13. Envelope of the PA input signal.

B. Compensation Results

Fig. 14 illustrates the spectra of the PA input, the PA output without linearization, and the PA output after the three different linearization tests: with the adopted 5th-order 1-tap memory-polynomial DPD, with the same DPD complemented by an ACC with a fixed emission time constant, and with the same DPD complemented by our proposed ACC with a state-dependent variable emission time constant. As the figure reveals, this simple DPD is not capable of linearizing the PA by itself up to an acceptable level due to its limited memory depth. In reality, for any DPD model to be able to successfully linearize a GaN HEMT-based PA excited by a waveform with a similar or higher level of long-term variability, it would either require a memory depth in the order of 10^3 to 10^6 samples or a highly complicated (and nonscalable) long-term formulation such as the one in [5]. Fig. 14 also demonstrates that the fixed-time-constant ACC provided some improvement in the suppression of out-of-band emissions over the DPD-only linearization—an improvement of 6.5 dB, which was very consistent with the results obtained in [6]. Finally, this reported experimental data also confirms that the proposed variable-time-constant ACC achieves the best level of linearization, over 15 dB better than the DPD-only scheme.

Fig. 15 illustrates the temporal evolution of the per-symbol error-vector magnitude (EVM) obtained for each test, in both root mean square (RMS) and maximum values. This figure is particularly effective at revealing the slow dynamic residual nonlinearity of the GaN HEMT-based PA that remains even after the linearization with the DPD, in Fig. 15(a), and the slightly better linearization with the DPD and the fixed-time-constant ACC, in Fig. 15(b). More specifically, it evidences the sudden—but transient—increase in the level of nonlinearity during the small-signal instants following large-signal input excitations, as discussed at length throughout this paper. Moreover, Fig. 15(c) demonstrates that the proposed variable-time-constant ACC is able to completely compensate the long-term memory effects of the PA and provide, in conjunction with the low-complexity DPD unit, exceptional levels of linearity and signal quality. The overall EVM was 2.4 % RMS and 16.1 % peak for the test with only the DPD, 1.6 % RMS and 10.8 % peak for the test with the DPD and the fixed-time-constant ACC, and 0.9 % RMS and 3.6 % peak for the test with the DPD and the proposed variable-time-constant ACC.

Finally, we measured the power-added efficiency (PAE) of the GaN HEMT-based PA with and without using the proposed

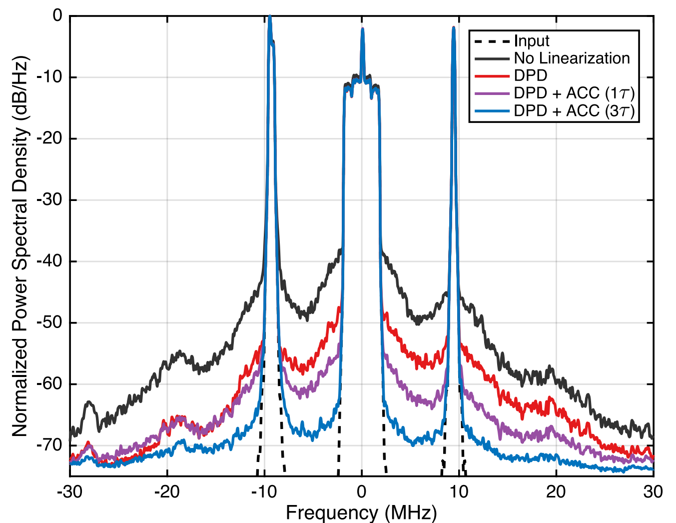

Fig. 14. Spectra of the PA input, the PA output without linearization, the PA output with linearization using a simple memory-polynomial DPD, the PA output with linearization using this same DPD and an ACC with a fixed emission time constant, and the PA output with linearization using the DPD and our proposed ACC with a state-dependent variable emission time constant.

ACC. For the 5G NR linearization tests detailed in this section, the results were an average PAE of 6.9 % without the ACC and a PAE of 6.5 % with the ACC. Since the obtained PAEs were so low because of the very large peak-to-average power ratio (PAPR) of the 5G NR test signal, we repeated the measurement of the PAE for a different input excitation (and without the DPD—only the PA by itself, or the PA when compensated by the ACC) in order to rule out any observation problems that might have arisen from our initial choice of input excitation. Thus, we synthesized a frequency-flat multi-tone signal with a bandwidth of 20 MHz, a peak available power of 30 dBm, and a PAPR of 3 dB. The results were a PAE of 55.7 % without the ACC and a PAE of 55.8 % with the ACC. Finally, as a validity check, we measured the PAE for a two-tone input excitation with a frequency separation of 100 kHz and a peak available power of 30 dBm. The results were a PAE of 55.2 % without the ACC and a PAE of 55.1 % with the ACC.

X. Conclusion

In this paper we presented a charge-trapping model with a variable emission time constant and its implementation as a feedforward analog circuit for the compensation of long-term memory effects in GaN HEMT-based PAs. The behavioral nature of the adopted model allows it to capture both charge-trapping and electro-thermal long-term memory phenomena simultaneously and grants it the advantage of being simple to implement as an electronic analog circuit. Compared to previous models with a fixed emission time constant, the proposed model and its analog implementation provide the ability to more accurately predict and compensate the dynamic trapping state for a wider range of time scales (from microseconds to milliseconds and beyond) and larger PA signal excursions (where the variability of the emission time constant is greater). This is especially relevant for GaN HEMT-based PAs targeted

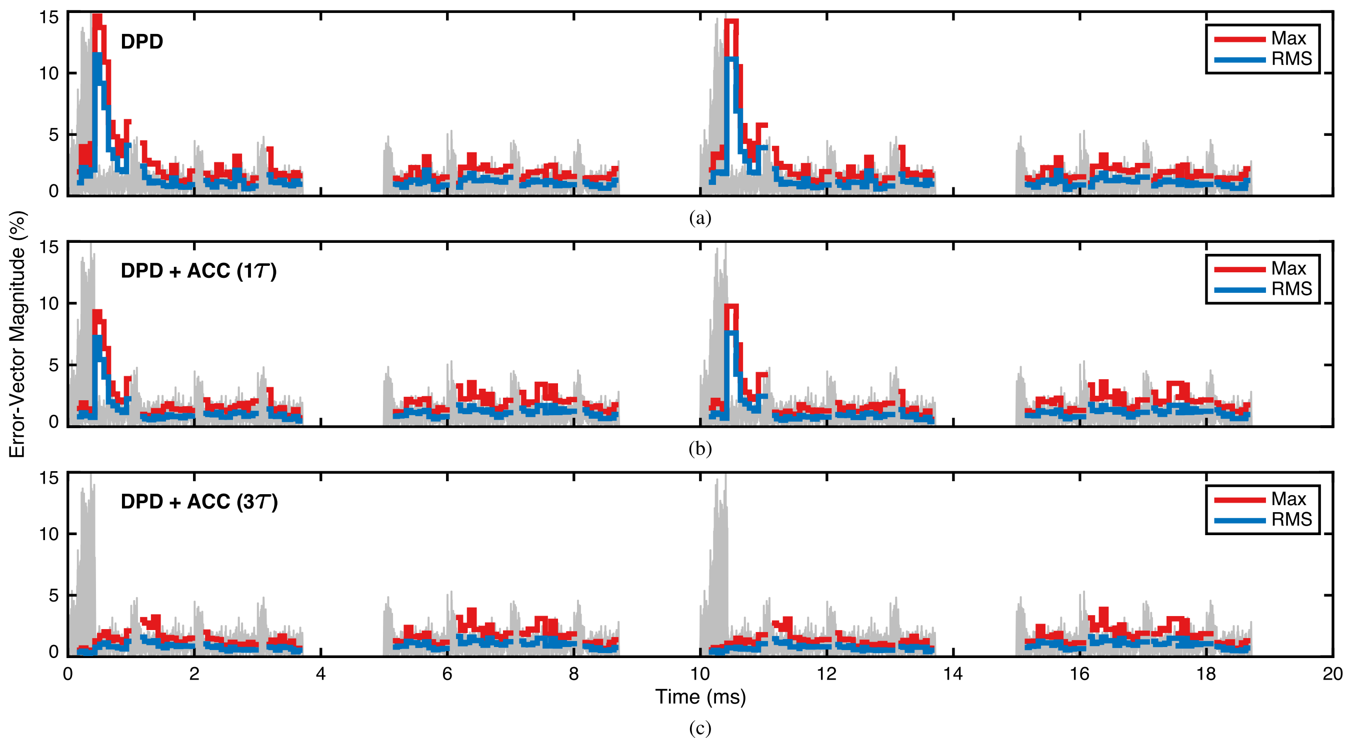

Fig. 15. Temporal evolution of the EVM of the PA output after (a) linearization using a simple memory-polynomial DPD, (b) linearization using this same DPD and an ACC with a fixed emission time constant, and (c) linearization using the DPD and our proposed ACC with a state-dependent variable emission time constant. In the background, a representation of the input envelope is shown for visual reference.

for 5G NR communications, which feature very flexible frame structures with highly variable signal durations. Moreover, the proposed ACC allows for the adaptation of its parameters and the adjustment of its compensation dynamics to better accommodate the operating conditions of the GaN HEMT-based PA, e.g., the ambient temperature.

In order to demonstrate and validate the effectiveness of the model and the ACC, we performed three independent sets of measurements: the transient pulse response, the two-tone response, and the dynamic gain profile of a 2.2 GHz PA based on a 15 W 28 V GaN HEMT. All of these observations were consistent in demonstrating the desired compensation of the long-term PA dynamics. Finally, we demonstrated a hybrid analog/digital 5G NR linearization scenario where our proposed ACC was used in conjunction with a low-complexity memory-polynomial DPD to successfully linearize a GaN HEMT-based PA. When compared to a DPD-only linearization scheme, the introduction of our proposed ACC led to an improvement of the out-of-band emissions by over 15 dB and an improvement of the peak EVM by over 10 p.p. at essentially no cost to the PAE of the GaN HEMT-based PA under test.

While charge-trapping phenomena remain pervasive in GaN HEMT technology and the resulting long-term memory effects prevent it from being deployed in critical applications, external circuit-level solutions such as our ACC can be used to further increase the deployment of high-power high-efficiency GaN HEMT-based PAs. Although our ACC implementation was just a proof of concept, it was sufficient for demonstrating not only that these long-term memory effects can be compensated, but also how they were, indeed, compensated. We envision, then, a high-power high-efficiency GaN HEMT-based PA with an integrated and co-designed low-power analog signal processing unit responsible for the compensation of the long-term memory effects caused by thermal and charge-trapping phenomena. For the linearization of this augmented PA with no apparent long-term memory effects, only a low-complexity low-power DPD unit should be required.

Acknowledgment

The authors would like to thank Dr. L. C. Nunes for providing the PA hardware required for testing the hypothesis and J. L. Gomes for interesting technical discussions regarding some of the observations dealt with in this work.

References

[1] R. S. Pengelly, S. M. Wood, J. W. Milligan, S. T. Sheppard, and W. L. Pribble, “A review of GaN on SiC high electron-mobility power transistors and MMICs,” *IEEE Trans. Microw. Theory Techn.*, vol. 60, no. 6, pp. 1764–1783, Jun. 2012.

[2] T. Mizutani, Y. Ohno, M. Akita, S. Kishimoto, and K. Maezawa, “A study on current collapse in AlGaN/GaN HEMTs induced by bias stress,” *IEEE Trans. Electron Devices*, vol. 50, no. 10, pp. 2015–2020, Sep. 2003.

[3] D. Jin and J. A. del Alamo, “Mechanisms responsible for dynamic ON-resistance in GaN high-voltage HEMTs,” in *Proc. Int. Symp. Power Semicond. Devices ICs*, Bruges, Belgium, Jun. 2012, pp. 333–336.

[4] P. McGovern, J. Benedikt, P. J. Tasker, J. Powell, K. P. Hilton, J. L. Glasper, R. S. Balmer, T. Martin, and M. J. Uren, “Analysis of DC-RF dispersion in AlGaN/GaN HFETs using pulsed I-V and time-domain waveform measurements,” in *Proc. IEEE Int. Microw. Symp.*, Long Beach, CA, USA, Jun. 2005, pp. 503–506.

[5] F. M. Barradas, L. C. Nunes, T. R. Cunha, P. M. Lavrador, P. M. Cabral, and J. C. Pedro, "Compensation of long-term memory effects on GaN HEMT-based power amplifiers," *IEEE Trans. Microw. Theory Techn.*, vol. 65, no. 9, pp. 3379–3388, Sep. 2017.

[6] P. M. Tomé, F. M. Barradas, T. R. Cunha, and J. C. Pedro, "Hybrid analog/digital linearization of GaN HEMT-based power amplifiers," *IEEE Trans. Microw. Theory Techn.*, vol. 67, no. 1, pp. 288–294, Jan. 2019.

[7] K. Kunihiro and Y. Ohno, "A large-signal equivalent circuit model for substrate-induced drain-lag phenomena in HJFETs," *IEEE Trans. Electron Devices*, vol. 43, no. 9, pp. 1336–1342, Sep. 1996.

[8] M. J. Uren, J. Moreke, and M. Kuball, "Buffer design to minimize current collapse in GaN/AlGaN HFETs," *IEEE Trans. Electron Devices*, vol. 59, no. 12, pp. 3327–3333, Oct. 2012.

[9] R. Vetury, N. Q. Zhang, S. Keller, and U. K. Mishra, "The impact of surface states on the DC and RF characteristics of AlGaN/GaN HFETs," *IEEE Trans. Electron Devices*, vol. 48, no. 3, pp. 560–566, Mar. 2001.

[10] J. C. Pedro, L. C. Nunes, and P. M. Cabral, "Soft compression and the origins of nonlinear behavior of GaN HEMTs," in *Proc. Eur. Microw. Integr. Circuit Conf.*, Rome, Italy, Oct. 2014, pp. 353–356.

[11] O. Jardel, F. D. Groote, T. Reveyrand, J.-C. Jacquet, C. Charbonniaud, J.-P. Teyssier, D. Floriot, and R. Quere, "An electrothermal model for AlGaN/GaN power HEMTs including trapping effects to improve large-signal simulation results on high VSWR," *IEEE Trans. Microw. Theory Techn.*, vol. 55, no. 12, pp. 2660–2669, Dec. 2007.

[12] J. L. Gomes, L. C. Nunes, C. F. Gonçalves, and J. C. Pedro, "An accurate characterization of capture time constants in GaN HEMTs," *IEEE Trans. Microw. Theory Techn.*, vol. 67, no. 7, pp. 2465–2474, Jul. 2019.

[13] J. Delprato, D. Barataud, M. Campovecchio, G. Neveux, C. Tolant, and P. Eudeline, "Measured and simulated impact of irregular radar pulse trains on the pulse-to-pulse stability of microwave power amplifiers," *IEEE Trans. Microw. Theory Techn.*, vol. 62, no. 12, pp. 3538–3548, Dec. 2014.

[14] P. M. Tomé, F. M. Barradas, T. R. Cunha, and J. C. Pedro, "Compensation of the pulse-to-pulse instability of GaN HEMT-based power amplifiers," in *Proc. IEEE Int. Microw. Symp.*, Boston, MA, USA, Jun. 2019, pp. 408–411.

[15] G. Simin, A. Koudymov, A. Tarakji, X. Hu, J. Yang, M. A. Khan, M. S. Shur, and R. Gaska, "Induced strain mechanism of current collapse in AlGaN/GaN heterostructure field-effect transistors," *Appl. Phys. Lett.*, vol. 79, no. 16, pp. 2651–2653, Oct. 2001.

[16] S. Huang, S. Yang, J. Roberts1, and K. J. Chen, "Threshold voltage instability in Al2O3/GaN/AlGaN/GaN metal–insulator–semiconductor high-electron mobility transistors," *Jpn. J. Appl. Phys.*, vol. 50, no. 11R, p. 110202, Oct. 2011.

[17] D. Bisi, M. Meneghini, C. de Santi, A. Chini, M. Dammann, P. Brückner, M. Mikulla, G. Meneghesso, and E. Zanoni, "Deep-level characterization in GaN HEMTs–Part I: Advantages and limitations of drain current transient measurements," *IEEE Trans. Electron Devices*, vol. 60, no. 10, pp. 3166–3175, Oct. 2013.

[18] H. Kim, R. M. Thompson, V. Tilak, T. R. Prunty, J. R. Shealy, and L. F. Eastman, "Effects of SiN passivation and high-electric field on AlGaN-GaN HFET degradation," *IEEE Electron Device Lett.*, vol. 24, no. 7, pp. 421–423, Aug. 2003.

[19] B. P. Gila, M. Hlad, A. H. Onstine, R. Frazier, G. T. Thaler, A. Herrero, E. Lambers, C. R. Abernathy, S. J. Pearton, T. Anderson, S. Jang, F. Ren, N. Moser, R. C. Fitch, and M. Freund, "Improved oxide passivation of AlGaN/GaN high electron mobility transistors," *Appl. Phys. Lett.*, vol. 87, no. 16, p. 163503, Oct. 2005.

[20] S. Huang, Q. Jiang, S. Yang, C. Zhou, and K. J. Chen, "Effective passivation of AlGaN/GaN HEMTs by ALD-grown AlN thin film," *IEEE Electron Device Lett.*, vol. 33, no. 4, pp. 516–518, Feb. 2012.

[21] J. P. Ibbetson, P. T. Fini, K. D. Ness, S. P. DenBaars, J. S. Speck, and U. K. Mishra, "Polarization effects, surface states, and the source of electrons in AlGaN/GaN heterostructure field effect transistors," *Appl. Phys. Lett.*, vol. 77, no. 2, pp. 250–252, Jun. 2000.

[22] G. Koley and M. G. Spencer, "On the origin of the two-dimensional electron gas at the AlGaN/GaN heterostructure interface," *Appl. Phys. Lett.*, vol. 86, no. 4, p. 042107, Jan. 2005.

[23] S. C. Binari, P. B. Klein, and T. E. Kazior, "Trapping effects in GaN and SiC microwave FETs," *Proc. IEEE*, vol. 90, no. 6, pp. 1048–1058, Nov. 2002.

[24] S. Heikman, S. Keller, S. P. DenBaars, and U. K. Mishra, "Growth of Fe doped semi-insulating GaN by metalorganic chemical vapor deposition," *Appl. Phys. Lett.*, vol. 81, no. 3, pp. 439–441, Jul. 2002.

[25] M. J. Uren, K. J. Nash, R. S. Balmer, T. Martin, E. Morvan, N. Caillas, S. L. Delage, D. Ducatteau, B. Grimbert, and J. C. D. Jaeger, "Punch-through in short-channel AlGaN/GaN HFETs," *IEEE Trans. Electron Devices*, vol. 53, no. 2, pp. 395–398, Jan. 2006.

[26] J. C. Pedro, P. M. Cabral, T. R. Cunha, and P. M. Lavrador, "A multiple time-scale power amplifier behavioral model for linearity and efficiency calculations," *IEEE Trans. Microw. Theory Techn.*, vol. 61, no. 1, pp. 606–615, Dec. 2012.

[27] I. Angelov, L. Bengtsson, and M. Garcia, "Extensions of the Chalmers nonlinear HEMT and MESFET model," *IEEE Trans. Microw. Theory Techn.*, vol. 44, no. 10, pp. 1664–1674, Oct. 1996.

[28] J. Xu, R. Jones, S. A. Harris, T. Nielsen, and D. E. Root, "Dynamic FET model–DynaFET–for GaN transistors from NVNA active source injection measurements," in *Proc. IEEE Int. Microw. Symp.*, Tampa, FL, USA, Jun. 2014, pp. 1–3.

[29] P. Horowitz and W. Hill, *The Art of Electronics*, 3rd ed. New York, NY, USA: Cambridge University Press, 2015.

[30] P. M. Cabral, J. C. Pedro, and N. B. Carvalho, "Nonlinear device model of microwave power GaN HEMTs for high power-amplifier design," *IEEE Trans. Microw. Theory Techn.*, vol. 52, no. 11, pp. 2585–2592, Nov. 2004.

[31] J. Chani-Cahuana, P. N. Landin, C. Fager, and T. Eriksson, "Iterative learning control for RF power amplifier linearization," *IEEE Trans. Microw. Theory Techn.*, vol. 64, no. 9, pp. 2778–2789, Jul. 2016.

[32] L. C. Nunes, J. L. Gomes, P. M. Cabral, and J. C. Pedro, "A simple method to extract trapping time constants of GaN HEMTs," in *Proc. IEEE MTT-S Int. Microw. Symp.*, Philadelphia, PA, USA, Jun. 2018, pp. 716–719.

[33] N. Hansen and A. Ostermeier, "Completely derandomized self-adaptation in evolution strategies," *Evol. Comput.*, vol. 9, no. 2, pp. 159–195, Jun. 2001.

[34] *NR; Base station (BS) conformance testing Part 1: Conducted conformance testing*, 3rd Generation Partnership Project (3GPP) Technical Specification (TS) 38.141-1 Version 16.3.0, Mar. 2020.

Pedro M. Tomé (S'17) received the M.Sc. degree in electronic and telecommunications engineering from the University of Aveiro, Aveiro, Portugal, in 2016.

He is currently a student of the MAP-tele Doctoral Program in Telecommunications, a joint program between the University of Minho, Guimarães, Portugal, the University of Aveiro, and the University of Porto, Porto, Portugal. His current research interests include analog signal processing and the study, characterization, modeling, and compensation of electron trapping effects in GaN HEMT-based RF PAs.

Filipe M. Barradas (S'13-M'17) was born in Évora, Portugal, in July 1989. He received the M.Sc degree in electronics and telecommunications engineering from Universidade de Aveiro, Aveiro, Portugal, in 2012, and the PhD degree in electrical engineering at the same university in 2017.

He is currently a Research Assistant at Instituto de Telecomunicações, Aveiro, Portugal. His main interests include digital predistortion and behavioral modelling of RF PAs, as well as signal processing with applications on telecommunications. Other interests include design and analysis of nonlinear microwave circuits.

Dr. Barradas has been a reviewer for several IEEE journals.

Telmo R. Cunha (M'05) received the Diploma and Ph.D. degrees in electronics and computer engineering from the Universidade do Porto, Porto, Portugal, in 1996 and 2003, respectively.

He was formerly involved with the Astronomical Observatory, University of Porto, and, afterward, with Geonav Lda., a private company near Porto. Since 2004, he is an Assistant Professor with the Department of Electronics, Telecommunications and Informatics, University of Aveiro, Aveiro, Portugal, and also a Senior Research Engineer with the Institute of Telecommunications, University of Aveiro. He has been lecturing in the fields of control theory and electronics, and he has been involved in several national and international research projects. His current research interests include behavioral modeling and linearization applied to radio frequency and microwave devices.

Dr. Cunha has been a reviewer for several IEEE journals.

José C. Pedro (S'90–M'95–SM'99–F'07) received the Diploma, Ph.D. and Habilitation degrees in electronics and telecommunications engineering from the Universidade de Aveiro, Aveiro, Portugal, in 1985, 1993, and 2002, respectively.

He is currently a Full Professor with the Universidade de Aveiro and head of the Aveiro site of the Instituto de Telecomunicações. He has authored 2 books and authored or co-authored more than 200 papers in international journals and symposia. His current research interests include active device modelling and the analysis and design of various nonlinear microwave circuits.

Dr. Pedro was a recipient of various prizes including the 1993 Marconi Young Scientist Award, the 2000 Institution of Electrical Engineers Measurement Prize, the 2015 EuMC Best Paper Microwave Prize, and the Microwave Distinguished Educator Award. He has served the scientific community as a Reviewer and an Editor for several conferences and journals, namely, the IEEE TRANSACTIONS ON MICROWAVE THEORY AND TECHNIQUES, for which he was the Editor-in-Chief.

APPENDIX G

Paper J5

Characterization, Modeling, and Compensation of the Dynamic Self-Biasing Behavior of GaN HEMT-Based Power Amplifiers

Pedro M. Tomé, Filipe M. Barradas, Luís C. Nunes, João L. Gomes, Telmo R. Cunha, and José C. Pedro

Published In: IEEE Transactions on Microwave Theory and Techniques

Date of Publication: 17 July 2020

DOI: 10.1109/TMTT.2020.3006290

This is the authors' version of an article that has been published in the IEEE TRANSACTIONS ON MICROWAVE THEORY AND TECHNIQUES. Changes were made to this version by the publisher prior to publication.
The final version of the record is available at https://doi.org/10.1109/TMTT.2020.3006290.

Characterization, Modeling, and Compensation of the Dynamic Self-Biasing Behavior of GaN HEMT-Based Power Amplifiers

Pedro M. Tomé, *Student Member, IEEE,* Filipe M. Barradas, *Member, IEEE,* Luís C. Nunes, *Member, IEEE,* João L. Gomes, *Student Member, IEEE,* Telmo R. Cunha, *Member, IEEE,* and José C. Pedro, *Fellow, IEEE*

***Abstract*—Charge-trapping phenomena in radio-frequency (RF) power amplifiers (PAs) based on GaN high-electron-mobility transistor (HEMT) technology are understood to be responsible for the dynamic self-biasing behavior that leads to a seemingly intractable slow dynamic residual nonlinearity in communications applications. For this reason, and based on recent developments in the characterization and modeling of charge-trapping phenomena, in this paper we demonstrate how the dynamic self-biasing behavior of GaN HEMT-based PAs can be characterized, modeled, and compensated. First, we describe a method for the accurate characterization of the capture and emission dynamics of charge-trapping phenomena using transient two-tone large-signal RF measurements. Then, we demonstrate that the accurate modeling of these phenomena is contingent on the capture process being described by a state-variable time constant, rather than a fixed near-instantaneous time constant as is typically assumed. Finally, we propose a fully analog electronic circuit that implements an approximation of the Shockley–Read–Hall statistics-based physical model of charge trapping to compensate the dynamic self-biasing behavior of a 15 W GaN HEMT-based PA.**

***Index Terms*—Analog linearization, charge trapping, electron trapping, GaN high-electron-mobility transistor, long-term memory effects, self-biasing, virtual back gate.**

I. INTRODUCTION

POWER amplifiers (PAs) based on gallium nitride high-electron-mobility transistor (HEMT) technology have emerged as the most compelling solution for the transmission of high-power radio-frequency (RF) signals for cellular communications and radar applications [1]. However, despite their unmatched combination of very high output power levels, high power efficiencies and wide bandwidths of operation, the excessive level of nonlinearity typically presented by these PAs often precludes their actual deployment in the mobile communications infrastructure, where alternative silicon-based technologies are still the most prevalent. GaN HEMT-based PAs are unusually nonlinear in part due to the long-term memory effects caused by charge-trapping phenomena: the capture and emission of charge carriers in deep-level traps. These effects, which include current collapse [2], knee walkout [3] and dc–RF dispersion [4], lead to a slow dynamic nonlinearity that manifests itself as a seemingly intractable post-linearization residual distortion in communications applications [5] and a severe deterioration of the pulse-to-pulse stability in radar applications [6], [7].

In order to address these issues and ultimately deliver a GaN HEMT technology free from long-term memory effects, several experimental procedures have been proposed for the characterization of charge-trapping phenomena and the extraction of the parameters of relevant models. Among these, the most prevalent are based on pulsed [8]–[10] or double-pulsed [11] drain-current deep-level transient spectroscopy, low-frequency admittance measurements [12], and pulsed-RF active load-pull measurements [13]. Since these characterization procedures are performed on the discrete HEMT and require very specialized equipment, alternative methods targeting fully assembled GaN HEMT-based PAs have also been proposed. These include pulse-modulated [14] and two-tone-modulated [15] RF measurements-based procedures that only require equipment commonly available in most RF laboratories, such as a vector signal generator and a vector signal analyzer, and that can be performed much closer to the target operating conditions of the PA under test.

Charge trapping is characterized by highly asymmetric charge capture and emission processes [16]. While charge capture has traditionally been dismissed as a near-instantaneous process, recent developments in the characterization and modeling of charge-trapping phenomena have shown that the time constants associated with charge capture can be comparable to the slow-varying envelopes of modern radar or wireless communications signals, ranging from less than a microsecond up to a few tens of milliseconds [17]. This has uncovered the outstanding importance of the multiple-time-constant dynamic behavior of charge trapping in the pulse-to-pulse stability of GaN HEMT-based PAs for radar applications and in the linearization of GaN HEMT-based PAs for cellular base station transmitters. For this reason, in [18] we proposed a new method where transient two-tone RF measurements are used to accurately characterize the dynamics of charge-trapping capture and emission processes in GaN HEMT-based PAs by

Manuscript submitted April 21, 2020; revised June 7, 2020; accepted June 12, 2020.

This work was supported by FCT/MEC through National Funds under Project UID/EEA/50008/2013 (APIC) and Project PTDC/EEI-TEL/7049/2014 (Lin5GPA). The work of P. M. Tomé was supported by FCT/MEC under Ph.D. Grant PD/BD/128198/2016. This paper is an expanded version from the IEEE MTT-S International Microwave Symposium (IMS 2020), Los Angeles, CA, USA, June 21-26, 2020. *(Corresponding author: Pedro M. Tomé).*

The authors are with the Department of Electronics, Telecommunications and Informatics, Institute of Telecommunications, University of Aveiro, 3810–193 Aveiro, Portugal (e-mail: tome.p.m@ua.pt; filipebarradas@ua.pt; cotimos@ua.pt; joaolucas@ua.pt; trcunha@ua.pt; jcpedro@ua.pt).

tracking their dynamic self-biasing behavior across both the frequency and time domains, as illustrated in Fig. 1.

In this paper, we extend the work of [18] by demonstrating that the dynamic self-biasing behavior caused by charge-trapping phenomena—and the resulting long-term memory effects—can be compensated using an external analog circuit whose parameter extraction is based on our proposed transient two-tone RF characterization method. Our analog compensation circuit, which features a state-variable capture time constant and a fixed emission time constant, implements an approximation of a state-of-the-art charge-trapping physical model based on Shockley–Read–Hall statistics [17] and works by canceling out, in real time and based on the model-predicted trapping state, the threshold voltage variation experienced by the GaN HEMT in a GaN HEMT-based PA. This compensation strategy has been shown to greatly improve the linearizability of GaN HEMT-based PAs and reduce the slow dynamic residual nonlinearity that impairs this technology [19].

This paper is organized as follows. In Section II, we establish the baseline theoretical background on the effects of charge-trapping phenomena in GaN HEMT-based PAs. In Section III, we review the transient two-tone RF characterization method first proposed in [18]. In Section IV, we detail how this characterization method can inform the extraction of the parameters of relevant charge-trapping models. In Section V, we propose a new charge-trapping behavioral model based on the Shockley–Read–Hall statistics-based physical model, and detail its implementation as an analog electronic circuit. This analog circuit, whose parameters are extracted through our proposed characterization method, is then shown to be capable of compensating the dynamic self-biasing behavior of a GaN HEMT-based PA, as well as other transient long-term memory effects caused by charge-trapping phenomena. Finally, in Section VI, we provide some concluding remarks.

II. Theoretical Background

Charge trapping refers to an accumulation of charge in deep-level traps with energy levels near the middle of the band gap of a semiconductor. In GaN HEMTs, this is understood to be caused by large electric fields at the gate terminal (gate lag), the drain terminal (drain lag), or a combination of both. As a result of the accumulated charge, an equivalent net-negative gate electric potential is created and the conductivity of the GaN channel is decreased until the charge is released through thermal emission [20].

Charge-trapping phenomena in GaN HEMTs inherently present highly asymmetric capture and emission times [16], [17]. However, while it is generally believed that the asymmetry between the time constants associated with charge capture and emission is so great that the capture process can be considered nearly instantaneous, in [17] the authors demonstrated that this is not an accurate assumption. In reality, the time constants associated with charge capture can be comparable to the slow-varying envelopes of modern radar or wireless communications signals, ranging from less than a microsecond up to a few tens of milliseconds.

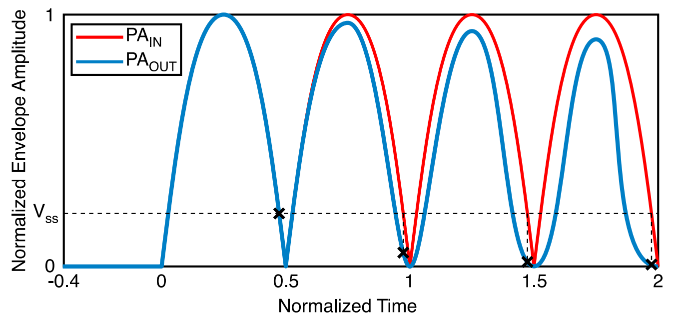

Fig. 1. Typical transient response of a GaN HEMT-based PA to a two-tone envelope excitation. Due to charge trapping, the PA gradually self-biases toward a deep class C and loses most of its small-signal gain.

The most common abstraction for charge-trapping phenomena in GaN HEMTs is a virtual back gate that charges and discharges at different rates [16], dynamically offsetting the threshold voltage of the HEMT and producing a self-biasing effect [21]. This self-biasing effect has been demonstrated to be so severe that a GaN HEMT-based PA biased in class B can easily degenerate into deep class C under normal operating conditions [22]. Since this effect depends on the long-term characteristics of the signal being transmitted by the PA, it is not surprising that conventional digital predistortion algorithms are not capable of delivering sufficient levels of linearization, as the transfer characteristics of the PA are continuously changing in time at a rate much slower than the observable time span of these algorithms (limited by the available sample memory), but also much faster than the rate at which the predistortion model parameters are adapted [5], [19].

In spite of the virtual back gate being just an abstraction, drift-diffusion simulations of AlGaN/GaN heterostructures suggest that there may indeed be an actual accumulation of charge beneath the gate of the HEMT [20]. Furthermore, the principle of a virtual back gate has been exploited to successfully compensate long-term memory effects in GaN HEMT-based PAs employing commercial GaN HEMTs [7], [19]. Thus, there are strong indications that the dynamic self-biasing behavior of GaN HEMT-based PAs can be attributed to charge-trapping phenomena and that an accurate characterization of these phenomena is essential for the compensation of this behavior.

III. Characterization

Previous efforts to characterize trapping-related time constants using large-signal two-tone excitations [15] identified that, for very low two-tone frequency separations Δf (<10 Hz), the small-signal gain of a GaN HEMT-based PA remains unchanged. This happens because, while there is a very significant accumulation of trapped charge during the large-signal portion of the envelope, the envelope is so slow that there is enough time for most of the trapped charge to be released through thermal emission by the time the envelope reaches a small-signal level. However, for larger Δf (0.1–1 kHz), it is found that the small-signal gain decreases because there is not enough time for the trapped charge to

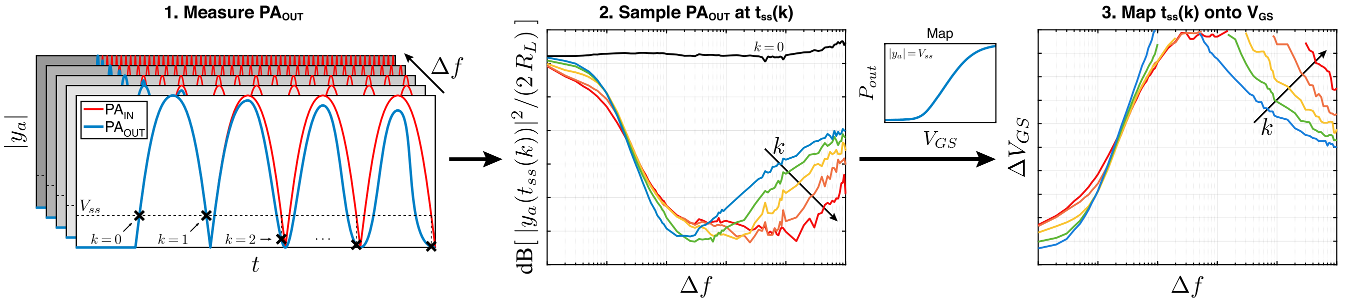

Fig. 2. Diagram of the proposed characterization method. First, the transient response of the PA to a series of large-signal two-tone excitations is measured. Then, specific small-signal points are selected at $t = t_{ss}(k)$. Finally, the equivalent gate–source voltage variation is estimated by mapping these points onto V_{GS} through the measured $P_{out}(V_{GS}, V_{ss})$ map. $y_a(t)$ is the PA output envelope, time-aligned with the corresponding two-tone input signal.

be released during the short period between the large-signal and small-signal parts of the sinusoidal envelope. For much larger Δf (>10 kHz), the envelope is too fast for there to be any significant emission of trapped charge, so the small-signal gain remains very low at a constant level.

Even though the method detailed in [15] is sufficient for the characterization of the steady-state balance between the capture and emission processes (as all measurements are done in steady-state conditions), it provides very little information on each process separately. For this reason, in [18] we introduced a new transient two-tone RF characterization method that allows for the accurate characterization of both capture and emission processes. Through this method, the gradual self-biasing of a GaN HEMT-based PA can be tracked at each envelope half-cycle and the dynamic variation of the HEMT's threshold voltage (or virtual back gate voltage) can be more comprehensively characterized. We assume that, in a realistic PA, the time constants associated with the bias networks are much shorter than those associated with thermal and charge-trapping phenomena, otherwise the efficiency of the PA would be extremely low for wideband excitations [23]. Our proposed method is graphically summarized in Fig. 2 and detailed as follows.

A. Transient Two-Tone RF Characterization Method

1) Measurements: First, the response of the PA under test to a constant small-signal continuous-wave (CW) excitation is measured as a function of the gate–source voltage. From this preliminary measurement results the map $P_{out}(V_{GS}, V_{ss})$, where P_{out} is the measured PA output power, V_{GS} is the gate–source voltage, and V_{ss} is the amplitude of the small-signal CW excitation. This map, which is assumed to be static, is used at a later stage to estimate the trapping state of the PA in the form of an equivalent variation of the HEMT's threshold voltage. Note that V_{GS} is only required to be swept from the PA's target bias point to increasingly negative voltages, since charge trapping always leads to an increase of the threshold voltage. Thus, unless the PA is intended to be biased in class A, the temperature throughout the sweep will be approximately constant, as the power dissipated due to the quiescent drain current will vary very little throughout the sweep.

Then, the transient response of the PA to a series of large-signal two-tone RF excitations with frequency separation Δf is measured, where Δf is a swept parameter. This can be done using a vector signal generator (VSG) and a vector signal analyzer (VSA). The VSG should be configured to generate one single instance of each waveform and to trigger the VSA measurement at the start of each waveform playback. In order to maintain the same initial conditions for all measurements (i.e., the same baseline trapping state), the charge accumulated as a result of each measurement should be allowed to be released through thermal emission prior to triggering the next measurement. Some strategies for achieving this include, e.g., waiting 30 s to 100 s between each measurement with the PA under a small-signal excitation, tracking the recovery of the PA's small-signal gain, or tracking the recovery of the PA's quiescent current. From these measurements results a dataset containing the transient responses of the PA to large-signal two-tone excitations with different frequency separations Δf.

2) Post-Processing: After performing the required measurements, all recorded time series must be aligned with their respective excitations in order to compensate the group delay introduced by the measurement setup. Since we consider that the measurements are performed using a VSG and a VSA, then the input excitation is never actually measured—it only exists as a digital set of samples in a computer. Thus, aligning the measured PA output with the input excitation consisted, in our case, in sliding the input excitation across time in order to maximize the cross-correlation between the two signals.

For optimal results, the alignment should not be done simply by cyclically shifting the samples of the input excitation vector, as this would limit the time resolution to the duration of one sampling period. Instead, a new input excitation vector should be generated by introducing a double-precision phase shift or time delay to the sampling of the respective sinusoid. Thus, optimum alignment requires an optimization process for finding t_0 such that $|x(n, t_0)| = |\sin(2\pi \cdot \Delta f/2 \cdot (n/f_s - t_0))|$ has maximum cross-correlation with the amplitude of the measured PA response $|y(n)|$, where $n = 0, 1, \cdots, N-1$ is the sample index and f_s is the sampling frequency. This can be done in an expedient fashion by minimizing the cost function $\lambda(t_0)$ defined in (1) using, e.g., gradient descent techniques or more advanced covariance matrix adaptation evolution strategies (CMA-ES) [24]. In the end, the adjusted time vector $t(n) = n/f_s - t_0$ is obtained.

$$\lambda(t_0) = \sum_{n=0}^{N-1} \left[\log\left(\frac{|y(n)|}{\max\{|y(n)|\}} \right) - \log(|x(n, t_0)|) \right]^2 \quad (1)$$

Note that the alignment process can be improved (and greatly accelerated) by considering just the first envelope cycle of each recorded time series, as this is the cycle with the most clearly defined (steepest) zero-crossing, as illustrated in Fig. 1. This is because the PA has not yet self-biased to a deep class C, where the zero-crossings of the sinusoidal envelope are flattened. Thus, for each time series, we determine t_0 using the first envelope cycle and delay/advance the whole time series by that amount. Furthermore, note that proper alignment is most critical at the small-signal parts of the envelope, as this is where the slope of the envelope amplitude is steepest. It is for this reason that $\lambda(t_0)$ includes the logarithm function—to magnify the small-signal amplitudes and prevent their squared errors from being outweighed by those of the large-signal parts of the envelope. For an example of how the logarithm function impacts the alignment results, see Fig. 3, where a zoomed-in view of an envelope zero-crossing is shown after alignment considering $\lambda(t_0)$ as defined in (1) (black and blue markers), and after alignment considering the more obvious—but less adequate—cost function defined in (2) (black and red markers).

$$\widehat{\lambda}(t_0) = \sum_{n=0}^{N-1} \left[\frac{|y(n)|}{\max\{|y(n)|\}} - |x(n, t_0)| \right]^2 \qquad (2)$$

After obtaining the aligned transient response $y_a(t)$ of the PA (in reality, the response is the same and it is the time vector that is shifted by t_0), it is sampled through linear interpolation at the instants where the amplitude of the respective two-tone excitation is equal to that of the small-signal CW excitation used in the preliminary measurement of the $P_{out}(V_{GS}, V_{ss})$ map (as represented in Fig. 1 by the black markers). In other words, the values of $y_a(t_{ss}(k))$ are recorded, where t_{ss} is defined in (3), $k = 1, 2, \cdots, K$ is the index of each half-cycle of the two-tone input excitation with frequency separation Δf (up to a total of K envelope half-cycles or amplitude periods), V_p is the peak amplitude of the two-tone input excitation, and V_{ss} is the amplitude of the CW excitation at which the $P_{out}(V_{GS}, V_{ss})$ map was measured. This results in a dataset

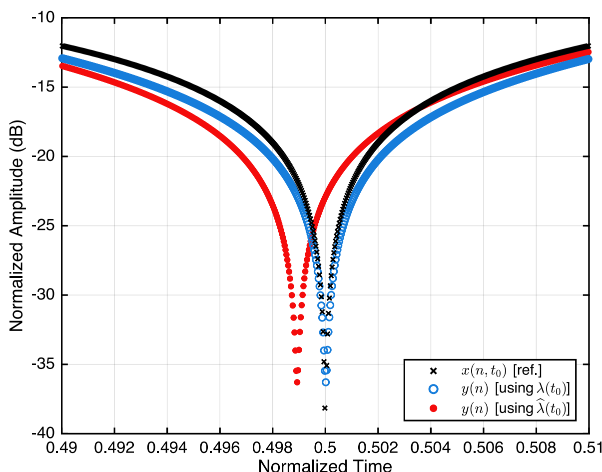

Fig. 3. Comparison between the envelope alignment results obtained with different optimization cost functions.

that provides a comprehensive characterization of the gradual self-biasing experienced by a GaN HEMT-based PA for a wide variety of amplitude-modulated excitation dynamics.

$$t_{ss}(k) = \frac{1}{\Delta f} \left[k - \frac{1}{\pi} \arcsin\left(\frac{V_{ss}}{V_p} \right) \right] \qquad (3)$$

B. *Experimental Results*

1) Measurement Setup: In order to characterize the dynamic self-biasing of a GaN HEMT-based PA, we assembled the measurement setup illustrated in Fig. 4(a). The in-phase and quadrature baseband waveforms of the transient two-tone input signals were generated using a Tektronix AWG70002A arbitrary waveform generator (AWG), which was connected to a Keysight E8267D PSG VSG for RF up-conversion. A Mini-Circuits ZHL-16W-43-S+ driver scaled the output of the VSG and provided the input excitations to the PA. The output of the PA was measured using a Keysight N9041B UXA VSA, which was preceded by an attenuator for the adequate adjustment of the VSA input power level. The dc power of the PA was sourced from a Keysight N6705C dc power analyzer, which was also used for sweeping V_{GS} during the measurement of the $P_{out}(V_{GS}, V_{ss})$ map.

Using this setup, we characterized the dynamic self-biasing behavior of a 1.6 GHz single-ended PA based on the 15 W 28 V Wolfspeed CGH27015F GaN HEMT. The PA, whose CW power-added efficiency was measured as greater than 56 %, was biased in class B at the root of g_{m3} [25], leading to a quiescent drain current of 40 mA. The bias voltages were, therefore, $V_{GG} = -2.7$ V and $V_{DD} = 28$ V. The two-tone excitations provided a peak available input power of 29 dBm and their frequency separation was varied from 10 Hz to 1 MHz. The $P_{out}(V_{GS}, V_{ss})$ map and the transient response of the PA at $t_{ss}(k)$ were measured for an input power level of 0 dBm (i.e., $V_{ss} = 316$ mV). The PA was measured for 100 periods of each input excitation, the last of which corresponded to a near-steady-state condition. In order to minimize the spurious effects of inevitable temperature drifts, all measurements were carried out at a controlled ambient temperature of 24 °C and the PA was provided with ample auxiliary active cooling.

2) Setup Calibration: Before performing the characterization procedure, the measurement setup was calibrated at the RF-input and RF-output planes of the PA (α and β in Fig. 4). First, the scattering parameters of a directional coupler were measured at its input port (1:IN), output port (2:OUT) and coupled port (3:CPL) using an Anritsu MS4647B vector network analyzer (VNA). Then, the PA was disconnected from the measurement setup and the directional coupler was connected in its stead at the same α and β planes of calibration (i.e., between the output of the driver and the input of the VSA attenuator). As shown in Fig. 4(b), the coupled port of the directional coupler was connected to a Keysight N1913A power meter (PM) through a Keysight E9301A average power sensor. This calibration setup allows for an accurate assessment of the absolute power levels at both calibration planes simultaneously by combining the average power measurement of the PM (traceable to an internal absolute-power standard), the scattering parameters of the directional coupler (traceable to a short-

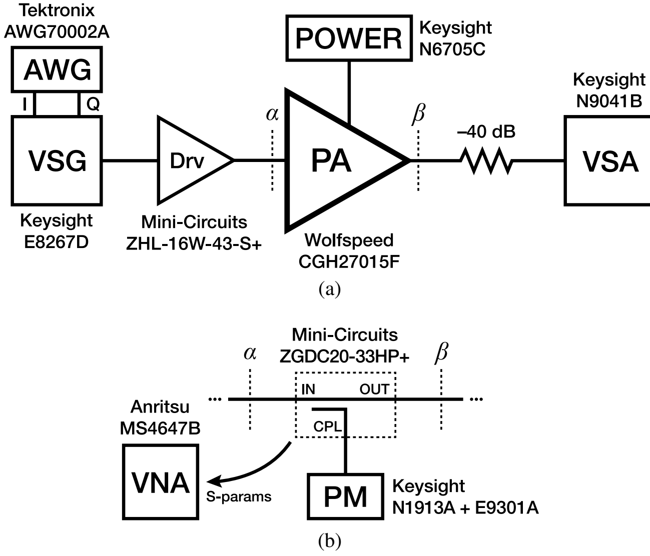

Fig. 4. Diagram of (a) the measurement setup for the characterization of the dynamic self-biasing behavior of a GaN HEMT-based PA, and (b) the calibration equipment. During calibration, the PA is disconnected from the measurement setup and the calibration equipment is connected in its stead at the α and β planes.

open-load-through standard), and the waveform measurement of the VSA (not traceable, but sufficiently accurate).

Finally, an iterative procedure was executed to obtain a set of calibration factors—Γ_{VSG}, defined in (4), and Γ_{VSA}, defined in (5)—that corrected the absolute peak power at both calibration planes up to an error of less than 0.01 dB. The procedure consisted in measuring the average power at the PM $P_{av}^{(\text{PM})}$; measuring the waveform at the VSA $y(n)$; and obtaining the calibration factors based on the peak power at the α-plane $P_{pk}^{(\alpha)}$, defined in (6); the peak power at the β-plane $P_{pk}^{(\beta)}$, defined in (7); and the peak power at the VSA $P_{pk}^{(\text{VSA})}$, defined in (8). In these equations, S is the scattering matrix of the directional coupler, $P_{pk,\text{dBm}}^{(\text{Target})} = 29$ dBm is the target peak power at the α-plane, $\sigma \leq 1$ is a learning-rate parameter, cf is the crest factor of $y(n)$, N is the number of samples of $y(n)$, and $R_L = 50\ \Omega$. The iterative calibration procedure was executed for each target excitation (i.e., for each Δf) until the desired level of accuracy was reached. After obtaining the calibration factors, the directional coupler was disconnected from the measurement setup and the PA was reconnected.

$$\Gamma_{\text{VSG}} := \Gamma_{\text{VSG}} - \sigma\Big[10\log_{10}\Big(10^3\, P_{pk}^{(\alpha)}\Big) - P_{pk,\text{dBm}}^{(\text{Target})}\Big] \quad (4)$$

$$\Gamma_{\text{VSA}} := \sqrt{P_{pk}^{(\beta)}\,/\,P_{pk}^{(\text{VSA})}} \quad (5)$$

$$P_{pk}^{(\alpha)} = \frac{cf^2}{(1-|S_{11}|^2)\,|S_{31}|^2}\, P_{av}^{(\text{PM})} \quad (6)$$

$$P_{pk}^{(\beta)} = \big(1-|S_{11}|^2\big)\,|S_{21}|^2\, P_{pk}^{(\alpha)} \quad (7)$$

$$P_{pk}^{(\text{VSA})} = \frac{cf^2}{2\,N R_L}\sum_{n=0}^{N-1}|y(n)|^2 \quad (8)$$

3) Characterization Results: In Fig. 5 we present the $P_{out}(V_{GS}, V_{ss})$ map resulting from the preliminary measurements at a CW input power level of 0 dBm. Moreover, in this figure we also show an example of the estimated trajectory of the gate–source voltage as a result of the gradual accumulation of trapped charge due to the large-signal two-tone excitation at $\Delta f = 100$ kHz (detailed in Section IV).

Finally, Fig. 6 illustrates the result of the characterization of the dynamic self-biasing behavior of the GaN HEMT-based PA. In this figure, the output power of the PA when measured at the instants where the level of the input large-signal two-tone excitation is 0 dBm (i.e., $|y_a(t_{ss}(k))|$, or the black markers in Fig. 1) is plotted as a function of two variables: the two-tone frequency separation Δf (the horizontal axis), and time (color-coded). Thus, Fig. 6 shows the temporal evolution of the small-signal output power of the PA for each transient two-tone large-signal excitation with frequency separation Δf: from an initial CW steady-state condition in black; to an output power level in blue following the very first input period (measured at $t = t_{ss}(1)$); and up to an output power level in red at the near-steady-state final condition following the one-hundredth input period (measured at $t = t_{ss}(100)$).

The results shown in Fig. 6 can be explained based on our understanding of the charge-trapping mechanism as follows. As the amplitude of the envelope of a two-tone excitation rises from zero to its peak value, the rate of capture of charge carriers by deep-level traps in the GaN HEMT exceeds the rate of emission, leading to an accumulation of trapped charge and a consequent reduction in the conductivity of the GaN channel. Conversely, as the amplitude descends from the peak toward zero, the rate of capture decreases below the rate of emission, leading to a net release of trapped charge and the consequent recovery of the conductivity of the GaN channel toward its initial state. For very low values of Δf, the envelope is slow enough for all trapped charge to be released between each input period, resulting in an unchanging small-signal PA output power. However, for larger values of Δf, the envelope is fast enough for some charge to remain trapped between input periods, resulting in a reduction of the output power of the PA. As the results demonstrate, this small-signal output power reduction can be as large as 25 dB, indicating a complete collapse of the small-signal transfer characteristics of the GaN HEMT and a clear degeneration of the operation of the GaN HEMT-based PA from class B to a deep class C.

In addition to evidencing the dynamic change in the class of operation of the PA, Fig. 6 also reveals the temporal evolution of this self-biasing behavior: from the very first input period to the last. This provides valuable information on the net state of the deep-level traps of the GaN HEMT at various stages of the descent from class B to class C. For instance, if the capture process were nearly instantaneous (as commonly assumed), then the deep-level traps would reach a maximum of trapped charge in the very first input period for all Δf considered, and the characterization results would present coincident temporal profiles. However, at higher Δf, the successive profiles in Fig. 6 indicate a progressively lower PA output power for the same PA input power, demonstrating that the first periods of the input excitation may not be sufficient to fully charge the

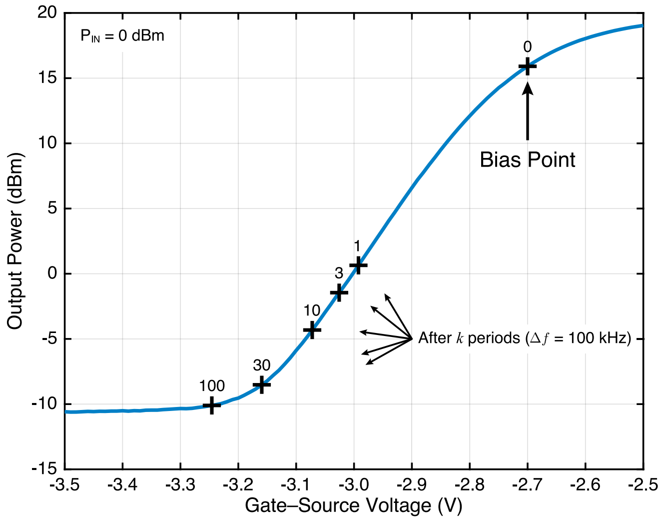

Fig. 5. Variation of the PA output power as a function of the gate–source voltage V_{GS} for a constant 0 dBm CW excitation. Also, in black markers, an example of the gradual self-biasing for Δf = 100 kHz.

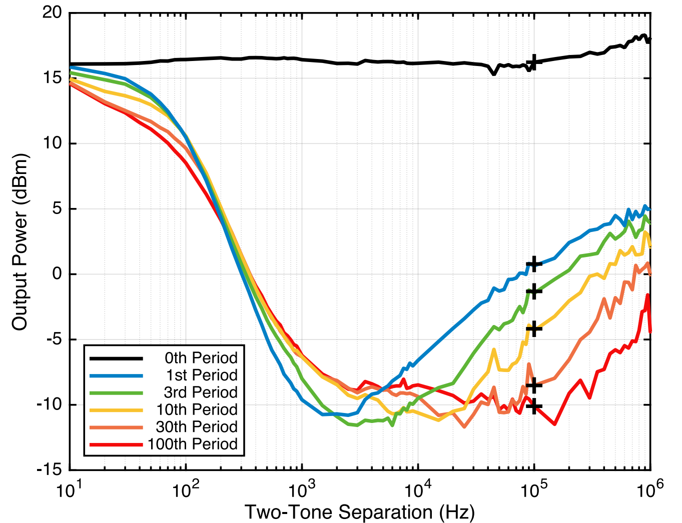

Fig. 6. Variation of the PA output power measured at the small-signal-input instants $t_{ss}(k)$ as a function of the two-tone frequency separation Δf. The markers in this figure refer to the markers in Fig. 5.

deep-level traps of the GaN HEMT. This is further evidence that the capture process in charge-trapping phenomena is much slower than what is commonly assumed, as explained in [17].

IV. Modeling

Now that the dynamic self-biasing behavior of GaN HEMT-based PAs can be accurately characterized, the next step toward its compensation consists in identifying the mechanism that causes it. In the previous sections, we suggested that this behavior can be attributed to the dynamic variation of the HEMT's threshold voltage. In this section, we demonstrate not only that our hypothesis is supported by physical models of charge trapping in GaN HEMTs, but also that the accurate prediction of the dynamic self-biasing behavior of GaN HEMT-based PAs is contingent on the accurate modeling of the charge-capture process.

Regardless of the internal structure (or mathematical formulation) of the model that is used for the compensation of the dynamic self-biasing behavior of a GaN HEMT-based PA, our compensation strategy—canceling out the dynamic variation of the HEMT's threshold voltage—dictates that the output of the model should be the instantaneous threshold voltage variation $\Delta V_{GS}(t)$. Moreover, since the compensation shall be carried out by an analog circuit, it is preferable that this model have a feedforward structure, so that the input signal of the model can be extracted from the input of the PA rather than from its output. Thus, the model should be of the form $\Delta V_{GS}(t) = f_M[v_x(t), \Psi_M]$, where $v_x(t)$ denotes the amplitude of the envelope of the PA's input excitation, and $f_M[\cdot]$ is an operator that denotes the dynamic model-defined mapping between $v_x(t)$ and $\Delta V_{GS}(t)$ using the set of model parameters Ψ_M.

A. Model Extraction

In order to extract the set of parameters Ψ_M for a given model, the target mapping between $v_x(t)$ and $\Delta V_{GS}(t)$ should first be obtained from the characterization results as follows.

Referring back to Section III-A, recall that $y_a(t_{ss}(k))$ (shown in Fig. 6) is the output of the PA at the instants where the input of the PA has an amplitude of V_{ss}. Since we measured a map $P_{out}(V_{GS}, V_{ss})$ (shown in Fig. 5) that relates P_{out} and V_{GS} for an input excitation with amplitude V_{ss}, then this map can be used to estimate the equivalent V_{GS} for each measured $y_a(t_{ss}(k))$—for instance, through linear interpolation of $|y_a(t_{ss}(k))|^2/(2\,R_L)$, where $R_L = 50\ \Omega$. This results in a vector $V_{GS}(t_{ss}(k))$ that contains an estimate of the equivalent gate–source voltage at each period of the transient response of the PA to a given large-signal two-tone excitation. Note that some estimates resulting from the interpolation may be indeterminate due to the sigmoid shape of the map; in these cases, we choose to discard the estimates. Finally, the variation of the threshold voltage due to charge trapping can be calculated by subtracting the gate bias voltage V_{GG} from all estimated $V_{GS}(t_{ss}(k))$. This results in a dataset $\Delta V_{GS}(\Delta f, k)$ that contains the variation of the threshold voltage of the GaN HEMT, for a two-tone excitation with frequency separation Δf, estimated at each period k, and under the biasing conditions imposed during the characterization (in our case, $V_{GG} = -2.7$ V and $V_{DD} = 28$ V).

Since $\Delta V_{GS}(\Delta f, k)$ provides a comprehensive characterization of the transient variation of the threshold voltage for a wide variety of amplitude-modulated excitation dynamics, it is suitable for the extraction of model parameters. This extraction can be done by employing an algorithm (e.g., CMA-ES) for the minimization of the mean square error between $\Delta V_{GS}(\Delta f, k)$ and $\Delta V_{GS}^{M}(\Delta f, k)$, for all Δf and all k, where $\Delta V_{GS}^{M}(\Delta f, k)$ is the threshold voltage variation predicted by the model. The predicted threshold voltage variation can be obtained by calculating the transient response of the model to the same set of two-tone excitations with varying frequency separation Δf, and then sampling it at $t_{ss}(k)$.

B. Model Definition

1) Jardel Model: Serving as the baseline comparison charge-trapping model throughout this paper, the Jardel model [10] establishes a relationship between the threshold voltage of a HEMT and its intrinsic drain–source voltage. Although this relationship cannot be directly applied to the RF envelope measurements proposed in the characterization method detailed in Section III, its dynamics (or mathematical formulation) certainly can, as shown in [5], [15]. Thus, throughout the rest of this paper, we will use "the Jardel model" as a shorthand for the dynamics expressed by the mathematical formulation proposed in [10] when applied to RF envelope measurements, rather than the literal physical phenomena described by this formulation.

The Jardel model, whose equivalent circuit is illustrated in Fig. 7, is characterized by an asymmetric charge (capture) and discharge (emission) process with different—but fixed—charge and discharge time constants, $\tau_c \approx R_c\, C$ and $\tau_e = R_e\, C$ respectively. This model, with a parameter set $\Psi_M = \{\tau_c,\, \tau_e,\, \kappa\}$, is defined as follows.

Let $v_x(t)$ denote the amplitude of the envelope of the PA's input excitation; $\Delta V_{GS}(t) = \kappa\, v_y(t)$ denote the threshold voltage variation predicted by the model, where κ is a scaling factor and $v_y(t)$ is the voltage at the capacitor; and $f_D(\cdot)$ denote the transfer function, defined in (9), of the ideal diode in Fig. 7.

$$f_D(x) \;=\; \begin{cases} x, & x \geq 0 \\ 0, & x < 0 \end{cases} \tag{9}$$

Then, the capture current $i_c(t)$ is defined as in (10), the emission current $i_e(t)$ is defined as in (11), and the net capacitor current $i_y(t)$ is defined as in (12).

$$i_c(t) \;=\; f_D\!\left(\frac{v_x(t) - v_y(t)}{R_c}\right) \tag{10}$$

$$i_e(t) \;=\; \frac{v_y(t)}{R_e} \tag{11}$$

$$i_y(t) \;=\; i_c(t) \;-\; i_e(t) \tag{12}$$

The voltage at the capacitor $v_y(t)$ is defined as in (13) and, using Euler's method, it can be discretized as in (14), where n denotes the sample index and f_s denotes the sampling frequency.

$$v_y(t) \;=\; \frac{1}{C}\int_{t_0}^{t} i_y(\tau)\, d\tau \;+\; v_y(t_0) \tag{13}$$

$$v_y(n+1) \;=\; v_y(n) \;+\; \frac{1}{f_s\, C}\; i_y(n) \tag{14}$$

2) SRH Model: While the Jardel model does support asymmetric capture and emission time constants, these time constants are fixed. However, in [17] the authors demonstrated, based on Shockley–Read–Hall (SRH) statistics and the works of [16], [26], that the capture process can be more accurately modeled with a time constant that varies with the instantaneous trapping state, becoming exponentially larger as the accumulated charge increases. Similar to the model proposed by Jardel *et al.* in [10], this model establishes a relationship between the threshold voltage of a HEMT and its intrinsic drain–source voltage. Again, for simplicity, we will use "the SRH model" as a shorthand for the mathematical formulation of the dynamics described by this model, since our target application is the modeling and compensation of an RF PA, and not the intrinsic characteristics of a discrete HEMT.

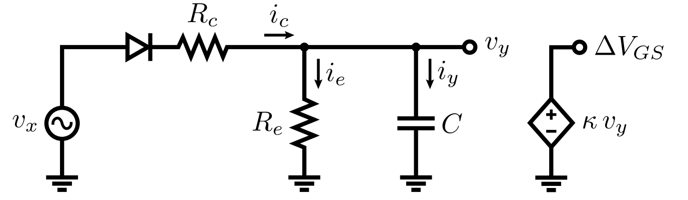

Fig. 7. Equivalent circuit of the Jardel model.

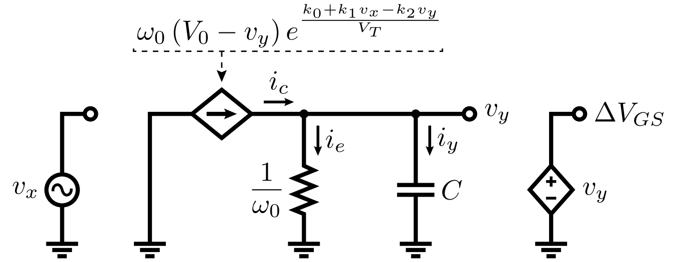

Fig. 8. Equivalent circuit of the SRH model.

The SRH model, whose equivalent circuit is illustrated in Fig. 8, is also characterized by an asymmetric charge (capture) and discharge (emission) process, but, whereas the capture rate in the Jardel model is defined by a fixed time constant, in the SRH model it is defined as a nonlinear function of the trapping state—for simplicity, though, we (and the authors of [17]) say that is defined by a time constant that varies with the trapping state. As in the Jardel model, the emission is modeled by a fixed time constant. This model, with a parameter set $\Psi_M = \{V_0,\, \omega_0,\, k_0,\, k_1,\, k_2\}$, is defined as follows.

Let $v_x(t)$ denote the amplitude of the envelope of the PA's input excitation; and $\Delta V_{GS}(t) = v_y(t)$ denote the threshold voltage variation predicted by the model, where $v_y(t)$ is the voltage at the capacitor. Then, the capture current $i_c(t)$ is defined as in (15), where $v_I(t) = k_0 + k_1\, v_x(t) - k_2\, v_y(t)$ and V_T is the thermal voltage; the emission current $i_e(t)$ is defined as in (16); and the net capacitor current $i_y(t)$ is defined as in (17).

$$i_c(t) \;=\; \omega_0\,(V_0 - v_y(t))\,\exp\!\left(\frac{v_I(t)}{V_T}\right) \tag{15}$$

$$i_e(t) \;=\; \omega_0\, v_y(t) \tag{16}$$

$$i_y(t) \;=\; i_c(t) \;-\; i_e(t) \tag{17}$$

Similar to the Jardel model, the voltage at the capacitor $v_y(t)$ is defined as in (13) and, using Euler's method, it can be discretized as in (14), where $C = 1$ F is merely an auxiliary variable for the equivalent-circuit representation in Fig. 8.

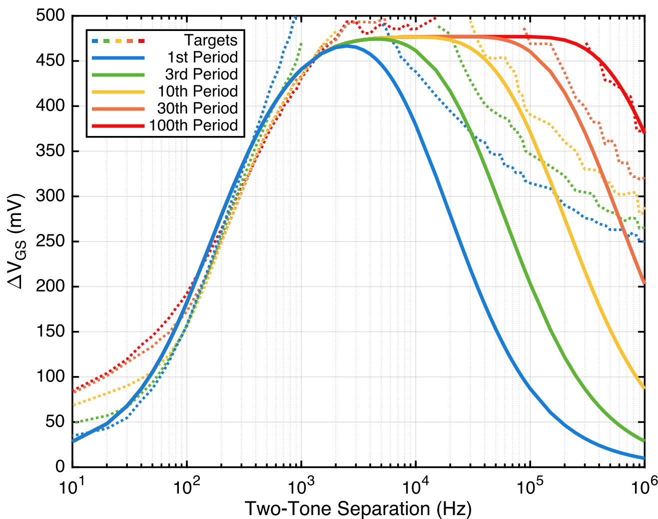

Fig. 9. Result of the extraction of the Jardel model and, in the background, the estimated variation of the threshold voltage of the GaN HEMT.

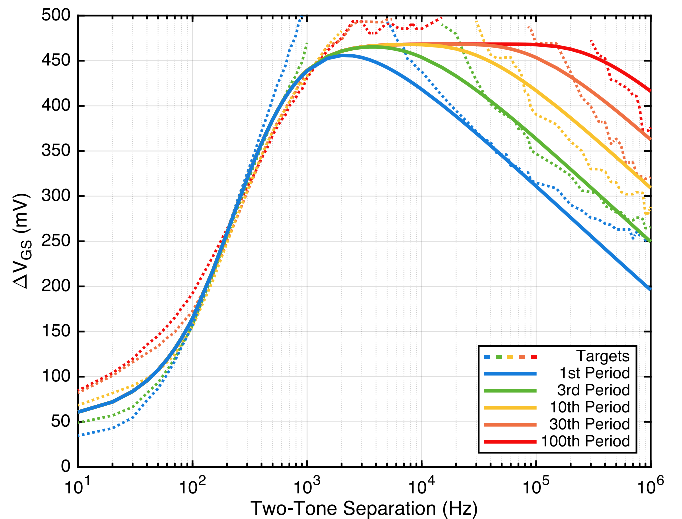

Fig. 10. Result of the extraction of the SRH model and, in the background, the estimated variation of the threshold voltage of the GaN HEMT.

C. Experimental Results

Fig. 9 illustrates the result of the extraction of the parameters of the Jardel model, as well as the target dataset $\Delta V_{GS}(\Delta f, k)$ that resulted from the characterization measurements. The extracted parameters were $\tau_c = 29.2$ μs, $\tau_e = 3.47$ ms, and $\kappa = 1.54$ V/V. As is shown by the red curve representing the one-hundredth envelope period (a near-steady-state condition), and, as has been previously demonstrated in [15], the Jardel model fits the estimated variation of the threshold voltage quite well under steady-state conditions. However, the figure also reveals that this model is not capable of predicting the transient behavior with sufficient accuracy because of the modeling of the capture process as a single fixed time constant.

Fig. 10 illustrates the result of the extraction of the parameters of the SRH model, as well as the target $\Delta V_{GS}(\Delta f, k)$ also shown in Fig. 9. The extracted parameters (for $V_T = 25.9$ mV and $V_0 = 1.00$ V) were $\omega_0 = 446$ rad/s, $k_0 = -63.7$ mV, $k_1 = 36.0$ mV/V, and $k_2 = 475$ mV/V. As the figure reveals, the state-variable time constant used to model the capture process greatly improves the ability of the model to predict the measured (estimated) transient ΔV_{GS} curves, especially at higher Δf. In addition, there is some agreement between the Jardel and SRH models, as the time constants associated with the emission process are relatively similar ($1/\omega_0 = 2.24$ ms).

Naturally, there is a limit to how accurate of a fit can be obtained with these models. First, because these models, despite being state-of-the-art, still do not provide a complete and accurate description of the dynamics of charge-trapping phenomena—for instance, the single fixed emission time constant considered by both the Jardel and the SRH models is known to be a gross simplification of the actual emission dynamics observed through transient current measurements [10], [17], [27]. Second, because these models were originally conceived for the prediction of either gate-lag or drain-lag phenomena, and not both phenomena simultaneously, as that would require a greater number of model parameters for the distinction between the different contributions of the gate and drain potentials. Third, because the response of these models is altered by our use of the PA's input envelope amplitude as their input signal, instead of the intrinsic voltage waveform that the original authors established. Fourth, because the RF measurements-based characterization results themselves are an inevitable combination of gate-lag phenomena, drain-lag phenomena, and thermal phenomena as well. Finally, because there may be other effects caused by charge-trapping phenomena that we are not taking into account (e.g., dynamic on-resistance). In any case, and in spite of these apparent limitations, in the next section we show that excellent compensation results can still be obtained using the SRH model when extracted based on our characterization method.

V. Analog Compensation

In the previous sections, we demonstrated how the dynamic self-biasing behavior of GaN HEMT-based PAs can be characterized and predicted in real time using the SRH physical model of charge trapping. In this section, we demonstrate that an approximation of this model can be implemented as a fully analog electronic circuit and used to compensate the dynamic self-biasing behavior of a GaN HEMT-based PA. For comparison purposes, we also implemented the Jardel model as an analog circuit and measured how well it compensates the dynamic self-biasing behavior of the same PA under the same conditions.

In order to compensate the dynamic self-biasing behavior of a GaN HEMT-based PA, our analog compensation circuit (ACC) employed the compensation strategy first proposed in [19] for mobile communications applications and later demonstrated in [7] for pulsed radar applications, which consists in canceling out the dynamic variation of the HEMT's threshold voltage by modulating the gate–source voltage. As illustrated in Fig. 11, the modulation is done by superimposing a compensation signal $\Delta V_{GS}(t)$ over the gate bias voltage V_{GG}, resulting in the compensated gate–source voltage $V_{GS}(t)$. The compensation signal is obtained by coupling the PA's input

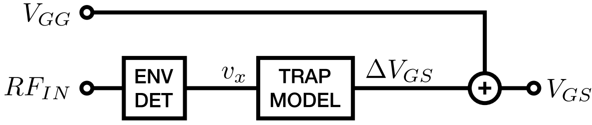

Fig. 11. Block diagram of the analog compensation circuit.

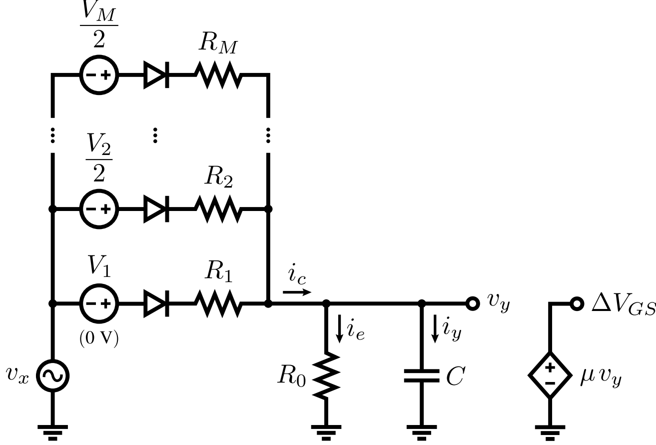

Fig. 12. Equivalent circuit of the piecewise-SRH model.

RF excitation into the input port of the ACC, demodulating it with an envelope detector, and finally processing it through a nonlinear filter, which is an analog implementation of a charge-trapping model. Naturally, the typical large-value bypass capacitor at the gate bias terminal of the PA should be removed, otherwise the V_{GS} modulation would be bypassed to ground.

A. Analog Compensation Circuit

1) Piecewise-SRH Model: While the SRH model does provide a very good fit to the dynamic threshold voltage variation estimated from the characterization results, its definition of the charge-capture process does not exactly lend itself to a direct implementation as an analog circuit. For this reason, we developed a new behavioral model that preserves the SRH model's characteristic state-variable capture time constant, yet whose analog implementation is straightforward.

In this model—the piecewise-SRH model, whose equivalent circuit is illustrated in Fig. 12—, the complex charge-capture process defined in the SRH model is approximated by a piecewise-linear function. In this function, the time constant of the charge-capture process is switched (or, more accurately, interpolated) between M different values, depending on the instantaneous trapping state and input excitation. The time-constant switching is carried out by a set of ideal diodes that are biased at the switching breakpoint voltages $V_m/2$, where $V_1 = 0$ V and $V_m < 0$ for all $m = 2, 3, \cdots, M$. By charging the capacitor C through every resistor R_m such that $v_x(t) - v_y(t) > -V_m/2$, this configuration allows for the interpolation between time constants rather than a hard switching between them, contributing to the smoothness of the model. As in the SRH model (as well as the Jardel model), the emission process is modeled by a fixed time constant $\tau_e = R_0\,C$. The piecewise-SRH model, with a parameter set $\Psi_M = \{R_0, R_1, \cdots, R_M, V_2, \cdots, V_M, C, \mu\}$, is defined as follows.

Let $v_x(t)$ denote the input excitation; $\Delta V_{GS}(t) = \mu\, v_y(t)$ the threshold voltage variation predicted by the model, where μ is a scaling factor; and $f_D(\cdot)$ the transfer function, defined in (9), of the ideal diodes in Fig. 12. Then, the capture current $i_c(t)$ is defined as in (18), the emission current $i_e(t)$ is defined as in (19), and the net capacitor current $i_y(t)$ is defined as in (20).

$$i_c(t) = \sum_{m=1}^{M} f_D\left(\frac{v_x(t) + V_m/2 - v_y(t)}{R_m}\right) \tag{18}$$

$$i_e(t) = \frac{v_y(t)}{R_0} \tag{19}$$

$$i_y(t) = i_c(t) - i_e(t) \tag{20}$$

Similar to the previous models, the voltage at the capacitor $v_y(t)$ is defined as in (13) and, using Euler's method, it can be discretized as in (14).

2) Implementation Details: In both the Jardel ACC, shown in Fig. 7, and the piecewise-SRH ACC, shown in Fig. 12, the ideal diodes were implemented as precision rectifier circuits where an operational amplifier compensates the forward voltage of a diode in a local feedback loop [28]. In the piecewise-SRH ACC, the $V_m/2$ voltage sources in the charge-capture path were implemented as conventional non-inverting summing-amplifier circuits based on an operational amplifier—it is for this reason that the breakpoint voltages are multiplied by a factor of 1/2.

In both ACCs, the envelope detector was implemented using an Analog Devices ADL5511 integrated circuit. The ideal diodes were implemented using Texas Instruments OPA659 voltage-feedback operational amplifiers with ultra-low input bias currents (to prevent the parasitic loading of trapping state integrator—the capacitor C) and Toshiba 1SS307E silicon switching diodes with ultra-low reverse-bias current and total capacitance. The scaling factors κ and μ were implemented using an Analog Devices AD8336 variable gain amplifier controlled by a pair of Analog Devices ADR510 precision voltage references. Finally, a 6.8 nF $\pm$ 1 % C0G/NP0 KEMET ceramic capacitor was chosen for the capacitor C. The implemented piecewise-SRH ACC and Jardel ACC are pictured in Fig. 13 and Fig. 14, respectively.

B. Experimental Results

Fig. 15 illustrates the result of the extraction of the parameters of the piecewise-SRH model. The extracted parameters were $R_0 = 330$ kΩ, $R_1 = 7.50$ kΩ, $R_2 = 1.80$ kΩ, $R_3 = 43.0$ Ω, $V_2 = -204$ mV, $V_3 = -330$ mV, $C = 6.80$ nF, and $\mu = 1.57$ V/V. For comparison with the parameters of the Jardel ACC ($\tau_e = 3.47$ ms and $\tau_c = 29.2$ µs), the time constants τ_m, defined as $\tau_m = R_m\,C$, were $\tau_0 = 2.24$ ms, $\tau_1 = 51.0$ µs, $\tau_2 = 12.2$ µs, and $\tau_3 = 292$ ns. Fig. 15 demonstrates, once again, that the state-variable capture time constant of the SRH model provides excellent agreement with

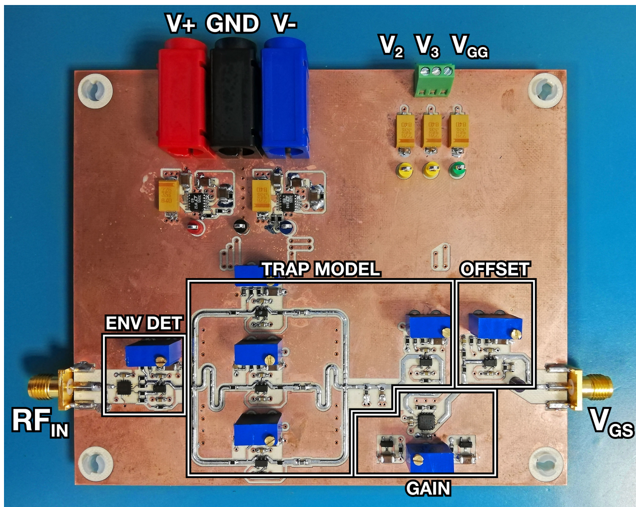

Fig. 13. Photograph of the piecewise-SRH ACC.

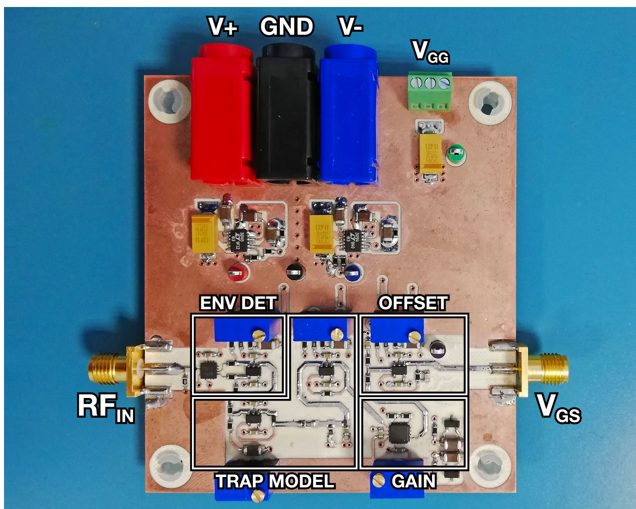

Fig. 14. Photograph of the Jardel ACC.

the measured (estimated) threshold voltage variation—even when simplified as a piecewise-linear function.

In order to validate the ability of the ACCs to compensate the dynamic self-biasing behavior of a GaN HEMT-based PA, we assembled the measurement setup illustrated in Fig. 16. This setup is similar to the one used for the characterization of the PA (Fig. 4(a)); however, instead of biasing the PA with a constant-voltage source, it was biased by the output of the ACC, whose input was extracted from the PA's input excitation with a directional coupler. After repeating the calibration procedure detailed in Section III-B, the dynamic self-biasing behavior of the ACC-assisted GaN HEMT-based PA was characterized and the following results were obtained.

Fig. 17 illustrates the result of the characterization of the PA when compensated by the Jardel ACC. As the model-fitting results indicated, the Jardel model does not provide a sufficiently accurate prediction of the instantaneous charge-trapping state for the dynamic self-biasing behavior of the GaN HEMT-based PA to be compensated at larger two-tone

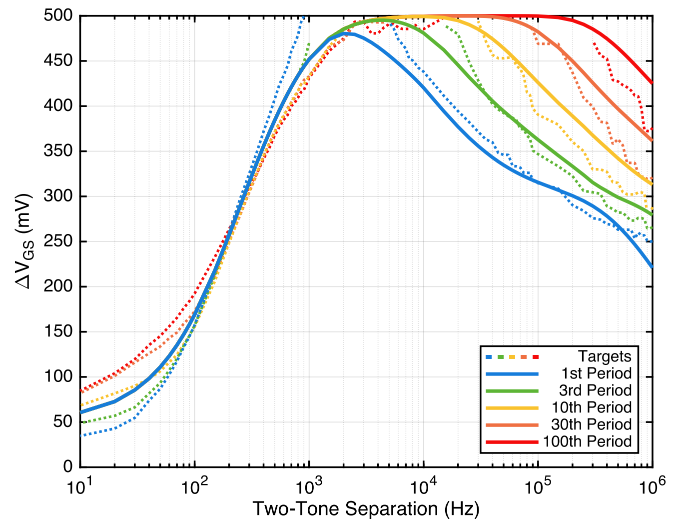

Fig. 15. Result of the extraction of the piecewise-SRH model and, in the background, the estimated variation of the threshold voltage of the GaN HEMT.

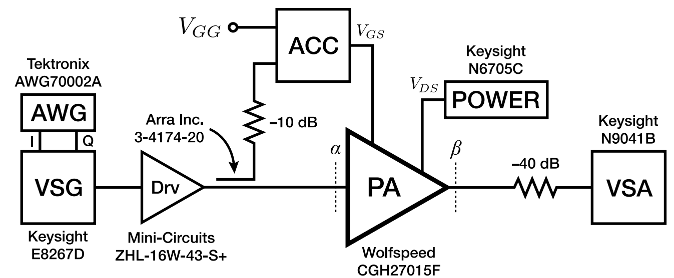

Fig. 16. Diagram of the measurement setup for the compensation of the dynamic self-biasing behavior of a GaN HEMT-based PA.

frequency separations. This is because the process of charge capture does not occur with a fixed time constant, but rather with a time constant that varies with the instantaneous charge-trapping state, becoming larger as the accumulated charge increases.

Fig. 18 illustrates the result of the characterization of the PA when compensated by the piecewise-SRH ACC. In contrast to the Jardel ACC, the piecewise-SRH ACC was able to compensate the dynamic self-biasing behavior of the PA across both frequency and time domains. These results demonstrate definitively that a model featuring a dynamic state-variable capture time constant is able to provide much more accurate information on the transient variation of a GaN HEMT's threshold voltage, allowing for the instantaneous correction (rather than an eventual steady-state correction) of the current collapse that would otherwise occur.

VI. Conclusion

In this paper we detailed a method for the characterization of the dynamic self-biasing behavior of GaN HEMT-based PAs using transient two-tone large-signal RF measurements. This method, which can be performed using conventional RF laboratory equipment, not only provides comprehensive measured data on the capture and emission dynamics of

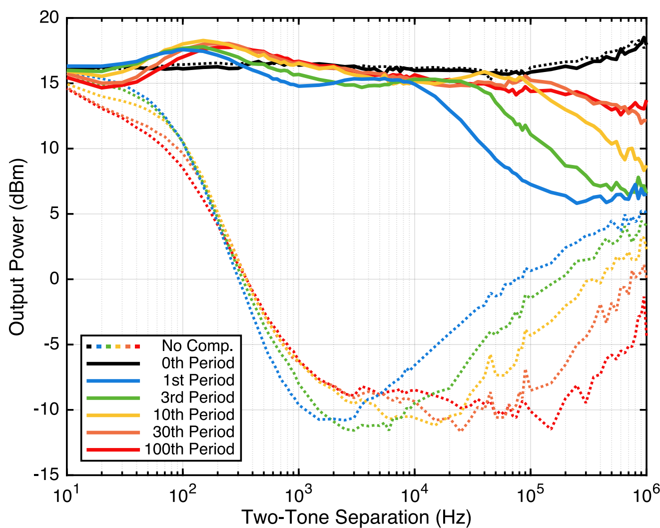

Fig. 17. Dynamic variation of the small-signal PA output power when compensated by the Jardel ACC.

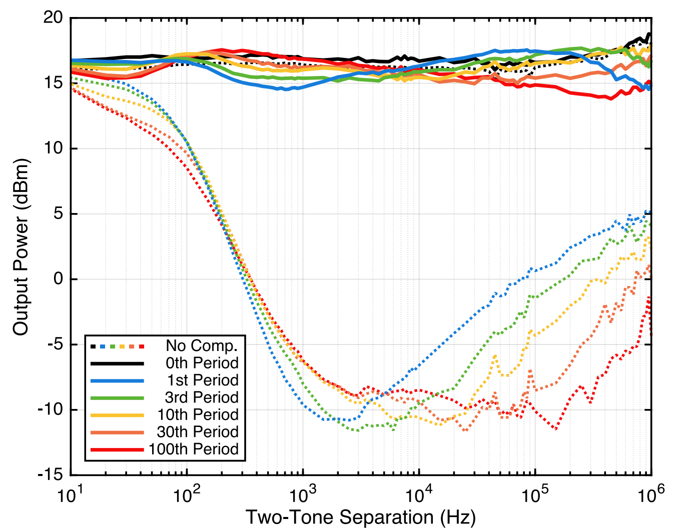

Fig. 18. Dynamic variation of the small-signal PA output power when compensated by the piecewise-SRH ACC.

charge-trapping phenomena, but also reveals that the charge-capture process can be much slower than what is traditionally assumed. This result is in agreement with recent publications on this topic [17].

After presenting our characterization method, we demonstrated that the accurate modeling of the dynamic self-biasing behavior of GaN HEMT-based PAs is contingent on the capture process being described by a state-variable time constant—more specifically, a time constant that increases with the accumulation of trapped charge, as formulated by the SRH physical model of charge trapping. This result underscores the importance of accurately characterizing and modeling the dynamics of charge capture: while previous publications have found moderate success in modeling charge-trapping phenomena in pulsed or steady-state conditions by dismissing the process of charge capture as a near-instantaneous event, this paper (in accordance with [17]) demonstrates that the charge-capture process has an important contribution to the transient behavior of charge-trapping phenomena and the long-term memory effects caused by them—a contribution that cannot be accurately predicted with a fixed capture time constant.

Finally, we proposed a behavioral model that approximates the SRH model with a piecewise-defined state-variable capture time constant, and implemented it as a fully analog electronic circuit for the compensation of the dynamic self-biasing behavior of a GaN HEMT-based PA. For comparison purposes, we also implemented the conventional charge-trapping model with a fixed capture time constant as an analog circuit. After characterizing the dynamic self-biasing behavior of the PA-under-test with and without the assistance of each of the analog compensation circuits, we verified that only the circuit based on the piecewise-SRH model was able to accurately preserve the class of operation of the PA and completely eliminate any transient symptom of current collapse during the transient evolution of the GaN HEMT's internal trapping state. Based on the work in [19], where an analog compensation circuit was paired with a digital predistorter to create a hybrid analog/digital linearization scheme, this result has important implications on the linearizability of GaN HEMT-based PAs for communications applications.

References

[1] R. S. Pengelly, S. M. Wood, J. W. Milligan, S. T. Sheppard, and W. L. Pribble, "A review of GaN on SiC high electron-mobility power transistors and MMICs," *IEEE Trans. Microw. Theory Techn.*, vol. 60, no. 6, pp. 1764–1783, Jun. 2012.

[2] T. Mizutani, Y. Ohno, M. Akita, S. Kishimoto, and K. Maezawa, "A study on current collapse in AlGaN/GaN HEMTs induced by bias stress," *IEEE Trans. Electron Devices*, vol. 50, no. 10, pp. 2015–2020, Sep. 2003.

[3] D. Jin and J. A. del Alamo, "Mechanisms responsible for dynamic ON-resistance in GaN high-voltage HEMTs," in *Proc. Int. Symp. Power Semicond. Devices ICs*, Bruges, Belgium, Jun. 2012, pp. 333–336.

[4] P. McGovern, J. Benedikt, P. J. Tasker, J. Powell, K. P. Hilton, J. L. Glasper, R. S. Balmer, T. Martin, and M. J. Uren, "Analysis of DC-RF dispersion in AlGaN/GaN HFETs using pulsed I-V and time-domain waveform measurements," in *Proc. IEEE Int. Microw. Symp.*, Long Beach, CA, USA, Jun. 2005, pp. 503–506.

[5] F. M. Barradas, L. C. Nunes, T. R. Cunha, P. M. Lavrador, P. M. Cabral, and J. C. Pedro, "Compensation of long-term memory effects on GaN HEMT-based power amplifiers," *IEEE Trans. Microw. Theory Techn.*, vol. 65, no. 9, pp. 3379–3388, Sep. 2017.

[6] J. Delprato, D. Barataud, M. Campovecchio, G. Neveux, C. Tolant, and P. Eudeline, "Measured and simulated impact of irregular radar pulse trains on the pulse-to-pulse stability of microwave power amplifiers," *IEEE Trans. Microw. Theory Techn.*, vol. 62, no. 12, pp. 3538–3548, Dec. 2014.

[7] P. M. Tomé, F. M. Barradas, T. R. Cunha, and J. C. Pedro, "Compensation of the pulse-to-pulse instability of GaN HEMT-based power amplifiers," in *Proc. IEEE Int. Microw. Symp.*, Boston, MA, USA, Jun. 2019, pp. 408–411.

[8] T. Mizutani, T. Okino, K. Kawada, Y. Ohno, S. Kishimoto, and K. Maezawa, "Drain current DLTS of AlGaN/GaN HEMTs," *Phys. Stat. Sol. (A)*, vol. 200, no. 1, pp. 195–198, Nov. 2003.

[9] J. Joh and J. A. del Alamo, "A current-transient methodology for trap analysis for GaN high electron mobility transistors," *IEEE Trans. Electron Devices*, vol. 58, no. 1, pp. 132–140, Nov. 2010.

[10] O. Jardel, F. D. Groote, T. Reveyrand, J.-C. Jacquet, C. Charbonniaud, J.-P. Teyssier, D. Floriot, and R. Quere, "An electrothermal model for AlGaN/GaN power HEMTs including trapping effects to improve large-signal simulation results on high VSWR," *IEEE Trans. Microw. Theory Techn.*, vol. 55, no. 12, pp. 2660–2669, Dec. 2007.

[11] A. Santarelli, R. Cignani, G. P. Gibiino, D. Niessen, P. A. Traverso, C. Florian, D. M. M. P. Schreurs, and F. Filicori, “A double-pulse technique for the dynamic I/V characterization of GaN FETs,” *IEEE Microw. Wireless Compon. Lett.*, vol. 24, no. 2, pp. 132–134, Dec. 2013.

[12] M. Bouslama, V. Gillet, C. Chang, J.-C. Nallatamby, R. Sommet, M. Prigent, R. Quéré, and B. Lambert, “Dynamic performance and characterization of traps using different measurements techniques for the new AlGaN/GaN HEMT of 0.15-μm ultrashort gate length,” *IEEE Trans. Microw. Theory Techn.*, vol. 67, no. 7, pp. 2475–2482, Apr. 2019.

[13] P. Roblin, D. E. Root, J. Verspecht, Y. Ko, and J. P. Teyssier, “New trends for the nonlinear measurement and modeling of high-power RF transistors and amplifiers with memory effects,” *IEEE Trans. Microw. Theory Techn.*, vol. 60, no. 6, pp. 1964–1978, May 2012.

[14] C. Florian, T. Cappello, A. Santarelli, D. Niessen, F. Filicori, and Z. Popović, “A prepulsing technique for the characterization of GaN power amplifiers with dynamic supply under controlled thermal and trapping states,” *IEEE Trans. Microw. Theory Techn.*, vol. 65, no. 12, pp. 5046–5062, Jul. 2017.

[15] L. C. Nunes, J. L. Gomes, P. M. Cabral, and J. C. Pedro, “A simple method to extract trapping time constants of GaN HEMTs,” in *Proc. IEEE MTT-S Int. Microw. Symp.*, Philadelphia, PA, USA, Jun. 2018, pp. 716–719.

[16] K. Kunihiro and Y. Ohno, “A large-signal equivalent circuit model for substrate-induced drain-lag phenomena in HJFETs,” *IEEE Trans. Electron Devices*, vol. 43, no. 9, pp. 1336–1342, Sep. 1996.

[17] J. L. Gomes, L. C. Nunes, C. F. Gonçalves, and J. C. Pedro, “An accurate characterization of capture time constants in GaN HEMTs,” *IEEE Trans. Microw. Theory Techn.*, vol. 67, no. 7, pp. 2465–2474, Jul. 2019.

[18] P. M. Tomé, F. M. Barradas, L. C. Nunes, J. L. Gomes, T. R. Cunha, and J. C. Pedro, “A transient two-tone RF method for the characterization of electron trapping capture and emission dynamics in GaN HEMTs,” in *Proc. IEEE Int. Microw. Symp.*, Los Angeles, CA, USA, Jun. 2020, pp. 428–431.

[19] P. M. Tomé, F. M. Barradas, T. R. Cunha, and J. C. Pedro, “Hybrid analog/digital linearization of GaN HEMT-based power amplifiers,” *IEEE Trans. Microw. Theory Techn.*, vol. 67, no. 1, pp. 288–294, Jan. 2019.

[20] M. J. Uren, J. Moreke, and M. Kuball, “Buffer design to minimize current collapse in GaN/AlGaN HFETs,” *IEEE Trans. Electron Devices*, vol. 59, no. 12, pp. 3327–3333, Oct. 2012.

[21] R. Vetury, N. Q. Zhang, S. Keller, and U. K. Mishra, “The impact of surface states on the DC and RF characteristics of AlGaN/GaN HFETs,” *IEEE Trans. Electron Devices*, vol. 48, no. 3, pp. 560–566, Mar. 2001.

[22] J. C. Pedro, L. C. Nunes, and P. M. Cabral, “Soft compression and the origins of nonlinear behavior of GaN HEMTs,” in *Proc. Eur. Microw. Integr. Circuit Conf.*, Rome, Italy, Oct. 2014, pp. 353–356.

[23] L. C. Nunes, D. R. Barros, P. M. Cabral, and J. C. Pedro, “Efficiency degradation analysis in wideband power amplifiers,” *IEEE Trans. Microw. Theory Techn.*, vol. 66, no. 12, pp. 5640–5651, Dec. 2018.

[24] N. Hansen and A. Ostermeier, “Completely derandomized self-adaptation in evolution strategies,” *Evol. Comput.*, vol. 9, no. 2, pp. 159–195, Jun. 2001.

[25] P. M. Cabral, J. C. Pedro, and N. B. Carvalho, “Nonlinear device model of microwave power GaN HEMTs for high power-amplifier design,” *IEEE Trans. Microw. Theory Techn.*, vol. 52, no. 11, pp. 2585–2592, Nov. 2004.

[26] J. G. Rathmell and A. E. Parker, “Circuit implementation of a theoretical model of trap centres in GaAs and GaN devices,” in *Proc. SPIE Microelectron. MEMS Nanotechnol.*, vol. 6798, Canberra, ACT, Australia, Dec. 2007, p. 67980R.

[27] P. M. Tomé, F. M. Barradas, T. R. Cunha, and J. C. Pedro, “A multiple-time-scale analog circuit for the compensation of long-term memory effects in GaN HEMT-based power amplifiers,” *IEEE Trans. Microw. Theory Techn.*, Jul. 2020, doi: 10.1109/TMTT.2020.3007713.

[28] P. Horowitz and W. Hill, *The Art of Electronics*, 3rd ed. New York, NY, USA: Cambridge University Press, 2015.

Pedro M. Tomé (S’17) received the M.Sc. degree in electronic and telecommunications engineering from the University of Aveiro, Aveiro, Portugal, in 2016.

He is currently a student of the MAP-tele Doctoral Program in Telecommunications, a joint program between the University of Minho, Guimarães, Portugal, the University of Aveiro, and the University of Porto, Porto, Portugal. His current research interests include analog signal processing and the study, characterization, modeling, and compensation of electron trapping effects in GaN HEMT-based RF PAs.

Filipe M. Barradas (S’13-M’17) was born in Évora, Portugal, in July 1989. He received the M.Sc degree in electronics and telecommunications engineering from Universidade de Aveiro, Aveiro, Portugal, in 2012, and the PhD degree in electrical engineering at the same university in 2017.

He is currently a Research Assistant at Instituto de Telecomunicações, Aveiro, Portugal. His main interests include digital predistortion and behavioral modelling of RF PAs, as well as signal processing with applications on telecommunications. Other interests include design and analysis of nonlinear microwave circuits.

Dr. Barradas has been a reviewer for several IEEE journals.

Luís C. Nunes (S’13-M’17) was born in Guarda, Portugal, in 1986. He received the M.Sc. and Ph.D. degrees in electrical engineering from the Universidade de Aveiro, Aveiro, Portugal, in 2010 and 2015, respectively.

From 2016 to 2017, he was an RF Design Engineer with Huawei Technologies, Stockholm, Sweden. He is currently a Researcher Assistant with the Institute of Telecommunications, Aveiro. His current research interests include active device modeling, nonlinear distortion analysis, and the design of microwave circuits, especially high-efficiency and linear power amplifiers.

Dr. Nunes is a member of the IEEE Microwave Theory and Techniques Society and the IEEE Electron Devices Society.

João L. Gomes (S’19) was born in Matosinhos, Portugal, in 1994. He received the M.Sc. degree in physics engineering from the Universidade de Aveiro, Aveiro, Portugal, in 2017, where he is currently pursuing the Ph.D. degree in electrical engineering.

Since 2018, he has been a Research Assistant with the Instituto de Telecomunicações, Aveiro. His current research interests include active device modeling and semiconductor physics modeling.

Telmo R. Cunha (M'05) received the Diploma and Ph.D. degrees in electronics and computer engineering from the Universidade do Porto, Porto, Portugal, in 1996 and 2003, respectively.

He was formerly involved with the Astronomical Observatory, University of Porto, and, afterward, with Geonav Lda., a private company near Porto. Since 2004, he is an Assistant Professor with the Department of Electronics, Telecommunications and Informatics, University of Aveiro, Aveiro, Portugal, and also a Senior Research Engineer with the Institute of Telecommunications, University of Aveiro. He has been lecturing in the fields of control theory and electronics, and he has been involved in several national and international research projects. His current research interests include behavioral modeling and linearization applied to radio frequency and microwave devices.

Dr. Cunha has been a reviewer for several IEEE journals.

José C. Pedro (S'90–M'95–SM'99–F'07) received the Diploma, Ph.D. and Habilitation degrees in electronics and telecommunications engineering from the Universidade de Aveiro, Aveiro, Portugal, in 1985, 1993, and 2002, respectively.

He is currently a Full Professor with the Universidade de Aveiro and head of the Aveiro site of the Instituto de Telecomunicações. He has authored 2 books and authored or co-authored more than 200 papers in international journals and symposia. His current research interests include active device modelling and the analysis and design of various nonlinear microwave circuits.

Dr. Pedro was a recipient of various prizes including the 1993 Marconi Young Scientist Award, the 2000 Institution of Electrical Engineers Measurement Prize, the 2015 EuMC Best Paper Microwave Prize, and the Microwave Distinguished Educator Award. He has served the scientific community as a Reviewer and an Editor for several conferences and journals, namely, the IEEE TRANSACTIONS ON MICROWAVE THEORY AND TECHNIQUES, for which he was the Editor-in-Chief.

APPENDIX H

Paper C3

Compensation of the Pulse-to-Pulse Instability of GaN HEMT-Based Power Amplifiers

Pedro M. Tomé, Filipe M. Barradas, Telmo R. Cunha, and José C. Pedro

Published In: 2019 IEEE/MTT-S International Microwave Symposium

Date of Conference: 2–7 June 2019

Conference Location: Boston, MA, USA

Date of Publication: 07 May 2019

DOI: 10.1109/MWSYM.2019.8700957

This is the authors' version of an article that has been published in the Proceedings of the 2019 IEEE MTT-S International Microwave Symposium. Changes were made to this version by the publisher prior to publication. The final version of the record is available at https://doi.org/10.1109/MWSYM.2019.8700957.

Compensation of the Pulse-to-Pulse Instability of GaN HEMT-Based Power Amplifiers

Pedro M. Tomé[1], Filipe M. Barradas[2], Telmo R. Cunha[3], José C. Pedro[4]
Instituto de Telecomunicações, Aveiro, Portugal
DETI, University of Aveiro, Portugal
[1]tome.p.m@ua.pt, [2]filipebarradas@ua.pt, [3]trcunha@ua.pt, [4]jcpedro@ua.pt

***Abstract*— In this paper we describe a method for compensating the pulse-to-pulse instability of GaN high-electron-mobility transistor (HEMT)-based power amplifiers (PAs) caused by electron-trapping effects. The method consists in generating a compensation signal based on measured data and using it to offset the dynamic threshold voltage modulation caused by the charge and discharge of the HEMT's traps. This method was verified with a pulsed radar waveform for moving target indication on a 15 W GaN HEMT-based PA, achieving an improvement of the peak output power of 0.85 dB and an improvement of the pulse-to-pulse amplitude stability of over 20 dB.**

***Keywords*— electron trapping, GaN high-electron-mobility transistor (HEMT), pulsed radar, pulse-to-pulse stability.**

I. Introduction

Modern radars use bursts of pulsed radio-frequency (RF) electromagnetic waves to irradiate a region of interest and detect the delayed reflections from targets in that region. Pulsed waveforms are especially interesting for moving target indication (MTI)—the distinction between moving targets (e.g., an aircraft) and stationary targets (e.g., the sea)—because equal transmitted signals result in equal reflected signals from stationary targets [1]. Thus, by analyzing the variations between successive pulses in the received waveforms, moving targets can be detected while stationary targets, or clutter, are suppressed [2].

Considering that MTI consists in analyzing the variations between the received pulses, all pulse variations caused by the radar system itself (as opposed to a moving target) negatively impact the suppression of clutter and may lead to false detections. Pulse-to-pulse stability, a measure of the envelope amplitude and phase variations between the transmitted pulses, is therefore a critical parameter for characterizing the performance of a pulsed radar.

Because pulsed radars require very high transmission power levels, GaN high-electron-mobility transistor (HEMT) technology constitutes an appealing solution for their solid-state implementation [3]. However, it is well known that GaN HEMT-based power amplifiers (PAs) suffer from both thermal and electron-trapping effects that severely deteriorate their linearity and, more specifically, their pulse-to-pulse stability [4]. To address this issue, in this paper we present a method for compensating these effects and improving the pulse-to-pulse amplitude stability of GaN HEMT-based PAs.

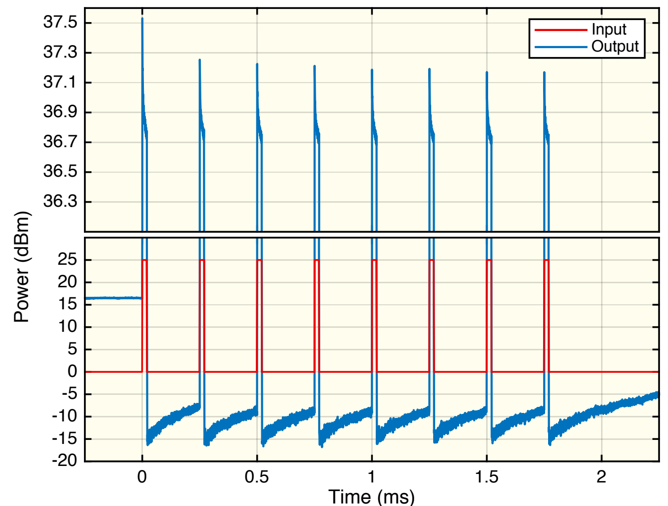

Fig. 1. Measured response of a GaN HEMT-based PA to a burst of square pulses with equal amplitude.

II. Pulse-to-Pulse Instability of GaN HEMTs

The typical response of a GaN HEMT-based PA to a burst of square pulses with equal envelope amplitude is presented in Fig. 1. Note how the pulses output by the PA are far from being square and not of equal amplitude. This is due to electron-trapping phenomena that dynamically change the threshold voltage of the HEMT (and consequently its gain) over three very distinct time scales: the pulse duration (20 μs), the pulse repetition period (250 μs), and the burst repetition period (7 ms).

During the on-times of the pulses in Fig. 1, the high voltage swings at the drain of the HEMT cause its traps to charge at a very fast rate. This produces an effect similar to a dynamic variation of the HEMT's threshold voltage [5], which explains the drops in output power. Moreover, during the off-times of the pulses, the traps are allowed to discharge and the threshold voltage of the HEMT begins its recovery toward its initial state. This is why the small-signal output is always ascending and why the output power at the beginning of each pulse's on-time is always higher than the output power at the end of the previous pulse's on-time.

As evidenced in Fig. 1, electron-trapping effects have several undesirable consequences: extreme nonlinearity, the loss of peak output power (over 0.8 dB in this case), and poor

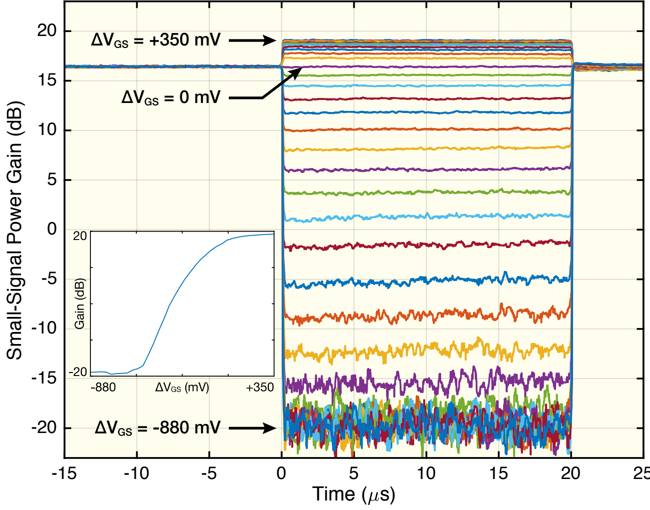

Fig. 2. Variation of the small-signal power gain of the GaN HEMT-based PA for various values of the gate–source voltage. Also, as a plot insert, the actual G^{SS} gain profile used for interpolation is displayed.

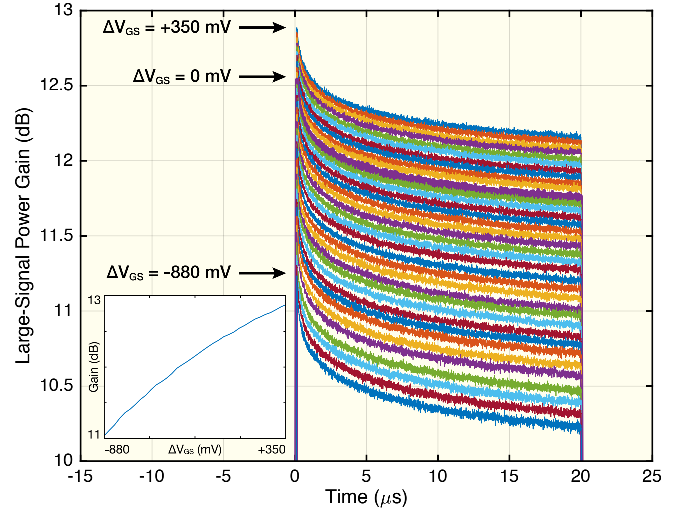

Fig. 3. Variation of the large-signal power gain of the GaN HEMT-based PA for various values of the gate–source voltage. Also, as a plot insert, the actual G^{LS} gain profile used for interpolation is displayed.

pulse-to-pulse amplitude stability—the output power varies not only within each pulse, but also within a burst from pulse to pulse and even between different bursts.

The pulse-to-pulse amplitude stability S_A of B pulse bursts, each composed of P pulses, can be defined as in (1), where $x_{p,b}$ denotes the complex envelope of the p-th pulse of the b-th burst, $|x_0|$ denotes the peak amplitude over all pulses (for normalization), and n denotes sampled time. This metric quantifies the amplitude variations of all pulses across all bursts. Therefore, as a measure of variation (or error), a lower value of S_A implies a greater stability (less error).

$$S_A(n) = \frac{1}{P-1} \sum_{p=1}^{P-1} \left[\overline{X_{p+1}}(n) - \overline{X_p}(n) \right]^2, \quad \text{where } \overline{X_p}(n) = \frac{1}{B} \sum_{b=1}^{B} \frac{|x_{p,b}(n)|}{|x_0|} \tag{1}$$

III. Compensation Method

In order to compensate the pulse-to-pulse amplitude instability of GaN HEMT-based PAs, the proposed method consists in varying the transconductance of the HEMT by applying a variable gate–source voltage $V_{GS} = V_{GG} + \Delta V_{GS}$, where V_{GG} is the constant gate bias voltage that sets the quiescent drain current and ΔV_{GS} is the compensation signal. Different transconductance modulation techniques have been shown to compensate other nonlinear effects caused by electron-trapping phenomena in GaN HEMTs [6].

To determine the compensation signal, we devised the following methodology. First, the small-signal (Fig. 2) and large-signal (Fig. 3) gains of the PA were measured as a function of the gate–source voltage. These measurements provide a mapping between the instantaneous PA output power level and the variation of the HEMT's threshold voltage under small-signal or large-signal excitations. Then, the response of the PA to a pulse train was measured and the corresponding variation of the threshold voltage was computed by linearly interpolating the measured small-signal and large-signal gain profiles at query points determined by the measured PA output response. Finally, the compensation signal was obtained by inverting the sign of the threshold voltage variation.

By applying this compensation signal to the gate of the HEMT, the variation of the threshold voltage is counteracted by an opposite variation of the gate–source voltage. This results in a new output response (to the same pulse train) that is much more linear than the first and thus features a much improved pulse-to-pulse amplitude stability. To further improve the pulse-to-pulse amplitude stability, we recalculated the compensation signal using the new output response of the PA and added the difference to the previous compensation signal. This process is summarized in Algorithm 1, where G^{SS} and G^{LS} are the small-signal and large-signal gain profiles, ΔV_{GS}^{SS} and ΔV_{GS}^{LS} are the corresponding gate–source voltage variations, and λ is an optional learning-rate parameter. Typically, only 1 to 5 iterations are necessary for an improvement of 20 dB.

Algorithm 1 Determination of the compensation signal ΔV_{GS}

Input: ΔV_{GS}^{SS}, G^{SS}, ΔV_{GS}^{LS}, G^{LS}, PA_{in}
Output: ΔV_{GS}
1: $\Delta V_{GS} := 0$
2: **while** necessary **do**
3: Measure PA_{out} in response to PA_{in} and ΔV_{GS}
4: $\Delta V_T :=$ interpolation of $(x, y) = \left(\{G^{SS}, G^{LS}\}, \{\Delta V_{GS}^{SS}, \Delta V_{GS}^{LS}\}\right)$ over $x = PA_{out}/PA_{in}$
5: $\Delta V_{GS} := \Delta V_{GS} - \lambda \Delta V_T$
6: **end while**
7: **return** ΔV_{GS}

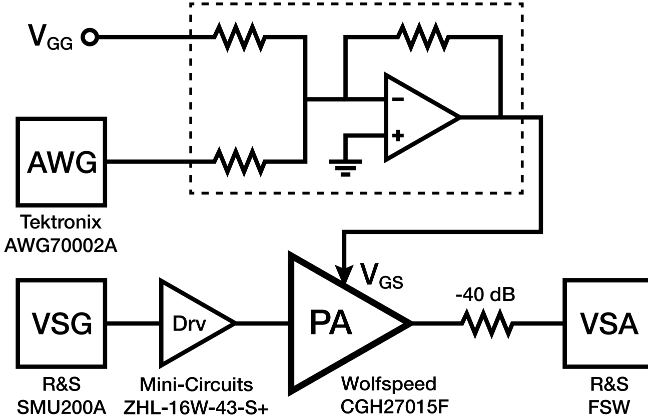

Fig. 4. Diagram of the laboratory setup.

IV. Implementation Details

The laboratory setup used to measure and compensate the pulse-to-pulse amplitude stability of a 1.6 GHz 15 W GaN HEMT-based PA biased in class B ($I_{DQ} \approx 2\%\ I_{DSS}$) is illustrated in Fig. 4. The instrumentation consisted of a Rohde & Schwarz SMU200A vector signal generator (VSG) for the generation of the PA input signal, a Tektronix AWG70002A arbitrary waveform generator (AWG) for the generation of the compensation signal, and a Rohde & Schwarz FSW vector signal analyzer (VSA) for the measurement of the PA output signal.

In order to successfully reproduce this work, it is critically important to ensure the repeatability of all measurements. This entails the setting of an initial thermal state by (1) biasing the HEMT at the desired quiescent point, (2) pre-heating the HEMT using a continuous train of large-signal pulses (for 3 minutes in our case), (3) waiting for the "hot" quiescent point to settle (1 minute in our case), and (4) adjusting the bias voltage to match the desired quiescent point. After setting the HEMT to this temperature-stable state, we ensured that all measurements were performed at the same electron-trapping state by using the sequencing capabilities of the VSG: contrary to usual practice, instead of continuously repeating a signal (e.g., one pulse, or a burst of pulses), the VSG was set up so that it would generate one single instance of that signal and immediately fall back to outputting a constant small-signal level. This guaranteed that two consecutive measurements always started at the same electron-trapping state, since there was enough time for the traps to discharge between the two measurements.

Another important aspect is the generation of the compensation signal by the AWG. For it to mimic the described behavior of the VSG, we connected one of the VSG's marker outputs to one of the AWG's external trigger inputs and set the AWG to single-shot external-trigger mode. Finally, we advanced all AWG output waveforms (by 2475 ns in our case) to ensure that both the VSG and the AWG provided synchronous excitations to the PA.

For the measurement of the PA output, a marker signal from the VSG should be connected to the trigger input of the VSA. Moreover, the VSA should be instructed to start the signal capture before the output of the VSG is enabled. Only this way can we be sure to measure the start of the very first pulse output by the PA: the one that is guaranteed to have no (additional) electron-trapping effects.

An inverting voltage-adder circuit was used to combine the constant gate bias voltage V_{GG} with the compensation signal ΔV_{GS}, resulting in the compensated gate–source voltage V_{GS}. The inverting topology of the voltage-adder is necessary to isolate the dc-coupled output of the AWG and the V_{GG} voltage source. Also, the typical large-value bypass capacitor at the gate bias terminal of the PA must be removed, otherwise the modulated V_{GS} would be bypassed to ground.

V. Results

Figs. 2 and 3 illustrate the measurements made for the extraction of the small-signal and large-signal gains of the PA as a function of the gate–source voltage. In order to obtain the former, the VSG was set up to output a constant power level of 0 dBm and the AWG was set up to output single pulses with a duration of 20 μs and varying amplitudes. In order to obtain the latter, the VSG was set up to output single pulses with a duration of 20 μs, a low-level of 0 dBm and a high-level of 25 dBm; the AWG was set up as in the first set of measurements.

As these figures reveal, the gain of the PA varies during the duration of the pulses: it increases for the small-signal test set and decreases for the large-signal test set. As explained, this is due to the discharging and charging of the HEMT's traps and consequent decrease or increase of the threshold voltage. Thus, the true gain of the PA (under the initial conditions established before) corresponds to the very first instant of each pulse, when the traps are "discharged" (they were actually charged to the state corresponding to a constant 0 dBm input).

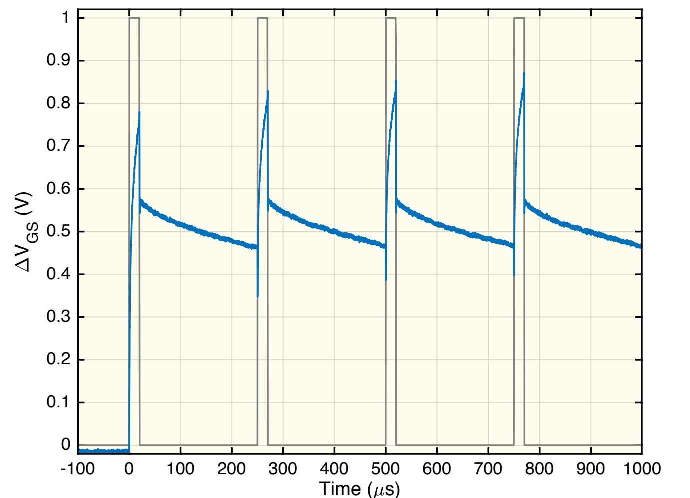

Fig. 5. The first millisecond of the signal that compensates the pulse-to-pulse instability of the GaN HEMT-based PA. Also, in the background, a representation of the first four input pulses is shown for visual reference.

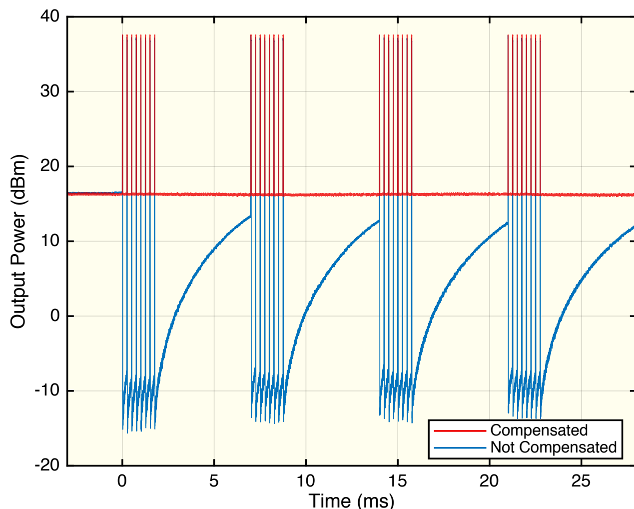

(a)

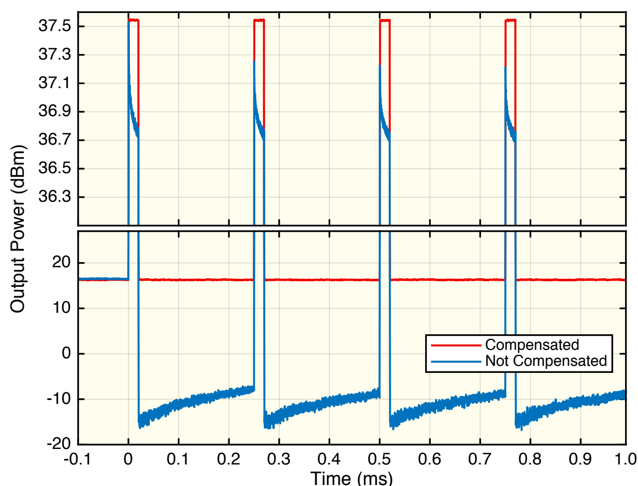

(b)

Fig. 6. (a) Complete and (b) zoomed-in view of the compensated and uncompensated responses of the GaN HEMT-based PA to a pulsed waveform.

After extracting the small-signal and large-signal gain profiles, the PA was submitted to an input signal that resembles those of pulsed radars: four bursts of eight pulses, with a pulse duration of 20 μs, a pulse repetition period of 250 μs, a burst repetition period of 7 ms, a low-level of 0 dBm, and a high-level of 25 dBm. After executing Algorithm 1, the compensation signal illustrated in Fig. 5 was obtained and, as Fig. 6 demonstrates, the PA was linearized.

Fig. 7 shows the pulse-to-pulse amplitude stability of the uncompensated and compensated PA outputs over all 32 pulses. As evidenced, a greater than 20 dB improvement was obtained.

VI. Conclusion

In this paper we presented a method for compensating the pulse-to-pulse amplitude instability of GaN HEMT-based PAs for their incorporation in pulsed radars for MTI. The method consists in measuring the small-signal and large-signal gain of the PA and computing a compensation signal based

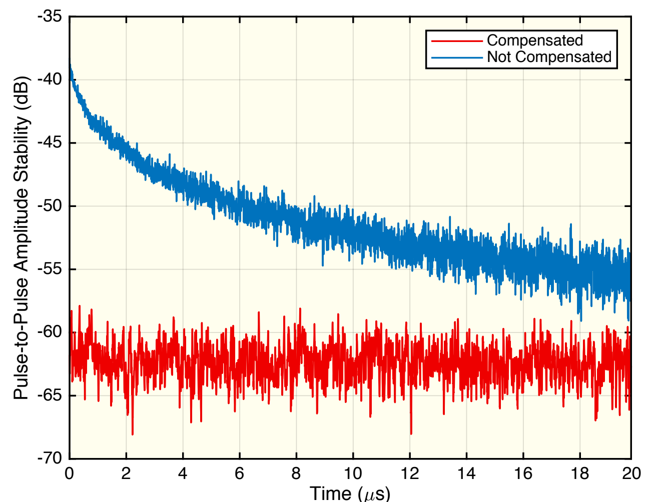

Fig. 7. Pulse-to-pulse amplitude stability of the compensated and uncompensated responses of the GaN HEMT-based PA to a pulsed waveform.

on the distorted response of the PA to a pulsed input signal. This compensation signal is then used to correct output power variations over all signal time scales simultaneously: within each pulse, between pulses in a burst, and between different pulse bursts. Our method was demonstrated to improve the peak output power of a 15 W GaN HEMT-based PA by 0.85 dB and the pulse-to-pulse amplitude stability by over 20 dB.

While a given compensation signal is specific to the input signal for which it was extracted, simple solutions for a more generalized compensation strategy could be realized, e.g., a lookup table of compensation signals for various pulse duty cycles.

Acknowledgment

This work was funded by FCT/MEC through national funds under the project UID/EEA/50008/2013 (APIC) and the project PTDC/EEI-TEL/7049/2014 (Lin5GPA). The work of P. M. Tomé was supported by FCT under Ph.D. Grant PD/BD/128198/2016.

References

[1] M. A. Richards, J. A. Scheer, and W. A. Holm, *Principles of Modern Radar: Basic Principles*, 1st ed. Edison, NJ, USA: SciTech Publishing, 2010.

[2] J. Delprato, D. Barataud, M. Campovecchio, G. Neveux, C. Tolant, and P. Eudeline, "Measured and simulated impact of irregular radar pulse trains on the pulse-to-pulse stability of microwave power amplifiers," *IEEE Trans. Microw. Theory Techn.*, vol. 62, no. 12, pp. 3538–3548, Dec. 2014.

[3] G. Formicone, J. Burger, and J. Custer, "150 V-bias RF GaN for 1 kW UHF radar amplifiers," in *Proc. IEEE Compound Semicond. Integr. Circuit Symp.*, Austin, TX, USA, Oct. 2016, pp. 1–4.

[4] S. Fakhfakh, A. Martin, M. Campovecchio, G. Neveux, and D. Barataud, "On-wafer time-domain and low-frequency measurements of GaN HEMTs for accurate trap modeling and its impact on pulse-to-pulse stability," in *Proc. Int. Workshop Integr. Nonlinear Microw. Millimetre-wave Circuits*, Brive La Gaillarde, France, Jul. 2018, pp. 1–3.

[5] K. Kunihiro and Y. Ohno, "A large-signal equivalent circuit model for substrate-induced drain-lag phenomena in HJFETs," *IEEE Trans. Electron Devices*, vol. 43, no. 9, pp. 1336–1342, Sep. 1996.

[6] P. M. Tomé, F. M. Barradas, T. R. Cunha, and J. C. Pedro, "Hybrid analog/digital linearization of GaN HEMT-based power amplifiers," *IEEE Trans. Microw. Theory Techn.*, vol. 67, no. 1, pp. 288–294, Jan. 2019.

APPENDIX I

Paper C4

A Transient Two-Tone RF Method for the Characterization of Electron Trapping Capture and Emission Dynamics in GaN HEMTs

Pedro M. Tomé, Filipe M. Barradas, Luís C. Nunes, João L. Gomes, Telmo R. Cunha, and José C. Pedro

Published In: 2020 IEEE/MTT-S International Microwave Symposium

Date of Conference: 21–26 June 2020

Conference Location: Los Angeles, CA, USA

Date of Publication: 21 June 2020

This is the authors' version of an article that has been published in the Proceedings of the 2020 IEEE MTT-S International Microwave Symposium. Changes were made to this version by the publisher prior to publication.

A Transient Two-Tone RF Method for the Characterization of Electron Trapping Capture and Emission Dynamics in GaN HEMTs

Pedro M. Tomé[1], Filipe M. Barradas[2], Luís C. Nunes[3], João L. Gomes[4], Telmo R. Cunha[5], José C. Pedro[6]
Instituto de Telecomunicações, Aveiro, Portugal
DETI, University of Aveiro, Portugal
{[1]tome.p.m, [2]filipebarradas, [3]cotimos, [4]joaolucas, [5]trcunha, [6]jcpedro}@ua.pt

***Abstract*— In this paper we propose an experimental method for the characterization and extraction of the time constants associated with the charge capture and emission processes of electron-trapping phenomena observed in radio-frequency (RF) power amplifiers (PAs) based on high-electron-mobility transistors (HEMTs). The method consists in the measurement of the transient response of a GaN HEMT-based PA to a series of large-signal two-tone RF excitations with increasing frequency separation, and the successive tracking of the gradual self-biasing experienced by the PA. With little requirements in terms of instrumentation and with applicability to fully assembled PAs, this simple method provides meaningful information on the dynamics of electron trapping close to the actual operating conditions of a GaN HEMT-based PA.**

***Keywords*— electron trapping, GaN HEMT, transient characterization, two-tone signal.**

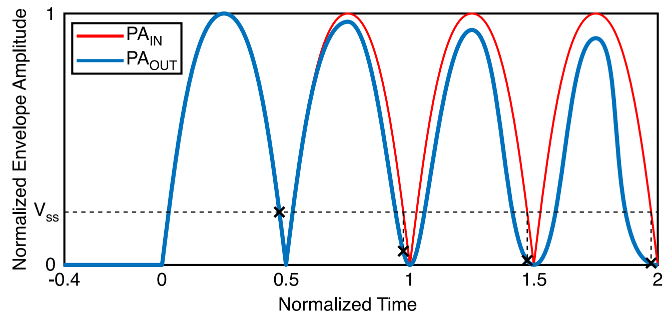

Fig. 1. Typical transient response of a GaN HEMT-based PA to a two-tone envelope excitation. Due to electron trapping, the PA gradually self-biases toward a deep class C and loses most of its small-signal gain.

I. Introduction

Electron-trapping phenomena are known to be a source of long-term memory effects that contribute to the extremely nonlinear behavior generally associated with radio-frequency (RF) power amplifiers (PAs) based on gallium nitride high-electron-mobility transistors (HEMTs). These effects, which include current collapse, knee walkout and dc–RF dispersion, lead to a seemingly intractable post-predistortion residual nonlinearity in communications applications [1] and a severe deterioration of the pulse-to-pulse stability in radar applications [2].

Electron trapping is characterized by highly asymmetric charge capture and emission processes. While charge capture has traditionally been relegated as a near-instantaneous process, recent developments in the characterization and modeling of electron-trapping phenomena have shown that the time constants associated with charge capture can range from less than a microsecond to a few tens of milliseconds [3]. This has uncovered the outstanding importance of the multiple-time-constant dynamic behavior of electron trapping in the pulse-to-pulse stability of GaN HEMT-based PAs, which has been found to be degraded by over 20 dB [2], [3].

In order to characterize electron-trapping phenomena and extract the parameters of relevant models, several experimental procedures have been proposed. The most prevalent extraction procedures are based on pulsed [4] and double-pulsed [5] I/V measurements, as well as low-frequency admittance measurements [6], which are performed on the discrete HEMT and require very specialized equipment. Alternative procedures include the measurement of two-tone RF signals [7], which can be performed on a fully assembled PA using equipment commonly available in most RF laboratories, such as a vector signal generator and a vector signal analyzer.

While this last procedure benefits from its simplicity of execution, much greater variety in excitation dynamics (compared to pulse-based methods), and from being performed much closer to the operating conditions of the GaN HEMT-based PA under test, the steady-state nature of its measurements impairs its ability to accurately characterize charge capture processes. For this reason, and because charge capture has recently been demonstrated to be of paramount importance in key GaN applications such as radar [2], [3], in this paper we propose a method for accurately characterizing and extracting the capture and emission time constants associated with electron-trapping phenomena using transient two-tone RF measurements.

II. Theoretical Background

Electron trapping—and, more generally, charge trapping—refers to an accumulation of charge with energy levels deep within the band gap of a semiconductor. In GaN HEMTs, this is understood to be caused by large electric fields at the gate terminal (gate lag), the drain terminal (drain lag), or a combination of both [8]. As a result of the accumulated charge, a net-negative electric potential is generated and the GaN channel is pinched-off. The HEMT then recovers when the charge is released. This phenomenon can be modeled as a virtual back gate that produces a self-biasing effect [9], dynamically modulating the conductivity of the GaN channel. Moreover, this process

inherently presents highly asymmetric capture (charge) and emission (discharge) times.

While it is generally believed that the asymmetry between the time constants associated with charge capture and emission is so great that the capture process can be considered instantaneous, in [3] the authors demonstrated that this is, in fact, incorrect. In reality, the time constants associated with charge capture can be comparable to the slow-varying envelopes of modern radar or wireless communications signals, ranging from less than a microsecond up to a few tens of milliseconds. It follows, then, that the self-biasing experienced by GaN HEMT-based PAs is not instantaneous, but is actually sufficiently slow to be measured for the characterization of charge capture processes even with common RF laboratory equipment. Thus, in this paper we show how both charge capture and emission can be accurately characterized through transient large-signal two-tone RF excitations with varying frequency separations Δf.

Previous efforts to characterize trapping-related time constants using two-tone excitations [7] correctly identified that, for very low Δf (less than 10 Hz), the small-signal gain of a GaN HEMT-based PA remains unchanged. This happens because, while there is a very significant accumulation of trapped charge during the large-signal portion of the envelope, the envelope is so slow that there is enough time for most of the trapped charge to be released through emission by the time the envelope reaches a small-signal level. However, for larger Δf (0.1–1 kHz), it is found that the small-signal gain decreases because there is not enough time for the trapped charge to be released during the short period between the large-signal and small-signal parts of the sinusoidal envelope. For much larger Δf (>10 kHz), the envelope is too fast for there to be any significant emission of trapped charge, so the small-signal gain remains very low at a constant level.

Even though this is sufficient to characterize the steady-state behavior of electron trapping, a simple modification—measuring the transient response instead of the steady-state response—allows for the extraction of much more information regarding the nonlinear dynamics of charge capture and emission. In effect, the gradual self-biasing of a GaN HEMT-based PA can be tracked at each envelope half-cycle, as shown in Fig. 1, and the dynamic variation of the HEMT's threshold voltage (or virtual back gate) can be more comprehensively characterized.

III. Characterization Procedure

A. Measurements

First, the transient response of the GaN HEMT-based PA under test to a series of large-signal two-tone RF excitations with increasing frequency separation Δf is measured. This can be done using a vector signal generator (VSG) and a vector signal analyzer (VSA). The VSG should be configured to generate one single instance of each waveform and to trigger the VSA measurement at the start of each waveform playback. In order to maintain the same initial conditions for all measurements, the charge accumulated as a result of each measurement should be released prior to triggering the next measurement. This can be done either by waiting 30 s to 100 s between each measurement with the PA under a small-signal excitation, or by actually tracking the recovery of the PA's small-signal gain or quiescent current. From these measurements we obtain a dataset containing the transient response of the PA to the two-tone excitation, from the first cycle to the N-th cycle, for each frequency separation Δf.

Then, the steady-state response of the PA to a constant small-signal continuous-wave (CW) excitation is measured as a function of the gate–source voltage V_{GS}. This can also be done with a VSG and a VSA while V_{GS} is swept. From these measurement we obtain a map between V_{GS} and the output power P_{out} of the PA for an input power level equal to that chosen for the CW excitation. This map is assumed to be static.

B. Post-Processing

After performing the required measurements, all recorded time series are aligned with their respective excitations in order to compensate the group delay introduced by the measurement setup. Since in this paper we consider the use of a VSG and VSA, the input excitation is never actually measured—it only exists in its virtual form in a computer. Thus, aligning the measured PA output with the input excitation means sliding the input excitation across time in order to maximize the cross-correlation between the two signals.

For optimum results, the alignment should not be done simply by cyclically shifting the samples of the input excitation vector. Instead, a new input excitation vector should be generated by introducing a double-precision delay to the sampling of the respective sinusoid (for the two-tone envelope with frequency separation Δf); this way, the precision of the alignment can be a fraction of one sample. Thus, optimum alignment requires an optimization process for finding t_0 such that $|x(t)| = |\sin(2\pi\ \Delta f/2\ (t - t_0))|$ has maximum cross-correlation with the amplitude of the measured PA response $|y(t)|$ at the small-signal parts of the envelopes. This can be done in an expedient fashion by minimizing the mean square error between $\log(|x(t)|)$ and $\log(|y(t)|/\max\{|y(t)|\})$ using, e.g., gradient descent techniques. Note that an optimum alignment is most critical at the small-signal parts of the envelopes; for this reason, we use the logarithm function to magnify the small-signal amplitudes and prevent their squared errors from being outweighed by those at the large-signal parts of the envelopes.

After obtaining the aligned transient response $y_a(t)$ of the PA (in reality, the response is the same and it is the time vector that is shifted by t_0), it was sampled at the instants where the amplitude of the respective two-tone excitation is equal to that of the small-signal CW excitation used in the measurement of the P_{out}-vs.-V_{GS} map. Thus, the values of $y_a(t_{ss}(k))$ were recorded, where t_{ss} is defined in (1), $k = 1, 2, \cdots, K$ is the index of each half-cycle of the two-tone input excitation with frequency separation Δf (up to a total of K half-cycles), V_{pk} is the peak amplitude of the two-tone input excitation, and V_{ss} is

the amplitude of the CW excitation at which the P_{out}-vs.-V_{GS} map was measured.

$$t_{ss}(k) = \frac{1}{\Delta f}\left[k - \frac{1}{\pi}\arcsin\left(\frac{V_{ss}}{V_{pk}}\right)\right] \quad (1)$$

At this point, it is important to understand that $y_a(t_{ss}(k))$ is the output of the PA at the instants where the input of the PA has an amplitude of V_{ss} (as represented in Fig. 1 by the black crosses). Since we measured a map that converts between V_{GS} and P_{out} for an input excitation with amplitude V_{ss}, then this map can be used to estimate the equivalent V_{GS} for each measured $y_a(t_{ss}(k))$, for instance, through linear interpolation. This results in a vector $V_{GS}(t_{ss}(k))$ that contains an estimate of the equivalent gate–source voltage at each half-cycle of the transient response of the PA to each large-signal two-tone excitation. Due to the sigmoid shape of the map, some estimates resulting from the interpolation may be indeterminate; in these cases, we choose to discard the estimates.

Finally, the variation of the threshold voltage due to electron trapping can be calculated by subtracting the gate bias voltage V_{GG} from all estimated $V_{GS}(t_{ss}(k))$. This results in a dataset $\Delta V_{GS}(\Delta f, k)$ that contains the variation of the threshold voltage of the GaN HEMT, for a two-tone excitation with frequency separation Δf, estimated at each half-cycle k. This dataset provides a comprehensive characterization of the gradual self-biasing experienced by a GaN HEMT-based PA for a wide variety of amplitude-modulated excitation dynamics.

IV. Experimental Results

In order to validate the proposed method, the measurement setup illustrated in Fig. 2 was assembled. The in-phase and quadrature baseband waveforms of the two-tone input signals were generated using a Tektronix AWG70002A arbitrary waveform generator (AWG), which was connected to a Keysight E8267D PSG VSG for RF up-conversion. A Mini-Circuits ZHL-16W-43-S+ driver scaled the output of the VSG and provided the input excitations to the PA. The output of the PA was measured using a Keysight N9041B UXA VSA. The dc power of the PA was sourced from a Keysight N6705C dc power analyzer, which was also used for sweeping V_{GS} during the measurement of the P_{out}-vs.-V_{GS} map.

Using this setup, the proposed method was applied to a 1.6 GHz single-ended PA based on the 15 W 28 V Wolfspeed CGH27015F GaN HEMT. The PA was biased in class B at a quiescent drain current of 40 mA. The two-tone excitations provided a peak available input power of 29 dBm and their frequency separation was varied from 10 Hz to 1 MHz. The P_{out}-vs.-V_{GS} map and the transient response of the PA at $t_{ss}(k)$ were measured for an input power level of 0 dBm. The PA was measured for 100 periods of each input excitation, the last of which should correspond to a near-steady-state condition.

Fig. 3 illustrates the output power of the PA across all Δf when measured at the instants where the level of the input two-tone excitation is 0 dBm, i.e., $|y_a(t_{ss}(k))|$ for all Δf. As expected, the obtained profiles reveal that the output power

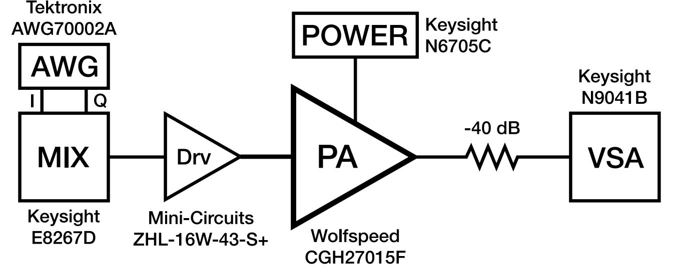

Fig. 2. Diagram of the measurement setup.

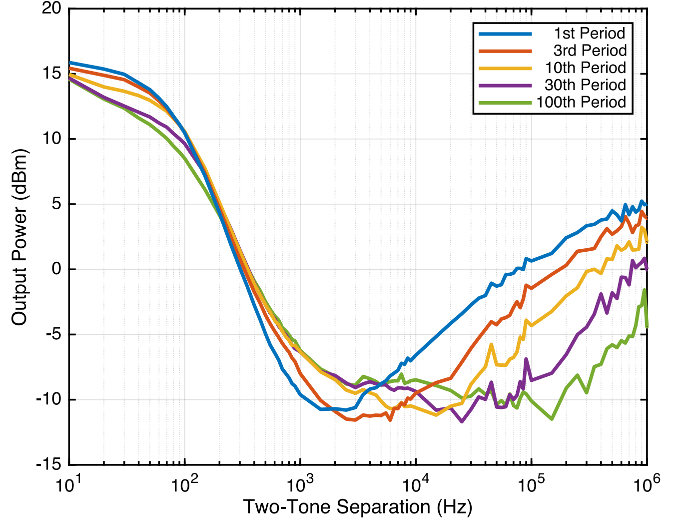

Fig. 3. Variation of the PA output power measured at the small-signal-input instants $t_{ss}(k)$ as a function of the two-tone frequency separation.

is high at low Δf and falls sharply as Δf increases thanks to the current collapse induced by electron trapping, up to a loss of 25 dB. This corresponds to a clear degeneration of the operation of the GaN HEMT-based PA from class B to a deep class C. Moreover, the various profiles show the temporal evolution of this self-biasing behavior: from the very first input period to the last. This provides valuable information on the net state of the deep-level traps of the GaN HEMT at various stages of the descent from class B to class C. For instance, at higher Δf it is clear that the first period of the input excitation is not enough to fully charge the deep-level traps, since successive profiles indicate a progressively lower PA output power for the same PA input power (0 dBm).

By interpolating these profiles through the P_{out}-vs.-V_{GS} map, the dynamic variation of the threshold voltage is obtained. This information can then be used as an optimization target for the extraction of the parameters of a variety of models. For instance, Fig. 4 illustrates the result of the extraction of the parameters of the ubiquitous and very established electron-trapping model with one capture time constant and one emission time constant [4]. As is shown (green line), and as has been previously demonstrated in [7], this model fits the measured variation of the threshold voltage quite well under steady-state conditions. However, we also show that it is not

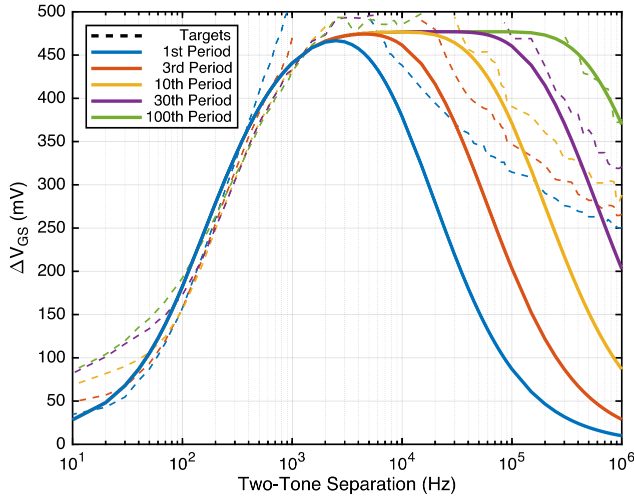

Fig. 4. Result of the extraction of an electron-trapping model with one capture time constant and one emission time constant.

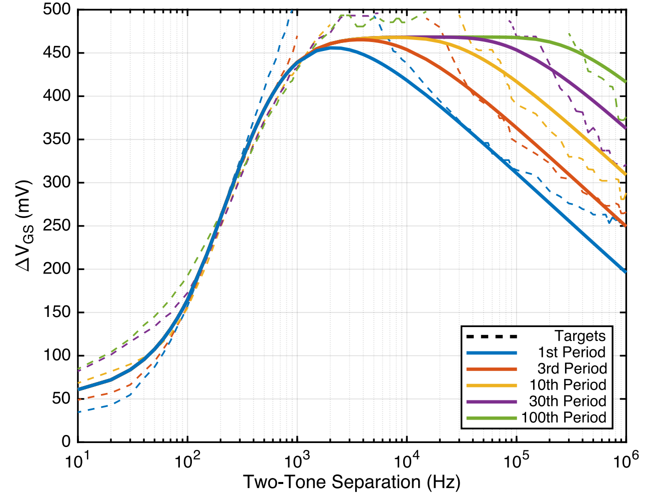

Fig. 5. Result of the extraction of an electron-trapping model based on Shockley–Read–Hall statistics.

capable of predicting the transient behavior with sufficient accuracy. In Fig. 5, the same data was used to extract the parameters of a model based on Shockley–Read–Hall statistics [3]. As is shown, this model provided a great improvement in the prediction of the transient variation of the threshold voltage of the GaN HEMT.

In order to ensure that the proposed method yields meaningful results, we compared the obtained time constants with the ones obtained through more established pulse-based methods. Although there are some minor differences—because not only are the extraction procedures different, but the excitations used for the extraction are widely different as well—, all methods point to a set of capture time constants that range from the microsecond range to the millisecond range and an emission time constant well in the millisecond range. Furthermore, the results obtained using the method reported in [7] are a small subset of the results obtained through the proposed method. Thus, the proposed method is consistent with prior more established methods and yields meaningful data for the extraction of dynamic electron-trapping models.

V. Conclusion

In this paper we proposed a method for the characterization and extraction of trapping-related capture and emission time constants based on the transient inspection of the dynamic self-biasing of GaN HEMT-based PAs. As a method that utilizes two-tone RF excitations, it does not require specialized and expensive pulsing equipment, and can instead be performed using a conventional vector signal generator and analyzer on a fully assembled PA. The proposed method provides comprehensive measured data on the dynamics of electron trapping close to the target operating conditions of the PA under test, and can be used for aiding in the modeling and linearization of GaN HEMT-based PAs [10].

Acknowledgment

This work was funded by FCT/MEC through national funds under the projects UID/EEA/50008/2013 (APIC) and PTDC/EEI-TEL/7049/2014 (Lin5GPA). The work of P. Tomé was supported by FCT under Ph.D. Grant PD/BD/128198/2016.

References

[1] F. M. Barradas, L. C. Nunes, T. R. Cunha, P. M. Lavrador, P. M. Cabral, and J. C. Pedro, "Compensation of long-term memory effects on GaN HEMT-based power amplifiers," *IEEE Trans. Microw. Theory Techn.*, vol. 65, no. 9, pp. 3379–3388, Sep. 2017.

[2] P. M. Tomé, F. M. Barradas, T. R. Cunha, and J. C. Pedro, "Compensation of the pulse-to-pulse instability of GaN HEMT-based power amplifiers," in *Proc. IEEE Int. Microw. Symp.*, Boston, MA, USA, Jun. 2019, pp. 408–411.

[3] J. L. Gomes, L. C. Nunes, C. F. Gonçalves, and J. C. Pedro, "An accurate characterization of capture time constants in GaN HEMTs," *IEEE Trans. Microw. Theory Techn.*, vol. 67, no. 7, pp. 2465–2474, Jul. 2019.

[4] O. Jardel, F. D. Groote, T. Reveyrand, J.-C. Jacquet, C. Charbonniaud, J.-P. Teyssier, D. Floriot, and R. Quere, "An electrothermal model for AlGaN/GaN power HEMTs including trapping effects to improve large-signal simulation results on high VSWR," *IEEE Trans. Microw. Theory Techn.*, vol. 55, no. 12, pp. 2660–2669, Dec. 2007.

[5] A. Santarelli, R. Cignani, G. P. Gibiino, D. Niessen, P. A. Traverso, C. Florian, D. M. M. P. Schreurs, and F. Filicori, "A double-pulse technique for the dynamic I/V characterization of GaN FETs," *IEEE Microw. Wireless Compon. Lett.*, vol. 24, no. 2, pp. 132–134, Dec. 2013.

[6] M. Bouslama, V. Gillet, C. Chang, J.-C. Nallatamby, R. Sommet, M. Prigent, R. Quéré, and B. Lambert, "Dynamic performance and characterization of traps using different measurements techniques for the new AlGaN/GaN HEMT of 0.15-μm ultrashort gate length," *IEEE Trans. Microw. Theory Techn.*, vol. 67, no. 7, pp. 2475–2482, Apr. 2019.

[7] L. C. Nunes, J. L. Gomes, P. M. Cabral, and J. C. Pedro, "A simple method to extract trapping time constants of GaN HEMTs," in *Proc. IEEE MTT-S Int. Microw. Symp.*, Philadelphia, PA, USA, Jun. 2018, pp. 716–719.

[8] M. J. Uren, J. Moreke, and M. Kuball, "Buffer design to minimize current collapse in GaN/AlGaN HFETs," *IEEE Trans. Electron Devices*, vol. 59, no. 12, pp. 3327–3333, Oct. 2012.

[9] J. C. Pedro, L. C. Nunes, and P. M. Cabral, "Soft compression and the origins of nonlinear behavior of GaN HEMTs," in *Proc. Eur. Microw. Integr. Circuit Conf.*, Rome, Italy, Oct. 2014, pp. 353–356.

[10] P. M. Tomé, F. M. Barradas, T. R. Cunha, and J. C. Pedro, "Hybrid analog/digital linearization of GaN HEMT-based power amplifiers," *IEEE Trans. Microw. Theory Techn.*, vol. 67, no. 1, pp. 288–294, Jan. 2019.

References

[1] *Transforming our world: The 2030 agenda for sustainable development*, Resolution A/RES/70/1, United Nations General Assembly, Sep. 2015.

[2] *IMT Vision—Framework and overall objectives of the future development of IMT for 2020 and beyond*, Recommendation ITU-R M.2083-0, Iternational Telecommunication Union, Radiocommunication Sector (ITU-R), Sep. 2015.

[3] Y. Kim, Y. Kim, J. Oh, H. Ji, J. Yeo, S. Choi, H. Ryu, H. Noh, T. Kim, F. Sun, Y. Wang, Y. Qi, and J. Lee, "New Radio (NR) and its evolution toward 5G-Advanced," *IEEE Trans. Wireless Commun.*, vol. 26, no. 3, pp. 2–7, Jul. 2019.

[4] "Study on requirements for NR beyond 52.6 GHz," 3rd Generation Partnership Project (3GPP), Technical Report (TR) 38.807 Version 16.0.0, Dec. 2019.

[5] H. Wang, X. Zhou, and M. C. Reed, "Coverage and throughput analysis with a non-uniform small cell deployment," *IEEE Trans. Wireless Commun.*, vol. 13, no. 4, pp. 2047–2059, Feb. 2014.

[6] X. Ge, S. Tu, G. Mao, C.-X. Wang, and T. Han, "5G ultra-dense cellular networks," *IEEE Trans. Wireless Commun.*, vol. 23, no. 1, pp. 72–79, Mar. 2016.

[7] J. G. Andrews, S. Buzzi, W. Choi, S. V. Hanly, A. Lozano, A. C. K. Soon, and J. C. Zhang, "What will 5G be?" *IEEE J. Sel. Areas Commun.*, vol. 32, no. 6, pp. 1065–1082, Jun. 2014.

[8] R. S. Pengelly, S. M. Wood, J. W. Milligan, S. T. Sheppard, and W. L. Pribble, "A review of GaN on SiC high electron-mobility power transistors and MMICs," *IEEE Trans. Microw. Theory Techn.*, vol. 60, no. 6, pp. 1764–1783, Jun. 2012.

[9] E. A. Jones, F. F. Wang, and D. Costinett, "Review of commercial GaN power devices and GaN-based converter design challenges," *IEEE Trans. Emerg. Sel. Topics Power Electron.*, vol. 4, no. 3, pp. 707–719, Jun. 2016.

[10] T. Mizutani, Y. Ohno, M. Akita, S. Kishimoto, and K. Maezawa, "A study on current collapse in AlGaN/GaN HEMTs induced by bias stress," *IEEE Trans. Electron Devices*, vol. 50, no. 10, pp. 2015–2020, Sep. 2003.

[11] D. Jin and J. A. del Alamo, "Mechanisms responsible for dynamic ON-resistance in GaN high-voltage HEMTs," in *Proc. Int. Symp. Power Semicond. Devices ICs*, Bruges, Belgium, Jun. 2012, pp. 333–336.

[12] P. McGovern, J. Benedikt, P. J. Tasker, J. Powell, K. P. Hilton, J. L. Glasper, R. S. Balmer, T. Martin, and M. J. Uren, “Analysis of DC-RF dispersion in AlGaN/GaN HFETs using pulsed I-V and time-domain waveform measurements,” in *Proc. IEEE MTT-S Int. Microw. Symp.*, Long Beach, CA, USA, Jun. 2005, pp. 503–506.

[13] F. M. Barradas, L. C. Nunes, T. R. Cunha, P. M. Lavrador, P. M. Cabral, and J. C. Pedro, “Compensation of long-term memory effects on GaN HEMT-based power amplifiers,” *IEEE Trans. Microw. Theory Techn.*, vol. 65, no. 9, pp. 3379–3388, Sep. 2017.

[14] J. Delprato, D. Barataud, M. Campovecchio, G. Neveux, C. Tolant, and P. Eudeline, “Measured and simulated impact of irregular radar pulse trains on the pulse-to-pulse stability of microwave power amplifiers,” *IEEE Trans. Microw. Theory Techn.*, vol. 62, no. 12, pp. 3538–3548, Dec. 2014.

[15] X. Liu, Q. Zhang, W. Chen, H. Feng, L. Chen, F. M. Ghannouchi, and Z. Feng, “Beam-oriented digital predistortion for 5G massive MIMO hybrid beamforming transmitters,” *IEEE Trans. Microw. Theory Techn.*, vol. 66, no. 7, pp. 3419–3432, May 2018.

[16] Y. Li, W. Cao, and A. Zhu, “Instantaneous sample indexed magnitude-selective affine function-based behavioral model for digital predistortion of RF power amplifiers,” *IEEE Trans. Microw. Theory Techn.*, vol. 66, no. 11, pp. 5000–5010, Aug. 2018.

[17] X. Wang, Y. Li, C. Yu, W. Hong, and A. Zhu, “Digital predistortion of 5G massive MIMO wireless transmitters based on indirect identification of power amplifier behavior with OTA tests,” *IEEE Trans. Microw. Theory Techn.*, vol. 68, no. 1, pp. 316–328, Nov. 2019.

[18] “*NR; Physical layer procedures for control*,” 3rd Generation Partnership Project (3GPP), Technical Specification (TS) 38.213 Version 16.2.0, Jun. 2020.

[19] M. A. Khan, J. N. Kuznia, A. R. Bhattarai, and D. T. Olson, “Metal semiconductor field effect transistor based on single crystal GaN,” *Appl. Phys. Lett.*, vol. 62, no. 15, pp. 1786–1787, Jan. 1945.

[20] T. Yamasaki, Y. Kittaka, H. Minamide, K. Yamauchi, S. Miwa, S. Goto, M. Nakayama, M. Kohno, and N. Yoshida, “A 68% efficiency, C-band 100W GaN power amplifier for space applications,” in *Proc. IEEE MTT-S Int. Microw. Symp.*, Anaheim, CA, USA, Jul. 2010, pp. 1384–1387.

[21] H. Shigematsu, Y. Inoue, A. Akasegawa, M. Yamada, S. Masuda, Y. Kamada, A. Yamada, M. Kanamura, T. Ohki, K. Makiyama, N. Okamoto, K. Imanishi, T. Kikkawa, K. Joshin, and N. Hara, “C-band 340-W and X-band 100-W GaN power amplifiers with over 50-% PAE,” in *Proc. IEEE MTT-S Int. Microw. Symp.*, Boston, MA, USA, Jul. 2009, pp. 1265–1268.

[22] S. Yoshida, M. Tanomura, Y. Murase, K. Yamanoguchi, K. Ota, K. Matsunaga, and H. Shimawaki, “A 76 GHz GaN-on-silicon power amplifier for automotive radar systems,” in *Proc. IEEE MTT-S Int. Microw. Symp.*, Boston, MA, USA, Jul. 2009, pp. 665–668.

[23] K. J. Chen, O. Häberlen, A. Lidow, C. lin Tsai, T. Ueda, Y. Uemoto, and Y. Wu, “GaN-on-Si power technology: Devices and applications,” *IEEE Trans. Electron Devices*, vol. 64, no. 3, pp. 779–795, Feb. 2017.

[24] U. K. Mishra, L. Shen, T. E. Kazior, and Y.-F. Wu, "GaN-based RF power devices and amplifiers," *Proc. IEEE*, vol. 96, no. 2, pp. 287–305, Feb. 2008.

[25] P. G. Neudeck, R. S. Okojie, and L.-Y. Chen, "High-temperature electronics—A role for wide bandgap semiconductors?" *Proc. IEEE*, vol. 90, no. 6, pp. 1065–1076, Nov. 2002.

[26] M. Micovic, D. F. Brown, D. Regan, J. Wong, Y. Tang, F. Herrault, D. Santos, S. D. Burnham, J. Tai, E. Prophet, I. Khalaf, C. McGuire, H. Bracamontes, H. Fung, A. K. Kurdoghlian, and A. Schmitz, "High frequency GaN HEMTs for RF MMIC applications," in *Proc. IEEE Int. Electron Devices Meeting*, San Francisco, CA, USA, Dec. 2016, pp. 1–4.

[27] Y.-f. Wu, M. Moore, A. Saxler, T. Wisleder, and P. Parikh, "40-W/mm double field-plated GaN HEMTs," in *Proc. Device Res. Conf.*, State College, PA, USA, Jun. 2006, pp. 151–152.

[28] K. Shinohara, D. C. Regan, Y. Tang, A. L. Corrion, D. F. Brown, J. C. Wong, J. F. Robinson, H. H. Fung, A. Schmitz, T. C. Oh, S. J. Kim, P. S. Chen, R. G. Nagele, A. D. Margomenos, and M. Micovic, "Scaling of GaN HEMTs and Schottky diodes for submillimeter-wave MMIC applications," *IEEE Trans. Electron Devices*, vol. 60, no. 10, pp. 2982–2996, Jul. 2013.

[29] Y. Tang, K. Shinohara, D. Regan, A. Corrion, D. Brown, J. Wong, A. Schmitz, H. Fung, S. Kim, and M. Micovic, "Ultrahigh-speed GaN high-electron-mobility transistors with f_T/f_{max} of 454/444 GHz," *IEEE Electron Device Lett.*, vol. 36, no. 6, pp. 549–551, Apr. 2015.

[30] S. Keller, G. Parish, P. T. Fini, S. Heikman, C.-H. Chen, N. Zhang, S. P. DenBaars, U. K. Mishra, and Y.-F. Wu, "Metalorganic chemical vapor deposition of high mobility AlGaN/GaN heterostructures," *J. Appl. Phys.*, vol. 86, no. 10, pp. 5850–5857, Nov. 1996.

[31] I. P. Smorchkova, C. R. Elsass, J. P. Ibbetson, R. Vetury, B. Heying, P. Fini, E. Haus, S. P. DenBaars, J. S. Speck, and U. K. Mishra, "Polarization-induced charge and electron mobility in AlGaN/GaN heterostructures grown by plasma-assisted molecular-beam epitaxy," *J. Appl. Phys.*, vol. 86, no. 8, pp. 4520–4526, Sep. 1999.

[32] S. Yoshida, S. Misawa, and S. Gonda, "Improvements on the electrical and luminescent properties of reactive molecular beam epitaxially grown GaN films by using AlN-coated sapphire substrates," *Appl. Phys. Lett.*, vol. 42, no. 5, pp. 427–429, Jan. 1983.

[33] H. Amano, N. Sawaki, I. Akasaki, and Y. Toyoda, "Metalorganic vapor phase epitaxial growth of a high quality GaN film using an AlN buffer layer," *Appl. Phys. Lett.*, vol. 48, no. 5, pp. 353–355, Aug. 1986.

[34] J. W. P. Hsu, D. V. Lang, S. Richter, R. N. Kleiman, A. M. Sergent, and R. J. Molnar, "Nature of the highly conducting interfacial layer in GaN films," *Appl. Phys. Lett.*, vol. 77, no. 18, pp. 2873–2875, Oct. 2000.

[35] W. E. Hoke, A. Torabi, J. J. Mosca, R. B. Hallock, and T. D. Kennedy, "Rapid silicon outdiffusion from SiC substrates during molecular-beam epitaxial growth of AlGaN/GaN/AlN transistor structures," *J. Appl. Phys.*, vol. 98, p. 084 510, Oct. 2005.

[36] S. Heikman, S. Keller, S. P. DenBaars, and U. K. Mishra, "Growth of Fe doped semi-insulating GaN by metalorganic chemical vapor deposition," *Appl. Phys. Lett.*, vol. 81, no. 3, pp. 439–441, Jul. 2002.

[37] C. Poblenz, P. Waltereit, S. Rajan, S. Heikman, U. K. Mishra, and J. S. Speck, "Effect of carbon doping on buffer leakage in AlGaN/GaN high electron mobility transistors," *J. Vac. Sci. Technol. B*, vol. 22, no. 3, pp. 1145–1149, May 2004.

[38] V. Desmaris, M. Rudzinski, N. Rorsman, P. R. Hageman, P. K. Larsen, H. Zirath, T. C. Rodle, and H. F. F. Jos, "Comparison of the dc and microwave performance of AlGaN/GaN HEMTs grown on SiC by MOCVD with Fe-doped or unintentionally doped GaN buffer layers," *IEEE Trans. Electron Devices*, vol. 53, no. 9, pp. 2413–2417, Aug. 2006.

[39] M. J. Uren, K. J. Nash, R. S. Balmer, T. Martin, E. Morvan, N. Caillas, S. L. Delage, D. Ducatteau, B. Grimbert, and J. C. D. Jaeger, "Punch-through in short-channel AlGaN/GaN HFETs," *IEEE Trans. Electron Devices*, vol. 53, no. 2, pp. 395–398, Jan. 2006.

[40] M. Micovic, P. Hashimoto, M. Hu, I. Milosavljevic, J. Duvall, P. J. Willadsen, W.-S. Wong, A. M. Conway, A. Kurdoghlian, P. W. Deelman, J.-S. Moon, A. Schmitz, and M. J. Delaney, "GaN double heterojunction field effect transistor for microwave and millimeterwave power applications," in *Proc. IEEE Int. Electron Devices Meeting*, San Francisco, CA, USA, Dec. 2004, pp. 1–4.

[41] J. Liu, Y. Zhou, J. Zhu, K. M. Lau, and K. J. Chen, "AlGaN/GaN/InGaN/GaN DH-HEMTs with an InGaN notch for enhanced carrier confinement," *IEEE Electron Device Lett.*, vol. 27, no. 1, pp. 10–12, Dec. 2005.

[42] T. Palacios, A. Chakraborty, S. Heikman, S. Keller, S. P. DenBaars, and U. K. Mishra, "AlGaN/GaN high electron mobility transistors with InGaN back-barriers," *IEEE Electron Device Lett.*, vol. 27, no. 1, pp. 13–15, Dec. 2005.

[43] X. Wang, S. Huang, Y. Zheng, K. Wei, X. Chen, H. Zhang, and X. Liu, "Effect of GaN channel layer thickness on dc and RF performance of GaN HEMTs with composite AlGaN/GaN buffer," *IEEE Trans. Electron Devices*, vol. 61, no. 5, pp. 1341–1346, Apr. 2014.

[44] A. Malmros, P. Gamarra, M. Thorsell, H. Hjelmgren, C. Lacam, S. L. Delage, H. Zirath, and N. Rorsman, "Impact of channel thickness on the large-signal performance in InAlGaN/AlN/GaN HEMTs with an AlGaN back barrier," *IEEE Trans. Electron Devices*, vol. 66, no. 1, pp. 364–371, Dec. 2018.

[45] O. Ambacher, B. Foutz, J. Smart, J. R. Shealy, N. G. Weimann, K. Chu, M. Murphy, A. J. Sierakowski, W. J. Schaff, L. F. Eastman, R. Dimitrov, A. Mitchell, and M. Stutzmann, "Two dimensional electron gases induced by spontaneous and piezoelectric polarization in undoped and doped AlGaN/GaN heterostructures," *J. Appl. Phys.*, vol. 87, no. 1, pp. 334–344, Dec. 1999.

[46] Y. C. Kong, Y. D. Zheng, C. H. Zhou, Y. Z. Deng, S. L. Gu, B. Shen, R. Zhang, R. L. Jiang, Y. Shi, and P. Han, "Study of two-dimensional electron gas in AlN/GaN heterostructure by a self-consistent method," *phys. stat. sol. (b)*, vol. 241, no. 4, pp. 840–844, Feb. 2004.

[47] G. Koley and M. G. Spencer, "On the origin of the two-dimensional electron gas at the AlGaN/GaN heterostructure interface," *Appl. Phys. Lett.*, vol. 86, no. 4, p. 042 107, Jan. 2005.

[48] Y. Cai, Y. Zhou, K. J. Chen, and K. M. Lau, "High-performance enhancement-mode AlGaN/GaN HEMTs using fluoride-based plasma treatment," *IEEE Electron Device Lett.*, vol. 26, no. 7, pp. 435–437, Jun. 2005.

[49] X. Hu, G. Simin, J. Yang, M. A. Khan, R. Gaska, and M. S. Shur, "Enhancement mode AlGaN/GaN HFET with selectively grown pn junction gate," *Electron. Lett.*, vol. 36, no. 8, pp. 753–754, Apr. 2000.

[50] Y. Uemoto, M. Hikita, H. Ueno, H. Matsuo, H. Ishida, M. Yanagihara, T. Ueda, T. Tanaka, and D. Ueda, "Gate injection transistor (GIT)—a normally-off AlGaN/GaN power transistor using conductivity modulation," *IEEE Trans. Electron Devices*, vol. 54, no. 12, pp. 3393–3399, Nov. 2007.

[51] F. Bernardini, V. Fiorentini, and D. Vanderbilt, "Spontaneous polarization and piezoelectric constants of III-V nitrides," *Physical Rev. B*, vol. 56, no. 16, R10024–R10027, Oct. 1997.

[52] J. P. Ibbetson, P. T. Fini, K. D. Ness, S. P. DenBaars, J. S. Speck, and U. K. Mishra, "Polarization effects, surface states, and the source of electrons in AlGaN/GaN heterostructure field effect transistors," *Appl. Phys. Lett.*, vol. 77, no. 2, pp. 250–252, Jun. 2000.

[53] Y. Zhang, I. P. Smorchkova, C. R. Elsass, S. Keller, J. P. Ibbetson, S. Denbaars, U. K. Mishra, and J. Singh, "Charge control and mobility in AlGaN/GaN transistors: Experimental and theoretical studies," *J. Appl. Phys.*, vol. 87, no. 11, pp. 7981–7987, May 2000.

[54] I. P. Smorchkova, L. Chen, T. Mates, L. Shen, S. Heikman, B. Moran, S. Keller, S. P. DenBaars, J. S. Speck, and U. K. Mishra, "AlN/GaN and (Al,Ga)N/AlN/GaN two-dimensional electron gas structures grown by plasma-assisted molecular-beam epitaxy," *J. Appl. Phys.*, vol. 90, no. 10, pp. 5196–5201, Oct. 2001.

[55] D. K. Ferry, *Semiconductor Transport*. New York, NY, USA: CRC Press, 2000.

[56] L. Hsu and W. Walukiewicz, "Effect of polarization fields on transport properties in AlGaN/GaN heterostructures," *J. Appl. Phys.*, vol. 89, no. 3, pp. 1783–1789, Jan. 2001.

[57] L. Shen, S. Heikman, B. Moran, R. Coffie, N.-Q. Zhang, D. Buttari, I. Smorchkova, S. Keller, S. P. DenBaars, and U. K. Mishra, "AlGaN/AlN/GaN high-power microwave HEMT," *IEEE Electron Device Lett.*, vol. 22, no. 10, pp. 457–459, Oct. 2001.

[58] R. S. Balmer, K. P. Hilton, K. J. Nash, M. J. Uren, D. J. Wallis, A. Wells, M. Missous, and T. Martin, "AlGaN/GaN microwave HFET including a thin AlN carrier exclusion layer," *phys. stat. sol. (c)*, vol. 0, no. 7, pp. 2331–2334, Nov. 2003.

[59] N. Goyal and T. A. Fjeldly, "Effects of strain relaxation on bare surface barrier height and two-dimensional electron gas in $Al_xGa_{1-x}N$/GaN heterostructures," *J. Appl. Phys.*, vol. 113, no. 1, p. 014 505, Jan. 2013.

[60] O. Ambacher, J. Majewski, C. Miskys, A. Link, M. Hermann, M. Eickhoff, M. Stutzmann, F. Bernardini, V. Fiorentini, V. Tilak, B. Schaff, and L. F. Eastman, "Effects of strain relaxation on bare surface barrier height and two-dimensional electron gas in $Al_xGa_{1-x}N$/GaN heterostructures," *J. Phys. Condens. Matter*, vol. 14, no. 13, pp. 3399–3434, Mar. 2002.

[61] L. Shen, R. Coffie, D. Buttari, S. Heikman, A. Chakraborty, A. Chini, S. Keller, S. P. DenBaars, and U. K. Mishra, "High-power polarization-engineered GaN/AlGaN/GaN HEMTs without surface passivation," *IEEE Electron Device Lett.*, vol. 25, no. 1, pp. 7–9, Feb. 2004.

[62] T. Kikkawa, M. Nagahara, N. Okamoto, Y. Tateno, Y. Yamaguchi, N. Hara, K. Joshin, and P. M. Asbeck, "Surface-charge controlled AlGaN/GaN-power HFET without current collapse and gm dispersion," in *Proc. IEEE Int. Electron Devices Meeting*, Washington, DC, USA, Dec. 2001, pp. 1–4.

[63] G. Meneghesso, F. Rampazzo, P. Kordos, G. Verzellesi, and E. Zanoni, "Current collapse and high-electric-field reliability of unpassivated GaN/AlGaN/GaN HEMTs," *IEEE Trans. Electron Devices*, vol. 53, no. 12, pp. 2932–2941, Nov. 2006.

[64] O. Mitrofanov, M. Manfra, and N. Weimann, "Impact of Si doping on radio frequency dispersion in unpassivated GaN/AlGaN/GaN high-electron-mobility transistors grown by plasma-assisted molecular-beam epitaxy," *Appl. Phys. Lett.*, vol. 82, no. 24, pp. 4361–4363, Jun. 2003.

[65] R. Coffie, D. Buttari, S. Heikman, S. Keller, A. Chini, L. Shen, and U. K. Mishra, "p-capped GaN-AlGaN-GaN high-electron mobility transistors (HEMTs)," *IEEE Electron Device Lett.*, vol. 23, no. 10, pp. 588–590, Dec. 2002.

[66] B. M. Green, K. K. Chu, E. M. Chumbes, J. A. Smart, J. R. Shealy, and L. F. Eastman, "The effect of surface passivation on the microwave characteristics of undoped AlGaN/GaN HEMTs," *IEEE Electron Device Lett.*, vol. 21, no. 6, pp. 268–270, Jun. 2000.

[67] H. Kim, R. M. Thompson, V. Tilak, T. R. Prunty, J. R. Shealy, and L. F. Eastman, "Effects of SiN passivation and high-electric field on AlGaN-GaN HFET degradation," *IEEE Electron Device Lett.*, vol. 24, no. 7, pp. 421–423, Aug. 2003.

[68] A. Chini, D. Buttari, R. Coffie, S. Heikman, S. Keller, and U. K. Mishra, "12 W/mm power density AlGaN/GaN HEMTs on sapphire substrate," *Electron. Lett.*, vol. 40, no. 1, pp. 73–74, Jan. 2004.

[69] J. Kotani, M. Tajima, S. Kasai, and T. Hashizume, "Mechanism of surface conduction in the vicinity of Schottky gates on AlGaN/GaN heterostructures," *Appl. Phys. Lett.*, vol. 91, no. 9, p. 093 501, Aug. 2007.

[70] B. P. Gila, M. Hlad, A. H. Onstine, R. Frazier, G. T. Thaler, A. Herrero, E. Lambers, C. R. Abernathy, S. J. Pearton, T. Anderson, S. Jang, F. Ren, N. Moser, R. C. Fitch, and M. Freund, "Improved oxide passivation of AlGaN/GaN high electron mobility transistors," *Appl. Phys. Lett.*, vol. 87, no. 16, p. 163 503, Oct. 2005.

[71] S. Huang, Q. Jiang, S. Yang, C. Zhou, and K. J. Chen, "Effective passivation of AlGaN/GaN HEMTs by ALD-grown AlN thin film," *IEEE Electron Device Lett.*, vol. 33, no. 4, pp. 516–518, Feb. 2012.

[72] M. Sudow, M. Fagerlind, M. Thorsell, K. Andersson, N. Billstrom, P.-Å. Nilsson, and N. Rorsman, "An AlGaN/GaN HEMT-based microstrip MMIC process for advanced transceiver design," *IEEE Trans. Microw. Theory Techn.*, vol. 56, no. 8, pp. 1827–1833, Jul. 2008.

[73] Y.-F. Wu, A. Saxler, M. Moore, R. P. Smith, S. Sheppard, P. M. Chavarkar, T. Wisleder, U. K. Mishra, and P. Parikh, "30-W/mm GaN HEMTs by field plate optimization," *IEEE Electron Device Lett.*, vol. 25, no. 3, pp. 117–119, Mar. 2004.

[74] A. Brannick, N. A. Zakhleniuk, B. K. Ridley, J. R. Shealy, W. J. Schaff, and L. F. Eastman, "Influence of field plate on the transient operation of the AlGaN/GaN HEMT," *IEEE Electron Device Lett.*, vol. 30, no. 5, pp. 436–438, Apr. 2009.

[75] Y. Ando, Y. Okamoto, H. Miyamoto, T. Nakayama, T. Inoue, and M. Kuzuhara, "10-W/mm AlGaN-GaN HFET with a field modulating plate," *IEEE Electron Device Lett.*, vol. 24, no. 5, pp. 289–291, Jul. 2003.

[76] Y. Okamoto, Y. Ando, K. Hataya, T. Nakayama, H. Miyamoto, T. Inoue, M. Senda, K. Hirata, M. Kosaki, N. Shibata, and M. Kuzuhara, "Improved power performance for a recessed-gate AlGaN-GaN heterojunction FET with a field-modulating plate," *IEEE Trans. Microw. Theory Techn.*, vol. 52, no. 11, pp. 2536–2540, Nov. 2004.

[77] R. Thompson, T. Prunty, V. Kaper, and J. R. Shealy, "Performance of the AlGaN HEMT structure with a gate extension," *IEEE Trans. Electron Devices*, vol. 51, no. 2, pp. 292–295, Jan. 2004.

[78] W. Saito, T. Nitta, Y. Kakiuchi, Y. Saito, K. Tsuda, I. Omura, and M. Yamaguchi, "Suppression of dynamic on-resistance increase and gate charge measurements in high-voltage GaN-HEMTs with optimized field-plate structure," *IEEE Trans. Electron Devices*, vol. 54, no. 8, pp. 1825–1830, Jul. 2007.

[79] W. Saito, Y. Kakiuchi, T. Nitta, Y. Saito, T. Noda, H. Fujimoto, A. Yoshioka, T. Ohno, and M. Yamaguchi, "Field-plate structure dependence of current collapse phenomena in high-voltage GaN-HEMTs," *IEEE Electron Device Lett.*, vol. 31, no. 7, pp. 659–661, May 2010.

[80] H. Wang, J. Wei, R. Xie, C. Liu, G. Tang, and K. J. Chen, "Maximizing the performance of 650-V p-GaN gate HEMTs: Dynamic RON characterization and circuit design considerations," *IEEE Trans. Power Electron.*, vol. 32, no. 7, pp. 5539–5549, Sep. 2016.

[81] S. A. Vitusevich, O. A. Antoniuk, M. V. Petrychuk, S. V. Danylyuk, A. M. Kurakin, A. E. Belyaev, and N. Klein, "Low-frequency noise in AlGaN/GaN HEMT structures with AlN thin film layer," *phys. stat. sol. (c)*, vol. 3, no. 6, pp. 2329–2332, Jun. 2006.

[82] R. Vetury, N. Q. Zhang, S. Keller, and U. K. Mishra, "The impact of surface states on the DC and RF characteristics of AlGaN/GaN HFETs," *IEEE Trans. Electron Devices*, vol. 48, no. 3, pp. 560–566, Mar. 2001.

[83] M. J. Uren, J. Moreke, and M. Kuball, "Buffer design to minimize current collapse in GaN/AlGaN HFETs," *IEEE Trans. Electron Devices*, vol. 59, no. 12, pp. 3327–3333, Oct. 2012.

[84] S. C. Binari, W. Kruppa, H. B. Dietrich, G. Kelner, A. E. Wickenden, and J. A. F. Jr, "Fabrication and characterization of GaN FETs," *Solid-State Electron.*, vol. 41, no. 10, pp. 1549–1554, Oct. 1999.

[85] L. Zhang, L. F. Lester, A. G. Baca, R. J. Shul, P. C. Chang, C. G. Willison, U. K. Mishra, S. P. Denbaars, and J. C. Zolper, "Epitaxially-grown GaN junction field effect transistors," *IEEE Trans. Electron Devices*, vol. 47, no. 3, pp. 507–511, Mar. 2000.

[86] S. A. Albahrani, D. Mahajan, J. Hodges, Y. S. Chauhan, and S. Khandelwal, "ASM GaN: Industry standard model for GaN RF and power devices—part-II: Modeling of charge trapping," *IEEE Trans. Electron Devices*, vol. 66, no. 1, pp. 87–94, Sep. 2018.

[87] T. Mizutani, T. Okino, K. Kawada, Y. Ohno, S. Kishimoto, and K. Maezawa, "Drain current DLTS of AlGaN/GaN HEMTs," *Phys. Stat. Sol. (A)*, vol. 200, no. 1, pp. 195–198, Nov. 2003.

[88] J. Joh and J. A. del Alamo, "A current-transient methodology for trap analysis for GaN high electron mobility transistors," *IEEE Trans. Electron Devices*, vol. 58, no. 1, pp. 132–140, Nov. 2010.

[89] O. Jardel, F. D. Groote, T. Reveyrand, J.-C. Jacquet, C. Charbonniaud, J.-P. Teyssier, D. Floriot, and R. Quere, "An electrothermal model for AlGaN/GaN power HEMTs including trapping effects to improve large-signal simulation results on high VSWR," *IEEE Trans. Microw. Theory Techn.*, vol. 55, no. 12, pp. 2660–2669, Dec. 2007.

[90] A. Santarelli, R. Cignani, G. P. Gibiino, D. Niessen, P. A. Traverso, C. Florian, D. M. M. -P. Schreurs, and F. Filicori, "A double-pulse technique for the dynamic I/V characterization of GaN FETs," *IEEE Microw. Wireless Compon. Lett.*, vol. 24, no. 2, pp. 132–134, Dec. 2013.

[91] J. L. Gomes, L. C. Nunes, C. F. Gonçalves, and J. C. Pedro, "An accurate characterization of capture time constants in GaN HEMTs," *IEEE Trans. Microw. Theory Techn.*, vol. 67, no. 7, pp. 2465–2474, Jul. 2019.

[92] N. K. Subramani, J. Couvidat, A. A. Hajjar, J.-C. Nallatamby, R. Sommet, and R. Quéré, "Identification of GaN buffer traps in microwave power AlGaN/GaN HEMTs through low frequency S-parameters measurements and TCAD-based physical device simulations," *IEEE J. Electron Devices Soc.*, vol. 5, no. 3, pp. 175–181, Mar. 2017.

[93] M. Bouslama, V. Gillet, C. Chang, J.-C. Nallatamby, R. Sommet, M. Prigent, R. Quéré, and B. Lambert, "Dynamic performance and characterization of traps using different measurements techniques for the new AlGaN/GaN HEMT of 0.15-μm ultrashort gate length," *IEEE Trans. Microw. Theory Techn.*, vol. 67, no. 7, pp. 2475–2482, Apr. 2019.

[94] S. D. Nsele, L. Escotte, J.-G. Tartarin, S. Piotrowicz, and S. L. Delage, "Broadband frequency dispersion small-signal modeling of the output conductance and transconductance in AlInN/GaN HEMTs," *IEEE Trans. Electron Devices*, vol. 60, no. 4, pp. 1372–1378, Mar. 2013.

[95] C. Potier, A. Martin, M. Campovecchio, S. Laurent, R. Quere, J. C. Jacquet, O. Jardel, S. Piotrowicz, and S. Delage, “Trap characterization of microwave GaN HEMTs based on frequency dispersion of the output-admittance,” in *Proc. Eur. Microw. Integr. Circuit Conf.*, Rome, Italy, Dec. 2014, pp. 464–467.

[96] J. L. Gomes, L. C. Nunes, and J. C. Pedro, “Explaining the different time constants extracted from low frequency Y_{22} and I_{DS}-DLTS on GaN HEMTs,” in *Proc. IEEE MTT-S Int. Microw. Symp.*, Los Angeles, CA, USA, Jun. 2020, pp. 432–435.

[97] F. D. Groote, P. Roblin, Y.-S. Ko, C.-K. Yang, S. J. Doo, M. V. Bossche, and J.-P. Teyssier, “Pulsed multi-tone measurements for time domain load pull characterizations of power transistors,” in *Proc. ARFTG Microw. Meas. Conf.*, Boston, MA, USA, Jun. 2009, pp. 1–4.

[98] P. Roblin, D. E. Root, J. Verspecht, Y. Ko, and J. P. Teyssier, “New trends for the nonlinear measurement and modeling of high-power RF transistors and amplifiers with memory effects,” *IEEE Trans. Microw. Theory Techn.*, vol. 60, no. 6, pp. 1964–1978, May 2012.

[99] L. C. Nunes, J. L. Gomes, P. M. Cabral, and J. C. Pedro, “A simple method to extract trapping time constants of GaN HEMTs,” in *Proc. IEEE MTT-S Int. Microw. Symp.*, Philadelphia, PA, USA, Jun. 2018, pp. 716–719.

[100] H. Hasegawa, T. Inagaki, S. Ootomo, and T. Hashizume, “Mechanisms of current collapse and gate leakage currents in AlGaN/GaN heterostructure field effect transistors,” *J. Vac. Sci. Technol. B*, vol. 21, no. 4, pp. 1844–1855, Aug. 2003.

[101] I. Angelov, L. Bengtsson, and M. Garcia, “Extensions of the Chalmers nonlinear HEMT and MESFET model,” *IEEE Trans. Microw. Theory Techn.*, vol. 44, no. 10, pp. 1664–1674, Oct. 1996.

[102] S. DasGupta, M. Sun, A. Armstrong, R. J. Kaplar, M. J. Marinella, J. B. Stanley, S. Atcitty, and T. Palacios, “Slow detrapping transients due to gate and drain bias stress in high breakdown voltage AlGaN/GaN HEMTs,” *IEEE Trans. Electron Devices*, vol. 59, no. 8, pp. 2115–2122, May 2012.

[103] D. Bisi, M. Meneghini, C. de Santi, A. Chini, M. Dammann, P. Brückner, M. Mikulla, G. Meneghesso, and E. Zanoni, “Deep-level characterization in GaN HEMTs-Part I: Advantages and limitations of drain current transient measurements,” *IEEE Trans. Electron Devices*, vol. 60, no. 10, pp. 3166–3175, Sep. 2013.

[104] J. G. Rathmell and A. E. Parker, “Circuit implementation of a theoretical model of trap centres in GaAs and GaN devices,” in *Proc. SPIE Microelectron. MEMS Nanotechnol.*, vol. 6798, Canberra, ACT, Australia, Dec. 2007, 67980R.

[105] S. C. Binari, P. B. Klein, and T. E. Kazior, “Trapping effects in GaN and SiC microwave FETs,” *Proc. IEEE*, vol. 90, no. 6, pp. 1048–1058, Nov. 2002.

[106] A. C. Clarke, “Extra-terrestrial relays,” *Wireless World*, vol. 51, no. 10, pp. 305–308, Oct. 1945.

[107] J. R. Pierce, “Orbital radio relays,” *Jet Propulsion*, vol. 25, no. 4, pp. 153–157, Apr. 1955.

[108] H. Girard and K. Feher, "A new baseband linearizer for more efficient utilization of earth station amplifiers used for QPSK transmission," *IEEE J. Sel. Areas Commun.*, vol. 1, no. 1, pp. 46–56, Jan. 1983.

[109] G. Satoh and T. Mizuno, "Impact of a new TWTA linearizer upon QPSK/TDMA transmission performance," *IEEE J. Sel. Areas Commun.*, vol. 1, no. 1, pp. 39–45, Jan. 1983.

[110] C. Haskins, "Diode predistortion linearization for power amplifier RFICs in digital radios," M.S. thesis, Virginia Polytechnic Institute and State University, 2000.

[111] K. Yamauchi, K. Mori, M. Nakayama, Y. Itoh, Y. Mitsui, and O. Ishida, "A novel series diode linearizer for mobile radio power amplifiers," in *Proc. IEEE MTT-S Int. Microw. Symp.*, San Francisco, CA, USA, Jun. 1996, pp. 831–834.

[112] Y. Shen, B. Hraimel, X. Zhang, G. E. R. Cowan, K. Wu, and T. Liu, "A novel analog broadband RF predistortion circuit to linearize electro-absorption modulators in multiband OFDM radio-over-fiber systems," *IEEE Trans. Microw. Theory Techn.*, vol. 58, no. 11, pp. 3327–3335, Nov. 2010.

[113] R. Zhu, Z. Xuan, Y. Zhang, X. Zhang, and D. Shen, "Novel broadband analog predistortion circuit for radio-over-fiber systems," in *Proc. IEEE MTT-S Int. Microw. Symp.*, Phoenix, AZ, USA, May 2015, pp. 1–4.

[114] J. Yi, Y. Yang, M. Park, W. Kang, and B. Kim, "Analog predistortion linearizer for high-power RF amplifiers," *IEEE Trans. Microw. Theory Techn.*, vol. 48, no. 12, pp. 2709–2713, Dec. 2000.

[115] S.-Y. Lee, Y.-S. Lee, S.-H. Hong, H.-S. Choi, and Y.-H. Jeong, "Independently controllable 3rd- and 5th-order analog predistortion linearizer for RF power amplifier in GSM," in *Proc. IEEE Asia-Pacific Conf. Adv. Syst. Integr. Circuits*, Fukuoka, Japan, Aug. 2004, pp. 146–149.

[116] Y.-S. Lee, M.-W. Lee, S.-W. Jung, and Y.-H. Jeong, "Analog predistortion power amplifier using IMD sweet spots for WCDMA applications," in *Proc. Asia-Pacific Microw. Conf.*, Bangkok, Thailand, Jun. 2008, pp. 1–4.

[117] X. L. Sun, S. W. Cheung, and T. Yuk, "Design of a fifth-order analog predistorter for base station HPA of cellular mobile systems," *Microw. J.*, vol. 54, no. 8, pp. 86–102, Aug. 2011.

[118] Y. Kim, K.-K. Jeon, E.-K. Kim, and B.-C. Kim, "An analog linearizer based on amplitude modulation with even harmonic signals," *Microw. J.*, vol. 52, no. 2, pp. 80–90, Feb. 2009.

[119] Y. Kim, I.-S. Chang, and Y.-C. Jeong, "An analog predistortion linearizer design," *Microw. J.*, vol. 48, no. 2, pp. 118–126, Feb. 2005.

[120] H. E. Jones, "Dual output synchronous detector utilizing transistorized differential amplifiers," US3241078 A, Mar. 1966.

[121] E. Westesson and L. Sundström, "A complex polynomial predistorter chip in CMOS for baseband or IF linearization of RF power amplifiers," in *Proc. IEEE Int. Symp. Circuits Syst.*, Orlando, FL, USA, May 1999, pp. 207–209.

[122] E. Westesson and L. Sundström, "Low-power complex polynomial predistorter circuit in CMOS for RF power amplifier linearization," in *Proc. European Solid-State Circuits Conf.*, Villach, Austria, Sep. 2001, pp. 486–489.

[123] T. Rahkonen, O. Kursu, M. Riikola, J. Aikio, and T. Tuikkanen, "Performance of an integrated 2.1 GHz analog predistorter," in *Proc. Int. Workshop Integr. Nonlinear Microw. Millimiter-Wave Circuits*, Aveiro, Portugal, Jan. 2006, pp. 34–37.

[124] F. Roger, "A 200mW 100MHz-to-4GHz 11th-order complex analog memory polynomial predistorter for wireless infrastructure RF amplifiers," in *Proc. IEEE Int. Solid-State Circuits. Conf.*, San Francisco, CA, USA, Mar. 2013, pp. 94–95.

[125] L. Gatet, H. Tap-Béteille, M. Lescure, D. Roviras, and A. Mallet, "Functional tests of a 0.6 μm CMOS MLP analog neural network for fast on-board signal processing," *Analog Integr. Circuits Signal Processing, Springer*, vol. 54, no. 3, pp. 219–227, Mar. 2008.

[126] B. Gilbert, "A precise four-quadrant multiplier with subnanosecond response," *IEEE J. Solid-State Circuits*, vol. 3, no. 4, pp. 365–373, Dec. 1968.

[127] L. Gatet, F. Bony, H. Tap-Beteille, E. Moutaye, F. Jayat, D. Roviras, and F. Gizard, "Embedded updating system based on integrated NNs in order to achieve adaptative predistortion of nonlinear HPA characteristics," in *Proc. IEEE Instrum. Meas. Technol. Conf.*, Singapore, Singapore, May 2009, pp. 1–4.

[128] B. Mulliez, E. Moutaye, H. Tap, L. Gatet, and F. Gizard, "Predistortion system implementation based on analog neural networks for linearizing high power amplifiers transfer characteristics," in *Proc. Int. Conf. Telecommun. Signal Process.*, Rome, Italy, Jul. 2013, pp. 412–416.

[129] J. Kim and K. Konstantinou, "Digital predistortion of wideband signals based on power amplifier model with memory," *Electronics Letters*, vol. 37, no. 23, pp. 1417–1418, Nov. 2001.

[130] D. R. Morgan, Z. Ma, J. Kim, M. G. Zierdt, and J. Pastalan, "A generalized memory polynomial model for digital predistortion of RF power amplifiers," *IEEE Trans. Signal Process.*, vol. 54, no. 10, pp. 3852–3860, Sep. 2006.

[131] E. Ngoya, C. Quindroit, and J.-M. Nebus, "Improvements on long term memory modeling in power amplifiers," in *Proc. IEEE MTT-S Int. Microw. Symp.*, Boston, MA, USA, Jun. 2009, pp. 1–4.

[132] J. C. Pedro and S. A. Maas, "A comparative overview of microwave and wireless power-amplifier behavioral modeling approaches," *IEEE Trans. Microw. Theory Techn.*, vol. 53, no. 4, pp. 1150–1163, Apr. 2005.

[133] A. Katz, J. Wood, and D. Chokola, "The evolution of PA linearization: From classic feedforward and feedback through analog and digital predistortion," *IEEE Microw. Mag.*, vol. 17, no. 2, pp. 32–40, Feb. 2016.

[134] J. C. Pedro, P. M. Cabral, T. R. Cunha, and P. M. Lavrador, "A multiple time-scale power amplifier behavioral model for linearity and efficiency calculations," *IEEE Trans. Microw. Theory Techn.*, vol. 61, no. 1, pp. 606–615, Jan. 2013.

[135] C. Maziere, A. Soury, E. Ngoya, and J. M. Nebus, “A system level model of solid state amplifiers with memory based on a nonlinear feedback loop principle,” in *Proc. Eur. Microw. Conf.*, Paris, France, Oct. 2005, pp. 1–4.

[136] S. Boumaiza and F. M. Ghannouchi, “Thermal memory effects modeling and compensation in RF power amplifiers and predistortion linearizers,” *IEEE Trans. Microw. Theory Techn.*, vol. 51, no. 12, pp. 2427–2433, Dec. 2003.

[137] A. S. Tehrani, T. Eriksson, and C. Fager, “Modeling of long term memory effects in RF power amplifiers with dynamic parameters,” in *Proc. IEEE MTT-S Int. Microw. Symp.*, Montreal, QC, Canada, Jun. 2012, pp. 1–3.

[138] “*GSM/EDGE radio transmission and reception*,” 3rd Generation Partnership Project (3GPP), Technical Specification (TS) 45.005 Version 14.3.0, Dec. 2017.

[139] K. Kunihiro and Y. Ohno, “A large-signal equivalent circuit model for substrate-induced drain-lag phenomena in HJFETs,” *IEEE Trans. Electron Devices*, vol. 43, no. 9, pp. 1336–1342, Sep. 1996.

[140] J. C. Pedro, L. C. Nunes, and P. M. Cabral, “Soft compression and the origins of nonlinear behavior of GaN HEMTs,” in *Proc. Eur. Microw. Integr. Circuit Conf.*, Rome, Italy, Oct. 2014, pp. 1–4.

[141] G. Simin, A. Koudymov, A. Tarakji, X. Hu, J. Yang, M. A. Khan, M. S. Shur, and R. Gaska, “Induced strain mechanism of current collapse in AlGaN/GaN heterostructure field-effect transistors,” *Appl. Phys. Lett.*, vol. 79, no. 16, pp. 2651–2653, Oct. 2001.

[142] S. Huang, S. Yang, J. Roberts1, and K. J. Chen, “Threshold voltage instability in Al2O3/GaN/AlGaN/GaN metal–insulator–semiconductor high-electron mobility transistors,” *Jpn. J. Appl. Phys.*, vol. 50, no. 11R, p. 110 202, Oct. 2011.

[143] P. Horowitz and W. Hill, *The Art of Electronics*, 3rd. New York, NY, USA: Cambridge University Press, 2015.

[144] J. Xu, R. Jones, S. A. Harris, T. Nielsen, and D. E. Root, “Dynamic FET model–DynaFET–for GaN transistors from NVNA active source injection measurements,” in *Proc. IEEE Int. Microw. Symp.*, Tampa, FL, USA, Jun. 2014, pp. 1–3.

[145] P. M. Cabral, J. C. Pedro, and N. B. Carvalho, “Nonlinear device model of microwave power GaN HEMTs for high power-amplifier design,” *IEEE Trans. Microw. Theory Techn.*, vol. 52, no. 11, pp. 2585–2592, Nov. 2004.

[146] J. Peroulas and A. You, “Method and apparatus for linearizing a non-linear power amplifier,” US8482349 B2, Jul. 2013.

[147] J. Chani-Cahuana, P. N. Landin, C. Fager, and T. Eriksson, “Iterative learning control for RF power amplifier linearization,” *IEEE Trans. Microw. Theory Techn.*, vol. 64, no. 9, pp. 2778–2789, Jul. 2016.

[148] N. Hansen and A. Ostermeier, “Completely derandomized self-adaptation in evolution strategies,” *Evol. Comput.*, vol. 9, no. 2, pp. 159–195, Jun. 2001.

[149] “*NR; Base station (BS) conformance testing Part 1: Conducted conformance testing*,” 3rd Generation Partnership Project (3GPP), Technical Specification (TS) 38.141-1 Version 16.3.0, Mar. 2020.

[150] M. A. Richards, J. A. Scheer, and W. A. Holm, *Principles of Modern Radar: Basic Principles*, First. Edison, NJ, USA: SciTech Publishing, 2010.

[151] G. Formicone, J. Burger, and J. Custer, "150 V-bias RF GaN for 1 kW UHF radar amplifiers," in *Proc. IEEE Compound Semicond. Integr. Circuit Symp.*, Austin, TX, USA, Oct. 2016, pp. 1–4.

[152] S. Fakhfakh, A. Martin, M. Campovecchio, G. Neveux, and D. Barataud, "On-wafer time-domain and low-frequency measurements of GaN HEMTs for accurate trap modeling and its impact on pulse-to-pulse stability," in *Proc. Int. Workshop Integr. Nonlinear Microw. Millimetre-wave Circuits*, Brive La Gaillarde, France, Jul. 2018, pp. 1–3.

[153] C. Florian, T. Cappello, A. Santarelli, D. Niessen, F. Filicori, and Z. Popović, "A prepulsing technique for the characterization of GaN power amplifiers with dynamic supply under controlled thermal and trapping states," *IEEE Trans. Microw. Theory Techn.*, vol. 65, no. 12, pp. 5046–5062, Jul. 2017.

[154] L. C. Nunes, D. R. Barros, P. M. Cabral, and J. C. Pedro, "Efficiency degradation analysis in wideband power amplifiers," *IEEE Trans. Microw. Theory Techn.*, vol. 66, no. 12, pp. 5640–5651, Dec. 2018.